University of South Wales

2059391

Bound by
Abbey
Bookbinding Co.
105 Cathays Terrace, Cardiff CF24 4HU
South Wales, U.K. Tel: (029) 2039 5882
www.bookbindersuk.com
Email: mail@bookbindersuk.com

Time-frequency analysis of Doppler ultrasound blood flow signals: An investigation into automated diagnosis of vascular disease

Ralf Patz

A thesis submitted in partial fulfilment of the requirements
of the University of Glamorgan for the degree of
Doctor of Philosophy

School of Electronics
University of Glamorgan
Pontypridd
CF37 1DL

23rd May 2003

Certificate of Research

This is to certify that, except where specific reference is made, the work described in this thesis is the result of the candidate. Neither this thesis, nor any part of it, has been presented, or is currently submitted, in candidature for any degree at any other University.

Signed .....
Candidate

Signed .....
Director of Studies

Date 14/11/2003

Acknowledgments

I like to thank all my friends and colleagues who have supported and encouraged me throughout the course of this work. To name all here would be impossible as I would certainly forget someone. However, I like to acknowledge some people individually.

Firstly, I like to thank my Director of Studies, Prof. M. A. Wahab, for his supervision and guidance. His continuous support throughout this project and his comments during the writing of this thesis were invaluable. My gratitude also extends to my supervisor, Prof. R. J. Williams, for his valuable suggestions.

I would also like to thank Dr. N. Gough and G. Baily from Huntleigh Diagnostics Ltd for their assistance and to acknowledge the support and help from Prof. J. Woodcock and L. Boden from the University Hospital of Wales College of Medicine.

Many thanks also go to Frank and Ulli, with whom I had many fruitful discussions regarding signal processing.

I would also like to thank Sahar and Iain for volunteering for the laborious job of proof-reading this thesis.

Thanks to Nathalie, who put up with me during the long hours I spent on this project, for her never-ending support and encouragement.

Finally, I would like to thank my family for their support.

Abstract

This study investigated an automated classification and diagnosis process for Doppler ultrasound blood flow signals to support clinical decision making. This process is used in this study to diagnose the severity of vascular disease in the lower limb. The study reviewed the existing methods for clinical decision making and proposed a multi-stage process of pre-processing, feature extraction and classification. Each stage was investigated separately and then combined to an automated classification and diagnosis process. Clinical Doppler ultrasound blood flow signals from the lower limb were used to compare existing methods with the novel methods proposed in this study.

The pre-processing stage normally requires the intervention of an operator to select a noise reduction threshold. The novel approach of utilising the Wavelet-based noise reduction method in this study has removed the need for human intervention. Detailed investigations of the feature extraction stage were conducted with the aim to automate and improve the algorithms. Results from these investigations showed that the algorithms proposed in this study, not only automated, but also improved the extraction of the feature vector. Artificial Neural Networks (ANNs) were used to investigate the classification of the Doppler ultrasound blood flow signals into different classes of disease severity.

The results from the investigation into the overall process have proven the full automation of the classification and diagnosis process. This study demonstrated that the introduction of the algorithms proposed in this study significantly improved the diagnosis result over traditional manual methods.

Contents

List of Figures

List of Tables

Glossary

Symbol	Description
α	Angle between ultrasound receiver and moving particles
Δf	Frequency resolution
Δt	Time resolution
η	Learning rate increase factor
$\Psi^*_{(b,a)}$	Complex conjugate of $\Psi_{(b,a)}$
$\Psi^{2p+1}_{j+1}(t)$	Wavelet Packet Transform coefficient
$\Psi_{(b,a)}(t)$	Mother wavelet
ρ	Learning rate decrease factor
σ	Standard deviation
ξ	Percentage of error increase
a	Wavelet Transform scale parameter
$a(k)$	Actual output of the k^{th} signal vector
b	Wavelet Transform translation parameter
BW	Bandwidth
c	Speed of an ultrasonic wave in surrounding material
d	Length of the maximum frequency envelope in samples
D_{est}	Estimated cardiac peak-to-peak distance
e	Combined blood flow envelope
$e(k)$	Error of the k^{th} signal vector
e_f	Forward blood flow envelope

e_r	Reverse blood flow envelope
F_d	Doppler frequency
F_t	Frequency of wave transmitted from the ultrasonic probe
f_{centre}	Filter centre frequency
f_{max}	Maximum frequency
f_{mean}	Mean frequency
f_{MFE}	Fundamental frequency of the maximum frequency envelope
f_s	Time domain sampling frequency
$g[n]$	High-pass filter coefficients
$h[n]$	Low-pass filter coefficients
j	Number of time slots fitting into the signal
k	Index of harmonic number
L	Root level of Wavelet Transform decomposition
L_w	Short-Time Fourier transform window length
lr	Learning rate
M	Length of the filter bank
m	Short-Time Fourier transform window index
mc	Momentum
MFE_{95}	Maximum Frequency Envelope created using the percentile method
MFE_{Dist}	Maximum Frequency Envelope created using the distance method
N	Sample length
n	Discrete sample index
N_s	Length of the signal
N_w	Length of the Short-Time Fourier transform window
$O(N)$	Number of multiplications and additions
o_w	Overlap of the Short-Time Fourier transform window
$P_B[b,t]$	Cumulative power matrix
P_T	Total cumulative power
$P_{f_{max}}$	Cumulative power at the maximum frequency
P_{N95}	95% power vector
Q	Relative bandwidth
r	Level of Wavelet Packet decomposition
T	Wavelet coefficient threshold
$t(k)$	Target output of the k^{th} signal vector

v	Velocity
V_{max}	Maximum velocity of the blood flow
V_{mean}	Mean velocity of the blood flow
V_{min}	Minimum velocity of the blood flow
$w(m)$	Short-Time Fourier transform window
$W(x[n])$	Wavelet Transform of $x[n]$
x	Input data
$x(t)$	Continuous input data
$X[k]$	Fourier transform of $x[n]$
$x[n]$	Discrete input data

Abbreviations

ABPI	Ankle-Brachial Pressure Index
ANN	Artificial Neural Network
AQD	Adaptive Constant-Q Distribution
AR	Autoregressive Modelling
ARMA	Autoregressive Moving Average Modelling
BD	Bessel Distribution
BP	Back-Propagation
CFA	Common Femoral Artery
CWD	Choi-Williams Distribution
DFT	Discrete Fourier Transform
DWMTM	Double Window Modified Trimmed Mean
ECG	Electrocardiogram
EIA	External Iliac Artery
FFT	Fast Fourier Transform
FIR	Finite Impulse Response
FN	False Negative Decision
FP	False Positive Decision
HWI	Height Width Index
HWI	Height Width Index
LTA	Laplace Transform Analysis
MA	Moving Average Modelling

MFE	Maximum Frequency Envelope
MLM	Maximum Likelihood Method
MSE	Mean-Square-Error
PCA	Principal Component Analysis
PI	Pulsatility Index
PLI	Path Length Index
PWTT	Pulse Wave Transit Time
RFRI	Relative Flow Rate Index
RI	Pourcelot's Resistance Index
RID	Reduced Interference Distribution
RMSE	Root-Mean-Square-Error
ROC	Receiver Operating Characteristic
RTR	Rise Time Ratio
SBI	Spectral Broadening Index
SDTI	Systolic Decay Time Index
SNR	Signal-to-Noise Ratio
SPWD	Smoothed Pseudo Wigner Distribution
STFT	Short-Time Fourier Transform
TFA	Transfer Function Analysis
TFD	Time-Frequency Distribution
TN	True Negative Decision
TP	True Positive Decision
WPT	Wavelet Packet Transform
WT	Wavelet Transform

Chapter 1

Introduction

1.1 Background of study

Vascular disease is one of the major causes of mortality in the developed world, with atherosclerosis as one of the most common types. The factors associated with the development of arterial disease include high concentration of cholesterol in blood, smoking, high blood pressure and diabetes [1, 2]. Atherosclerosis in the lower limb progresses over time and causes intermittent claudication due to the narrowing of the artery. Symptoms include pain and cramping in the leg muscles whilst walking.

In the past, angiography was considered the 'gold standard' for the assessment of lower limb arterial disease. Angiography relies on X-ray in conjunction with X-ray contrast media and provides an anatomical view of the vascular system. It is therefore, an invasive method with its associated risks to the patient [2].

However, in recent years the Doppler ultrasound spectrum and image were used for the investigation of vascular disease [2]. The advantage of Doppler ultrasound is that it is a non-invasive technique for the assessment of hemodynamic flow conditions within blood vessels and cardiac cavities [3]. Diagnostic information is extracted

from the Doppler blood flow signal which results from the backscattering of the ultrasonic beam by moving red blood cells [4].

Duplex scanning provides a functional map of the vascular segment in the form of a colour flow image. Blood flow in arteries and veins is colour coded and superimposed onto the anatomical view which is provided by pulse echo imaging. Spectral Doppler analysis allows the recording of Doppler waveforms from a vessel and to visualise flow patterns within the vessel. The shape of the Doppler waveform is linked to the severity of the disease and therefore, spectral Doppler analysis allows the clinician to grade the severity of the disease [2]. The indices extracted from the Doppler waveform are used to improve the diagnosis. Spectral Doppler analysis is used on its own in flowmeters or together with the Doppler image in a Duplex scanner.

Duplex scanning together with spectral Doppler analysis provide a functional view and a Doppler waveform from the vessel, enabling the diagnosis of the vascular system. Although, this is generally true, there are vascular segments that cannot be visualised using Duplex scanning. The aorto-iliac segment, for example, lies behind the peritoneum, which contains the bowel. Obesity and bowel gas can cause unsatisfactory results of the Duplex image scan. Spectral Doppler analysis using the Doppler waveform is in these cases the only available method. The spectrum of the Doppler blood flow signal, the extracted Doppler blood velocity waveform and indices can generally provide good diagnostic tools for the detection of disease in the aorto-iliac segment, but are less sensitive to disease in the femoral-popliteal segment [1, 5]. In cases where the femoral-popliteal segment is also diseased the accuracy of the existing indices, such as the Pulsatility Index (PI), to detect arterial disease in the aorto-iliac segment is dramatically reduced [6, 7].

Spectral Doppler analysis is a non-trivial problem. Due to the random spatial

distribution of red blood cells and the dynamics of the cardiovascular system, the Doppler blood flow signal is a time-varying random signal which requires time-frequency analysis to determine its power and frequency variation over time [8]. The time-frequency distribution of the Doppler blood flow signal is usually computed using the Short-Time Fourier Transform, and the resulting distribution is called the spectrogram or sonogram. For most clinical applications, the three-dimensional sonogram is interpreted subjectively by clinicians and trained operators to determine clinical conditions, such as extracranial carotid disease and occlusive arterial disease of the lower limb [9].

Several computational techniques were suggested to remove the subjectivity from the blood flow Doppler ultrasound diagnosis process. The majority of these methods utilised the maximum frequency envelope of the sonogram, thus discarding the information contained in the power components at other frequencies. Crude indices, such as the PI and Resistance index, were used to quantify the features of the sonogram and more complex methods such as the Laplace Transform and Principal Components Analysis were proposed [6,7,10–16]. Most of these computational techniques did not provide a reliable alternative to subjective visual inspection of the sonogram which is still widely used [17].

A pilot study carried out by the University of Glamorgan and the University of Wales College of Medicine demonstrated that new classification techniques, which use the maximum frequency envelope, can distinguish between Doppler ultrasound signals that are recorded from different parts of the body. The classification was performed by Artificial Neural Networks (ANNs) [18]. Although ANNs were also used to classify signals from diseased arteries [1, 19, 20], the pre-processing of the signals was still dependent on decisions by an operator. Such dependency can only be removed by introducing a fully automated classification and diagnosis system.

An automated system will reduce the variability introduced by the operator and provide support to the clinician. Such a system will not be aimed to replace the decision making process for major surgery, but to indicate at an early stage if further investigations, such as angiography and colour Doppler imaging, are required.

Furthermore, more advanced analysis techniques have become available recently. Emerging multi-resolution signal analysis techniques, such as the Wavelet Transform, provided promising solutions to signal processing and analysis problems in a wide range of applications such as speech recognition, condition monitoring of machinery and medical diagnosis [21–25].

Commercial Doppler ultrasound blood flow diagnostic equipment range from low cost portable flowmeters to expensive stand-alone scanners. Portable flowmeters provide crude blood velocity measurement with audible output of the Doppler signal. Stand-alone scanners are available with analysis features including sonogram generation and maximum frequency envelope extraction. Imaging Doppler ultrasound systems provide an accurate diagnosis of the disease in blood vessels, but they are very expensive and are not suitable for use in primary healthcare.

Therefore, there is a significant need for research work into reliable processing and analysis methods of Doppler ultrasound blood flow signals to provide automated diagnosis of cardiovascular disease. This requires investigation of the applicability of modern signal analysis methods and pattern recognition techniques to complex non-stationary Doppler ultrasound clinical signals.

1.2 Aims and objectives of the study

This study was aimed at addressing the limitations of existing analysis methods of blood flow Doppler ultrasound signals that have prevented the emergence of

fully automated diagnosis systems for the assessment of vascular diseases. This was achieved by investigating the effectiveness of innovative signal processing techniques and their impact on transforming the complex non-stationary Doppler ultrasound signal into forms that are suitable for automated feature extraction and clinical decision making. More specifically, the objectives of the research work included:

- Review of previous research work and techniques, which were used in the field of Doppler ultrasound blood flow analysis.
- Investigation into novel techniques for processing Doppler ultrasound blood flow signals with emphasis on the Wavelet Transform for noise reduction and signal transformation.
- Investigation into feature extraction and classification methods for Doppler ultrasound blood flow signals.
- Application of signal processing and analysis techniques to real lower limb Doppler ultrasound blood flow signals for the purpose of fully automated clinical decision making. This involved the investigation of the feasibility of detecting the presence of significant aorto-iliac disease on the basis of the common femoral artery waveform, regardless of the state of the femoral-popliteal segment.

1.3 Collaboration

This work was conducted with the support of the University of Wales College of Medicine and Huntleigh Healthcare Ltd who provided recordings of clinical Doppler ultrasound blood flow signals and advice on practical problems associated with the assessment of vascular disease.

1.4 This thesis

This thesis addresses the issues identified earlier and presents the research work conducted in this study.

Chapter 2 presents the literature review and covers the origins of the Doppler ultrasound blood flow signal and its capture mechanisms. It details previous work in the processing and transformation of these signals to enable clinical personnel to assess the presence and degree of the cardiovascular disease. It outlines previous research into quantifying the profile of Doppler ultrasound signals, feature extraction and automated diagnosis.

Chapter 3 presents the investigations into the transformation of the blood flow signal into the time-frequency domain. Furthermore, the investigation of the automation of the background noise reduction is described. Results from applying different noise reduction techniques are presented.

Feature extraction from the sonogram is presented in chapter 4. This chapter presents the investigations into the required processing stages from the sonogram to the extraction of the feature vector that can be presented to a classifier. This included the computation of the maximum frequency envelope of the sonogram, as one of the most important feature vectors of the blood flow signal, and the extraction of a single cardiac cycle. A new approach of presenting the feature vector to the classifier using the Wavelet Transform is proposed and the calculation of an additional feature, the Spectral Broadening Index (SBI), is shown.

Chapter 5 presents the reasons for choosing ANNs as the preferred classifier and their performance measures. The clinical lower limb blood flow signals used in this study are detailed in chapter 5. The transformation of these signals into a range of ANN feature vectors is described. This is included with a full presentation of the

overall results of the study.

The discussion of the individual investigations and the overall results of this study is presented in chapter 6, which include signal transformation and feature extraction together with classification and decision making processes. Each investigation covered in chapters 3 to 5 is discussed individually before the effects of the combination of the different processing algorithms are discussed.

Chapter 7 presents conclusions resulting from the comprehensive literature review and the research work conducted by the candidate. Suggestions of further work for the research are also presented.

Chapter 2

Doppler Ultrasound blood flow measurements and analysis - Review of literature

This chapter presents a review of previous work in Doppler ultrasound blood flow measurements for the diagnosis of vascular disease. The literature review covers the physics and acquisition methods of Doppler ultrasound blood flow signals (section 2.1). It presents the signal processing and transformation methods used to convert the blood flow signal into forms suitable for use in clinical diagnosis (section 2.2 and 2.3). The analysis techniques utilised for extracting relevant features from the Doppler ultrasound signal to aid the clinical diagnosis process are presented with previous work on the interpretation of these features including classification and decision making (section 2.4 and 2.5). A review of the research into automated systems for Doppler ultrasound blood flow classification and decision making is given in section 2.6. The chapter concludes with section 2.7, which outlines the limitations of previous processing and analysis methods of blood flow signals. It also identifies

the areas where further research work is needed to improve the automated clinical decision making process relating to the diagnosis of vascular diseases.

2.1 Doppler ultrasound blood flow measurements

2.1.1 Blood flow and cardiovascular disease

The vascular system consists of trees of elastic arteries and veins, which are connected together at the very end of their branches. The heart represents a pulsatile pump driving the blood through the vascular system. The blood flow velocity profile in the arteries depends greatly on the pressure generated by the heart, the position within the tree, the elasticity of the artery segment and the impedance of the vascular bed supplying the organs [26].

Woodcock [27] suggested that the Doppler blood flow velocity waveform of each artery in the human body has a unique characteristic by which it may be identified. Figure 2.1 shows a typical blood flow velocity waveform of (a) a common carotid artery and (b) a common femoral artery (CFA) which respectively, provides a low and high resistance vascular bed.

The velocity waveform in figure 2.1 represents only the maximum blood flow velocity. Blood does not flow with one velocity through the cardiovascular vessels, rather it flows with a number of different velocities forming a velocity profile across the vessel diameter. The blood cells close to the vessel's wall flow slower than the cells in the middle of the vessel. This 'shearing' effect causes a parabolic velocity distribution over the diameter of the vessel [17] as shown in Figure 2.2.

In pulsatile arteries the shape of the velocity profile varies with time because the

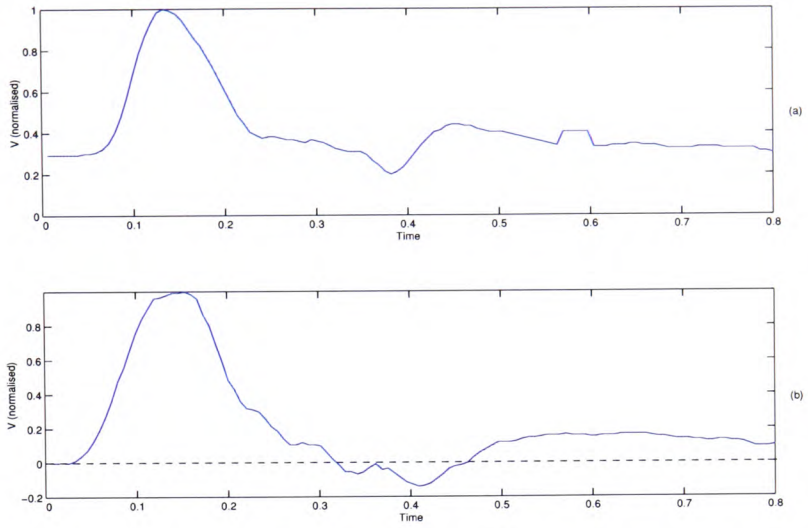

Figure 2.1: Typical blood flow velocity waveforms from healthy patients supplying (a) a low resistance (common carotid artery) and (b) a high resistance (common femoral artery) vascular bed. Both waveforms are normalised to 1.

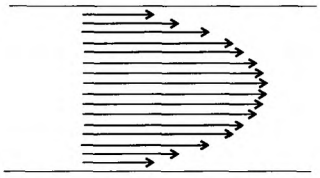

Figure 2.2: Velocity profile for laminar flow in a vessel.

pressure is time variant. Some arteries even show reverse blood flow in some parts of the velocity profile (Figure 2.1).

Atherosclerotic plaque, termed stenosis, on the vessel's wall reduces its cross-section and can lead to a reduction in blood flow. The effects of the stenosis are a reduction in blood flow, only detectable in severe cases, turbulent blood flow and a dampening of the velocity waveform.

Figure 2.3 shows the effect of plaque on the arterial blood flow. The velocity of the blood increases within the stenosis, which causes flow disturbances at the exit of the stenosis when it interacts with the slower moving blood. The flow disturbance introduces new velocities and broadens the spectrum of blood velocities in this area.

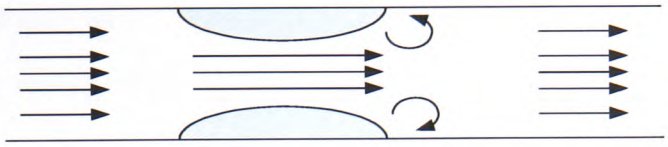

Figure 2.3: Effect of a stenosis on the blood flow velocity.

A damped velocity waveform is the result in the post-stenotic region. In severe stenosis, the human body tries to bypass this area to offset the reduced flow by expanding some of the smaller vessels [26]. In addition, some vessels show a decreased velocity, and in severe stenosis cases a delayed systolic upstroke and decreased pulsatility [28].

This is why many researchers have attempted to link the shape of the velocity waveform to the degree of vascular disease [29]. The velocity waveform of the CFA, for example, is in the absence of any cardiovascular disease triphasic, which means it consists of a forward flow component, followed by a reverse flow component and then a second forward flow component. In the presence of cardiovascular disease, the waveform can show some of the features mentioned above. It is therefore, important to extract and analyse features such as the maximum velocity waveform and the width of the velocity spectrum.

2.1.2 Blood flow measurement

The measurement of blood flow velocity in the cardiovascular system using commercial equipment is based on the transmission of ultrasound waves and the reception of their echoes. An ultrasound transducer emits an ultrasonic beam, normally in the range of 2 - 8 MHz, which penetrates the human tissue. To reduce attenuation, a gel material is used at the interface point between the skin and the transducer.

The transducer receives the reflected ultrasound waves, also called back-scatter,

from the moving blood cells. Figure 2.4 illustrates the measurement scheme of blood flow velocity in an artery using an ultrasound probe.

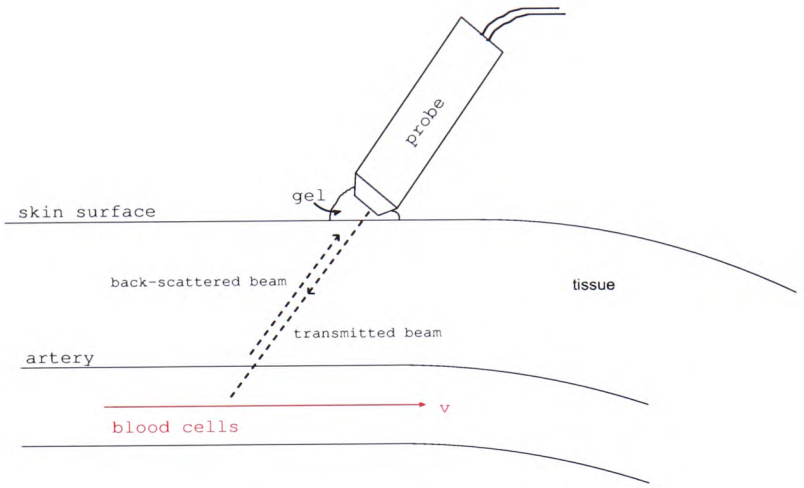

Figure 2.4: Ultrasound blood flow scan.

In ultrasonic blood flow velocity measurement it is assumed that the red blood cells are the major source of back-scattering of the ultrasonic wave. White blood cells, which are much larger, are found in a much smaller quantity in blood than red blood cells. Because red blood cells are much smaller than the incident ultrasonic beam wavelength, they are effectively point targets for this beam. The scattering coefficient of point targets depends only on the volume of the corpuscle and its acoustic mismatch with the suspending plasma [3]. Red blood cells are not the only source for the back-scatter of the ultrasonic wave. Boundaries between tissues with different densities reflect the ultrasound wave but do not introduce a frequency shift. Movements of these boundaries, such as the artery wall, cause a frequency shift in the reflected ultrasound beam. This represents a high energy component in the back-scattered wave relative to the energy of the blood flow components.

2.1.3 The Doppler blood flow signal

The Doppler effect is used to measure blood flow velocity from the back-scattered ultrasound signal. The frequency shift between the transmitted and received ultrasound signals, or the Doppler frequency (F_d), depends on the speed of the object, v, and the speed of the ultrasound wave in the surrounding material, c. For ultrasonic equipment there is also a need to take the angle, α, between the receiver and the moving particles into account. The equation for the Doppler Shift frequency is,

$$F_d = 2 \cdot F_t \cdot \frac{v}{c} \cdot \cos(\alpha) \tag{2.1}$$

where F_t is the transmitted frequency.

In order to determine the absolute blood flow velocity the angle α and the properties of the medium must be known. The speed of the ultrasound wave in tissue, c, is 1540 ms^{-1}. Using typical transmission frequencies of 2 - 8 MHz in commercial devices, the Doppler shift frequency can be as high as 20 kHz in arteries with stenosis [29]. The Doppler shift frequency lies therefore, in the audible range of the human ear and can be listened to as an audio signal using Doppler ultrasound flowmeters. The received and demodulated back-scattered and Doppler shifted signal is also called the Doppler Signal.

It was mentioned earlier that blood does not flow with one velocity through the cardiovascular vessels, but rather with a number of different velocities forming a velocity profile across the vessel diameter. The Doppler signal, therefore, does not only contain a single frequency, but a spectrum of frequencies, termed the Doppler spectrum. The intensity of a frequency component in the Doppler spectrum relates directly to the amount of blood cells flowing with the corresponding velocity. The Doppler spectrum is normally displayed as a frequency-density or power spec-

trum. This representation is used to display the velocity distribution over the with ultrasound insonated vessel diameter at one moment in time [17].

Another way to display the Doppler spectrum is to project it over time by placing it in the time-frequency domain. The time-frequency domain representation, termed spectrogram or sonogram, allows the observation of blood flow over time and the comparison of the velocities over a cardiac cycle. The power spectrum can be considered as a slice of the time-frequency spectrum at a certain time.

The Doppler spectrum also contains frequencies independent from blood flow. These frequency components originate mainly from the vessel's wall movement and the movement of the probe itself. The two sources are based on reflection and can be very energetic, which may distort the spectrum [17].

2.1.4 Doppler ultrasound in the lower limb artery

The previous sections described the blood flow and its measurement using Doppler ultrasound. This study investigated the Doppler ultrasound blood flow signal in the lower limb artery, namely the CFA. The arterial anatomy of the vascular tree in the lower limb is presented before the previous research in this area of the vascular system is reviewed.

2.1.4.1 Lower limb anatomy

The arterial anatomy of the aorto-iliac and femoral-popliteal segment is shown in figure 2.5. The inguinal ligament marks the change from the external iliac artery (EIA) to the CFA. This point was the dividing point for the two segments used in this study. The first segment was the aorto-iliac segment, which runs from the infrarenal aorta down to the distal EIA, and was described as the proximal segment. The second was the femoral-popliteal segment, which was described as the distal

segment. This segment comprised of the CFA, the superficial femoral artery and the popliteal artery down to its trifurcation [1].

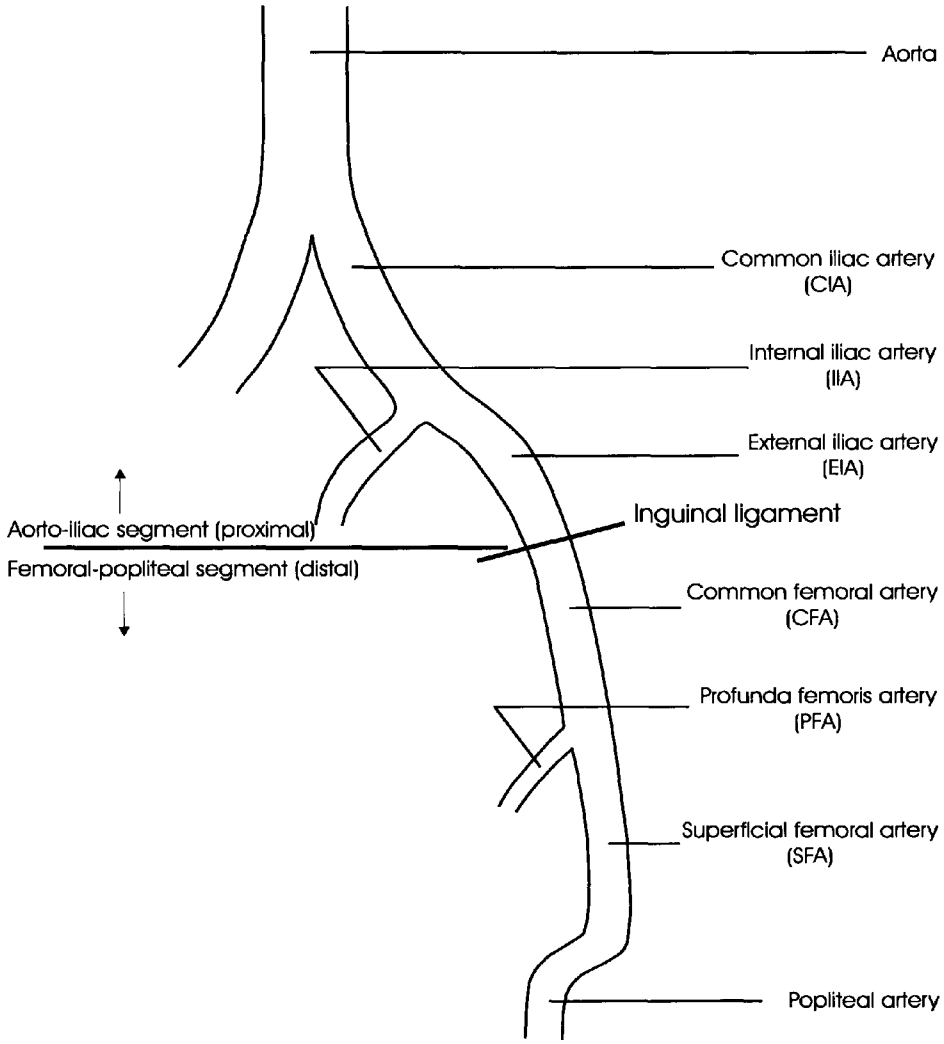

Figure 2.5: Arterial anatomy of the aorto-iliac and femoral-popliteal segment [2].

As the aorto-iliac segment lies behind the peritoneum, which contains the bowel, the imaging of these vessels can be difficult due to overlying bowel gas [2]. The signals used in this study were chosen to investigate the ability to recognise the absence or presence of significant aorto-iliac disease (proximal disease) from the CFA Doppler ultrasound blood flow signals, regardless of the state of the distal

vascular tree. Significant disease was defined as a stenosis of 50 to 100%, which was in accordance with clinical practice.

2.1.4.2 Research in lower limb arteries

The research methodology employed consisted of analysing the acquired time domain signals and extraction of the maximum frequency envelope (MFE) for direct diagnosis or further classification. Angiography was usually used to determine the state of the disease to provide a 'gold standard' for comparison with the results from the researched methods. It has also been the definitive test for lower limb arterial disease. However angiography provides an anatomic view and not a functional one. One of its limitations was that it was subject to wide inter-observer variability. Furthermore, angiography could be misleading, especially with unipolar views, due to an eccentric atherosclerotic lesion [30].

Blood flow in the CFA is normally oscillatory and triphasic. The presence of atherosclerosis changes the vessel size, elasticity and geometry of the affected artery. It can therefore, be expected that atherosclerosis would influence the shape of the waveform. Empirical observations, summarised by Johnston *et al* [31], indicated that the amplitude of the blood flow velocity wave decreased, the peak was delayed, and the reverse flow component became progressively attenuated, when measured distal to a stenosis.

One problem with the examination of the CFA is that the contribution of the stenosis in the distal and proximal segment in combined common femoral disease is difficult to estimate. For medical treatment it is important to identify if proximal disease is present, as it is treated before the distal disease [32]. Doppler ultrasound was therefore, investigated to overcome this problem.

The most widely used form of Doppler ultrasound waveform analysis is still visual

interpretation by a human observer. Rosfors *et al* [33] found that a human observer achieved only a low sensitivity and specificity to proximal disease (56% and 39%) from the CFA waveform. Another study by Walton *et al* [34] also assessed human interpretation of the CFA waveform. They found that the experienced clinician had problems to differentiate between 0-25% and 25-50% proximal stenosis, but was able to identify a significant proximal stenosis or an occlusion (sensitivity = 87% and specificity = 88%).

The role of the Pulsatility Index (PI) in the quantification of stenosis in CFAs was investigated by Johnston *et al* [35]. Their study found that the PI is capable of separating signals into two classes of disease severity. The boundary of the classes was at 50%. Distal disease was not taken into account in their study. Humphries *et al* [36] investigated the Rise Time Ratio (RTR), the Pulse Wave Transit Time (PWTT), the PI and the Laplace damping factor for CFA and popliteal artery waveforms. Angiography was used as the 'gold standard'. The study found that the indices were able to differentiate between segments with no significant and significant disease, but were unable to separate the mild and moderate disease groups within the no significant disease class. No definitions for the boundaries of the different classes were given. In a study, Demorais *et al* [37] were able to distinguish significant from not significant disease using the PI. The results were compared with direct pressure measurements.

Nicolaides *et al* [38] derived several spectral parameters which were sensitive to proximal disease. These parameters included simple measurements such as the waveform height, acceleration and initial deceleration times, and were compared with angiography. The parameters did not prove very successful individually and a multivariate analysis was performed. Although the final result was a successful separation between less than 10% and greater than 10% stenosis in 86% of cases,

the partition of the two classes makes the transferability of the result doubtful.

Johnston *et al* [6] investigated the PI, the Height Width Index (HWI), the Path Length Index (PLI) and the Laplace Transform Analysis (LTA). The classification rate was highest in the PI (96%), followed by the HWI (95.6%), the PLI (91.6%) and the LTA (88.9%). However, a significant decrease of the accuracy of these indices was noticed in the presence of significant distal disease. A study into the relationship between proximal stenosis and PI was carried out on dogs by Evans *et al* [10]. The study found that the PI distal to high stenoses was low, but otherwise the PI took on a wide range of values. This effect was also reported later by other researchers [7, 15].

Hoskins [29], reviewing results of earlier research in the lower limb artery, stated that researchers found a loss of pulsatility in waveforms collected distal to occlusive vascular disease. Furthermore, the peak velocity increased in the presence of a stenosis. He discussed further results from the PI, the LTA and the Principal Component Analysis (PCA). Mixed results were found in the investigation of these three methods. The latter two methods were solely used as research tools as they are complex to implement and only offer little improvement over the PI.

Several papers previously examined the use of the LTA in Doppler ultrasound analysis. Baird *et al* [15] studied the Laplace damping factor and found that it could separate signals with no disease from signals with mild disease. Furthermore, the Laplace damping factor was able to differentiate between mild proximal disease and a significant proximal disease regardless of the state of distal segment (sensitivity = 85% and specificity = 84%). However, the result showed that the sensitivity of the PI was reduced dramatically if the distal segment was occluded. This was confirmed in a study by Baker *et al* [7]. In a further study, Baker *et al* [39] found similar results when comparing the LTA to the mean frequency envelope and the MFE.

A number of papers investigated the performance of PCA. Macpherson *et al* [12] compared the PCA with the LTA and the PI, using direct pressure measurements as 'gold standard'. The results showed that the PCA correctly identified 89% of signals from arteries with severe proximal disease, and 81% of signals from arteries with mild proximal disease. The study also showed that the PCA was less sensitive to significant distal disease.

In a study to separate normal and diseased proximal arteries, Smith *et al* [20] compared the performance of an ANN with a Bayesian classifier based on PCA. Although the study used only 11 features from the MFE, it found that the ANN outperformed the Bayesian classifier significantly. Another study using the ANN to classify arteries with and without proximal disease was conducted by Wright *et al* [1, 18, 19]. The study investigated two cases; the separation of the arteries into no significant (less than 50% stenosis) and significant disease (greater than or equal 50% stenosis), and the separation of the arteries into no significant, significant (50 to 99% stenosis) disease and occlusion (equal or above 99% stenosis). The study was conducted using arteries with disease in multiple segments and achieved classification rates of 82.5% and 71% for the separation into two classes and three classes, respectively.

2.2 Signal processing

Signal processing in the wider context normally includes all algorithms designed to modify a signal. In this study the signal processing stage refers to the early processing before the transformation of the Doppler signal into another domain.

2.2.1 The time domain signal

Commercial Doppler ultrasound flowmeters and scanners provide unidirectional and bidirectional signals at their output. The unidirectional output signal consists of one channel containing the forward and reverse blood flow. In this format no differentiation of the flow direction can be made. In contrast, bidirectional Doppler ultrasound flowmeters and scanners provide a two channel output with separate forward and reverse flow components [17]. The bidirectional Doppler signal is normally used for research purposes as it provides more information about the blood flow.

2.2.2 Filtering

In section 2.1.3 it was shown that the Doppler signal does not only contain the blood flow velocity, but also components originating from the blood vessel wall and ultrasound probe movements. Although both components can be very energetic, high-pass filtering is able to reduce the amplitude of these low frequency components considerably [17]. Keenan *et al* [40] investigated the removal of wall-motion artefacts using linear prediction filtering. Although their study showed improved results for the linear prediction filtering when compared to high-pass filtering, it should be noted that the cut-off frequency of the high-pass filter was rather high at 200 Hz.

2.3 Signal transformation

The directional Doppler signal obtained from the Doppler scanner needs to be transformed into a format that can be interpreted more effectively than the time domain signal. The blood flow velocity waveform is usually used in the clinical application of Doppler ultrasound analysis as well as in research applications. The transformation into the blood flow velocity waveform can either be direct or via the time-frequency

spectrum.

A simple direct transformation of the time domain Doppler signal into a waveform proportional to the mean blood flow velocity utilises a zero-crossing detector. This method, which is effectively a simple frequency-to-voltage conversion, was widely used in the past due to its simplicity. However, it suffers from many inherent errors including noise sensitivity, high amplitudes at low frequencies from unrelated sources and meaningless outputs due to simultaneous blood flow in both directions [31].

The presence of these errors made the zero-crossing detector inadequate for the quantitative analysis of Doppler signals. Johnston *et al* [31] reported two other methods to derive the blood flow velocity waveform directly from the Doppler signal. The first moment processor used an analogue operation to extract the mean velocity, while the frequency follower method employed a phase-locked loop to track the mean and maximum velocities. Both methods have some or all the problems associated with the zero-crossing detector.

The second approach for the determination of the blood flow velocity waveform is the transformation of the Doppler signal into the time-frequency domain followed by the application of a feature extraction algorithm. The extraction algorithm is reviewed in section 2.4.

Historically, the Fast Fourier Transform (FFT) has been the standard method used in blood flow Doppler ultrasound signal processing to derive the power spectrum. Its algorithm decomposes a stationary signal into sinusoidal components [41].

To calculate the spectra of discrete signals, the discrete Fourier transform (DFT) is used. The DFT is defined as,

$$X[k] = \sum_{n=0}^{N-1} x(n) e^{-j2\pi nk/N} \quad k = 0, 1, ..., N-1 \tag{2.2}$$

Where, $X[k]$ is the Fourier transform, x the input signal, n the index of the discrete input sample, k the harmonic number of the transform component and N the number of consecutive samples of the signal. The transform component used in the Fourier Transform is a sinusoidal wave of infinite length [42].

Using the standard FFT to derive the frequency spectrum of a signal does not provide any time information, and is not suitable for the analysis of non-stationary signals. Since the Doppler blood flow signal varies with time, an alternative algorithm is required to process it.

In order to display the power spectrum of the Doppler signal over time the Short-Time Fourier Transform (STFT) has been utilised. The STFT uses a sliding window to analyse the part of the signal which falls within the boundaries of the window. It is the most popular time-frequency distribution (TFD) used in Doppler blood flow analysis. The square modulus of the STFT is also called the spectrogram. It transforms the signal using a moving window $w(m)$, with the window length L_w, in the interval $0 \leq m \leq L_w - 1$ and is given by [42],

$$X(n,k) = \sum_{m=0}^{L_w-1} x(n+m)w(m)e^{-j2\pi mk/N} \quad 0 \leq k \leq N-1 \tag{2.3}$$

where, $X(n,k)$ is the transformed input signal, x is the input signal, n the position of the discrete sample, k the harmonic number of the transform component and N the number of consecutive samples of the signal. Although this approach creates a time-frequency representation without adding too much computational complexity, it suffers from limitations due to the fixed time-frequency resolution once a window length is chosen.

Because the Doppler ultrasound blood flow signal is assumed to be non-stationary [43], the FFT is not suitable for its analysis. The STFT, however, allows the pro-

cessing of non-stationary signals by assuming that small sections of the signal are stationary [42]. The calculated spectrum for each time window is normally displayed with the previous spectra in a time-frequency plane using colour for power intensity. This complex spectrum is called a time-frequency spectrum and displays the Doppler frequency components, which represents blood flow velocity, over time [17].

The selection of the window length is always a trade-off between time resolution at higher frequencies and the frequency resolution at lower frequencies. The fact that the time and frequency resolutions cannot be made better simultaneously is known as the Heisenberg uncertainty principle [41].

$$\Delta f \cdot \Delta t \geq \frac{1}{4\pi} \tag{2.4}$$

where Δf is the frequency resolution and Δt the time resolution.

One of the main drawbacks of the STFT is that it uses only a single window length to capture a slice of the signal under observation. The use of this single window makes it difficult to optimally analyse the whole frequency spectrum of a signal. Higher frequencies require a short window to achieve good time resolution, whilst lower frequencies need a long window to obtain a sufficient frequency resolution.

The Wavelet Transform (WT) overcomes the time-frequency resolution problem by using short windows at high frequencies and long windows at low frequencies. The WT is therefore, able to analyse signals with a constant relative bandwidth (constant-Q) [44]. With BW being the bandwidth and f_{centre} the centre frequency of the passband of a bandpass filter, the narrowness of the filter can be expressed as,

$$Q = \frac{BW}{f_{centre}} \tag{2.5}$$

The WT of a signal, $x(t)$, is defined by,

$$W_\Psi x(b,a) = \frac{a}{2\pi\sqrt{a^n}} \int_{-\infty}^{\infty} x(t)\Psi^*_{(b,a)}(t)dt \tag{2.6}$$

with the analysing or mother wavelet Ψ defined as,

$$\Psi_{(b,a)}(t) = \frac{1}{\sqrt{a^n}}\Psi\left(\frac{t-b}{a}\right) \tag{2.7}$$

In the above equations $\Psi^*_{(b,a)}$ is the complex conjugate of $\Psi_{(b,a)}$, n a constant, b the translation parameter and a the scale parameter, which can dilate and compress the wavelet and does not have units. The term translation corresponds to time and scale is defined as reciprocal of the frequency.

The principal operation of the WT is as follows: the 'mother', or analysing, wavelet is used as the basis for a set of orthogonal low-pass and high-pass filter parameters, which will be used to split the signal into a low frequency and a high frequency part at $^1/_4$ of the sampling frequency. The low frequency part is called the approximation space, while the high frequency part is called the detail space. This decomposition process is repeated on the approximation space only. Because the maximum frequency of the approximation space is only $^1/_4$ of the original sampling frequency, the approximation space is decimated by 2 before being decomposed again.

Figure 2.6 shows the decomposition tree of the WT, where W_L^0 and W_L^1 denote the approximation and the detail, respectively. The subscript indicates the level of decomposition.

The approximation and detail spaces can be displayed in a two-dimensional plane, representing a TFD. Figure 2.7 shows an example of the time-frequency boxes for the WT. The scale has been relabelled to frequency $(1/scale)$ to conform with

other TFDs.

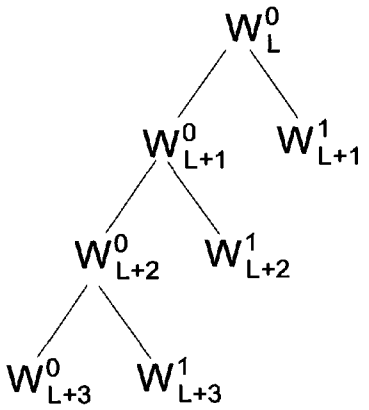

Figure 2.6: Decomposition tree of wavelet transform.

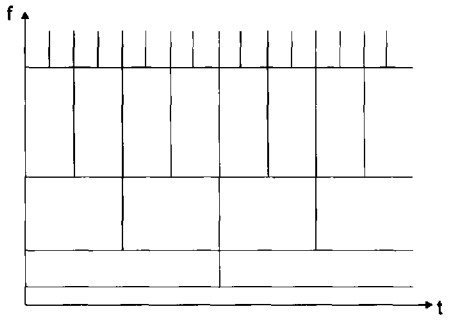

Figure 2.7: Tiling of the time-frequency plane using time-frequency boxes of a wavelet basis.

Three main areas of application can be identified for the WT: signal transformation, signal compression, and noise reduction (denoising). The result of the signal transformation is similar to the STFT except that the resulting spectrum is in the time-scale domain. By varying the window size during the analysis, the WT is able to emphasise signal components that may not be detected using the STFT. Signal compression and noise reduction using the WT is achieved by decomposing the signal into detail and approximation coefficients, calculating a threshold and removing coefficients below it and reconstructing the signal from the remaining coefficients. During signal compression all approximation coefficients are kept and the threshold

is only applied to the detail coefficients. The noise reduction algorithm applies the threshold to all coefficients.

The WT has been used in various fields, including medical signal processing. In the area of Doppler ultrasound, the WT was utilised in parametric measurements of coronary blood flow [45], arterial pressure and blood velocity pulsations [46], and noise removal from the MFE [47]. Matani *et al* [48] compared the WT with the STFT using simulated and real Doppler ultrasound blood flow signals from an area near the mitral valve in the left ventriculus. Although using only half a cardiac cycle of the one directional signal, the study reported an improved time-frequency resolution of the WT over the STFT. A discussion of the application of the WT to Doppler ultrasound quadrature signals using an embolic Doppler signal was presented by Aydin *et al* [49]. Güler *et al* [50] compared the STFT, AR modelling and the WT with Doppler ultrasound signals to detect aorta failure. Although their investigation showed that the WT performed best, it is important to note that the window used for the STFT was chosen to be 25.6 ms. Further research has been done in the area of speckle noise reduction in images taken from the replay of laser holograms [51].

The WT, compared to the STFT, has the ability to vary the time-frequency resolution. This leads to a multi-resolution representation for non-stationary data. A disadvantage of the WT is the relatively poor frequency resolution in the high frequency region (Figure 2.7). It is therefore difficult to discriminate between two close high frequency components within a signal. A difficulty also arises when comparing two signals at their maximum frequency, as the frequency resolution may be poor.

The generalised form of the fixed dyadic construction of the WT is the Wavelet Packet Transform (WPT). The WPT does not only decompose the approximation spaces to construct new approximation and detail spaces, but also decomposes the

detail spaces. The intervals on the frequency axis may, therefore, vary and each of the intervals is covered by the time-frequency boxes of wavelet packet functions [41]. This generalised form can provide a complete level-by-level decomposition, which is able to provide a better frequency resolution at higher frequencies than the WT. The recursive splitting of the approximations and detail spaces is represented in a binary tree. If L is the level at the root of the tree, then any node in the tree is labelled by the parameters j and p. The depth of the node is expressed by $j - L \geq 0$, while p gives the number of nodes on its left at the same depth. An example of a complete tree is shown in figure 2.8.

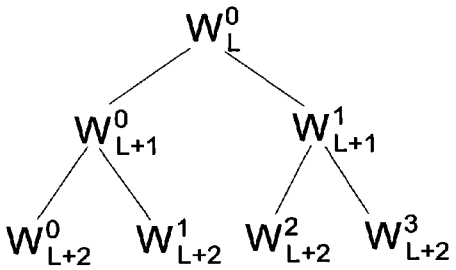

Figure 2.8: Binary decomposition tree of wavelet packet spaces.

The calculation of the tree is defined by the following two equations [41],

$$\Psi^{2p}_{j+1}(t) = \sum_{n=-\infty}^{+\infty} h[n]\Psi^{p}_{j}(t - 2^j n) \tag{2.8}$$

and

$$\Psi^{2p+1}_{j+1}(t) = \sum_{n=-\infty}^{+\infty} g[n]\Psi^{p}_{j}(t - 2^j n) \tag{2.9}$$

where $\Psi^{2p+1}_{j+1}(t)$ are the WPT coefficients over time, n the sample number, $h[n]$ the low-pass filter and $g[n]$ the high-pass filter.

Figure 2.9 shows an example of the time-frequency boxes for the WPT. In this example not all approximation and detail spaces are decomposed to the same level,

resulting in time-frequency boxes of different sizes.

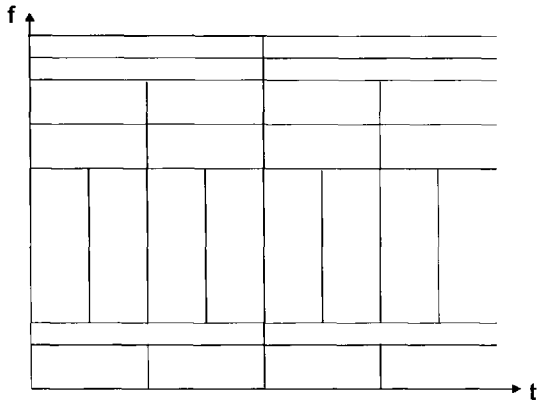

Figure 2.9: Arbitrary tiling of the time-frequency plane using time-frequency boxes of wavelet packet functions.

Areas where the WPT has been used include: speech compression [52], respiratory sound classification [53], classification of ferromagnetic objects in an underwater environment [54] and signal and image denoising [55–57].

Alternative spectral estimation methods were investigated by various researchers. David *et al* [58] applied the FFT method, the maximum likelihood method (MLM), the Burg autoregressive algorithm, and the modified covariance approach to autoregressive modelling to simulated and experimental Doppler blood flow signals. The investigation compared the effects of the signal-to-noise ratio (SNR) and the signal bandwidth on the performance of the four methods. Their research showed that the autoregressive algorithm and the MLM performed best given that the model order was chosen appropriately.

Guo *et al* [8] compared three TFDs with the STFT and autoregressive modelling (AR) using simulated common femoral signals. The three methods used were the Choi-Williams distribution (CWD), the Reduced Interference distribution (RID) and the Bessel distribution (BD), all of which can be used with non-stationary signals. The study found that the BD performed best, but that the CWD and AR

also provided a good TFD of Doppler signals.

Spectral estimation methods were investigated by Vaitkus *et al* [59, 60]. Specifically the DFT, AR, moving average (MA) and autoregressive moving average (ARMA) models were used. It was found that the AR and ARMA models provided better results than the DFT, whilst computationally more complex.

More studies were conducted using these and other methods as alternatives to the STFT. These studies investigated AR, MA and ARMA, CWD, BD, RID, the Smoothed Pseudo Wigner Distribution (SPWD) and the Adaptive Constant-Q Distribution (AQD) [25,50,61–64]. They reported that the alternative methods offered advantages over the STFT, but not sufficient to replace the STFT in the analysis of Doppler ultrasound blood flow signals.

Kadado *et al* [61], for example, found that the ARMA estimator was potentially superior to the STFT, but this depended on the correct estimation of the system order. Jensen *et al* [62], on the other hand, found that the AR algorithm yielded good results on simulated data, but no conclusive result could be found for *in-vivo* data. Contradicting results were reported by Forsberg *et al* [64] and Guo *et al* [8]. Both investigated the BD, and whilst Guo *et al* reported a good result for the BD, Forsberg *et al* did not confirm this. In fact, their study showed that the BD had problems even with noise free signals. Forsberg *et al* concluded that while the AQD yielded the best result, it required a long processing time of 10 minutes compared to 0.3 s for the STFT.

For *in-vivo* data the STFT proved to be the best TFD. Overall, all studies concluded that the STFT was the best compromise due to its simplicity and processing speed. Furthermore, none of the alternative spectral estimation methods provided a practical approach for analysing Doppler ultrasound signals. This might be due to the added complexity of these methods and the small improvement offered by them.

2.4 Feature extraction

The Doppler blood flow velocity waveforms or spectra are usually treated as N-dimensional vectors. The separation of normal and abnormal waveforms is a problem of separating individual vectors in this vector space. In general, the input vector, in the time or time-frequency domain, is too large to process directly. Feature extraction methods are employed to produce feature vectors of a lower dimension. This can be achieved by combining significant features of the waveform into one parameter or by using a model to describe the shape of the waveform [17].

The Doppler spectrum in the time-frequency plane is used in two ways to analyse blood flow. Firstly, the spectral content is utilised as an image of the velocity profile. Secondly, the outline of the velocity spectrum, called the MFE, is used on its own for the purpose of assessing blood flow or as a basis for further processing.

2.4.1 The Maximum Frequency Envelope (MFE)

Typically, the MFE of the spectrogram describes the boundary which encloses 95% of the signal energy with reference to the zero line. This is often referred to as the 95% MFE. Figure 2.10 shows an example of the spectrogram (square modulus of the STFT) for the forward blood flow component of a CFA and its 95% MFE. The spectrogram of figure 2.10a was generated by the candidate using an 128-point STFT with a Hamming time window and an overlap of 50%.

Each column in figure 2.10b represents a time interval equivalent of 128-points. The 95% MFE is normally calculated from the sonogram by adding all frequency components in each time interval. The 95% MFE for this time interval is found where 95% of the total power is.

A general definition was given by Mo *et al* [43],

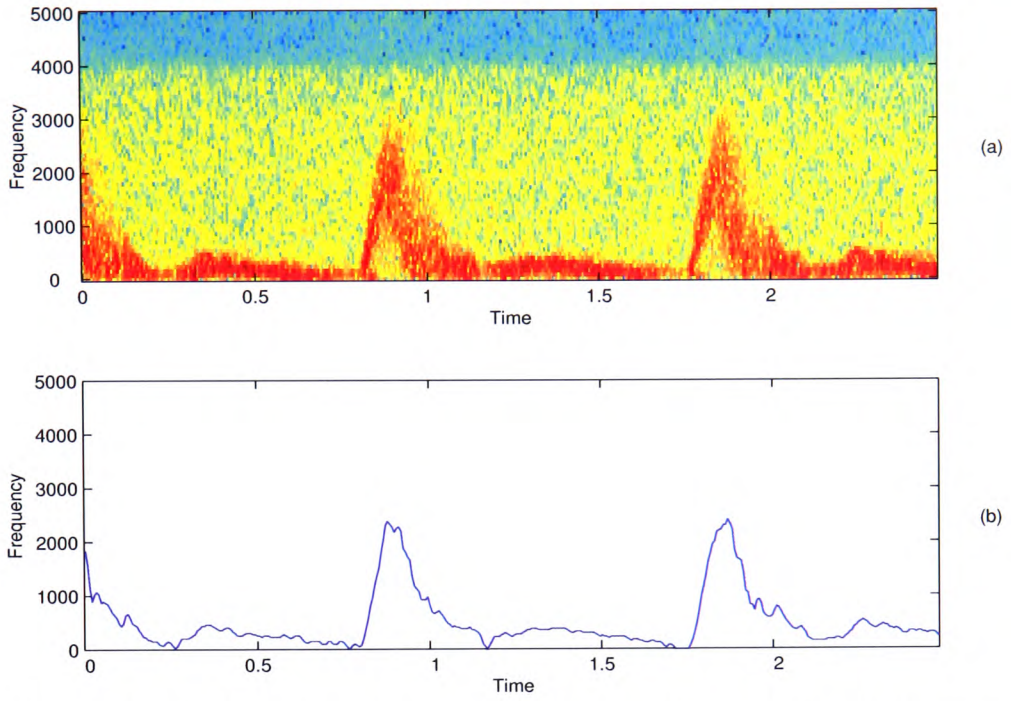

Figure 2.10: Spectrogram of common femoral forward flow (128-point STFT, 50% overlap, Hamming window) and 95% MFE.

$$P_{fmax} = \frac{(100 - \alpha)}{100} \cdot P_T \tag{2.10}$$

where P_T is the total cumulative power of each time interval, P_{fmax} the cumulative power at the maximum frequency and α a chosen parameter, usually 5%.

High frequency noise in the sonogram has a strong influence on calculating the MFE and is generally removed by setting all values below a certain threshold to zero. This process is commonly referred to as grass-cutting [17].

2.4.2 Normalised frequency indices

The MFE is a simple method of describing the maximum blood flow velocity over time, which is an important feature of a vessel under observation. When blood flows

through a stenosis its velocity increases to maintain the same flow rate as in the pre- and post-stenotic regions of the vessel [17]. The absolute value of the frequency shift at a particular point in the cardiac cycle such as the peak systole is therefore, used for quantitative assessment purposes, or alternatively, indices are derived from the shape of the MFE [29]. Several of the indices are based on the ratio of the height of one feature to another within a cardiac cycle. The advantage of having a ratio is the independence of the attack angle, which is the angle between the ultrasound probe and the vessel.

The most widely used index is the Pulsatility Index (PI). The PI is calculated by the peak-to-peak excursion divided by the mean height of the MFE over one cardiac cycle [4, 65, 66]. This is given by,

$$PI = \frac{V_{max} - V_{min}}{V_{mean}} \tag{2.11}$$

where V_{max}, V_{min}, and V_{mean} describe respectively the maximum, minimum and mean velocity of the blood flow within one cardiac cycle as shown in figure 2.11.

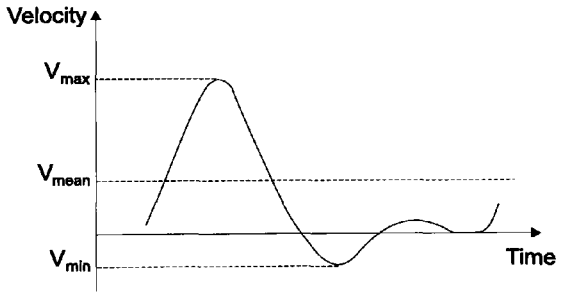

Figure 2.11: Pulsatility index (PI)

The simplicity of calculating the PI made it a popular method to quantify the pulsatility or the damping of a Doppler waveform, and therefore, providing information about the severity of the stenosis [17].

Studies related to the PI and cardiovascular disease have covered various cardi-

ovascular segments [7, 12, 15, 16, 32, 67]. Although the PI can be a useful objective method to assess the pulsatility of a waveform, great care must be taken in utilising it as it is affected by changes in distal arteriolar resistance [10] and by distal disease [12].

Other indices, such as Pourcelot's Resistance Index (RI), are used to describe waveforms from common carotid arteries and in neonatal cerebral haemodynamics [17]. The RI is a widely used index of pulsatility, and is given by,

$$RI = \frac{V_{max} - V_{min}}{V_{max}} \tag{2.12}$$

where V_{max}, V_{min}, and V_{mean} were already defined in figure 2.11.

A variety of studies were performed using the RI to detect waveform changes for different conditions [17].

Special indices were introduced to take into account the physiological peculiarities of the vessel under observation. The A/B ratio is an example of an index that uses special features of the waveform from the common carotid and supraorbital arteries [17]. The index uses the two peaks of the waveform during systole and is calculated by dividing the amplitude of the first peak by that of the second (Figure 2.12),

$$A/B = \frac{A}{B} \tag{2.13}$$

Several researchers did not only include the height of recognisable features of the waveform, but also their time relationship. Examples of these indices are the Systolic Decay Time Index (SDTI), Height Width Index (HWI), Path Length Index (PLI) and Relative Flow Rate Index (RFRI) [17].

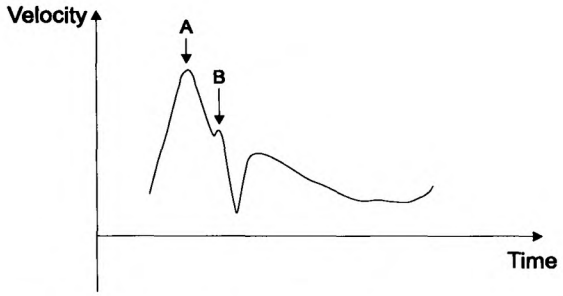

Figure 2.12: A/B index parameters for common carotid and supraorbital arteries.

2.4.3 Spectral broadening indices

All indices mentioned above were concerned with the MFE and ignore the remaining contents of the Doppler spectrum. The Doppler spectrum includes information about the velocity distribution within the ultrasound beam, which is thought to be of diagnostic importance [2, 14]. Sonograms from normal vessels, for example, show a clear window under the systolic peak, whilst diseased vessels show a smaller or no window. It is believed that the window is the result of the flat velocity profile found in healthy vessels. Proximal stenosis introduces turbulence (figure 2.13) which leads to a spectral broadening of the Doppler spectrum and to a reduction of the window below the systolic peak [17].

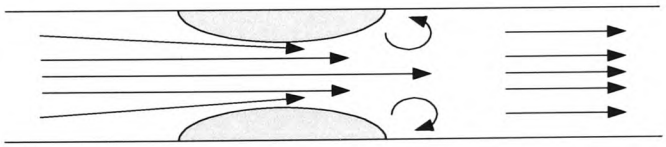

Figure 2.13: Flow disturbance

An early definition of fractional broadening was proposed by Bodily et al. [68]. This definition led to the empirical relationship for a spectral broadening index (SBI),

$$SBI(1) = k \cdot \frac{f_{max} - f_{min}}{f_{max} + f_{min}} \tag{2.14}$$

where f_{max} and f_{min} are the maximum and minimum frequency at peak systole, and k an experimentally derived constant (k=0.47).

Kassam *et al* [69, 70] identified the relative stability of the maximal and mean Doppler frequencies in contrast with the variability of the minimal frequency. As a result, Kassam *et al* proposed another definition of the SBI,

$$SBI(2) = \frac{f_{max} - f_{mean}}{f_{max}} \cdot 100 \tag{2.15}$$

where f_{max} and f_{mean} are the maximum and mean frequency at peak systole, respectively. Although the $SBI(2)$ is potentially affected by other factors, a close linear relationship was observed between the severity of the stenosis and the $SBI(2)$ [9, 71]. Figure 2.14 shows the sonogram of the forward flow of a CFA used in this study. Superimposed on the sonogram are the maximum (95% MFE), minimum (5% MFE) and mean frequency envelopes.

Other researcher defined similar spectral broadening indices. Many studies compared quantitative indices of spectral broadening with known disease conditions. Rittgers *et al* [72] found that the systolic window decreased with the increase of the degree of the stenosis. In a study, Brown *et al* [73] found that the SBI was linearly related to the degree of the stenosis with severities exceeding 45%. An increased sensitivity and specificity for stenoses of more than 25% diameter reduction was reported by Sheldon *et al* [74].

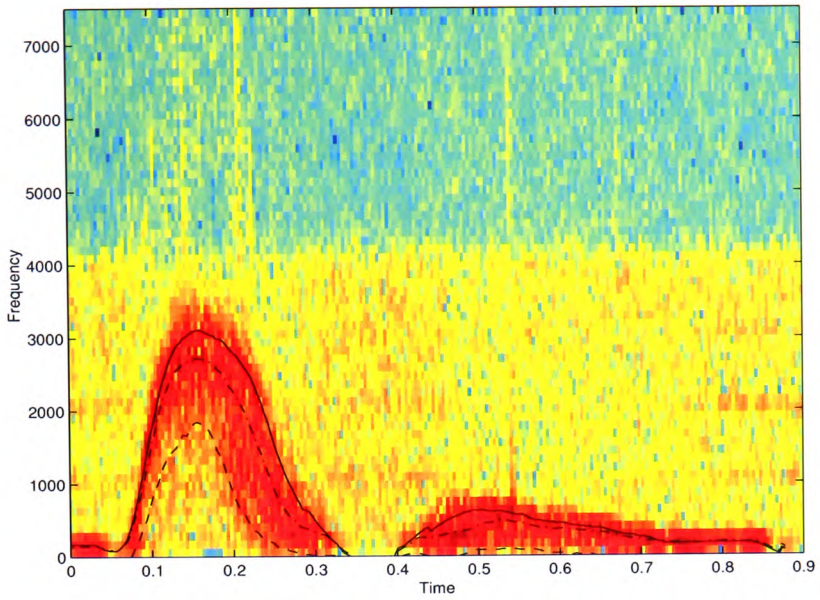

Figure 2.14: Spectral Broadening Parameters in the spectrogram. The solid line represents the 95% MFE, the dot-dashed line the mean frequency, and the dashed line the 5% MFE.

2.4.4 Laplace Transform

More complex analysis methods have been applied to relate the Doppler velocity waveform shape to vascular disease. The Laplace Transform Analysis (LTA) method was developed to model the waveform shape mathematically from a simple equivalent electrical circuit of flow in the lower limb [75,76]. Studies using the LTA produced three parameters from the frequency domain [76] or time domain [77]. These parameters were related to the arterial wall elasticity, distal impedance and proximal arterial diameter. Although initially this technique was thought to be an attractive approach, several investigations showed contradictory results and illustrated that some features of the Doppler waveform were unaccounted for in the LTA [11,17,77]. Evans *et al* [11] compared the LTA method to the PI and the Principal Component Analysis (PCA) in an animal model and found that the LTA method could only distinguish clearly very tight stenosis (greater than 92%). Furthermore, the chief

advantage of the LTA method was reported to be its independence of changes in the peripheral resistance. Evans's study could not verify this and reported that the dampening factor δ may be subject to considerable variation at low values of peripheral resistance. This result was supported in a study by Law *et al* [77].

2.4.5 Principal Component Analysis

Principal Component Analysis (PCA) is an alternative approach that resembles Fourier analysis. In both methods, a waveform is broken down into a number of basic components. Fourier analysis uses sinusoids as base components, whilst PCA uses base components determined by an analysis of the population of waveforms under consideration. The shape of the base components is chosen so that a minimum number of components are needed to reconstruct individual waveforms of the population signals [29]. For this reason PCA is included as a feature extraction method rather than a signal transformation method.

PCA was applied to the MFE of common carotid waveforms where it only demonstrated marginal improvement in diagnostic performance over the A/B ratio [78]. It was also applied to the whole spectrum where the overall accuracy was 89% for PCA compared to 75% for the A/B ratio [79].

2.5 Decision making and diagnosis

After the feature extraction stage the information available for classification and diagnosis are reduced to a lower dimension. In the case of an index, it is reduced to one dimension. Traditionally, classification and diagnosis is performed by subjective analysis. For automated diagnosis, the extracted features are used as inputs for pattern recognition algorithms such as Artificial Neural Networks (ANN) or statistical

algorithms.

2.5.1 Subjective interpretation

The subjective interpretation of blood flow, either by visual examination of the Doppler spectrum and MFE, or audibly from the Doppler Shift signals provided by commercial equipment, are common methods for the assessment of blood flow characteristics. These can be very powerful methods when utilised by an experienced clinician [34]. However, they rely on the experience of the user and are subjective. Furthermore, it is not easy to compare diagnostic results with other medical centres. On the other hand, some clinicians believed that more objective methods may sometimes ignore details, that are obvious to the experienced operator [1].

2.5.2 Direct interpretation of indices

By using the indices from the feature extraction stage a more objective method of classifying blood flow signals was provided. Simple thresholding methods can be applied to the indices to separate healthy and diseased vessels. Although these indices neglected much of the information available in the Doppler signal, research showed that they provide indications of the the state of the vessel under observation. Although research showed that this is true in the majority of the cases, it also demonstrated that misclassification happened for healthy and diseased vessels.

2.5.3 Statistical Methods

Statistical signal classification is based on probabilistic terms. A hypothesis, H_k, defines that an unknown signal belongs to a certain class c_k with a probability density p_k. In a two class situation it is the task of the classifier to place the unknown

signal into one of the classes based on the hypothesis. The probability densities for each class, which are normally *a priori* unknown, are needed to make this decision. Bayes decision theory, for example, requires *a priori* knowledge of the conditional probability densities. These give the probability that a signal belongs to a certain class when certain features are present. Other statistical classification algorithms, such as the k-Nearest Neighbour (k-NN) classification, do not use *a priori* knowledge for the probability density. Instead the probabilities of the features are estimated from available data [80].

Different diagnosis and decision making methods for vascular disease using Doppler ultrasound blood flow signals were utilised by a number of researchers. Evans and Caphrihan [81] investigated one statistical and three deterministic classification methods of Doppler ultrasound blood flow signals from the hind limb of a dog. The methods used were the Bayes, nearest neighbour, generalised linear function iteration and the potential function methods. No single best method was identified in Evans's study. Similar results were obtained by Greene *et al* [82], who investigated five different statistical methods.

2.5.4 Artificial Neural Networks

Artificial Neural Networks (ANNs) are modelled on the structure of the human brain. These mathematical tools are based on modelling how the human brain learns to recognise patterns. ANNs offer promising solutions for problems which are difficult to solve by traditional mathematical and statistical approaches. A number of different network types were proposed and the selection of the optimum paradigm and structure for a specific problem is normally based on experience or by experimentation. ANNs are generally considered to be suitable for different application areas including [83–85]:

- Decision theory, including non-linear mapping between high-dimensional spaces.
- Associative memory.
- Clustering or compression.
- Generation of structured sequences or pattern.
- Classification.
- Pattern Recognition.

ANNs were successfully used in a diverse range of pattern recognition tasks, such as character recognition, speech recognition, radar signal analysis, adaptive noise cancellation, classification of seismic waves, radar signal classification and fault detection of motors [83,86]. Amongst the benefits of using an ANN for pattern recognition and classification are [87,88]:

- Ability to learn - ANNs are normally not programmed, but trained using a set of training vectors. This allows the ANN to be adaptable.
- Parallel processing with reduced execution time.
- Fault tolerance due to distributed knowledge representation in neuron weights.
- Associative storage of information - recall of similar pattern from input pattern or generalisation.
- Robustness against noise and faults.
- Contextual information - knowledge is part of the structure and the computation process.

Some of the disadvantages of ANNs include [87,88],

- Knowledge is only possible through learning - it is difficult to built an ANN with basic knowledge.
- No analysis of knowledge or the problem solving process is possible.
- Training can be relatively slow.
- Trial-and-Error approach when training the ANN.
- Variety of ANN paradigms and architectures exist, making selection difficult.

ANNs were also widely used in medical signal classification and recognition. In ECG analysis, back-propagation (BP) ANNs were able to classify the ST-T segments of ECG signals with accuracies of 90% to 95% [89].

A number of researchers applied ANNs to Doppler shift signals [18–20, 90]. Baykal *et al* [90] used a Self-Organising Map (SOM) ANN to classify umbilical arterial blood flow. The study reported 92% to 98% classification rates. ANNs were also applied to Doppler ultrasound blood flow waveforms by Smith *et al* [20]. Smith's study investigated and compared the classification of a multi-layer ANN with a Bayesian classifier based on the PCA of the MFE. The study showed that classification using the ANN was superior to the Bayesian classifier. The work of Wright *et al* [1,19] showed that Doppler ultrasound diagnostics can also benefit from the application of ANNs. Results from a feasibility study into the classification of different arteries of the human body showed a high success rates, which included 100% for the common carotid, 92% for the common femoral and 96% for the popliteal arteries [18]. Another study showed that ANNs can be used successfully in the classification of the severity of aorto-iliac disease from CFA signals [19].

So far, ANN applications in Doppler blood flow analysis have used the MFE as an input vector. Although this approach produced encouraging results, it still neglected other information present in the Doppler signal, which may support the classification process.

ANNs consists of interconnected artificial neurons as shown in figure 2.15 and figure 2.16. The key parameters that determine the behaviour of a neuron are its activation function and the pattern of weighted connections over which it sends and receives signals [91].

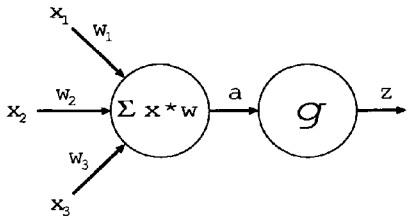

Figure 2.15: Artificial neuron model.

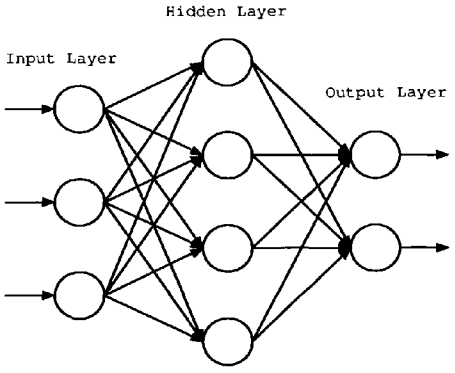

Figure 2.16: An example of an artificial neural network.

The input signal, x_i, at input i is first multiplied by a parameter, w_i, known as weight, and is then summed with all the other weighted input signals to give,

$$a = \sum_{i=0}^{d} w_i x_i \tag{2.16}$$

The final output, z, of the neuron is the result of applying an activation function, g, to the sum of the weighted inputs,

$$z = g(a) \tag{2.17}$$

There are a number of activation functions commonly used for neurons including linear, threshold, threshold linear and sigmoidal functions. The sigmoid function is the most frequently used activation function and is given by [91],

$$g(a) = \frac{1}{1 + e^{-a}} \quad with\ 0 < g(a) < 1 \tag{2.18}$$

or

$$g(a) = \frac{1 - e^{-a}}{1 + e^{-a}} \quad with\ -1 < g(a) < 1 \tag{2.19}$$

ANNs are normally classified by the way they are trained and interconnected. In terms of training, learning can either be supervised or unsupervised. Also, the network may have feedback from the output of a neuron to its input. Three main neural network paradigms have been widely reported in the literature:

- Feed-forward error back propagation (BP) network.
- Massively interconnected networks, such as Hopfield nets.
- Self-Organisation networks or Kohonen networks.

The back propagation and Hopfield network are examples of supervised learning paradigms, whilst the Kohonen network maps input signals to its output classes without supervised training [91].

The majority of ANNs used were feed-forward networks. The term feed-forward refers to the signal flow, which is from the input to the output. No feedback is implemented, although the learning error may be propagated back from the output to the previous layers in some learning paradigms.

The back propagation paradigm is the most frequently used algorithm for adjusting the weights of a multilayer neural network during training. The training uses three steps:

- Feed-forward of the input training vector.
- Calculation and back-propagation of the error.
- Adjustment the network weights.

2.6 Automated Doppler ultrasound analysis

The automation of the Doppler ultrasound blood flow analysis was only addressed by a few previous studies. Fully automated analysis system were not reported in the literature.

A semi-automatic algorithm for the extraction of the cardiac cycle from the MFE was reported by Evans [92]. The study described a pulse-foot-seeking algorithm that was used successfully on a large number of Doppler ultrasound blood flow signals. The algorithm relied on the manual selection of the heart rate range by an operator and therefore, was not completely automated.

A microcomputer-based system with a waveform identification process to extract a cardiac cycle for the calculation of the PI was described by Johnston *et al* [93]. The system was able to identify and extract 96% of the waveforms, using visual feedback as guidance. Although the system automated some tasks in the extraction

process, it was not an automated system for Doppler ultrasound blood flow analysis. A similar system was reported by Greene *et al* [82].

Automated systems were reported by Başaran *et al* [94] and Das *et al* [95]. Başaran *et al* reported an automated system based on the PI, RI and AB ratio, but no results were given. A knowledge-based Doppler ultrasound blood flow measurement system was described by Das *et al*. This system used a statistical database with known classifications for comparison with the obtained data set. Feature extraction was performed using ARMA. The time-varying ARMA coefficients were determined by using an ANN. Unfortunately, the work did not provide any results for comparison. The main reason for this was that the system was not fully implemented.

An automated analysis system for Doppler ultrasound was reported by Tschirren *et al* [96–98]. This system processed VCR-recorded image sequences and extracted the MFE. No further analysis or classification of the signals was performed.

2.7 Summary

This chapter has provided an overview of the literature survey that was conducted during the study. The survey covered the diagnostic methodologies of vascular diseases based on the processing, analysis and interpretation of Doppler ultrasound blood flow signal.

Although most researchers and clinical practioners believe that the blood flow signal contains a wealth of information about the state of the monitored blood vessel and any disease condition present, limited work was done to extract a wide range of significant features from the Doppler ultrasound signal.

To date medical diagnosis of vascular disease is based on the subjective inter-

pretation of the Doppler signal or its derivatives by experienced clinicians. These diagnoses can be as crude as assessing the disease condition by listening to the audio output of the blood turbulence or reading the average blood velocity, both of which are produced by low cost commercial flowmeters. Subjective diagnosis by visual interpretation of the spectrogram of the Doppler signal, which is produced by more sophisticated blood flow analysis medical instruments, can be inaccurate, inconsistent and significantly limit the involvement of more medical practitioners in diagnosing vascular disorders, especially at the primary healthcare level. Furthermore, certain vascular segments, such as the aorto-iliac segment, are difficult to visualise using Doppler imaging techniques due to their anatomic location.

Previous research work was conducted to extract features from blood flow signals and relate these features to the disease condition. All previous methods relied on the MFE of the Doppler signal's spectrogram, which was in turn derived by using the well established STFT. Various indices were proposed to quantify the profile of the MFE and relate it to specific disease conditions. Unfortunately, these indices were too simple to provide a significant improvement over subjective analysis methods and could not provide a reliable approach for detecting the state of a blood vessel.

Other researchers proposed more complex signal analysis and classification methods such as PCA and LTA. However, the degree of success of these methods was limited relative to the utilisation of simple indices. More encouraging results were reported in relation to the application of ANNs to the MFE of the spectrogram as a direct feature vector. As with previous approaches, this work was only based on the MFE and neglected any other information present in the Doppler signal and its spectrogram.

In summary, the review of literature in this study has revealed the following shortcomings in previous research work conducted to process, analyse and achieve

objective interpretation methodologies of Doppler ultrasound blood flow signals:

- The initial processing stages of the Doppler signal, especially in relation to noise reduction were not covered by previous work, despite the fact that the noise content of any signal can have a significant effect on subsequent processing and feature extraction processes including the generation of the spectrogram.

- The transformation of the Doppler signal to the time-frequency domain was mostly conducted using the STFT, although researchers acknowledge the fact that the signal is non-stationary, thus potentially limiting the validity of this method. Very little work has been reported on investigating modern multi-resolution transforms, such as the WT, as viable and more accurate alternatives to the STFT.

- To date, almost all research work on interpreting the Doppler signal was based on the MFE of the spectrogram and the indices derived from it. Possible features which may be embedded in the Doppler signal and its transforms, such as the SBI, were investigated but not combined with the MFE.

- All previous methodologies proposed to automate the interpretation of the Doppler signal and the diagnosis of vascular disease, did not eliminate the need for human intervention to establish various parameters during the signal processing stages, thus limiting their practical benefits.

- It is currently difficult to detect the presence of disease in the aorto-iliac segment (proximal) using Doppler imaging methods due to the location of the vessels. The accuracy of current indices and methods decreases when a disease in the femoral-popliteal segment (distal) is present. This represents a

serious diagnostic limitation.

The initial objectives of this study were aimed at investigating new methodologies to overcome the above limitations. The literature review has confirmed the importance of these objectives in filling a significant gap in previous research work in the field.

Chapter 3

Signal Conditioning and Transformation

This chapter presents the experimental work that was conducted in relation to signal conditioning and transformation. Section 3.1 provides a description of the Doppler ultrasound blood flow signal and the processing stages which were utilised in the study to investigate automated clinical decision making. The sources of the Doppler ultrasound blood flow signals which were used in this study are described in section 3.2. This section also presents the clinical signal acquisition programme.

Signal processing for the rejection of low frequency components in the blood flow signals is presented in section 3.3. An investigation into the use of the Wavelet Packet Transform (WPT) as an alternative Doppler ultrasound blood flow signal transformation algorithm is presented in section 3.4 and compared with the Short-Time Fourier Transform (STFT).

Section 3.5 presents the investigations conducted into overall noise reduction strategies for the Doppler signal. Wavelet denoising is applied to the time and the time-frequency domain and compared with traditional thresholding.

3.1 Processing of the blood flow signal

The Doppler ultrasound blood flow signal received by the transducer of the flowmeter is a complex and non-stationary waveform. The signal contains information on blood flow resulting from the back-scatter of the incident ultrasound signal from the red blood cells. The generation of the blood flow signal has already been covered in section 2.1.

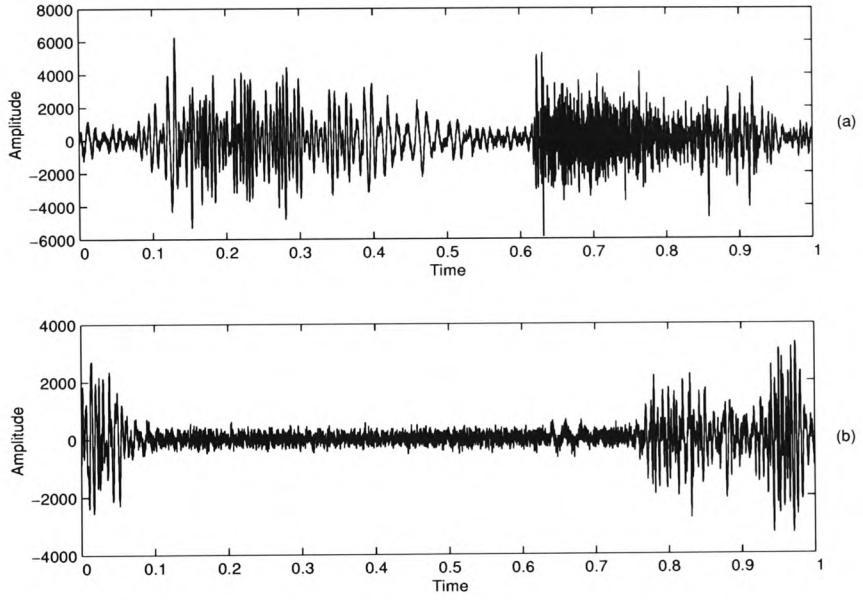

Figure 3.1: Time domain Doppler ultrasound signal from a common femoral artery, with (a) representing forward and (b) reverse blood flow.

The complex Doppler signal is usually demodulated at the receiver section of a standard flowmeter to produce two quadrature signals. These quadrature signals can be used directly in a STFT process to generate the sonogram. However, it is common to process the quadrature signals further to convert them into forward and reverse blood flow signal components. Figure 3.1 shows an example of these two components for a common femoral artery (CFA) signal. Each of these components can be transformed into the time-frequency domain using the STFT. The

forward and reverse blood flow signals are available as outputs from most commercial flowmeters and scanners. Therefore, all the processing stages up to the point of generating these two signal components did not form part of this study, but they were utilised for data collection.

This study was concerned with investigating signal processing techniques and methodologies that will enable the utilisation of the forward and reverse blood flow signals to provide automated clinical decision making strategies. The signal processing and analysis strategy proposed for this study is shown in the block flow diagram of figure 3.2. This strategy enables the partitioning of the ultimate aim of achieving an automated clinical decision making methodology into four distinct stages: signal conditioning, signal transformation, feature extraction and classification. Each of these stages will be investigated separately and then linked to the other stages.

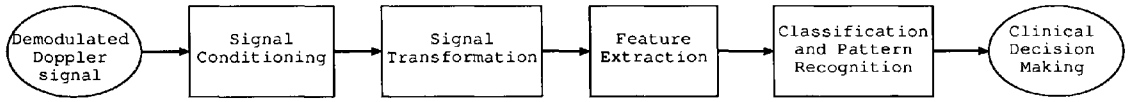

Figure 3.2: Automated clinical decision making strategy for Doppler ultrasound blood flow.

3.2 Data acquisition

The starting point of the signal processing flow is the time domain forward and reverse blood flow signal. To enable the evaluation and assessment of the investigated processing methods, clinical signals were obtained through collaboration with the University of Wales College of Medicine (UWCM). UWCM has an active clinical and research section covering the diagnosis of vascular disease using Doppler ultrasound at its Department of Bioengineering and Medical Physics.

The signals for this study were collected by UWCM from the CFAs of patients with and without lower limb vascular disease. Details about the severity of vascular disease associated with the selected signals is given in section 5.4.

The collection was made from the two-channel audio outputs of a Toshiba 270A Duplex scanner with a 5 MHz linear array probe (3.75 MHz Doppler reference frequency) and recorded to metal audio cassettes. An analogue cassette tape recorder (Pioneer CT-1160R) was used for these recordings. Figure 3.3 shows the configuration of the data collection system. The angle between probe and vessel has a direct impact on the absolute value of the Doppler frequency (equation 2.1) and was kept between 50 and 60 degrees during data collection. This ensured that the signals could be compared with each other and corresponds with the clinical practice. Furthermore, the sample volume was kept to approximately half the size of the vessel, as a large sample volume which encompasses almost the entire vessel would have resulted in spectral broadening from the slower blood flow close to the vessel wall [99]. This type of spectral broadening cannot be distinguished from the clinically relevant spectral broadening caused by turbulence in the proximity of a stenosis and therefore needs to be avoided.

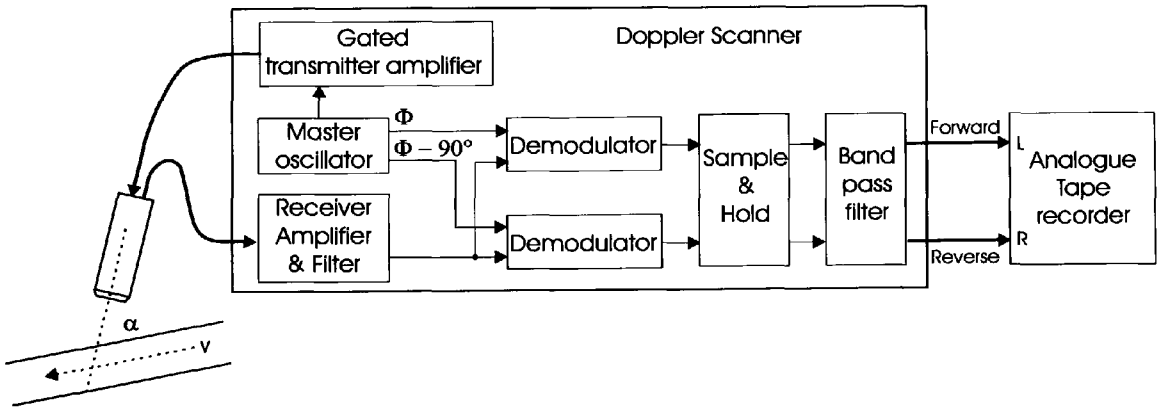

Figure 3.3: Block diagram of the data collection system.

The maximum Doppler shift frequency encountered in all signals was always less

than 7 kHz. Digitisation of the flow signals was performed using a TMS320C30 PC signal processing board at a sampling rate of 15 kHz. The digitised signals were stored in individual files on a Personal Computer (PC). The digital data acquisition system is shown in figure 3.4.

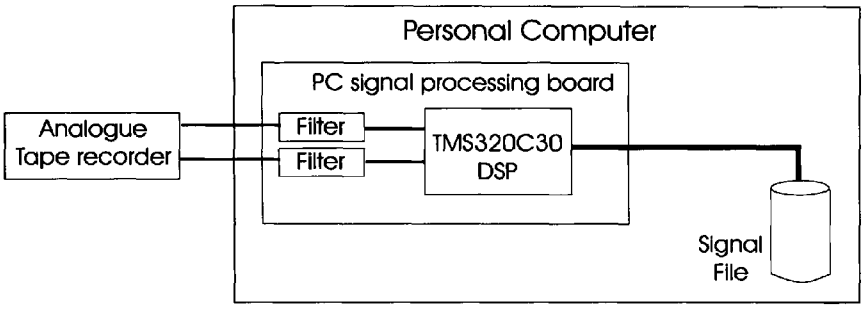

Figure 3.4: Block diagram of the digital data acquisition system.

3.3 Signal conditioning

In addition to the blood flow related components, Doppler ultrasound signals contain a number of components that originate from other sources. Two of these components are caused by the movement of the blood vessel's wall and the ultrasound probe during the measurement. Reflections of the ultrasonic beam from other sources, such as tissue boundaries, may also result in noise and a significant reduction in the quality of the signal.

The removal or reduction of these components is very important to ease any further processing of the Doppler ultrasound signals and improve the accuracy of the results. The investigation covered in this section focused on the removal of the unwanted low frequency components with known sources and characteristics. Section 3.5 concentrates on the removal or reduction of the noise components in the Doppler ultrasound signal, which emanates from various sources and cannot

be removed by simple filtering, because their characteristics are unknown and time variant.

The pulsatile nature of blood flow, which has its source in the heart, causes the diameter of the blood vessel to change. This vessel wall movement results in a frequency component below 100 Hz [1] . Another major unwanted signal component originates from the movement of the ultrasound probe during the measurement and also results in low frequency components. Because these components have lower frequencies than the components resulting from blood flow, a high-pass filter can be used to reduce their amplitude.

A suitable high-pass filter must attenuate the low frequency components without influencing the higher frequency ones. The filter chosen in this study was a digital filter with the following characteristics,

- 8^{th} order finite impulse response (FIR) filter.
- Cut-off frequency of 100 Hz.
- Roll-off of 48 dB/octave.

The filter parameters were chosen to provide sufficient attenuation without unnecessary computational complexity. To avoid distorting the blood flow signal a zero-phase-shift FIR filter was used. In comparison with linear phase filters, which delay the filter output by a fixed number of samples, the delay using the zero-phase-shift FIR filter is zero. It also reduces the filter startup transients. The roll-off was chosen to provide good attenuation without the startup effects of a higher order filter. The 8^{th} order FIR filter provided the optimum characteristic in this study.

Although it is possible to use the high-pass filter which is part of the Doppler ultrasound scanner, it was decided not to do so and to perform this operation as

part of the signal conditioning stage. This allowed the flexibility to change the filter characteristics and observe the effect. The FIR filter was implemented in software after digitising the signal.

3.4 Signal transformation

Section 2.3 outlined the algorithms used commercially or in research to analyse Doppler ultrasound blood flow signals in the time-frequency domain. Traditionally, the STFT algorithm is used to display the time-frequency distribution (TFD) of the Doppler ultrasound signal. Various other spectral estimation methods were investigated by different researchers. The WT and the WPT offered alternative approaches for spectral estimation.

The aim of the spectral estimation of Doppler ultrasound blood flow signals is to obtain a true representation of the spectrum, a good time and frequency resolution and a high signal-to-noise ratio (SNR). The WT features a good time but a poor frequency resolution at high frequencies, and a poor time but good frequency resolution at low frequencies. In particular, the poor frequency resolution at high frequencies makes the WT unsuitable for the estimation of the spectrum as a dampening of the blood flow would be difficult to detect. Another disadvantage is the poor time resolution at low frequencies, which would make it difficult to detect the start of the cardiac cycle.

The WPT is a relatively new tool and has not yet been applied to the Doppler ultrasound signal. Unlike the WT it does not lack the frequency resolution at high frequencies or the time resolution at low frequencies.

Two methods were used to compare the STFT and the WPT. The first method was to generate a number of artificial signals and to compare the results of the

two techniques. The second method was to visually compare the algorithms when applied to a real CFA blood flow signal.

3.4.1 Short-Time Frequency Transform (STFT)

The STFT produces a TFD by multiplying the signal by a sliding time window and analysing the resulting time domain frames using the FFT. Each frame is transformed into the frequency domain and provides the frequency spectrum for the time interval covered by the frame in the time domain. Placed alongside each other, with the frequency along the y-axis and the amplitude along the z-axis, the frames form a time-frequency plot. The mathematical description of the discrete STFT was given by Oppenheim [42] and is listed in chapter 2 (equation 2.3).

Figure 3.5 shows an example of the STFT. The instantaneous frequency of an artificially created signal is shown in Figure 3.5a. This signal is used as an example to illustrate the properties of the STFT. The properties of this signal and the reasoning for its use are explained in section 3.4.3, where the STFT and the WPT are compared. A number of STFT windows were used such as the Hanning, Hamming and a rectangular function, however the Hamming window function was found to perform best. The signal was sampled at 15kHz and a STFT with a Hamming window of 128 points and a 50% overlap was used. Figure 3.5b shows the three-dimensional time-frequency plot or spectrogram. In this plot, the amplitude is represented by colours for convenience.

The time and frequency resolution are important measures for the accuracy of any TFD. The time-frequency resolution is bound by Heisenberg's uncertainty principle [41],

$$\Delta f \cdot \Delta t \geq \frac{1}{4\pi} \tag{3.1}$$

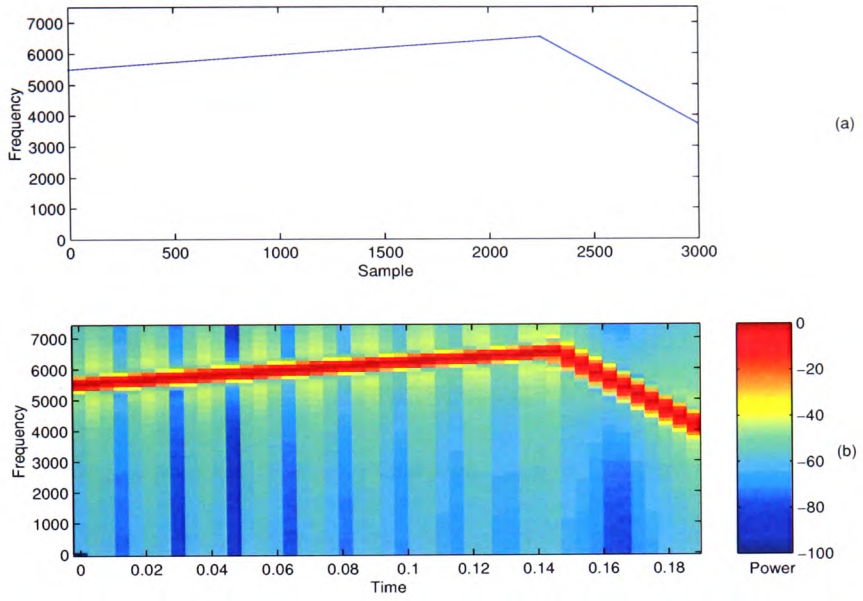

Figure 3.5: Time-frequency representation of a single sinusoidal wave analysed using the STFT with an 128-point Hamming window with 50% overlap (b). The frequency of the sinusoidal wave is governed by the vector in (a).

The time and frequency resolutions of the STFT can be found from the TFD matrix and are given in equation 3.2.

$$\Delta f = \frac{f_s}{w}, \quad \Delta t = \frac{w}{f_s} \tag{3.2}$$

where w is the length of the window used and f_s the sampling frequency. A sampling frequency of 15 kHz and an 128-point STFT window were used.

From equation 3.2 it follows that the time and the frequency resolutions amounted to 8.53 ms and 117.19 Hz, respectively. The STFT assumes that the signal is stationary during the time period of 8.53 ms. No overlap was taken into account in this calculation and transitions between two consecutive time intervals may exhibit discontinuities. The Heisenberg product $(\Delta f \cdot \Delta t)$ for these parameters is equal to

1.

By including a 50% overlap, the spectrogram appears smoother as more FFTs were performed. The division of the signal length by the increased number of FFTs gives the appearance of a higher time resolution, which is not the case because the underlying FFT was still performed on an 128-point long section of the signal [100].

3.4.2 Wavelet Packet Transform (WPT)

The WPT decomposes a signal into wavelet packet coefficients, which can be used to represent the signal in the time-frequency domain. The calculation of the wavelet packet coefficients is performed using a filter bank algorithm that generalises the fast discrete Wavelet Transform (WT) [41]. The equations for the approximation and detail spaces were listed in chapter 2 (equations 2.6 and 2.7).

An example of the WPT TFD for the same signal of figure 3.5 is shown in figure 3.6. The instantaneous frequency of the signal is shown in figure 3.6a. Figure 3.6b shows the time-frequency matrix of this signal, which was sampled at 15 kHz and analysed using a discrete Meyer wavelet packet at decomposition level 6.

Unlike the STFT, which uses sinusoidal bases, the WPT can use a number of different wavelet packets as its bases. Amongst these bases are:

- Haar
- Daubechies 1 - 10
- Symlets 2 - 8
- Coiflets 1 - 5
- Bi-orthogonal
- Reverse Bi-orthogonal
- Discrete Meyer

The importance of choosing the correct wavelet packet base can be seen in figure 3.7. The signal described by the instantaneous frequency in figure 3.6a has been analysed using a discrete Meyer (figure 3.7a) and a bi-orthogonal 1.3 wavelet packet

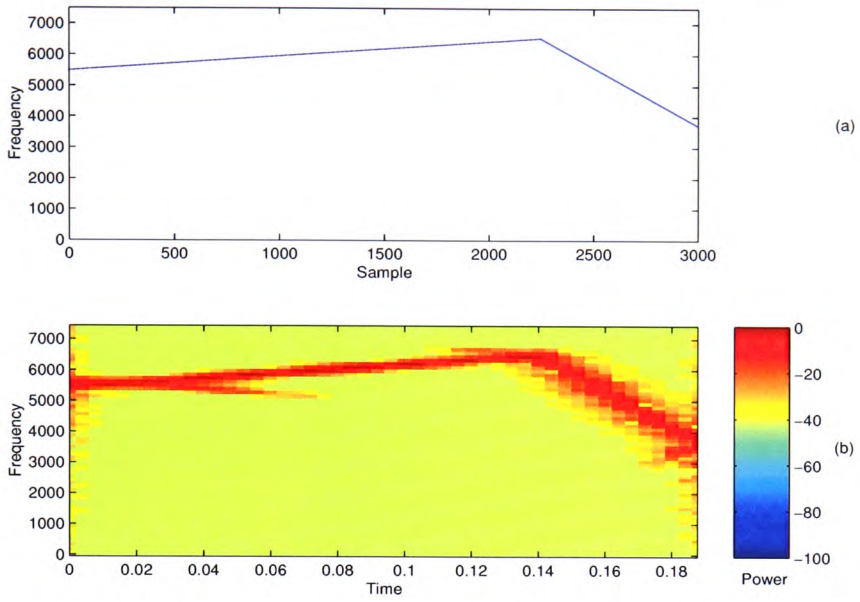

Figure 3.6: Time-frequency representation of a single sinusoidal wave analysed using the WPT at decomposition level 6 with a discrete Meyer wavelet packet (b). The frequency of the sinusoidal wave is governed by the vector in (a).

base (figure 3.7b). It was found in this study that the discrete Meyer wavelet packet base provides the best TFD amongst the investigated bases.

The time and frequency resolutions of the WPT were derived here and are expressed using equation 3.3.

$$\Delta f = \frac{f_s/2}{2^D}, \quad \Delta t = \frac{2^D}{f_s} \tag{3.3}$$

where f_s is the sampling frequency and D the level of decomposition. For a sampling frequency of 15 kHz and a decomposition level of 6, the time resolution is 4.267 ms and the frequency resolution is 117.1875 Hz. The Heisenberg product for the WPT is equal to $\frac{1}{2}$.

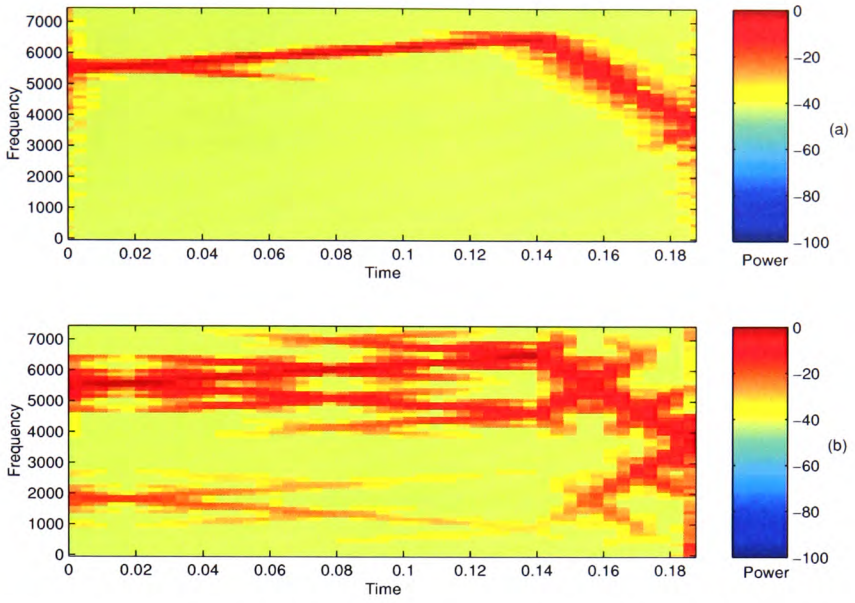

Figure 3.7: Time-frequency representation of a single sinusoidal wave analysed using the WPT at decomposition level 6 with a discrete Meyer wavelet (a) and a bi-orthogonal 1.3 (b) wavelet packet.

3.4.3 Comparison of the STFT and the WPT

The comparison of the STFT and the WPT was conducted using artificially created signals and an example of a real common femoral blood flow signal. The sampling frequency of all signals was 15 kHz. All signals were analysed with the STFT of an 128-point window and 50% overlap. The signals were also transformed using the WPT with a discrete Meyer wavelet packet base and a decomposition level of 6. In order to observe the effect of noise on the time-frequency matrix, gaussian noise was added to the artificial signals to give a SNR of 10 dB.

The power in the TFD plots were set to a range between -100 dB and 0 dB to ease the visual comparison between them. The calculated time-frequency matrix was also scaled so that the maximum power of the matrix was at 0dB.

The two artificial signals were constructed using the following frequency equations,

$$f_1 = \begin{cases} \frac{60Hz}{128 \text{ samples}} \cdot n + 5500Hz & : \quad 0 \leq n < \frac{3}{4}N \\ -\frac{480Hz}{128 \text{ samples}} \cdot n + 14987.96875Hz & : \quad \frac{3}{4}N \leq n < N \end{cases} \tag{3.4}$$

and

$$f_2 = \begin{cases} 5000Hz & : \quad \frac{N}{4} \leq n \leq \frac{N}{4} + 50 \text{ samples} \\ 5500Hz & : \quad \frac{N}{2} \leq n \leq \frac{N}{2} + 750 \text{ samples} \\ 3000Hz & : \quad otherwise \end{cases} \tag{3.5}$$

where f_1 and f_2 are the frequencies of the two signals, N the length of the signal in samples, and n describes the position of the sample. The length of the artificial signals were set to 0.2 s, which is equivalent to 3000 samples.

Signal f_1 was created to show the time and frequency resolution using a ramp signal. The signal is divided into a slow rising and a fast falling section. The slopes of the frequency were derived from the time and frequency resolution of the STFT and the WPT. The frequency in the first section rises with a gradient of 7031.25 Hz/s, which is equivalent to 60 Hz/8.53 ms (STFT) or 30 Hz/4.267 ms (WPT). This gradient was chosen because the changes in frequency over one time-frequency bin is approximately 50% of the frequency resolution of the STFT (Δf = 117.19 Hz). The gradient of the second section of the signal f_1 is -56250 Hz/s, which is equivalent to -480 Hz/8.53 ms (STFT) or -240 Hz/4.267 ms (WPT). This choice was made because the frequency has to change faster than the frequency resolution over one WPT time slot (64 points or 4.267 ms). The WPT was used as a reference because it has a higher time resolution than the STFT. The frequency change is approximately 200% of the frequency resolution. The constant terms in equation 3.4 were derived from the values described in this paragraph.

The second signal, f_2, was created to investigate the time-frequency spectrum

when sudden frequency changes occur within a signal. The signal consisted of a base frequency and two frequency pulses. The first pulse had a very short duration, which was shorter than the time resolution of the WPT. The second pulse was longer, covering a number of STFT windows.

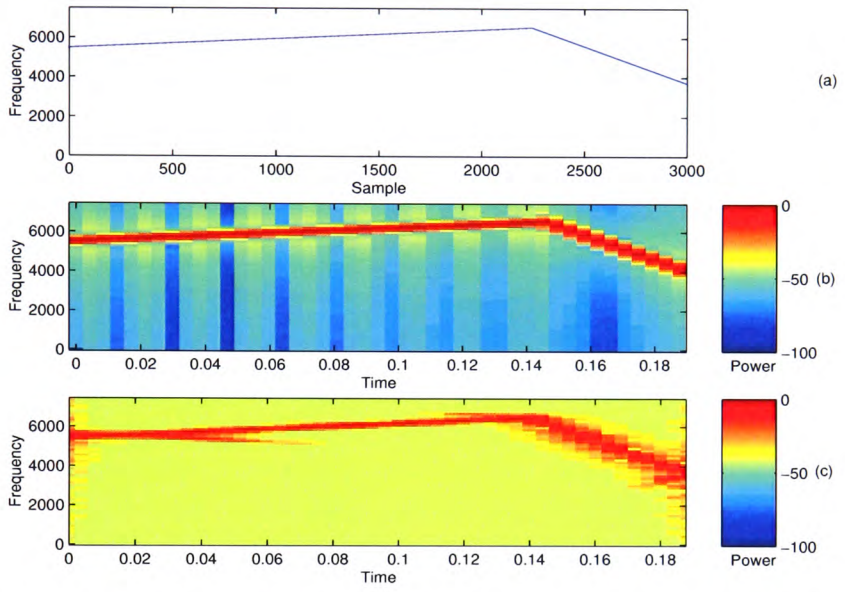

Figure 3.8: Time-frequency representation of a single sinusoidal wave analysed using the STFT with an 128-point window and 50% overlap (b) and the WPT at decomposition level 6 with a discrete Meyer wavelet packet (c). The instantaneous frequency is given by the vector in (a).

To compare the TFDs of the two methods both distributions are shown together in figure 3.8. The same signal of figures 3.5 and 3.6 was used. The figure shows that both methods resulted in the correct spectrum, although the WPT displayed the signal with a wider frequency bandwidth than that of the actual signal. Notably, the noise floor of the STFT is lower than that of the WPT.

The two observations were repeated in figure 3.9. It shows the TFD of a sinusoidal wave with a constant frequency, which changes to a different frequency for two different periods of time. The signal broadens in the frequency direction but

there is little leakage in the direction of the time axis. The result of the WPT is almost the reverse with most of the leakage being in the direction of the time axis and a reduced frequency broadening. The figure shows that the STFT represents the signal better than the WPT.

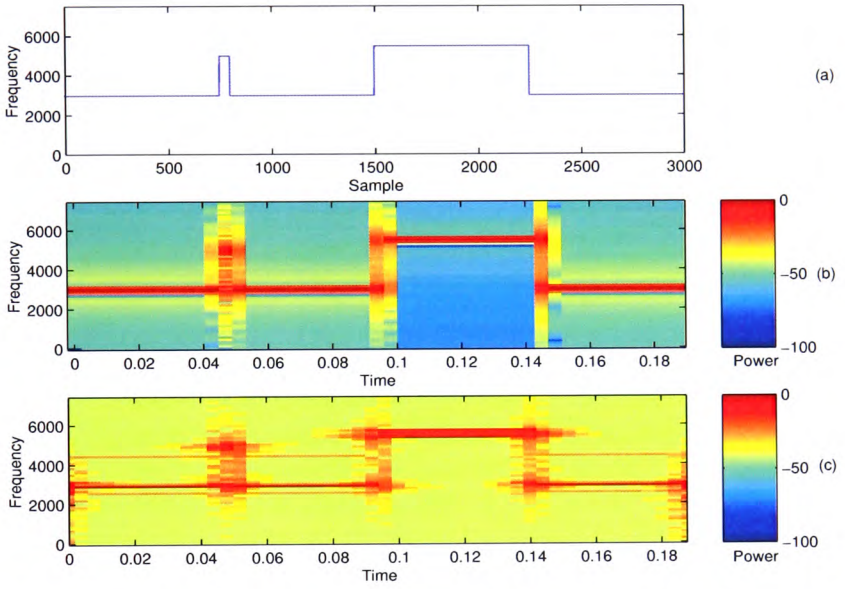

Figure 3.9: Time-frequency representation of a single sinusoidal wave analysed using the STFT with an 128-point window and 50% overlap (b) and the WPT at decomposition level 6 with a discrete Meyer wavelet packet (c). The instantaneous frequency is given by the vector in (a).

Figures 3.8 and 3.9 displayed the result of the two methods when applied to a noise free signal. In order to evaluate the effect of noise on the TFD, Gaussian noise with an amplitude of -10 dB below the signal amplitude was added to both artificial signals in the time domain. A SNR between 0 and 20 dB can typically be found at the output of a Doppler ultrasound scanner [101]. The resulting TFDs for the STFT and the WPT are shown in figure 3.10 for signal f_1 and figure 3.11 for signal f_2.

In both figures it can be seen that the noise floor of the TFD is higher than shown

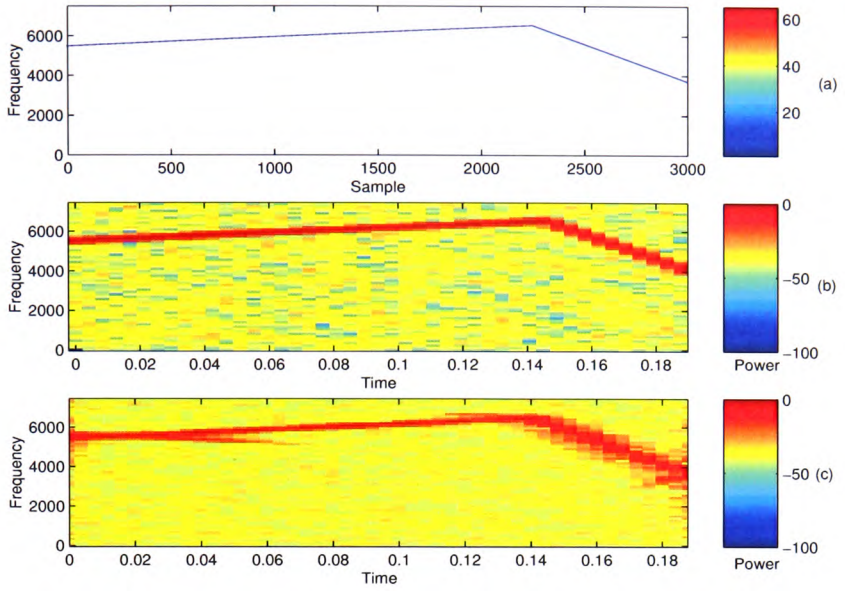

Figure 3.10: Time-frequency representation of a noisy single sinusoidal wave analysed using the STFT with an 128-point window and 50% overlap (b) and the WPT at decomposition level 6 with a discrete Meyer wavelet packet (c). The instantaneous frequency is given by the vector in (a).

previously. Although the noise floors of both methods were quite close, the STFT still yielded a better result. As before the time-frequency signal representation from the WPT created a wider signal with some additional frequency components.

The level of the noise floor in the STFT and the WPT was investigated further. Three different levels of noise were added to the time domain signal f_1 (equation 3.4), and the noise floor of these three and the noise-free signal was measured in the time-frequency domain. The measurement was taken by averaging the four lowest frequency bins over half the length of the TFD. This area did not contain any signal components. The results of the measurement showed that the STFT had generally a lower noise floor, although the difference between the noise floor in the STFT and the WPT decreased with higher noise levels in the time domain signal. Table 3.1 presents the results of this experiment.

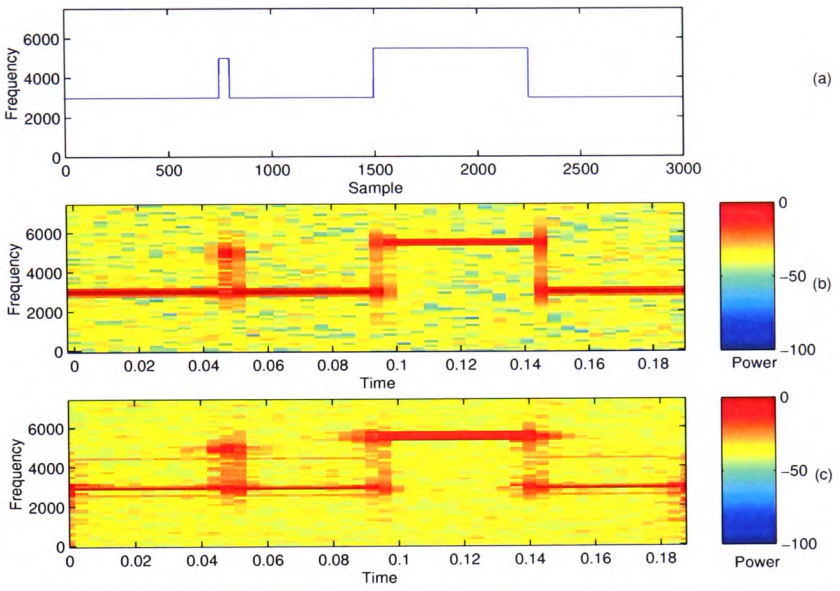

Figure 3.11: Time-frequency representation of a noisy sinusoidal wave analysed using the STFT with an 128-point window and 50% overlap (b) and the WPT at decomposition level 6 with a discrete Meyer wavelet packet (c). The instantaneous frequency is given by the vector in (a).

SNR in the time domain signal	Noise floor in the STFT	Noise floor in the WPT
no noise	-65.7 dB	-42.0 dB
20 dB	-59.5 dB	-42.0 dB
10 dB	-40.0 dB	-37.7 dB
5 dB	-32.5 dB	-31.7 dB

Table 3.1: Level of the noise floor in the STFT and the WPT.

Table 3.2 compares the time and frequency resolution of the STFT and the WPT for different parameters using a sampling frequency of 15 kHz. These values were calculated using equations 3.2 and 3.3. The table shows that the WPT at decomposition level 6 provides a frequency resolution equal to the 128-point STFT with and without 50% overlap. The time resolution of the STFT when used without the 50% overlap is only half of the WPT's time resolution. The time resolution of the STFT seems to improve when a 50% overlap is used, which is misleading as the underlying analysis is still based on an 128-point FFT. The use of the overlap resulted in a smoother display with more data points on the time axis. Therefore, the WPT at level 6 provides a better time resolution compared with STFT (128-point window). A decomposition to level 7 improved the frequency resolution but had the same time resolution as the STFT with an 128-point window.

The second investigation was the use of the two above analysis methods on a real common femoral blood flow signal. Figure 3.12 shows the TFD of a common femoral signal. The result from the STFT, with an 128-point window and 50% overlap, is displayed in figure 3.12(a), whilst the result of the WPT is shown in figure 3.12(b). The WPT used a discrete Meyer wavelet packet base and a decomposition level of 6. Because the lowest power in the STFT matrix was at -120 dB, the scale of figure 3.12 was set between 0 dB and -120 dB.

	STFT without overlap		STFT with 50% overlap		WPT	
	128-points	256-points	128-points	256-points	level 6	level 7
Δt	8.53 ms	17.06 ms	8.53 ms (*4.27 ms*)	17.06 ms (*8.53 ms*)	4.27 ms	8.53 ms
Δf	117.19 Hz	58.59 Hz	117.19 Hz	58.59 Hz	117.19 Hz	58.59 Hz

Table 3.2: Time and frequency resolution of the STFT and WPT at f_s=15 kHz. Values in brackets give the apparent and not the real resolution.

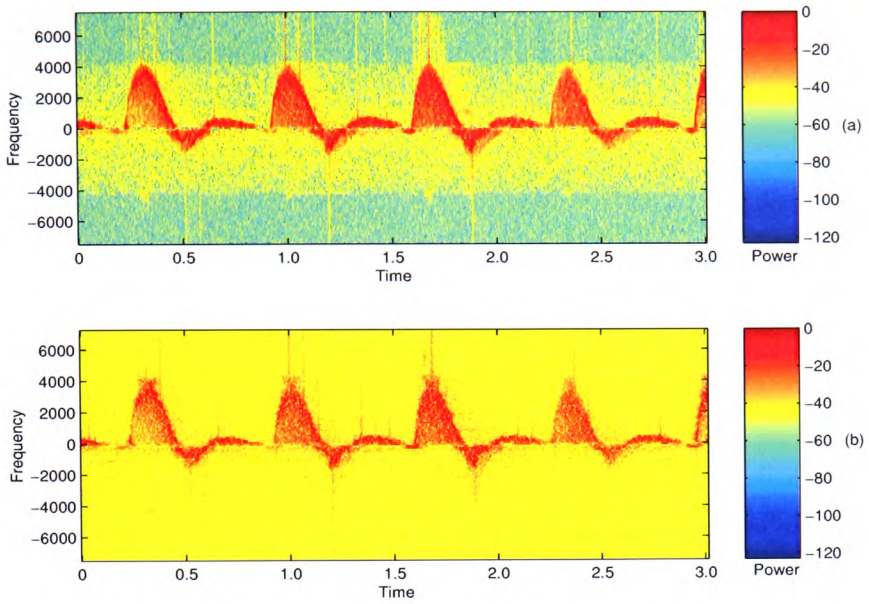

Figure 3.12: Time-frequency representation of a common femoral signal using the STFT with an 128-point window and 50% overlap (a) and the WPT at decomposition level 6 with a discrete Meyer wavelet packet (b).

From figure 3.12 it can be clearly seen that the STFT matrix in part a has a lower noise floor than the WPT in part b.

Another method to visually compare the two techniques was to utilise the extracted maximum frequency envelope (MFE). Figure 3.13 shows the MFE extracted from both, the STFT and the WPT spectrograms. The same, manually selected, threshold was applied to both matrices before the MFE was extracted. In addition a 10-point moving average filter was used to smoothen the MFE. It can be seen that the WPT delivers a very similar result to the STFT when using a discrete Meyer wavelet packet. The MFE extraction algorithm is described in chapter 4.

Another comparison between the two algorithms was made in the area of computational complexity. A number of different implementations exist for both the STFT and the WPT. Equations 3.6 and 3.8 give the numbers of multiplications and additions necessary for the STFT and WPT, respectively [100,102]. These equations

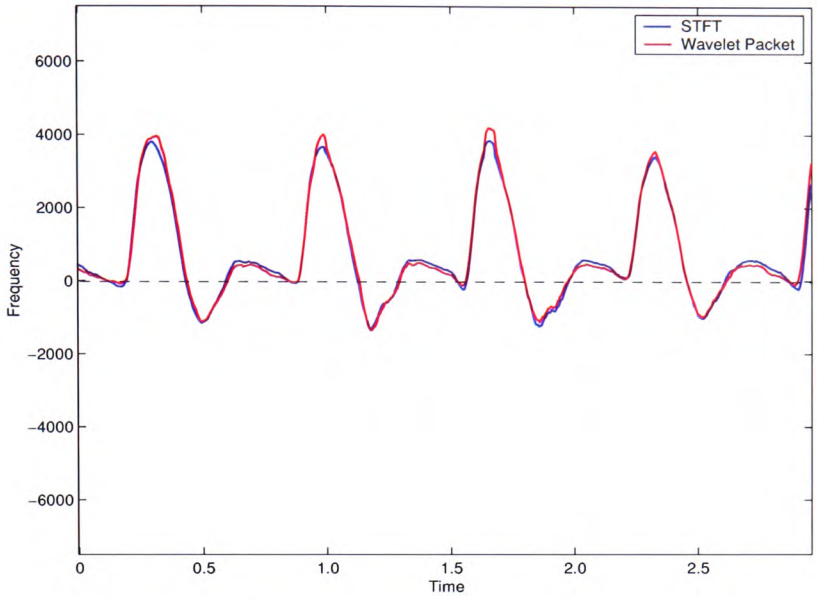

Figure 3.13: MFE of a common femoral signal extracted from the sonogram (STFT, 128-point window, 50% overlap) (blue) and the WPT (decomposition level 6, discrete Meyer wavelet packet) (red).

are based on a standard implementation of the algorithms, with the STFT using the FFT as basis.

$$O(N)_{STFT} = j \cdot N_w \cdot log_2 N_w \tag{3.6}$$

with

$$j = \frac{N_s}{(1 - o_w) \cdot N_w} \tag{3.7}$$

and

$$O(N)_{WPT} = 4 \cdot M \cdot N_s \cdot r \tag{3.8}$$

where $O(N)$ is the number of multiplications and additions required, j the num-

ber of STFT windows fitting into the signal of length N_s, M the length of the filter bank used, r the level of the WPT decomposition, o_w the overlap of the STFT window and N_w the length of the STFT window.

A 10,000 sample long signal was used to compare the numbers of multiplications and additions quantitative. The STFT used an 128-point window and 50% overlap. The length of the filter for the WPT was 62 points for the discrete Meyer wavelet base and the decomposition level was 6. The ratio between both numbers of multiplications and additions was 106.3 in favour for the STFT. The measurement of the execution time on a Pentium II 450 MHz computer using Matlab 6.1 showed that the STFT required 50 ms, whilst the WPT required 1.81 s. This is a ratio of 36.2 in favour of the STFT. The difference in the result is likely to be due to the implementation of the algorithms in Matlab 6.1.

3.4.4 Summary of the STFT and WPT investigations

The previous section compared two spectral estimation algorithms with regard to their time-frequency resolution and noise performance. The STFT was used because it is the traditional algorithm employed in Doppler ultrasound blood flow analysis. The alternative approach, the WPT algorithm, was chosen as it had not been applied to the Doppler ultrasound blood flow signal previously. It was preferred to the WT because of the improved frequency resolution at high frequencies and the improved time resolution at low frequencies.

The investigations showed that both algorithms provided a good representation of the underlying spectrum. The WPT showed either an improved time or frequency resolution, depending on the chosen decomposition level. Although this was an advantage for the WPT, it had the disadvantage of a higher noise floor than the STFT. The noise floor is a very important factor for the automated processing of

Doppler ultrasound blood flow signals. The lower the noise floor, the better and simpler the feature extraction process.

The STFT was preferred in this study because of its lower noise floor. The disadvantage of having a lower time resolution, based on equal frequency resolutions, did not influence the extraction of the MFE. When used with an overlap the STFT provided as many samples for the MFE as the WPT. The fact that the underlying time resolution was less did not effect the outcome (figure 3.13).

3.5 Overall noise reduction

The Doppler ultrasound signal is a very low level signal with noise components from various sources. The main source of noise is the scattering and reflection of the transmitted ultrasound wave from objects other than red blood cells, such as tissue boundaries. Other sources are electronic noise components from the amplifier and filter stages of the receiver, and quantisation noise added during digitising. It is believed that the noise floor is also a function of the probe positioning and is influenced by the experience of the clinician [2, 3].

Figure 3.14 shows the spectrogram of the forward blood flow of one of the common femoral Doppler ultrasound signals used in this study. In this three dimensional plot, the signal power in dB (decibel) is represented by colours ranging from blue to red. This signal was transformed into the time-frequency domain using an 128-point STFT with a Hamming window and 50% overlap.

The signal components of interest (red) have a higher power and can easily be separated from the noise floor (yellow/blue) by visual examination. Automated separation is more difficult and requires significant reduction or complete removal of the noise components.

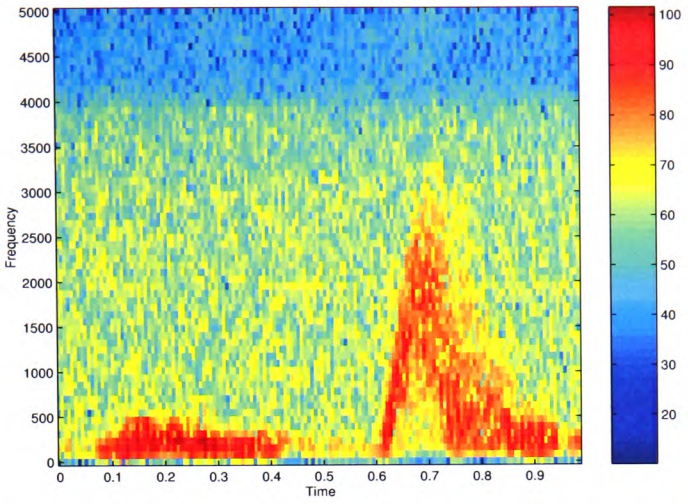

Figure 3.14: Spectrogram of a common femoral artery using an 128-point Hamming window and 50% overlap.

A possible method of reducing noise in a signal is to employ a low-pass filter. The drawback of a low-pass filter is that it can only be used when the signal and the noise occupy fixed and separate frequency bands. In cases where the signal and noise cannot be clearly differentiated, which is the case with Doppler Ultrasound blood flow signals, other methods must be considered.

Several methods were investigated in this study to reduce noise in the Doppler ultrasound signal. These methods felt into three categories. The first applied a manually selected threshold, also known in the literature as grass-cutting. The other two methods were novel in their application to noise reduction in Doppler ultrasound blood flow signals and used the WT in the time and time-frequency domains.

3.5.1 Thresholding

The thresholding technique, also known as grass-cutting in Doppler ultrasound processing, sets all points in a spectrogram to zero power level if they fall below an

empirically determined threshold level. This is aimed at removing background noise and enabling the extraction of specific features from the spectrogram, such as the MFE.

The threshold is based on the maximum power level of either the entire spectrogram or the current time window. The first approach uses a percentage of the maximum power in the spectrogram, usually 3% - 15%, to express the threshold, whilst the second approach uses a dB value based on the current time window, usually 6 dB to 9 dB. Both methods were reported in the literature [17]. The first approach was used to determine the grass-cutting threshold and to compare the thresholding method with the other noise reduction methods proposed in this study.

The selection of the threshold value for grass-cutting has a significant impact on the resulting spectrogram and the subsequently extracted features. To illustrate the effect of different threshold values, one of the signals recorded from the CFA was utilised as an example. The spectrogram of this signal was subjected to grass-cutting at 0%, 3% and 7% of the maximum power level. The three MFEs extracted from the spectrogram are shown in figure 3.15. Since the MFE defines the profile of the blood flow signal in the time-frequency domain, it is clear that this profile is greatly influenced by the selection of the threshold value. The MFE plots of figure 3.15 were calculated using the 95% MFE algorithm defined in section 4.1.

Appropriate thresholds for all signals used in this investigation were determined manually during this study to provide a comparison for the automated process. Figure 3.16 shows the distribution of the optimum thresholds found for these signals. It illustrates that the optimum threshold level varied considerably.

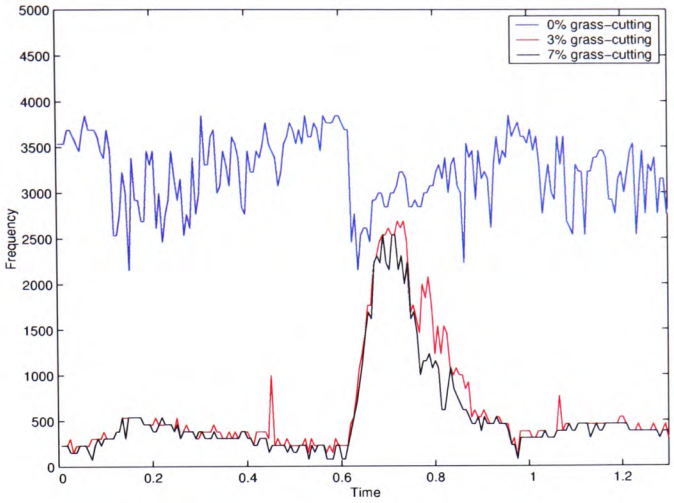

Figure 3.15: 95% MFEs extracted with 0% (blue), 3% (red) and 7% (black) grass-cutting thresholds.

3.5.2 Time domain noise reduction

The reduction of the noise in the spectrogram is very important for the following signal processing stages. Figure 3.15 demonstrated the importance of the selection of the appropriate grass-cutting threshold for the identification of the blood profile and further processing. To eliminate the need for user interaction, namely the selection of the correct grass-cutting threshold, this study investigated the application of wavelet-based noise reduction, or denoising, algorithms.

Wavelet denoising is based on the orthogonal decomposition of the signal using the WT. The wavelet-based decomposition of a signal produces a low-pass and a high-pass filtered signal, each half the length of the original signal. The high-pass filtered signal is the difference between the original signal and the low-pass filtered signal, which is also called approximation. The high-pass filtered signal is also named detail. The approximation of the original signal is further decomposed into another set of detail and approximation. The number of decompositions performed can be identified by the value of the wavelet decomposition level. A decomposition

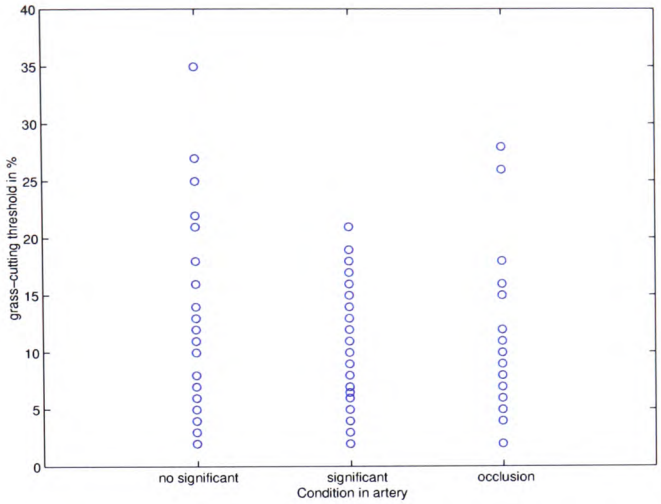

Figure 3.16: Distribution of the grass-cutting thresholds for the signals used in this study separated by disease severity.

of the original signal at level 1 therefore, produces one detail and one approximation. Another feature of the WT is that it allows the full reconstruction of the original signal from the approximation and detail coefficients.

The decomposition of a noisy signal produces detail and approximation coefficients linked to the noise and the signal of interest. The wavelet coefficients associated with the noise are much lower in value than the signal coefficients. It is therefore, possible to calculate a threshold for the wavelet coefficients, and to set all coefficients below the threshold to zero. Two algorithms exist for the tresholding of the wavelet coefficients. Hard-thresholding sets all coefficients below the threshold level to zero, whilst soft-thresholding subtracts, in addition, the threshold value from the remaining coefficients. The denoised signal can be reconstructed from the thresholded wavelet coefficients.

The denoising algorithm utilised in this study is based on the WT introduced in section 2.3. Equation 3.9 defines the transformation of the original signal $x[n]$ into the wavelet coefficients w, consisting of the coefficients corresponding to the signal,

θ, and the noise, z [103].

$$w = W(x[n]) = \theta + z \tag{3.9}$$

The algorithm used to find the threshold for the coefficients is defined by the following equation [104]:

$$T = \sigma \cdot \sqrt{2logN} \tag{3.10}$$

where σ is the standard deviation and N the length of the coefficient vector. An individual threshold was derived for each wavelet coefficient vector (details and approximation) and applied as a soft-threshold. The soft-thresholding algorithm is described in the following equation:

$$w_{thresh} = sgn(w) \cdot (|w| - T) \tag{3.11}$$

where w_{thresh} are the thresholded wavelet coefficients.

Two approaches were considered for investigating the time domain denoising of the Doppler ultrasound signal using wavelets. In the first approach, wavelet denoising was applied to individual sections of the signal. In the second approach, wavelet denoising was applied to the whole signal.

The investigation included denoising using the following wavelets:

- Haar
- Daubechies 1 - 10
- Symlets 2 - 8
- Coiflets 1 - 5
- Bi-orthogonal
- Reverse Bi-orthogonal
- Discrete Meyer

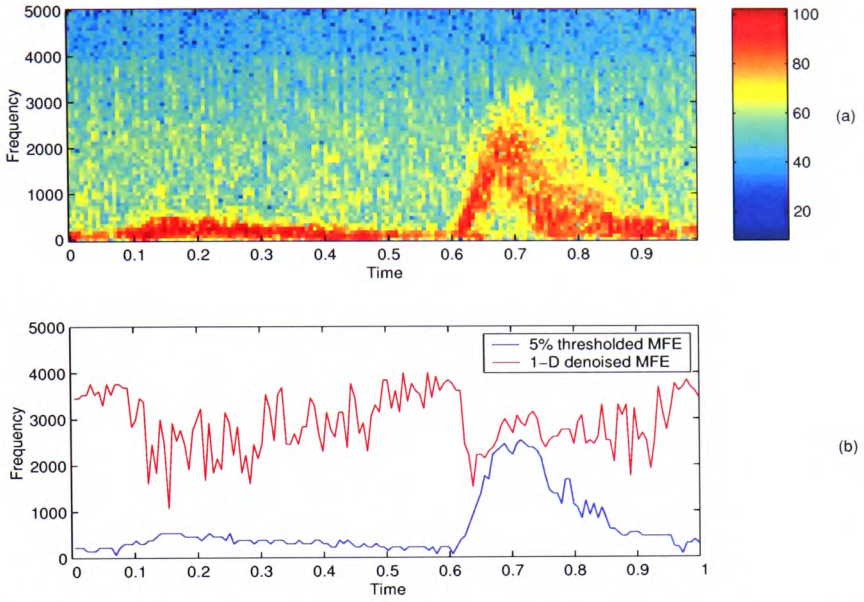

Figure 3.17: Spectrogram (a) and MFE (b) of a common femoral artery blood flow signal, pre-processed (128-points) using a discrete Meyer wavelet at Level 5.

The discrete Meyer wavelet at level 5 produced the best results by visual inspection of the spectrogram and by comparing the extracted MFE with that produced using thresholding.

Figure 3.17 (a) shows the spectrogram of the blood flow signal of figure 3.14 after applying wavelet denoising to the time domain signal using the first approach. To avoid boundary effects, denoising was applied to signal sections equivalent to those of the STFT window used to create the spectrogram. The wavelet used in denoising the signal was the discrete Meyer wavelet at decomposition level 5.

Figure 3.17 (b) shows the MFE of the denoised signal as derived from the spectrogram of figure 3.17 (a) and the MFE produced from the original spectrogram of figure 3.14 after applying a 5% thresholding. Both MFEs were calculated using the 95% MFE algorithm described in section 4.1. It can be observed that wavelet denoising of the individual sections of the signal reduced the background noise level

in some areas of the spectrogram, but the separation between the signal and the noise components is not sufficiently clear. Furthermore, the MFE of the denoised signal significantly differed from that produced by thresholding.

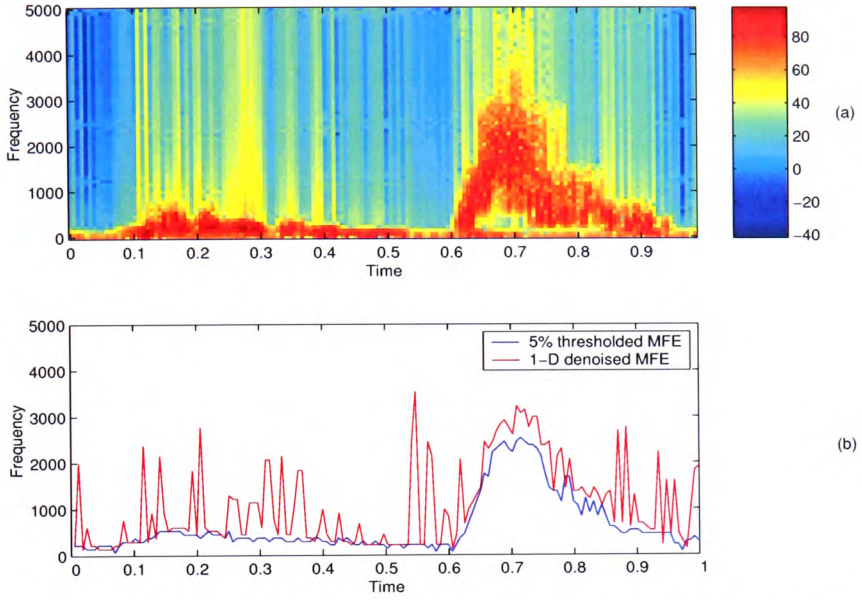

Figure 3.18: Spectrogram (a) and MFE (b) of a common fermoral artery, pre-processed using a discrete Meyer wavelet at Level 5.

Denoising the whole 1 s signal using the same discrete Meyer wavelet at level 5 produced significantly better results as shown in figure 3.18. Figure 3.18 (b) illustrates that the gap between the MFE of the denoised signal and the MFE of the thresholded signal has narrowed significantly in comparison with the results of figure 3.17 (b). With this approach, the results showed that the reduction of the noise floor was larger than that achieved with the first approach. However, local maxima or spikes relating to the noise components are still evident.

3.5.3 Time-frequency domain noise reduction

An alternative noise reduction approach was investigated by applying the wavelet denoising algorithm to the Doppler signal after its transformation into the time-

frequency domain. Here a two-dimensional wavelet decomposition was performed on the spectrogram using the definitions from equations 3.9 to 3.11. The resulting details and approximations were, like the original matrix, two-dimensional matrices.

The same set of wavelets investigated for the time domain denoising were used here. The bi-orthogonal 1.1 and Haar wavelets, both at decomposition level 9, produced the best result in terms of lowering the noise floor. Because these two wavelets are identical and often used in image processing, the Haar wavelet was used.

Figure 3.19 (a) shows the spectrogram of figure 3.14 after applying the two-dimensional wavelet noise reduction algorithm. A Haar wavelet at decomposition level 9 was used in this example and almost completely removed the background noise. It was found in this study that the two-dimensional wavelet denoising algorithm left a residual value in the area where the background noise was reduced. This residual value was constant over the entire matrix and was therefore removed.

Figure 3.19 (b) shows that the MFE derived from the denoised spectrogram of figure 3.19 (a) closely matched the one derived from the spectrogram of figure 3.14 after thresholding by 5%. Both MFEs were extracted using the 95% MFE algorithm. The result is clearly a significant improvement over wavelet-based denoising applied in the time domain and allows the automation of the MFE extraction process.

One problem that can still occur is the appearance of spikes within the denoised spectrogram. This occured when the background noise of the Doppler ultrasound signal was high. Figure 3.20(a) shows the spectrogram of such a signal together with the result of the wavelet denoising algorithm (figure 3.20(b)).

A sliding neighbourhood algorithm was used to remove these spikes from the denoised spectrogram. The algorithm used a 4-by-4 window and set the point under observation to one when 11 or more points in the window were not equal to zero

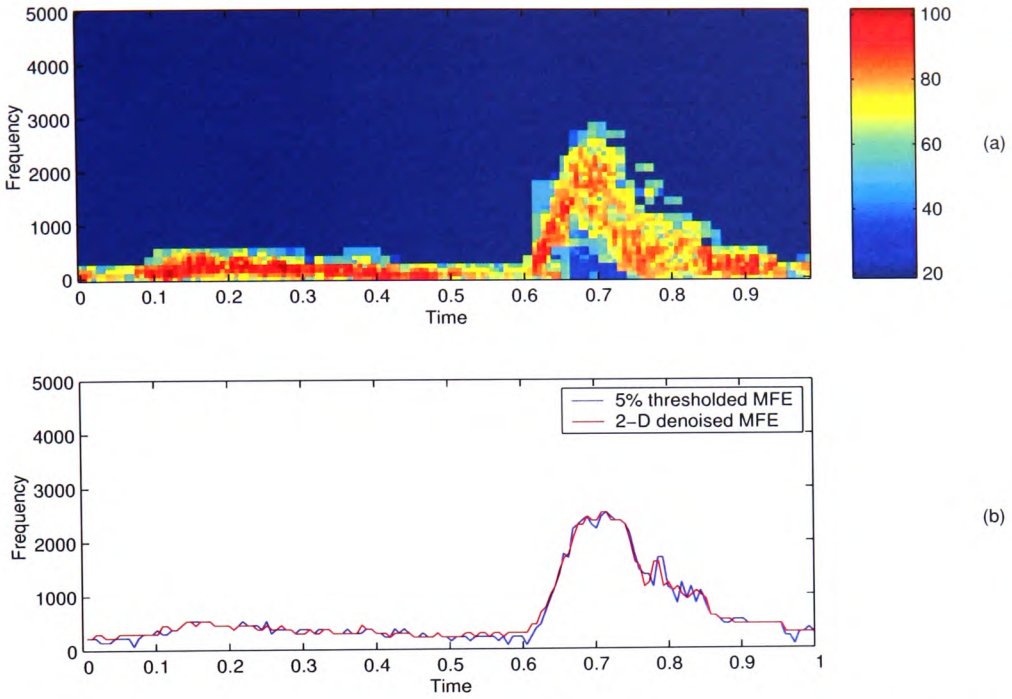

Figure 3.19: Spectrogram (a) and MFE (b) of a common fermoral artery, post-processed using a bi-orthogonal wavelet at Level 9.

(equation 3.12).

$$p_c = \begin{cases} 1 & : \sum_{k=1}^{16} p_k > 11 \\ 0 & : otherwise \end{cases} \tag{3.12}$$

where p_c is the point under observation and p_k the kth-point in the window. The use of this sliding neighborhood algorithm was described by Baykal *et al* [90] and it was found in this study that the 4-by-4 window provided an optimal response on these signals than a 3-by-3 or 5-by-5 window. The entire spike removal algorithm is described below,

1. A second matrix was created by copying the spectrogram matrix.

2. All non-zero components in the second matrix were set to one.

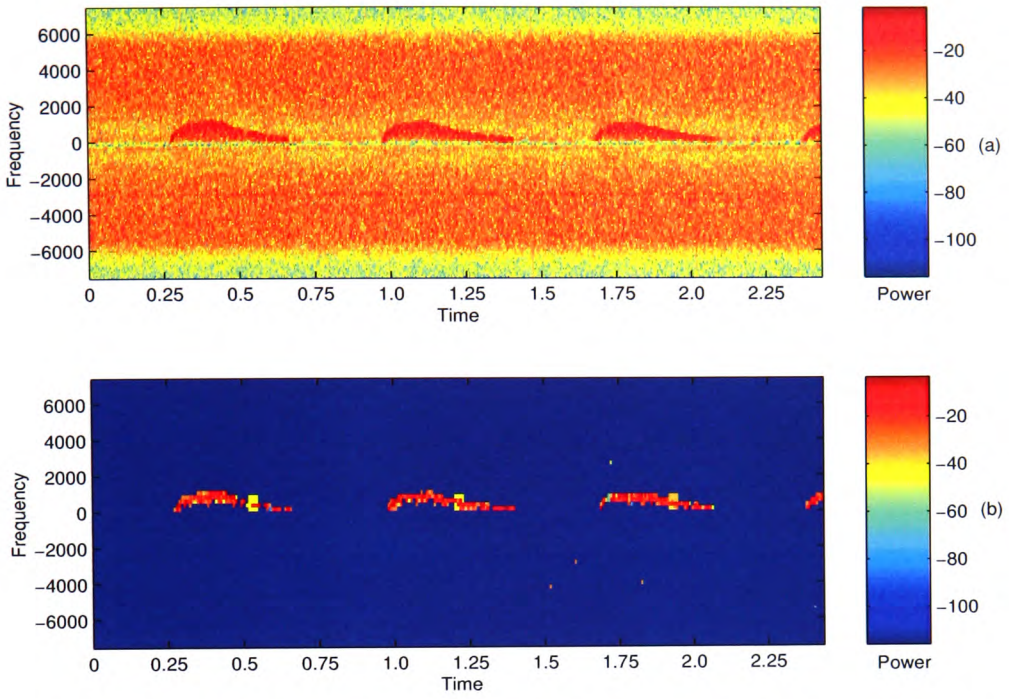

Figure 3.20: Spectrogram of a noisy common femoral artery (a) and the result of the wavelet-based denoising algorithm (b).

3. A 4-by-4 window was moved over the second matrix and the point under observation was set to 1, if the sum of all points in the window was greater than 10.

4. The modified second matrix was multiplied by the denoised spectrogram.

The result of this operation on the spectrogram in figure 3.20(a) can be seen in figure 3.21(b).

3.6 Summary

This chapter investigated the application of new and existing methods in the signal conditioning and feature extraction stages of the Doppler ultrasound blood flow signal analysis process for clinical decision making. These two stages present the

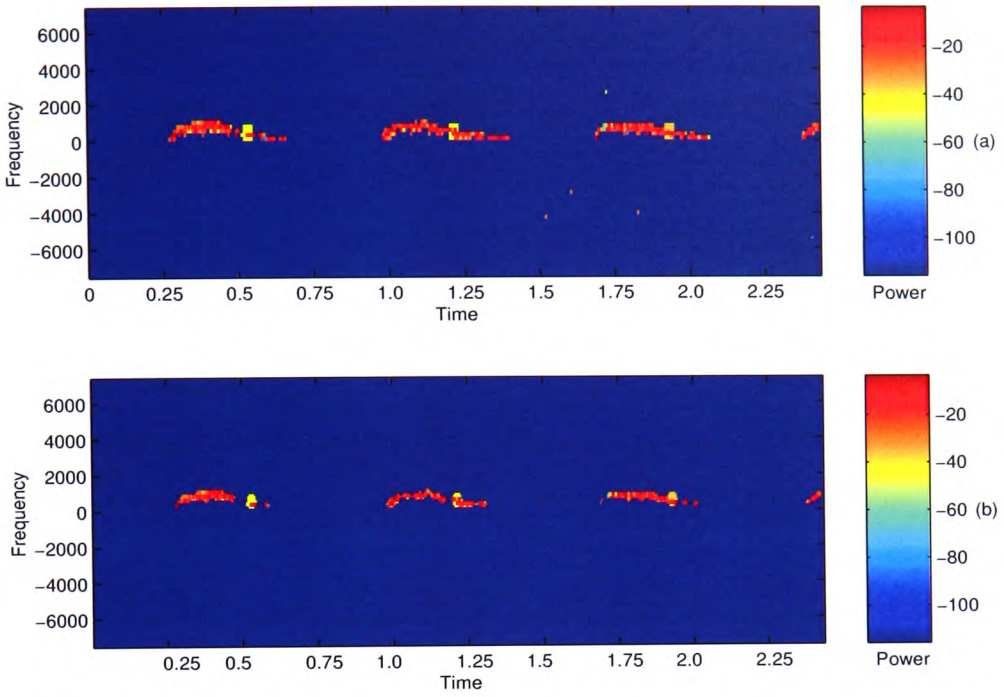

Figure 3.21: Denoised spectrogram of a noisy common femoral artery (a) and the result of the sliding neighbourhood operation (b).

basis for further processing and are key in improving the classification of Doppler ultrasound blood flow signals. Furthermore, the development of signal conditioning and feature extraction algorithms that eliminate any user intervention are crucial for achieving an automated clinical decision making process to diagnose vascular disease.

This chapter has investigated and proposed new signal conditioning and transformation methods and compared them to the methods reported in the literature. These novel approaches showed good results on the clinical signals used in this study. The main findings of this chapter were,

- The STFT was compared with the WPT with regard to true representation of the Doppler signal, noise floor, time and frequency resolution. Although the WPT offered a better underlying time resolution, the STFT performed better

overall.

- The novel approach of wavelet-based noise reduction for Doppler ultrasound blood flow signals in the time domain showed an improved SNR in the TFD, but was inferior to standard thresholding or grass-cutting approaches.
- The wavelet-based two-dimensional noise reduction algorithm, which was applied to the spectrogram of the Doppler ultrasound blood flow signal, showed very good results. This novel approach removed the noise floor of the spectrogram almost entirely without the need for any intervention by an operator.

Overall this chapter has shown that it is possible to automate the noise reduction stage in the analysis of Doppler ultrasound blood flow signals. This is a very important step towards the automation of the entire decision making and diagnosis process.

Chapter 4

Feature Extraction

The previous chapter presented the research conducted into the signal conditioning and transformation of Doppler ultrasound blood flow signals. The methods investigated formed the basis for the feature extraction stage of the decision making and diagnosis process. This chapter describes investigations relating to the feature extraction stage using the findings from the previous chapters.

The extraction of the features from the spectrogram consists of a number of steps. The most important feature of the Doppler ultrasound spectrogram is the maximum frequency envelope (MFE). Its extraction is presented in section 4.1, where the commonly used percentile method is compared with the newly proposed distance method. The blood flow of the common femoral artery (CFA) is normally triphasic. The next step is therefore, the combination of the forward and reverse blood flow signals to one MFE. Different approaches are presented in section 4.2 to combine these two signals. The classification of the Doppler ultrasound blood flow signals only requires a single cardiac cycle. Section 4.3 presents the extraction of this cardiac cycle from the combined MFE and compares two existing methods with a newly proposed method.

The MFE does not include all the information present in the spectrogram. The extraction of the Spectral Broadening Index (SBI) from the spectrogram was investigated in order to determine the relevance of this additional parameter for the classification stage in chapter 5 (section 4.4). Section 4.5 of this chapter presents the investigation into a new approach for length reduction of the MFE to improve the performance of the classification stage described in chapter 5.

The algorithms described in this chapter were applied to 320 signals, which were equally split between signals pre-processed using thresholding and wavelet denoising. On average, 5 cardiac cycles were present in each signal, giving approximately 1500 cardiac cycles for the testing and assessment of the algorithms.

4.1 Extraction of the maximum frequency envelope (MFE)

The spectrogram of the Doppler ultrasound blood flow signal is a complex plot relating the frequency and power of the signal at different time frames or STFT windows, which is shown in figure 4.1. The shape of the spectrogram relates the frequency and power variation in each cardiac cycle. Due to the complexity of the spectrogram, clinical decision making is usually based on its profile, a two dimensional view that illustrates changes in the maximum blood velocity over time. The profile of the spectrogram has become the main tool for the clinician to assess the presence of cardiovascular disease and its severity.

The MFE is widely used to quantify the blood velocity profile of the Doppler ultrasound signal. As a one dimensional vector enclosing the blood velocity spectrogram, it simplifies both, the visual and the mathematical analyses of the information provided by the Doppler ultrasound signal in comparison with the full three

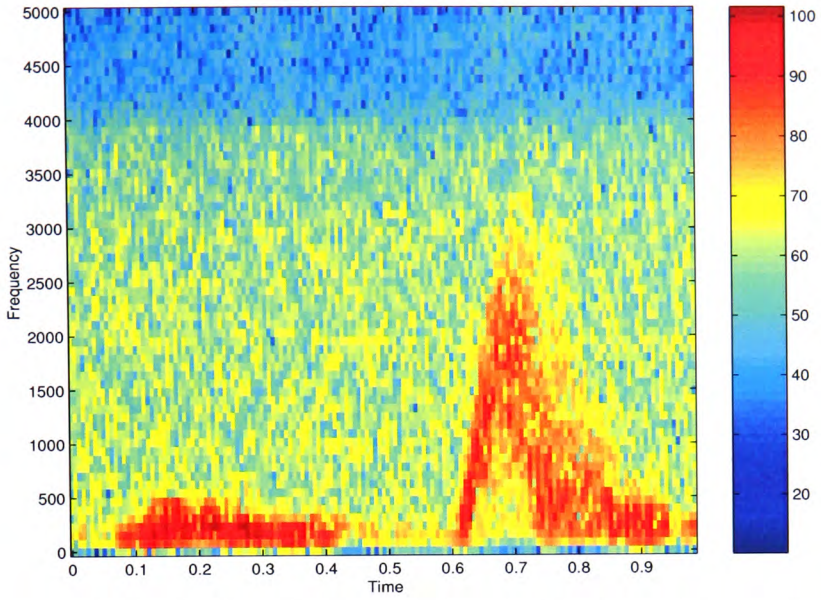

Figure 4.1: Spectrogram of a common femoral artery using an 128-point Hamming window and 50% overlap.

dimensional spectrogram. Although the MFE is an important feature of the Doppler ultrasound signal, the spectrogram may have additional diagnostic information. Part of this information can be captured in indices such as the Spectral Broadening Index (SBI). The SBI has been reviewed in chapter 2 and is introduced into the investigative part of this study in section 4.4.

This section presents the investigation into the techniques for extracting the MFE from the spectrogram. Chapter 3 showed the effects of the noise contents of the Doppler signal on the quality of the spectrogram and the accurate calculation of the MFE. Reducing the noise floor of the spectrogram produced a significant improvement in the MFE computation. In this part of the study the noise rejection capabilities of the MFE computation algorithms were investigated.

4.1.1 The percentile method

The 95% MFE of the spectrogram is defined as the envelope that encloses 95% of the signal's power with respect to the zero line or time axis. The 95% MFE was used in the past by researchers and can be found as a built-in function in many commercial Doppler ultrasound equipment [1, 18, 19, 43].

To illustrate the standard method of calculating the 95% MFE, the spectrogram of figure 4.1 is used. This figure can be viewed as a two-dimensional matrix, or image, with the value of each matrix element, or pixel, representing the signal power. Each column in the spectrogram represents the FFT of one time window or a section of the signal. In the case of figure 4.1 the window size is 128 samples, which is equivalent to 8.53 ms at a sampling frequency for the time domain signal of 15 kHz. Therefore, the spectrogram can be visualised as a horizontal stack of the FFTs applied to successive signal windows of equal length. The spectrogram was calculated using a STFT with a 50% overlap. The overlap provides an increased number of points in the time axis of the spectrogram and therefore, gives a smoother appearance. It does not increase the time resolution of the FFT as this depends on the size of the STFT window employed. Due to the 50% overlap the time period between each column of the spectrogram is halved to 4.27 ms. Each individual pixel is referred to as a frequency bin. The 95% MFE is calculated by locating the pixel or frequency bin in each column, below which lies 95% of the signal power.

To describe the percentile method, it is assumed that $y[n, t]$ represents each matrix element of the spectrogram. In this representation,

- $0 \leq n \leq N - 1$ is the number of the element along the frequency axis or the number of the frequency bin.
- $0 \leq t \leq M - 1$ is the number of the element along the time axis. As an

example, t=2 represents the FFT of the third window of the signal.

The vector containing the total power for each column of the spectrogram matrix is,

$$P_T[t] = \sum_{n=0}^{N-1} y[n,t] \tag{4.1}$$

The power enclosed by any matrix element, $y[n,t]$, and the zero line for any column, t, is given by,

$$P_B[b,t] = \sum_{n=0}^{b} y[n,t], \quad \text{for} \quad 0 \leq b < N-1 \tag{4.2}$$

where b is the row number, or frequency bin, in the new cumulative sum matrix P_B. Therefore, the matrix element that encloses 95% of the signal power for a matrix column t is termed as $N_{95}[t]$ and defined by the following equation:

$$P_{N95}[t] = 0.95 \cdot P_T[t] = \sum_{n=0}^{N_{95}[t]} y[n,t] \tag{4.3}$$

where $P_{N95}[t]$ contains the value for 95% of the total power at time interval t.

The MFE for the whole spectrogram, MFE_{95}, is the vector that consists of the index N_{95} of each column and is defined by,

$$MFE_{95} = \{N_{95}[0], N_{95}[1], \ldots, N_{95}[M-1]\} \tag{4.4}$$

or

$$MFE_{95}[t] = N_{95}[t] \tag{4.5}$$

To investigate the accuracy of the percentile method, analyses were conducted on clinical signals. Figure 4.2 illustrates a sample result from these analyses. This figure shows the FFT result of the 50^{th} time window of the signal shown in figure 4.1. This FFT plot illustrates the variation of signal power with frequency within the one time window. Clearly, the maximum frequency of this section of the blood flow signal is less than 500 Hz. The low power frequency components beyond 500 Hz are the noise components within the signal.

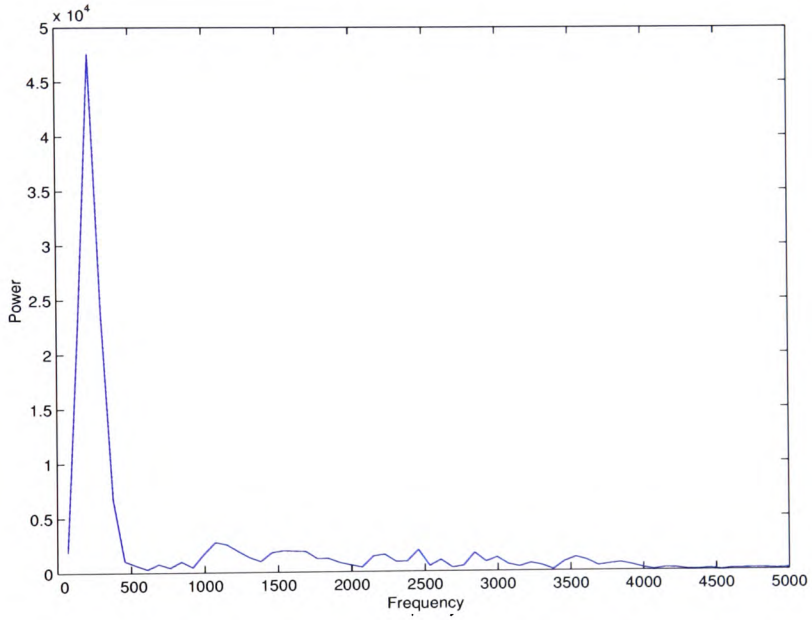

Figure 4.2: Frequency spectrum of a common femoral Doppler blood flow signal of the 50^{th} time interval (M=49) of the spectrogram in figure 4.1.

To calculate the maximum frequency point for the FFT in figure 4.2, the cumulative signal power was plotted against frequency as shown in figure 4.3. The horizontal line in this figure represents 95% of the maximum signal power level. The intersection of this line with the cumulative power graph should provide the required 95% MFE point. In this example, the MFE point was found to be close to 3500 Hz instead of the expected value of less than 500 Hz. The difference between

the calculated and expected values of the MFE was caused by the presence of noise. Figure 4.4 illustrates this weakness of the 95% MFE computation algorithm over the entire spectrogram in figure 4.1. The MFE is unusable if the algorithm is applied to the spectrogram without any prior noise reduction.

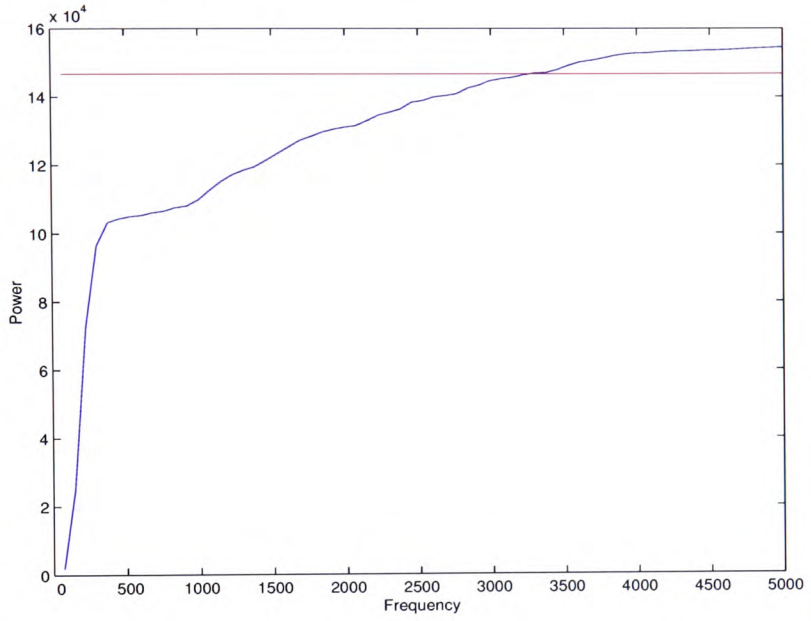

Figure 4.3: Cumulative sum and the 95% power level of the total power of the frequency spectrum of figure 4.1.

Previous researchers have used the thresholding algorithm described in section 3.5.1 to lower the noise floor and reduce the error in calculating the MFE.

Figures 4.5 and 4.6 show the result for the same time window of figure 4.2 after applying a 5% threshold. The MFE point in this case was calculated correctly. However, the problem here is the differences in the quality of the signal. A signal with a high noise floor requires a higher threshold value than a signal with a low noise floor. This requires manual variation of the threshold value for each Doppler ultrasound signal. Alternatively, the threshold can be set high enough so that it may cover several signals. The weakness of the first approach is the need for continuous human intervention and results in inconsistencies between different operators. The

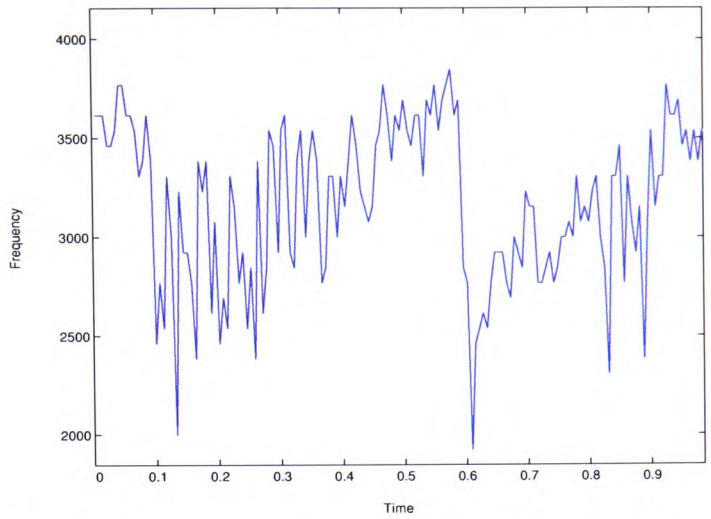

Figure 4.4: MFE of the common femoral Doppler blood flow signal shown in figure 4.1 without thresholding and calculated using the standard 95% algorithm.

second approach may cause the loss of a significant part of the actual signal with the noise components and may result in an inaccurate 95% power point calculation.

Figure 4.7 shows the frequency content of the signal in figure 4.1 at a different time interval. Instead of having a sharp power drop like the frequency spectrum in figure 4.2, this frequency spectrum trails off much slower. To illustrate the problem with thresholding the frequency spectrum, three example thresholds are indicated in the figure. Thresholds (a) and (b) shown in figure 4.7 give an example of the first approach, where two operators might have selected a different threshold. The difference in the maximum frequency between these two operators would be around 200 Hz. Threshold (c) is used to illustrate the second approach. In this case a threshold was selected so that it would cover a range of signals with different signal-to-noise ratios (SNR). It can be seen that a number of high frequency components with relatively high power content were removed. This might result in a lower maximum frequency than otherwise expected. The difference in the maximum frequency between threshold levels (a) and (c) is around 800 Hz.

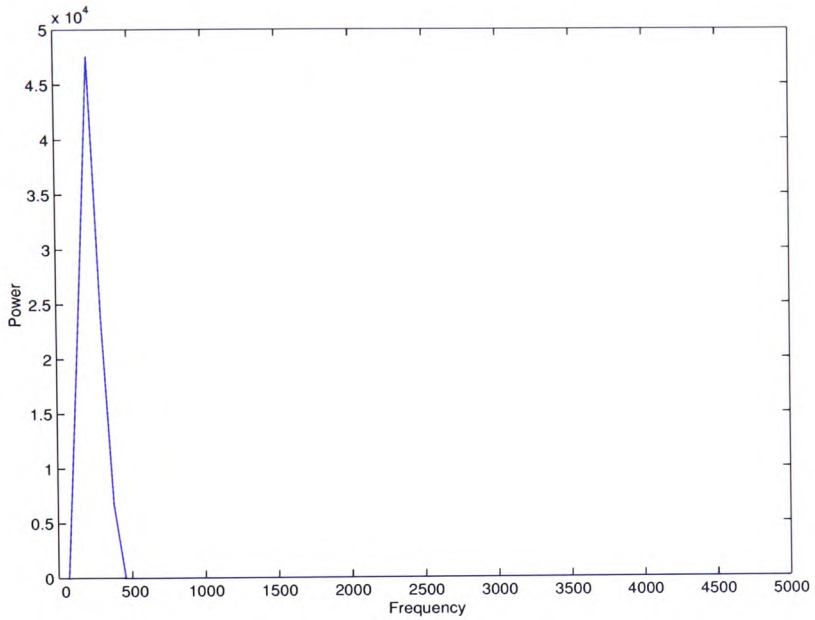

Figure 4.5: Frequency spectrum of a common femoral Doppler blood flow signal of the 50^{th} time interval (M=49) of the spectrogram in figure 4.1 after grass-cutting.

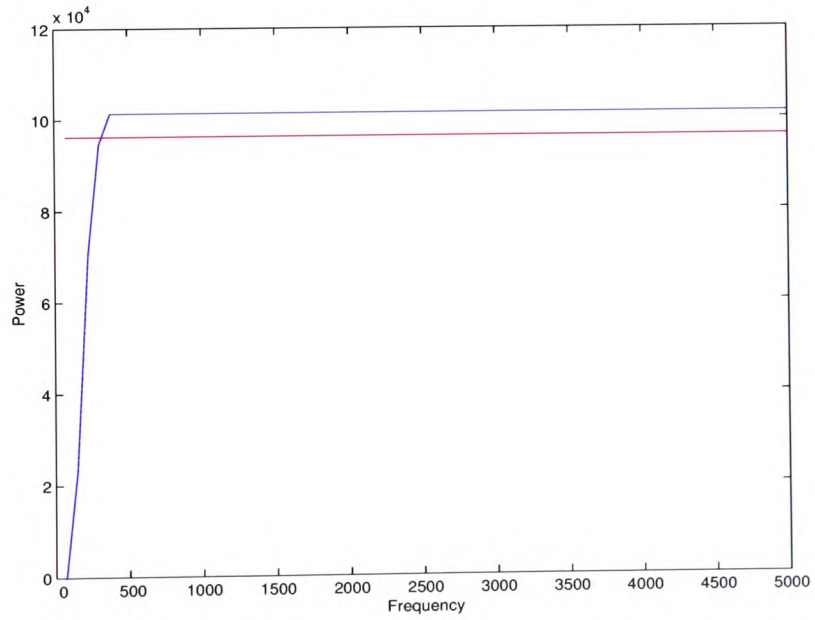

Figure 4.6: Cumulative sum and 95% of the total power level of a common femoral Doppler blood flow signal of time interval 49 after grass-cutting.

The usual practice of selecting the appropriate threshold for a signal is to vary the threshold until a smooth MFE appears. This method is not practical for automated processing. It was therefore, necessary to remove the need for this adjustment either by reducing the noise floor (chapter 3) or using an extraction algorithm that is less sensitive to noise. The next section develops and investigates the latter approach.

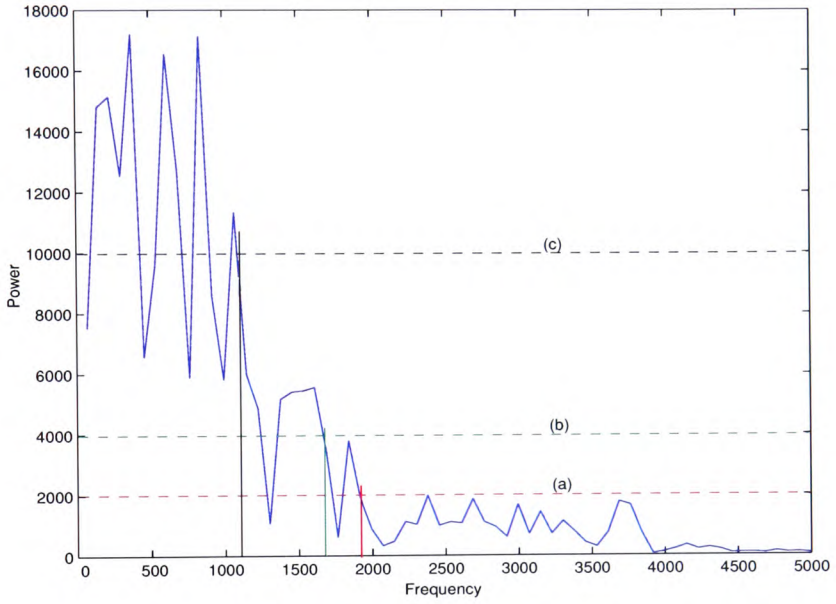

Figure 4.7: Frequency spectrum of the Doppler blood flow signal in figure 4.1 at time interval 125 with thresholds (a), (b) and (c).

4.1.2 The MFE distance method

To eliminate the need of threshold selection, an alternative method for the MFE extraction was developed and investigated in this study. This method is based on the fact that the cumulative sum of the frequency spectrum rises fast where the power of the frequency component is high. Above the maximum frequency the gradient of the cumulative sum is reduced because of the smaller power of the noise components. The graph of the cumulative sum therefore bends at the maximum frequency (figure 4.6). Connecting the start and end points of the cumulative power

vector with a straight line forms a triangle. This triangle has its greatest distance, with respect to the straight line base, at the maximum frequency, where the knee of the cumulative power graph presents the apex of the triangle. The frequency of the apex of the difference graph represents the maximum frequency point.

A mathematical description of this novel algorithm is given in equations 4.6 to 4.8. The matrix of the spectrogram is named $y[n,t]$, with $0 \leq n \leq N-1$ and $0 \leq t \leq M-1$. Where N and M are the number of elements along the frequency and time axes, respectively.

The matrix of the cumulative power, P_B, of the spectrogram matrix was defined earlier (equation 4.2), and is repeated here for convenience,

$$P_B[b,t] = \sum_{n=0}^{b} y[n,t], \quad \text{for} \quad 0 \leq b < N-1 \tag{4.6}$$

where $y[n,t]$ represents each matrix element in the spectrogram and b the row, or frequency bin, of the newly formed cumulative power matrix P_B.

The matrix containing the straight lines, $g[n,t]$, connecting the start and end points of the cumulative power matrix P_B is defined as,

$$g[n,t] = \frac{P_B[N-1,t] - y[0,t]}{N} \cdot n + y[0,t] \tag{4.7}$$

The point for the MFE within a column t is given by the largest value of the difference between the cumulative power vector and a straight line connecting the start and end points of this vector (equation 4.8).

$$MFE_{Dist}[t] = \max\left(P_B[n,t] - g[n,t]\right) \tag{4.8}$$

Therefore, the MFE over the entire spectrogram is given by,

$$MFE_{Dist} = \max\left(P_B[n] - g[n]\right) \tag{4.9}$$

Figure 4.8 shows the spectrogram of one of the common femoral signals used in this study. The noise floor in this signal ranged between -20dB and -30dB. Figure 4.9 investigates the signal further by considering the frequency content of the 181st time interval of the spectrogram ($t_{centre} = 0.7686s$).

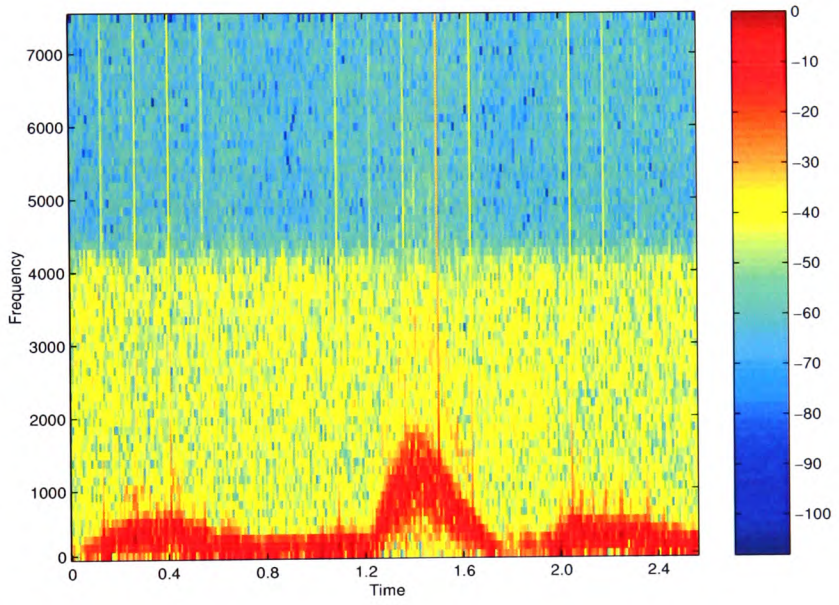

Figure 4.8: STFT spectrum of a clinical common femoral artery blood flow signal used in this study.

Figure 4.9a shows the FFT of this particular time interval and the maximum frequency, which was derived using the proposed distance method (figure 4.9b). The amplitude of the FFT spectrum drops off at the maximum frequency and the higher frequency noise components have a relatively low amplitude. The knee in the cumulative sum could be clearly identified at this frequency.

Figure 4.10a shows the FFT spectrum of a different time interval with its centre

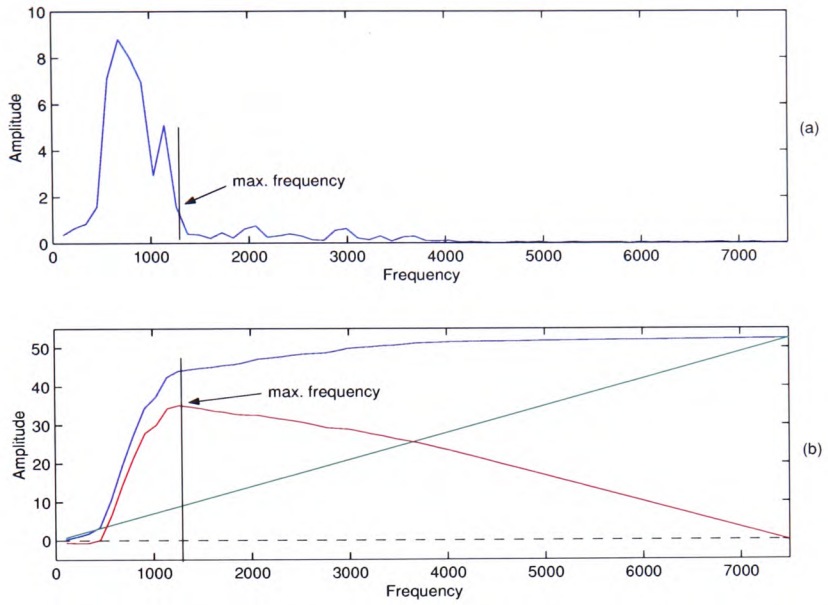

Figure 4.9: FFT spectrum of a common femoral Doppler blood flow signal without noise reduction (figure 4.8) at time interval t=0.7686s (interval 180)(a). Cumulative sum (blue), straight line (green) and difference graph (red) of the same time interval (b).

at t=0.8967s (column 210). Although the amplitude of the higher frequency noise components are the same as in figure 4.9a, the amplitude of the signal is much lower. This caused the cumulative sum not to have a pronounced knee compared to figure 4.9b, and in fact, it shows a second knee at a higher frequency. The second knee in the cumulative sum was caused by the drop off of the amplitude of the noise components. This was always present in the signals used in the study although it was much less pronounced in signals with larger signal amplitudes. The small amplitude of the signal resulted in the maximum frequency being estimated at a much higher value than what it should be.

Another example of the problem with time intervals where the amplitude of the signal was relatively low is shown in figure 4.11. The FFT spectrum of the signal with a relatively high noise floor is shown in figure 4.11a. Figure 4.11b shows that a clear knee cannot be identified in the cumulative sum vector and therefore, the maximum

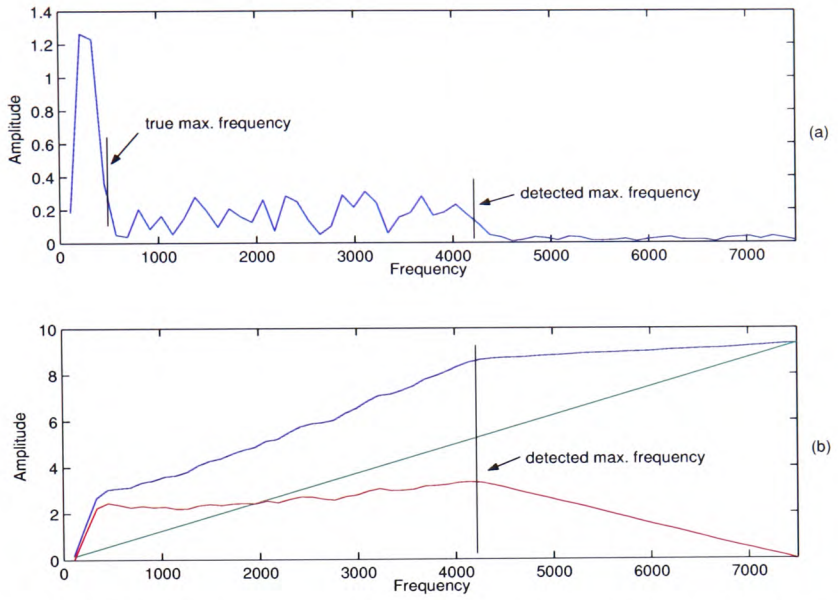

Figure 4.10: FFT spectrum of a common femoral Doppler blood flow signal without noise reduction (figure 4.8) at time interval t=0.8967s (interval 210)(a). Cumulative sum (blue), straight line (green) and difference graph (red) of the same time interval (b).

frequency would be estimated wrongly. This is similar to the the spectrum found in the reverse flow region where there was no significant reverse flow. This means that the reverse flow region was primarily composed of noise components. The frequency marked as true maximum frequency was detected from the sonogram.

By squaring the spectrogram, the SNR can be increased. Figure 4.12 shows the same signal and time interval as that of figure 4.10. It can be seen that in this case the maximum frequency was estimated correctly due to the increased SNR.

Increasing the SNR by squaring the FFT spectrum worked well for spectra where the signal was generally larger than the noise components. Otherwise, the problem remained or got worse. Figure 4.13 shows the MFE of the entire common femoral signal from figure 4.8. The MFE was extracted using the percentile method (95%) on a thresholded spectrogram (a), the distance method (b) and the distance method

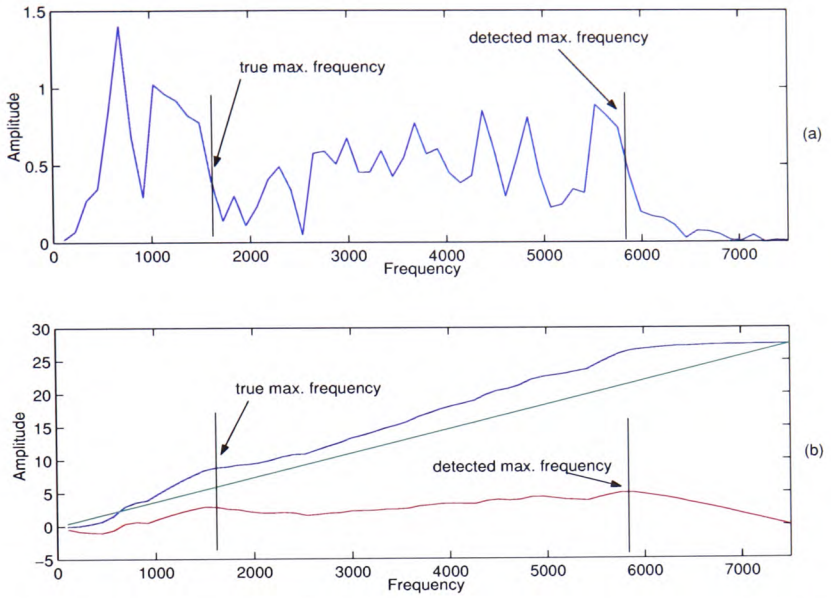

Figure 4.11: FFT spectrum of a noisy common femoral Doppler blood flow signal without noise reduction. Cumulative sum (blue), straight line (green) and difference graph (red) of the same time slot (b).

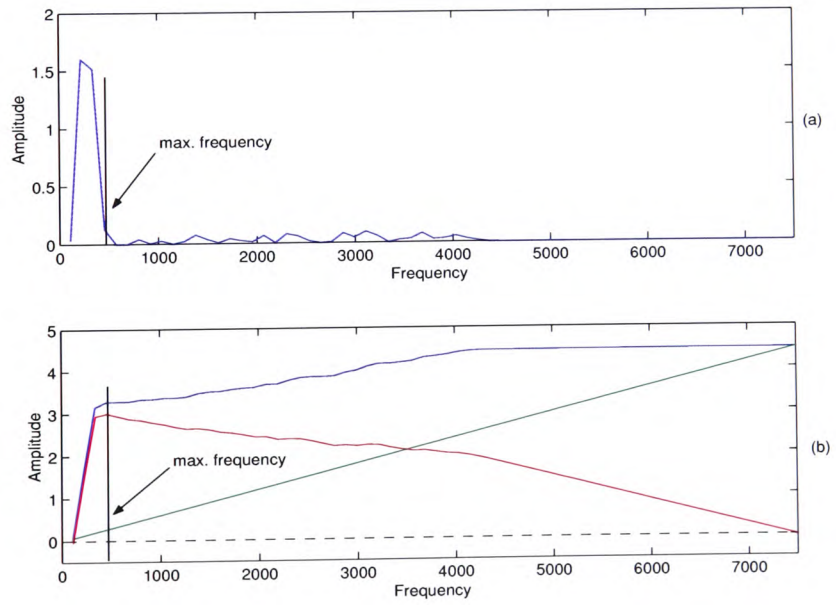

Figure 4.12: Squared FFT spectrum of a common femoral Doppler blood flow signal without noise reduction (figure 4.8) at time interval t=0.8967s (column 210)(a). Cumulative sum (blue), straight line (green) and difference graph (red) of the same time interval (b).

with squared FFT spectra (c). The figure shows that the distance method was able to deliver a MFE close to the one extracted by the percentile method, but failed where only noise is present.

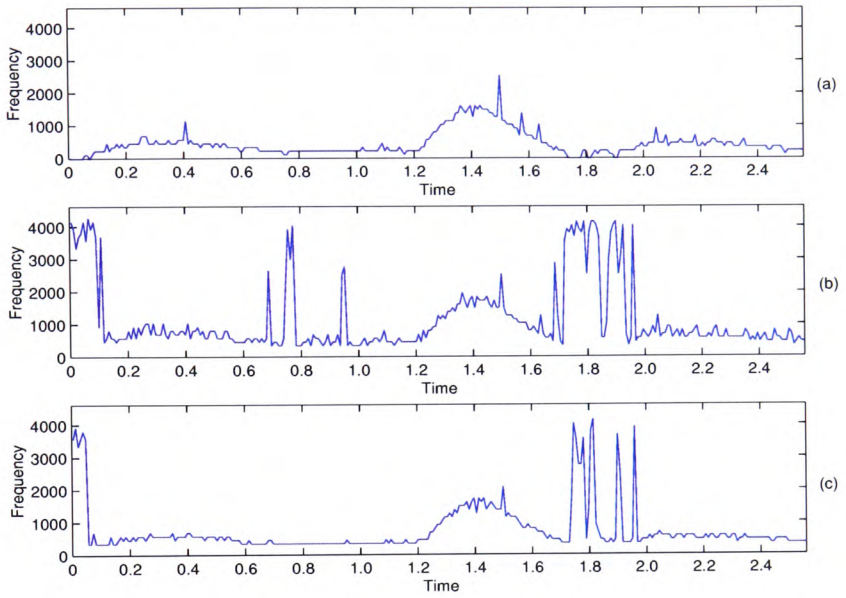

Figure 4.13: MFE of a common femoral signal (figure 4.8) using the percentile method (95%) (a), the distance method (b) and the distance method with squared FFT spectra (c).

Applying the distance method to the thresholded or wavelet denoised spectrogram yielded good results. The MFEs were very similar to the ones extracted using the percentile method, and had higher amplitudes as they were not only using 95% of the FFT spectrum power. Figures 4.14a and b show the MFE calculated using the distance and percentile methods (95%), respectively.

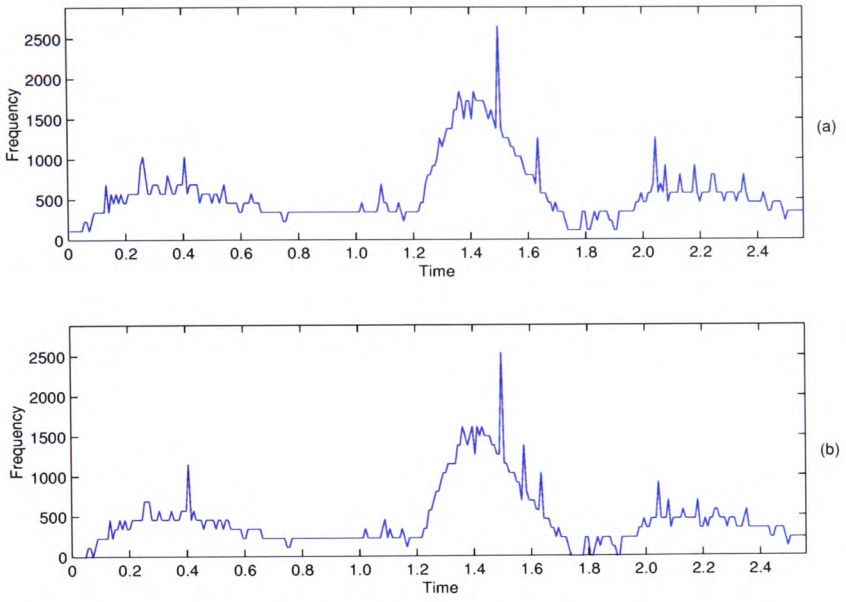

Figure 4.14: MFE of a common femoral signal using the distance method (a) and the percentile method (95%) (b).

4.2 The combination of the forward and reverse flow MFE

Section 4.1 described the extraction of the MFE using the forward flow only. The common femoral artery (CFA) does not only have forward but also reverse flow. In order to obtain the complete MFE, the forward and reverse flow envelopes must be combined. Figure 4.15 shows the MFE of the forward flow in blue and that of the reverse flow in red, both MFEs were created using the percentile method. To generate a smoother MFE a moving average algorithm was applied to both MFEs. In the literature, Evans [92] used a 5-point moving average algorithm in his attempt to smooth the MFEs, which had a sample period of 12.5 ms. As the MFEs in this study had a higher sample period (8.56 ms), it was found that a 10-point moving average was needed.

Although both MFE vectors could be used separately in the classification stage,

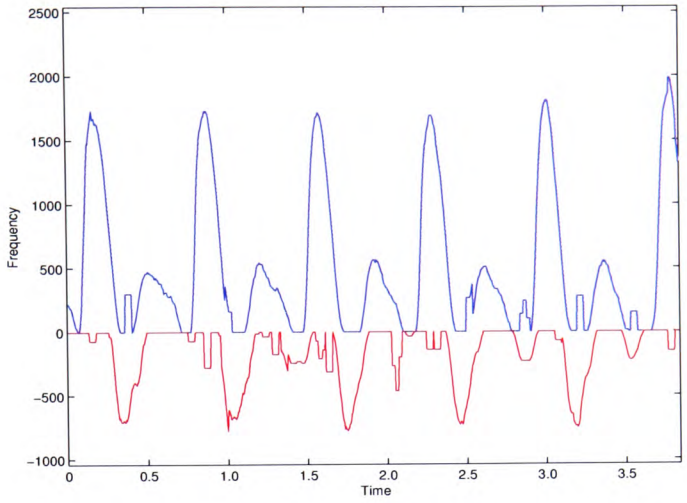

Figure 4.15: Forward (blue) and reverse (red) flow of a healthy common femoral artery.

it would mean that the feature vectors double in numbers. It is therefore, common to combine the forward and reverse flow envelopes to one MFE vector. Three methods of combination were investigated in this study. Two of these methods, the subtraction and the comparison methods were mentioned in the literature [18]. The third method, which is proposed in this study, is an improvement on the comparison method.

The subtraction method subtracts, or adds if the sign is taken into account, the reverse flow from the forward flow.

$$e[n] = e_f[n] - e_r[n] \tag{4.10}$$

where e_f is the forward flow MFE, e_r the reverse flow MFE, e the combined flow MFE and n the sample index.

This method delivered good results when no overlap between the forward and reverse flow occurred. Figure 4.16 shows the problem using the MFEs from figure 4.15 as an example. It shows that a forward flow component reduced the amplitude

of the reverse flow of the combined envelope at point 1. On four other positions (points 2 to 5), the amplitude of the forward flow waveform of the combined MFE was reduced or reversed by a reverse flow component. However, the advantage of this method was the smooth transitions from forward to reverse flow and vice versa.

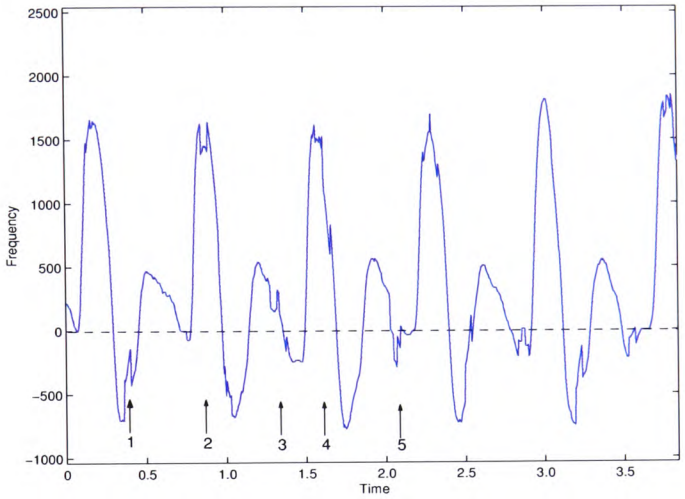

Figure 4.16: Combined MFE using the subtraction method.

The comparison method did not suffer from the problem of distorting the MFE amplitude. It simply compares the forward and reverse flow MFEs, point for point, and only utilises the largest value of the two MFEs.

$$e[n] = \begin{cases} e_f[n] & : \quad e_f[n] \geq |e_r[n]| \\ -|e_r[n]| & : \quad |e_r[n]| > e_f[n] \end{cases} \tag{4.11}$$

where e_f is the forward flow MFE, e_r the reverse flow MFE, e the combined flow MFE and n the sample index.

Figure 4.17 shows the combined MFE using the comparison method. The figure shows that there was no reduction in amplitude of the forward or reverse flow sections of the combined MFE. Large flow components still influenced the combined MFE. This is especially noticeable at points 1 to 4 of figure 4.17, where reverse and forward

flow components changed the direction of the combined MFE.

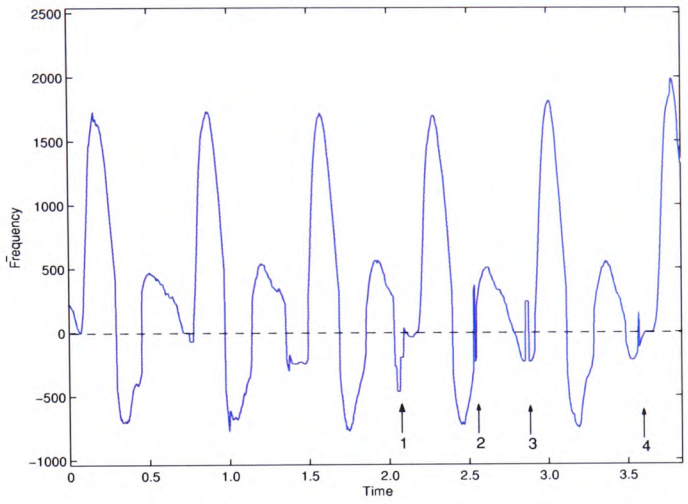

Figure 4.17: Combined MFE using the comparison method.

The points 2 and 4 in figure 4.17 showed spikes during the transition from reverse to forward flow. During these transitions the individual forward and reverse flow waveforms overlapped naturally. These spikes were caused by one signal being larger than the other for a short time, before it dropped to a lower value.

To reduce the influence of these components on the combined MFE during transitions, hysteresis was added to the comparison method. This third method is a novel way of combining the forward and reverse flow waveforms. The method did not only compare the forward and reverse flow MFEs point by point, but also looked at the previous point. In order to change the value from forward to reverse flow the reverse flow value must be larger than the forward flow value plus a small incremental value, the hysteresis parameter, and vice versa. Equations 4.12 and 4.13 describe the algorithm mathematically,

$$e[n] = \begin{cases} e_f[n] & : \ |e_r[n]| \leq (e_f[n] + \Delta_f) \text{ and } e[n-1] = e_f[n-1] \\ e_f[n] & : \ e_f[n] > (|e_r[n]| + \Delta_r) \text{ and } e[n-1] = e_r[n-1] \\ -|e_r[n]| & : \ |e_r[n]| > (e_f[n] + \Delta_f) \text{ and } e[n-1] = e_f[n-1] \\ -|e_r[n]| & : \ e_f[n] \leq (|e_r[n]| + \Delta_r) \text{ and } e[n-1] = e_r[n-1] \end{cases} \tag{4.12}$$

and

$$\Delta_f = 0.05 \cdot \max(e_f[n]), \quad \Delta_r = 0.05 \cdot \max(e_r[n]) \tag{4.13}$$

where e_f is the forward flow MFE, e_r the reverse flow MFE, e the combined flow MFE, Δ_f forward hysteresis parameter, Δ_r the reverse hysteresis parameter and n the sample index. The hysteresis parameter, Δ_f and Δ_r, were set empirically to 5% of the maximum value in the forward or reverse flow, respectively.

Figure 4.18 shows an example of the hysteresis method. The forward flow (blue), reverse flow (red) and the combined flow (black) in this figure were taken from one of the clinical signals used in this study. It can be seen that the combined and the forward flow MFE at point A had the same amplitude even though the reverse flow, point B, was larger. A change is only triggered when the absolute difference between the forward and the reverse flow MFE exceeded the forward flow hysteresis parameter Δ_f. Here, sample point D exceeded sample point C by this value and the combined flow MFE took the value of the reverse flow.

The overall result is shown in figure 4.19. Although there was still a change of direction at point 1, the other sections improved considerably. Also, the amplitude of the forward and reverse flow sections of the MFE in this method, like in the

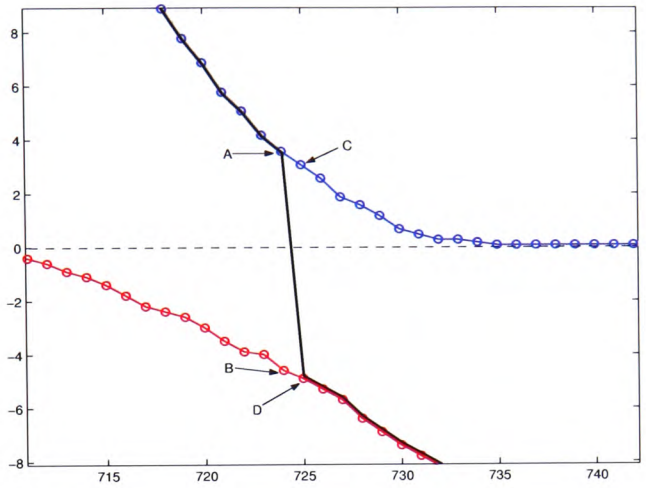

Figure 4.18: Principle of the hysteresis method. The blue curve is the forward flow MFE, the red curve is the reverse flow MFE and the black curve represents the combined flow MFE. The circles indicate the sample points.

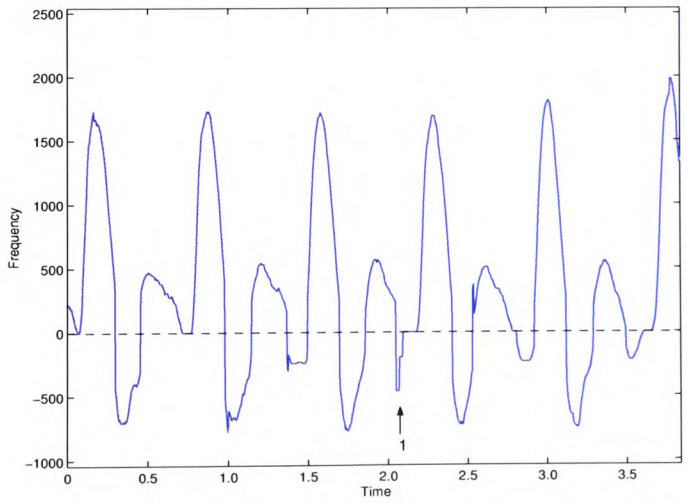

Figure 4.19: Combined MFE using the hysteresis method.

comparison method, were equal to the original respective forward and reverse flow MFEs.

4.3 Extraction of the cardiac cycle

The previous section investigated the extraction and combination of the MFE over the length of the available data record. For analysis, processing and comparison only one cardiac cycle was required to represent the signal. A number of strategies were used in the literature to define an individual cycle. These strategies ranged from using successive R-waves of the ECG signal [105] to windows around the cardiac peak [93]. A more natural dividing point for the cardiac cycle is the beginning of the systolic upstroke [106]. This point was also used for more complex analysis of the MFE [1,13,18,107]. A cardiac cycle was therefore, defined as the section between two successive starts of the systolic upstroke (figure 4.20).

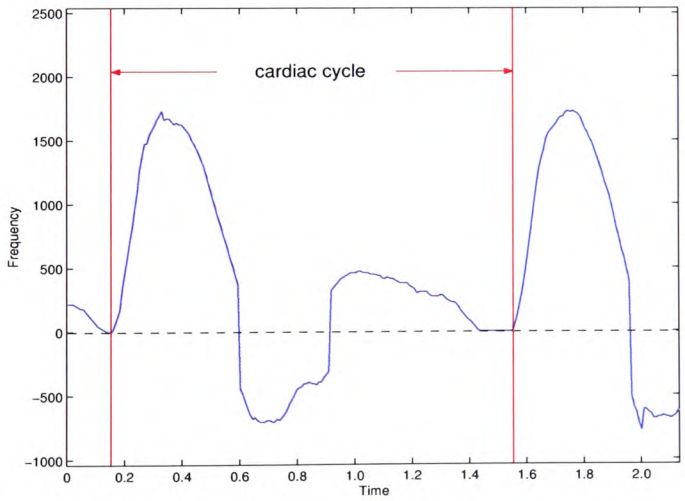

Figure 4.20: Start of cardiac cycle of a MFE extracted from a common femoral artery.

To achieve an automated extraction of the cardiac cycle, the start of the systolic upstroke needs to be found. This study investigated and compared two algorithms

for the determination of the start of the systolic upstroke and therefore, cardiac cycle. The first algorithm is the first-derivative method [18], the second is a pulse-foot-seeking algorithm based on the second derivative of the MFE, which was applied to a large number of waveforms [92]. In addition to these two algorithms, a third was proposed in this study, which was a modification of the pulse-foot-seeking algorithm to improve automated processing.

A further method for the extraction of the cardiac cycle was given by Wright [18]. This method was based on a matching filter using a portion of one cycle of the MFE. It was not taken into account because it depended on an operator selecting a portion of the envelope as the transfer function of the filter and was therefore, not suitable for automated processing.

4.3.1 Detection of the cardiac peak

The detection of the cardiac peak is a very important step in the extraction of the cardiac cycle. The cardiac peak consistently appears in almost all cardiac cycles and therefore, provides a reliable starting point. All algorithms for the extraction of the cardiac cycle investigated in this study used the cardiac peak as a starting point. Park [108] used an algorithm based on the direction of the slope and an adaptive threshold to select fundamental and harmonic peaks in music. A similar approach was made by Touch [109] to identify peaks in electrocardiogram signals using a fixed threshold. Other researchers also used the direction of the slope to detect peaks in physiological pressure signals. Two approaches were used in literature to avoid the detection of false peaks. A coarse beat detection using a low-pass filter [110] and a peak-to-peak rate estimation using the FFT of the signal [111].

The difficulties of finding the cardiac peak in a Doppler ultrasound blood flow signal is illustrated in figure 4.21. The figure shows three common femoral signals

with different properties. The frequency axes were scaled equally to highlight the differences. Figure 4.21(a) shows a common femoral MFE with significant disease. The minimum and maximum amplitudes in the signal are very close together and make it difficult to identify the peak of the systolic upstroke. Figure 4.21(b) in comparison shows a MFE with no significant disease. The signal had no offset and the peaks of the systolic upstroke are clearly identifiable. Another MFE with significant disease is shown in figure 4.21(c). Although, the minimum and maximum amplitudes are close, the peak of the systolic upstroke can be identified. One property that this signal had was its rather large offset, which was higher than the maximum amplitude of the signal in figure 4.21(a).

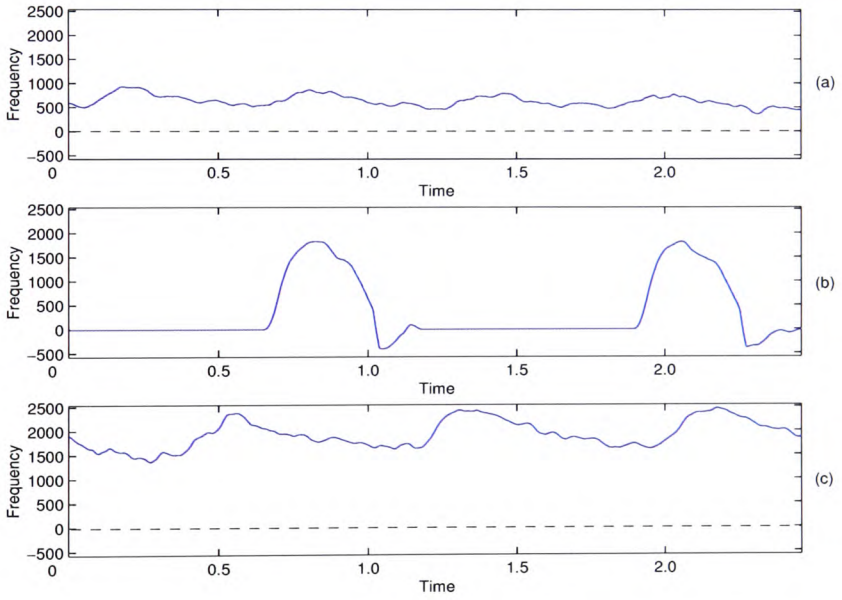

Figure 4.21: Three common femoral MFEs with different disease conditions. The MFEs in (a) and (c) are signals with significant disease, while the MFE in(b) has no significant disease.

Wright *et al* [18] presented a threshold-based approach to detect the cardiac peak when using the first-derivative method. Here the cardiac peak was found by setting a fixed threshold of 80% of the maximum value in the MFE. The method detected

the cardiac peaks correctly as long as all cardiac peaks in the MFE were larger than the threshold. Figure 4.22 shows the result of this method on two real signals used in this study. This approach worked well with the signal in figure 4.22(a), but failed with the signal in figure 4.22(b) by missing a peak.

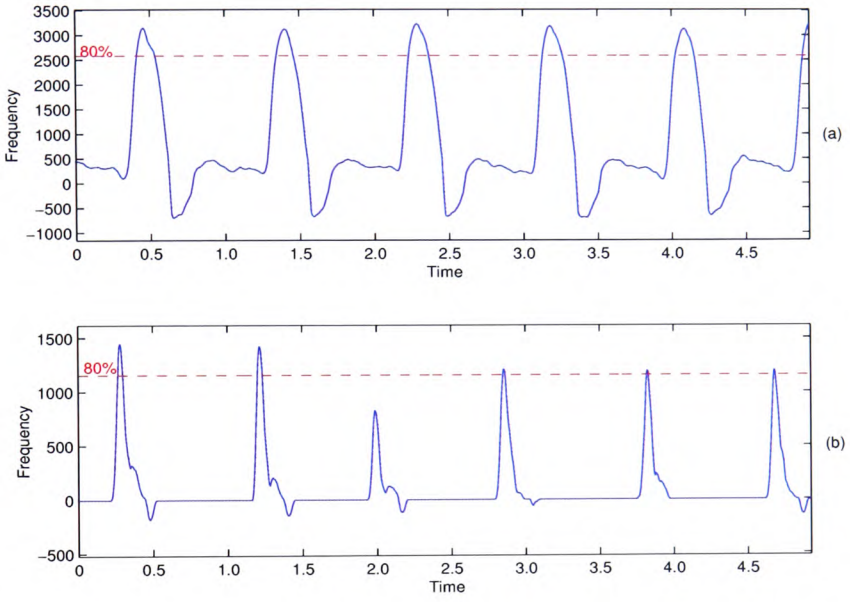

Figure 4.22: Cardiac peak detection using a fixed threshold. (a) Common femoral signal where all cardiac peaks exceed the fixed threshold. (b) Common femoral signal where not every cardiac peak exceeds the threshold.

The pulse-foot-seeking algorithm described by Evans [92] featured an automated method to detect the cardiac peaks. First the MFE was partitioned into sections of equal length. The length of each section depended on the heart rate and, for adults, was set to 375 ms for heart rates between 64 and 144 beats per minute (bpm) and 750 ms for heart rates between 32 and 72 bpm. The next step in this algorithm was the detection of the maximum in each section. Furthermore, maxima at the boundary of a section might have even greater values on the other side, or the next section, of the boundary. In this case they must be eliminated to find the true maxima. The last step was to search ± 375 ms, or ± 750 ms, from each

detected peak and to eliminate all peaks with smaller amplitudes. This method has reportedly been used successfully on a large data set [92].

Although Evans's pulse-foot-seeking algorithm was automated, it still depended on the correct setting of the current heart rate. This caused a problem as the heart rate of the signals used in this study varied between 50 and 130 bpm. In order to make the algorithm fully automated, a different cardiac peak detection algorithm was proposed in this study. The proposed algorithm could be partitioned into the following four steps,

1. Estimation of the cardiac peak-to-peak rate.
2. Rough detection of all peaks.
3. Removal of false peaks.
4. Marking of the detected peaks.

Estimation of the cardiac peak-to-peak rate

Before the cardiac peak-to-peak rate could be estimated, the MFE was filtered with a low-pass filter. This band-limited the signal and emphasised the fundamental frequency of the MFE, which was equal to the peak-to-peak frequency. The cut-off frequency of the low-pass filter was selected based on the highest possible frequency of the fundamental. The highest possible frequency for the fundamental in the MFE could be calculated from the maximum heart rate supported by the algorithm, which in this study was set to 150 bpm (2.5 beats per second). This heart rate is equivalent to 2.5 Hz for the fundamental frequency. The low-pass filter was a 4^{th} order zero phase-shift filter with Butterworth characteristic and a cut-off frequency of 2.5 Hz. The Butterworth filter characteristics was chosen for its flat frequency response in

the pass-band compared to other filter types. The filter order was selected to offer a good compromise between a good attenuation and the settling-time of the filter. A higher order filter would have provided more attenuation of the frequencies above the cut-off frequencies, but would have also increases the settling-time of the filter. This could lead to distortions at the beginning and the end of the signal waveform.

The estimation of the cardiac peak-to-peak rate was performed using the FFT. The fundamental frequency of the MFE was given by the position of the first peak in the FFT spectrum. The calculation was performed over the entire MFE, which consisted of a number of cardiac cycles. To simplify the FFT calculation it was assumed that the MFE had a length of one second. The resulting fundamental frequency of the MFE was therefore, equal to the number of expected peaks within the MFE. Figure 4.23 shows an example of the FFT of a common femoral MFE. The number of cardiac peaks is identical to the estimated frequency.

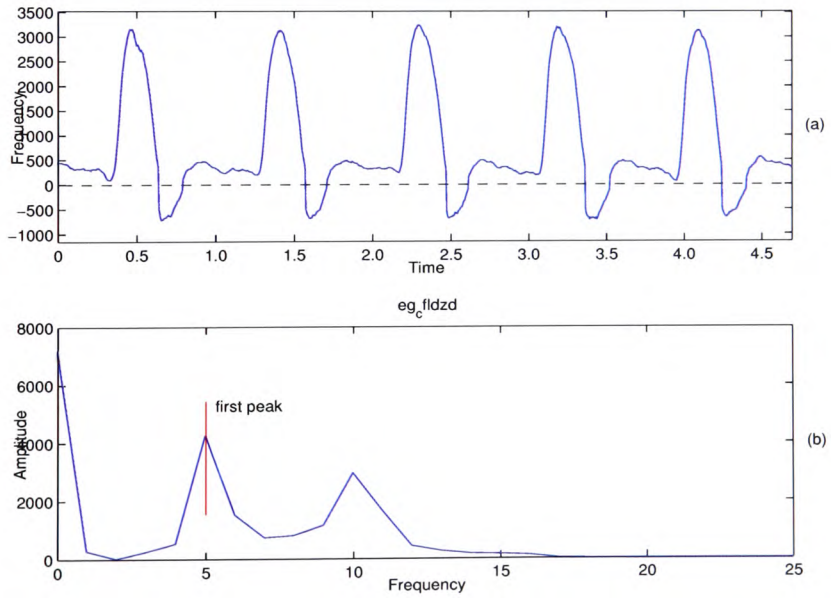

Figure 4.23: Cardiac peak-to-peak distance estimation using the FFT. (a) Common femoral MFE with 5 cardiac peaks. (b) FFT of a common femoral signal.

Rough detection of peaks

Once the fundamental frequency of the MFE, f_{MFE}, was found, the second stage of the algorithm was entered. The rough peak detection stage of the cardiac peak detection algorithm used the slope of the MFE to determine if a peak was present. The algorithm marked all points of the MFE where the slope turned from positive to negative. To avoid detecting every small peak, the original MFE was first filtered with a low-pass filter to smooth it. The cut-off frequency of the zero phase-shift low-pass filter was chosen to be 10 Hz, which is 4 times higher than the highest supported fundamental frequency. This smoothed the MFE without attenuating the signal. A 4^{th} order filter was chosen as it provided a good compromise between attenuation and settling-time.

To further reduce the number of false peaks, the DC offset of the MFE was filtered out with a high-pass filter. Removing the DC offset shifted the MFE around the zero-line and therefore, changed the amplitudes of some smaller peaks from positive to negative (figure 4.24 (a)). The cut-off frequency of the high-pass filter should be smaller than the lowest anticipated fundamental frequency. The algorithm covered a heart rate range between 50 and 150 bpm. The lowest fundamental frequency was therefore, 0.83 Hz. The filter was implemented as a zero phase-shift high-pass filter with a cut-off frequency 0.2 Hz, which was 4 times smaller than the lowest anticipated fundamental frequency. The filter order was set to two, because of the lower settling-time of the filter.

Removal of false peaks

The next stage of the cardiac peak detection was the removal of all false peaks. First, the markers for all detected peaks with negative amplitude were set to zero amplitude (figure 4.24 (b)). Second, the region of $\pm$N sample points around each

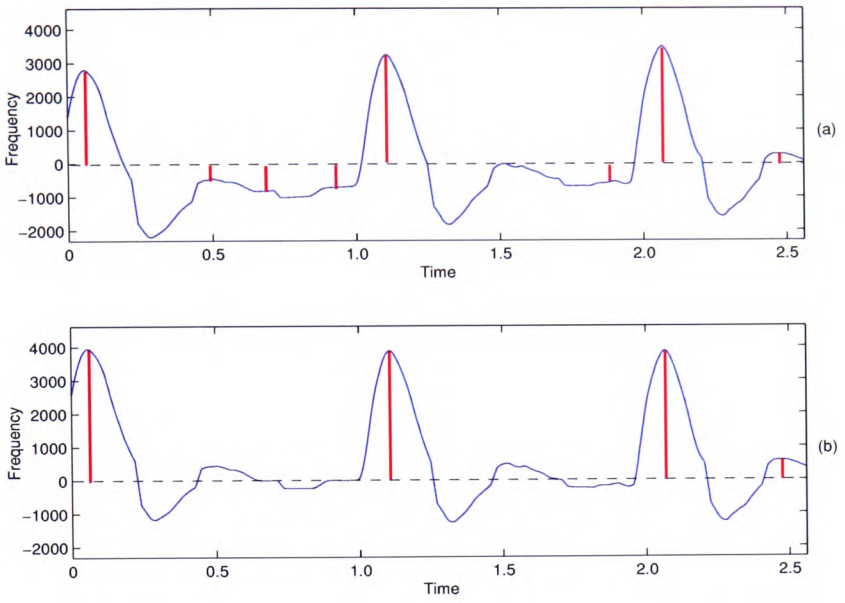

Figure 4.24: Common femoral MFE with detected peaks. (a) High-pass filtered MFE before removing non-positive peaks. (b) After removal of false peaks.

peak was searched for other peaks with a larger amplitude. If a larger peak was found in this region the marker for the current peak was set to zero. The length of the search window was based on the estimated cardiac peak-to-peak distance, D_{est}, which is given in samples by equation 4.14,

$$D_{est} = \frac{d}{f_{MFE}} \tag{4.14}$$

where d is the length of the MFE in samples and f_{MFE} its fundamental frequency. The length of the search window was set to a percentage of the estimated cardiac peak-to-peak distance. This was to allow for estimation errors and any variation in the heart rate. The minimum length of the search window should be 50% of the estimated cardiac peak-to-peak distance in order to cover the whole MFE. It was found that a length of 60% of the cardiac peak-to-peak distance worked well as a search window. Figure 4.25 shows an example of this process.

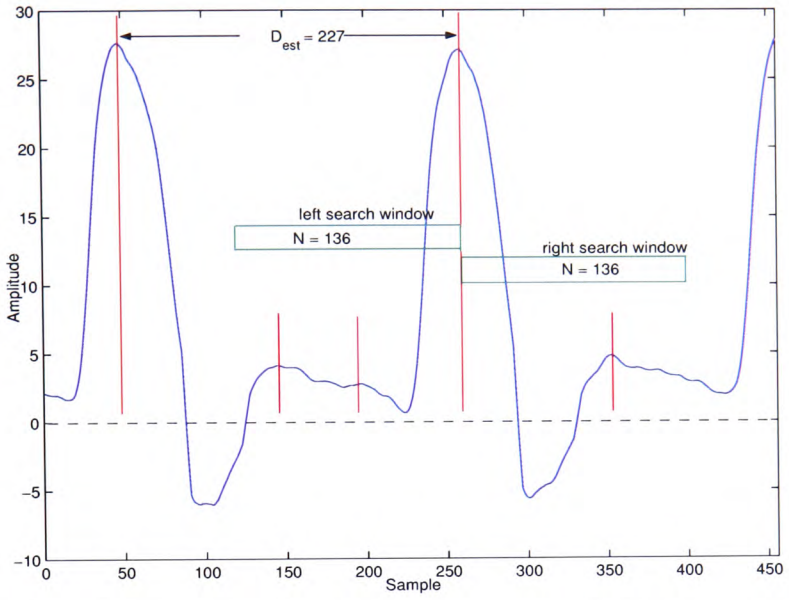

Figure 4.25: False cardiac peak elimination using a N-point long search window.

A different problem were peaks detected at the beginning and end of the MFE. These detected peaks might not be true peaks but local to the MFE if it was extended beyond the boundaries. One way of dealing with these peaks was to discard them completely if they fell within the search window at the beginning or the end of the MFE. Another approach was to discard only low amplitude peaks within these areas. This approach is illustrated in figure 4.26. The peak detection algorithm detected three peaks in this envelope. The first peak is a local peak and should not be included, otherwise the algorithm for detecting the start of a cardiac cycle would assume the start at this point, which is clearly wrong. The other two detected peaks were true cardiac peaks and should included. The search window introduced earlier eliminated all smaller peaks around the cardiac peaks (figure 4.25). Unfortunately, the falsely detected peak at the beginning of the MFE was outside this search window. In order to eliminate this local peak, the algorithm assumed a virtual peak at the beginning of the MFE. The amplitude of this virtual peak was set to 50% of

the mean amplitude of all detected cardiac peaks in the signal. A search window was placed on this virtual peak and all smaller peaks within this search window were removed. Larger peaks were retained and made true peaks. The 50% amplitude for the virtual peak was found empirically and worked well on all signals.

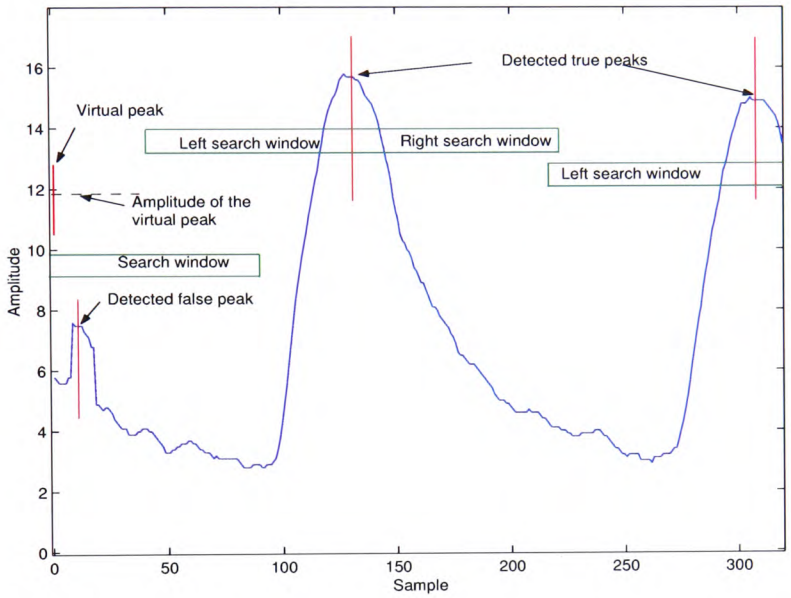

Figure 4.26: Boundary cardiac peak elimination using the search window.

Marking of the detected peaks

The final step of the algorithm was to mark the detected peak on the original MFE. Within the peak detection algorithm the MFE was filtered. Although a zero phase-shift filter was used a small deviation between the detected peak position and the actual peak position was found (figure 4.27). To adjust the position of the cardiac peak, the MFE sample points in a region around the detected cardiac peak position were compared with the value of the detected cardiac peak. The final detected peak marker was set to the largest value within this region. It was found that a region of ± 10 sample points around the detected peak was sufficient to adjust the final peak position.

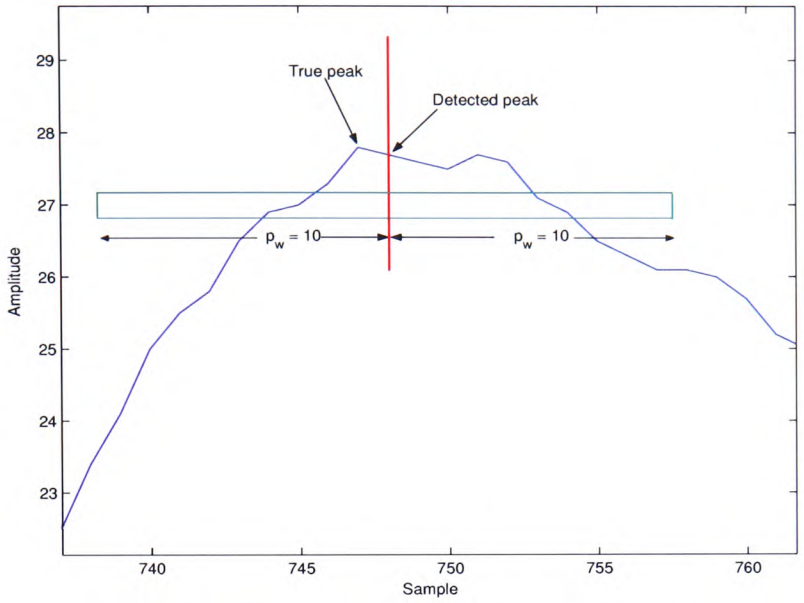

Figure 4.27: Adjustment of the detected cardiac peak using a ±10-point window, p_w.

4.3.2 The first-derivative method

The first-derivative method determined the beginning of the cardiac cycle as the steepest point on the MFE during the systolic upstroke. Wright *et al* [18] described the process as follows:

1. The cardiac cycle peaks were identified as the sections of the MFE with amplitudes above 80% of the maximum value present in the MFE.

2. The first derivative of the MFE was computed.

3. The maxima of the first derivative were located. Only the maxima that exceeded a threshold of 40% of the maximum value in the first derivative were included.

4. The start of the cardiac cycle was selected to be the point of the largest maxima of the first derivative in the rising portion of a cardiac cycle peak

(systolic upstroke).

Figure 4.28 shows the relationship between the MFE, first derivative of the MFE, the 80% and the 40% thresholds. Both thresholds identified the peaks of the respective waveforms. The 80% threshold was applied to the MFE and identified the cardiac peak. The 40% threshold identified the steepest part of the MFE when applied to the first derivative. The 40% threshold in figure 4.28 appears very high in relation to the first derivative waveform because it is 40% of the maximum value within the entire waveform. Figure 4.28 only shows a section of the waveform. The first derivative algorithm determined the start of a cardiac cycle by setting it to the maximum within the previously identified first derivative peak. This should be in front of the detected cardiac peak and is marked in figure 4.28 by the red line.

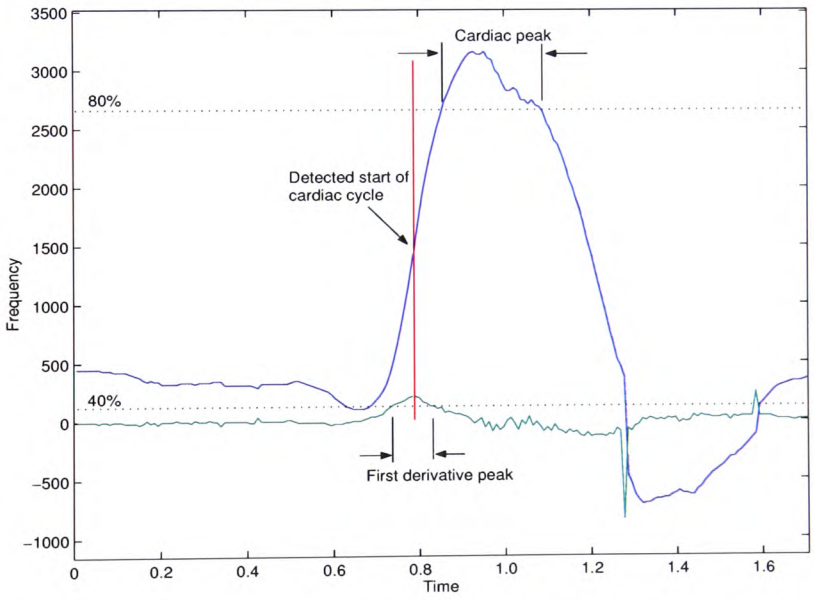

Figure 4.28: Calculation of the start of the cardiac cycle using the First-derivative method. MFE with 80% threshold, first derivative with 40% threshold and start of cardiac cycle marker (red).

The implementation of this algorithm in this study used a 64 ms window to define the maximum distance between the first derivative and the cardiac cycle

peak. Although Wright *et al* [19] did not mention the use of a window in their implementation, it was needed to ensure that the start of cardiac cycle marker was set within the systolic upstroke. If no window was used, the algorithm could find a large peak of the first derivative that occured before the systolic upstroke of the cardiac cycle. The window size was found empirically, but based on 10% of an average heart beat of 70 bpm (857 *ms* per cardiac cycle).

4.3.3 The pulse-foot-seeking algorithm

The pulse-foot-seeking algorithm described by Evans [92] used the first and second derivative of the MFE to determine the point where the change of steepness of the MFE was greatest. This point was termed as the pulse-foot of the MFE's cardiac cycle. The algorithm could be partitioned into the following stages:

1. Detection of the cardiac cycle peaks.
2. Calculation of the first derivative of the MFE.
3. Marking of the maximum values of the first derivative occurring within the first window prior to the cardiac cycle peaks.
4. Calculation of the second derivative.
5. Marking of the maximum values of the second derivative occurring within the second window prior to the first derivative markers. This marks the pulse-foot.

Figure 4.29 shows the steps of the pulse-foot-seeking algorithm. Part (a) shows the MFE with markers at the positions of the cardiac peaks (step 1). The results of step 3 are shown in part (b) of the figure. The red marker identifies the maxima of the first derivative within the systolic upstroke. The markers in part (c) identify the maxima of the second derivative of the MFE and therefore the pulse-foot.

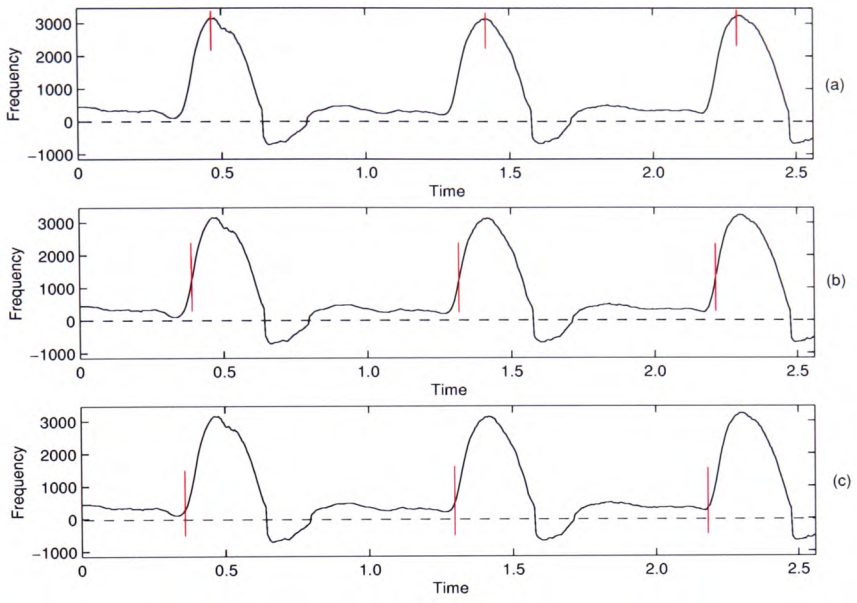

Figure 4.29: Operation of the pulse-foot-seeking algorithm using a MFE from a common femoral artery. The MFE and its cardiac cycle peak marker (a), the MFE and the first derivative peak marker (b), and the MFE with the second derivative peak marker (pulse-foot)(c).

To calculate the pulse-foot correctly the algorithm assumed that the cardiac cycle peak of the MFE and the first and second derivative peaks lied within a certain distance from each other. The algorithm therefore, defined two windows. The first window was used for the distance within which the peak of the first derivative should lie in relation to the cardiac peak of the MFE. The second window limited the maximum distance between the peaks of the first and second derivatives. In his study, Evans described these windows as being constant over a wide range of heart rates (32 - 144 bpm) for an adult. He gave these empirically determined windows as 187.5 ms and 100 ms, respectively. Figure 4.30 shows the relationship of the windows to the peaks.

The cardiac peak detection algorithm used in Evans's original pulse-foot seeking method and described in section 4.3.1, was not used here because it depended on

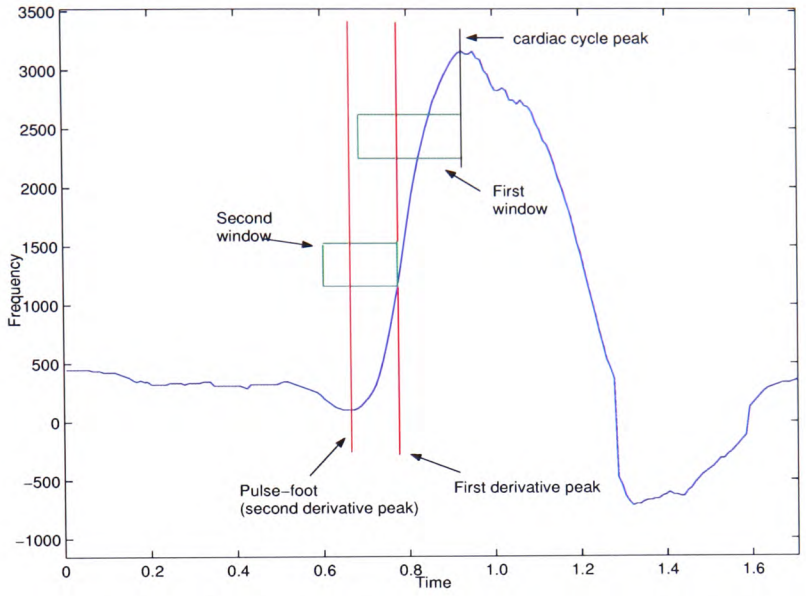

Figure 4.30: Calculation of the start of the cardiac cycle using the pulse-foot-seeking method.

the selection of a specific range of heart rates. Instead the fully automated method proposed in section 4.3.1 was used.

4.3.4 The modified pulse-foot-seeking algorithm

The pulse-foot-seeking algorithm worked with most signals and delivers better results than the first derivative method (section 4.3.2). Although the general performance was good, the two algorithms failed with some signals. A modified pulse-foot-seeking algorithm was therefore proposed in this study.

This modification to Evans's pulse-foot-seeking algorithm was related to the use of the second derivative. The modified pulse-foot-seeking algorithm is described below,

1. Detection of the cardiac cycle peaks.

2. Calculation of the first derivative of the MFE.

3. Marking of the maximum value of the first derivative occurring within the first window prior to the cardiac cycle peaks.

4. Starting from the first derivative marker to the left, search for the first non-positive first-derivative value prior to the first-derivative marker. The next sample is the pulse-foot.

The first three steps of the modified algorithm are identical to Evans's pulse-foot-seeking algorithm (section 4.3.3) and only step 4 was changed so as to provide an improved detection of the change of direction of the MFE and therefore, the pulse-foot. Similar to Evans's algorithm, the modified algorithm used a second window to select a region prior to the first-derivative marker. Within this region the modified algorithm searched, starting from the first derivative peak, to the left for the first non-positive value of the first derivative vector. The point to the right of it, which was a positive sample, represented the start of the cardiac cycle. This was the point where the MFE turned from falling or no change into the rising section, or the systolic upstroke. Figure 4.31 shows the algorithm with an example on a real common femoral MFE. The first window (blue) was set to the left of the cardiac peak and was used to find the first derivative peak, which is marked with a blue vertical line in the figure. The second window (green) defined a region to the left of the newly found first derivative peak and the algorithm searched for the first non-positive value of the first derivative within this window. The sample point after this was the pulse-foot, which was marked with a green vertical line. The length of the windows were found empirically. The first window had a length of 187.73 ms, which was equivalent to 44 samples of the MFE and equal to length of Evans's first window. The second window had a length of 426.67 ms, equivalent to 100 samples of the MFE.

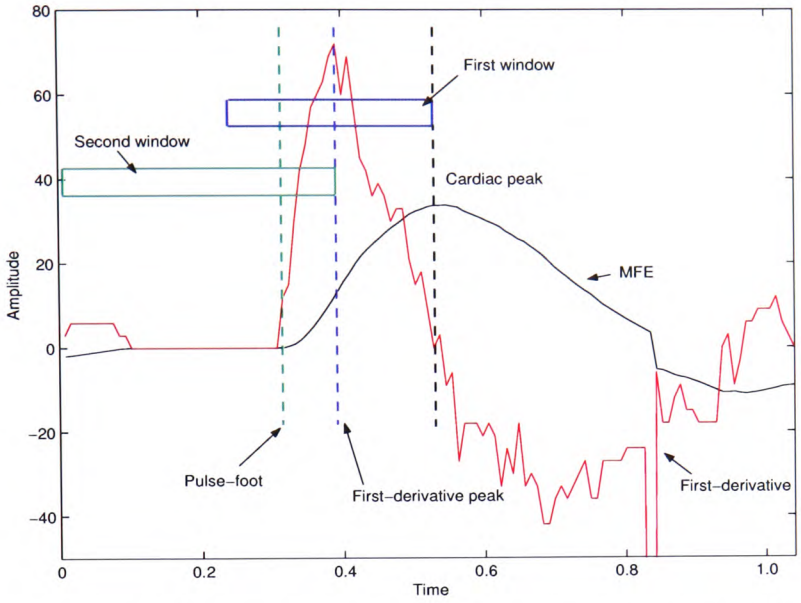

Figure 4.31: Calculation of the start of the cardiac cycle using the modified pulse-foot-seeking method.

The advantage of the proposed algorithm was that, whilst the second window was important, its maximum length was not critical. It could in fact extend to the beginning of the MFE. The minimum length of the second window, on the other hand, should cover at least the systolic upstroke.

4.3.5 Comparison of the cardiac cycle extraction algorithms

This section presents the results of comparing the performances of the first derivative, pulse-foot-seeking and modified pulse-foot-seeking algorithms. Three real common femoral MFEs were used to demonstrate the differences between the algorithms. Figures 4.32 to 4.34 show MFEs from healthy and diseased CFAs. The vertical markers in these figures identify the start of the cardiac cycle found by the modified pulse-foot-seeking (a), the Evans's pulse-foot-seeking (b) and the first derivative (c) algorithms. In all three figures it can be seen that the modified pulse-foot-seeking algorithm identified the start of the cardiac cycle correctly at

the beginning of the systolic upstroke. The start of the cardiac cycle found by the pulse-foot-seeking algorithm on the other hand varied between the pulse-foot and the rising section of the MFE. The first derivative algorithm worked correctly and located the start of the cardiac cycle in the rising section of the MFE. The algorithm was included for comparison.

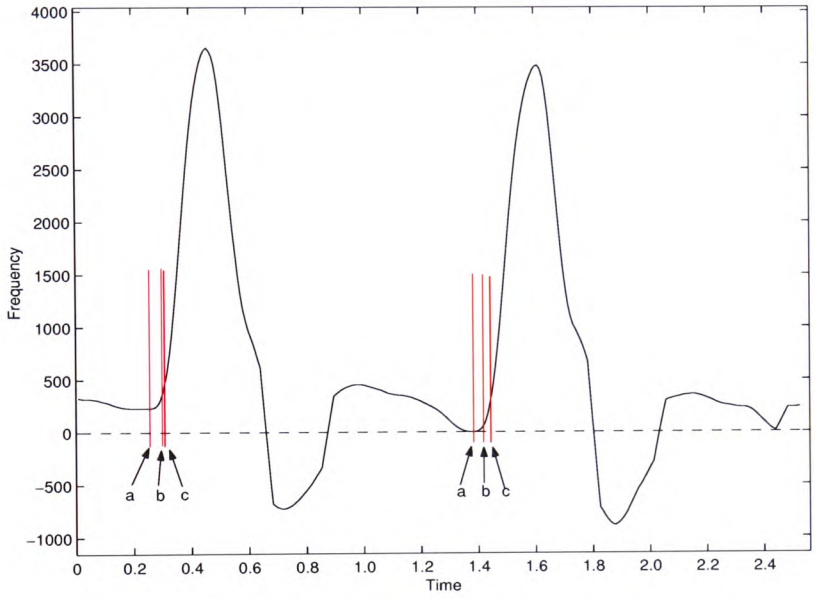

Figure 4.32: Comparison between the three cardiac cycle extraction algorithms. Modified pulse-foot-seeking algorithm (a), Evans's pulse-foot-seeking algorithm (b) and first-derivative algorithm (c).

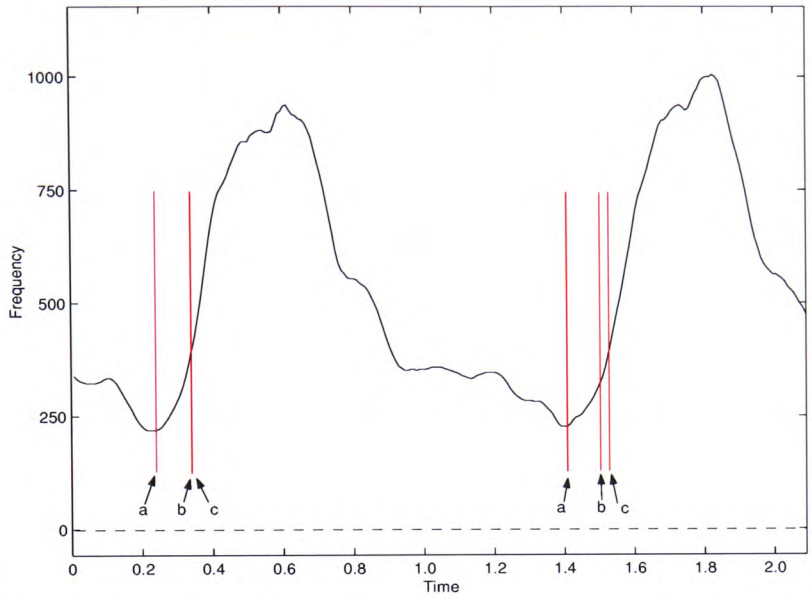

Figure 4.33: Comparison between the three cardiac cycle extraction algorithms. Modified pulse-foot-seeking algorithm (a), Evans's pulse-foot-seeking algorithm (b), first-derivative algorithm (c).

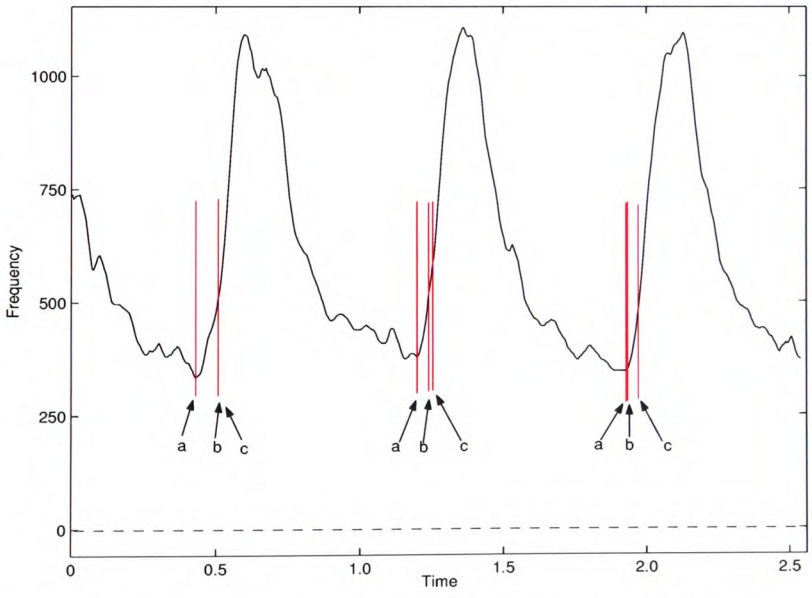

Figure 4.34: Comparison between the three cardiac cycle extraction algorithms. Modified pulse-foot-seeking algorithm (a), Evans's pulse-foot-seeking algorithm (b), first-derivative algorithm (c).

4.4 The Spectral Broadening Index

A number of indices were defined to aid the classification and diagnosis of arterial disease (section 2.4). Most of these indices can be calculated from the MFE and do not offer much more information than the MFE itself. To obtain more information about the signal without significantly increasing the size of the feature vector, the MFE together with other indices were considered.

A suitable index that provided additional information is the Spectral Broadening Index (SBI). A number of definitions for the SBI were found in literature. Johnston *et al* [71] defined the SBI as,

$$SBI = \frac{f_{max} - f_{mean}}{f_{max}} \cdot 100 \tag{4.15}$$

where f_{max} is the maximum frequency and f_{mean} the mean frequency at the systolic peak. The mean frequency was calculated using equation 4.16.

$$f_{mean} = \frac{\sum_{k=1}^{M} f_k \cdot A_k^2}{\sum_{k=1}^{M} A_k^2} \tag{4.16}$$

where f_k indicates an individual frequency bin in the spectrogram, M the maximum frequency index in the spectrogram and A_k the amplitude of an individual frequency bin [71].

The SBI gives a measure of the width of the window below the systolic peak, which is believed to be related to the severity of the disease [17]. Figure 4.35 shows the principle of the SBI calculation. The frequencies f_{max} and f_{mean} identify the maximum and the mean frequency at the cardiac peak, respectively.

Johnston's [71] approach was followed in this study and five samples at the systolic peak were used to calculate the SBI. These five samples of the maximum

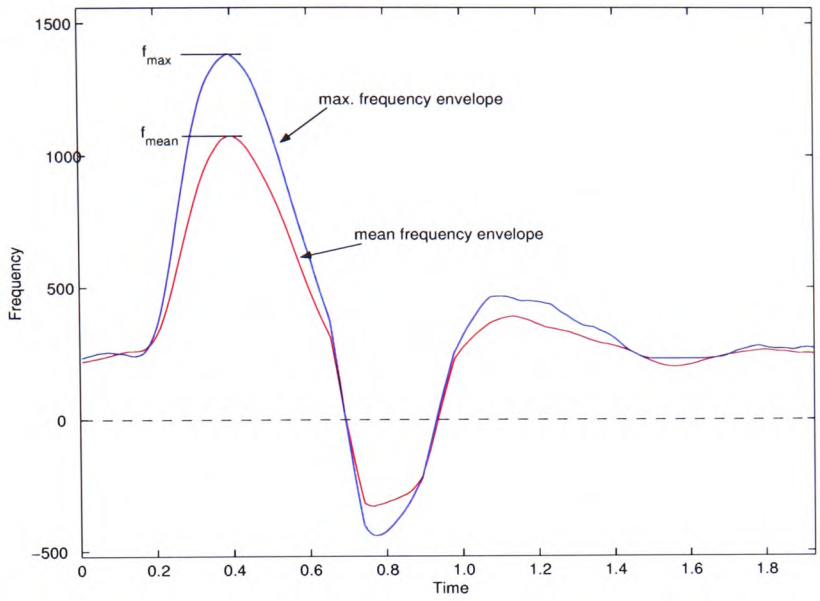

Figure 4.35: Calculation of the Spectral Broadening Index. f_{max} and f_{mean} identify the maximum and the mean frequency at the cardiac peak.

and mean frequency were added before they were used in equation 4.15. Equation 4.17 summarised this operation for the calculation of the SBI.

$$SBI = 100 - \frac{\sum_{N=1}^{5} f_{mean_N}}{\sum_{N=1}^{5} f_{max_N}} \cdot 100 \tag{4.17}$$

Figure 4.36 shows the distribution of the SBI over the signals used in this study. It shows a considerable overlap of the SBI value over the three diagnostic classes making it difficult to use the SBI on its own as an indicator for the presence of disease and its severity. However, the SBI might have some diagnostic value when used together with the MFE.

It can also be seen in figure 4.36 that some SBI values were negative. A negative value for the SBI is not possible as the mean frequency is normally lower than the maximum frequency. However, both noise reduction methods, threshold-

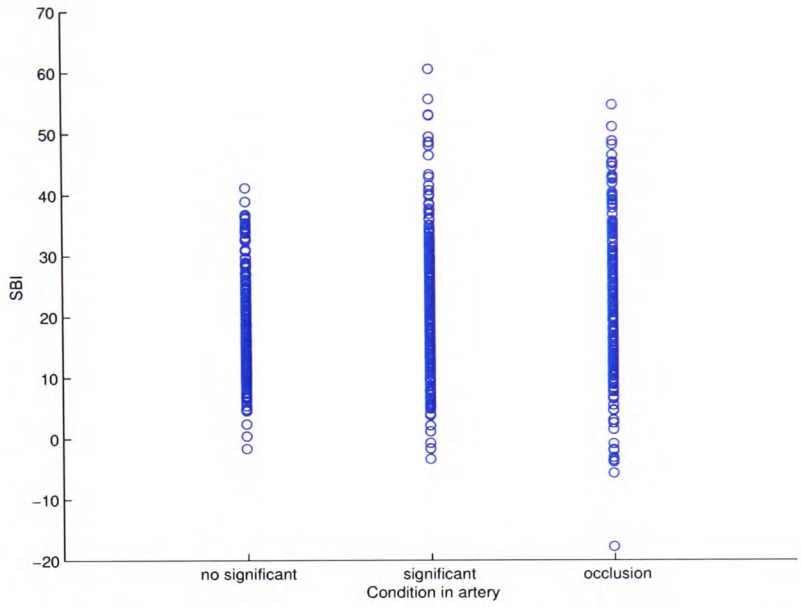

Figure 4.36: Distribution of the Spectral Broadening Index over the three diagnostic classes used in this study.

ing and wavelet denoising, used in this study reduce the bandwidth significantly in some signals. These signals had high noise contents, leading to a high threshold or strong wavelet denoising. Because of this narrow bandwidth the result of the mean frequency calculation was higher than the result of the 95% percentile algorithm, resulting in a negative SBI.

Figure 4.37(a) shows the original spectrogram of a signal. It can be seen that it has a very high noise floor, which is in some parts as high as the signal. The threshold to remove the noise floor must therefore be quite high, resulting in the thresholded spectrogram shown in figure 4.37(b). The remaining signal has a very narrow bandwidth, in fact the signal is only one or two frequency bins wide. Due to the fact that the maximum frequency was calculated as the frequency enclosing 95% of the power, it yields a lower frequency than the mean frequency algorithm. This fact is shown in figure 4.37(c), which shows the MFE and the mean frequency envelope for the forward blood flow only. During the cardiac peak the mean frequency

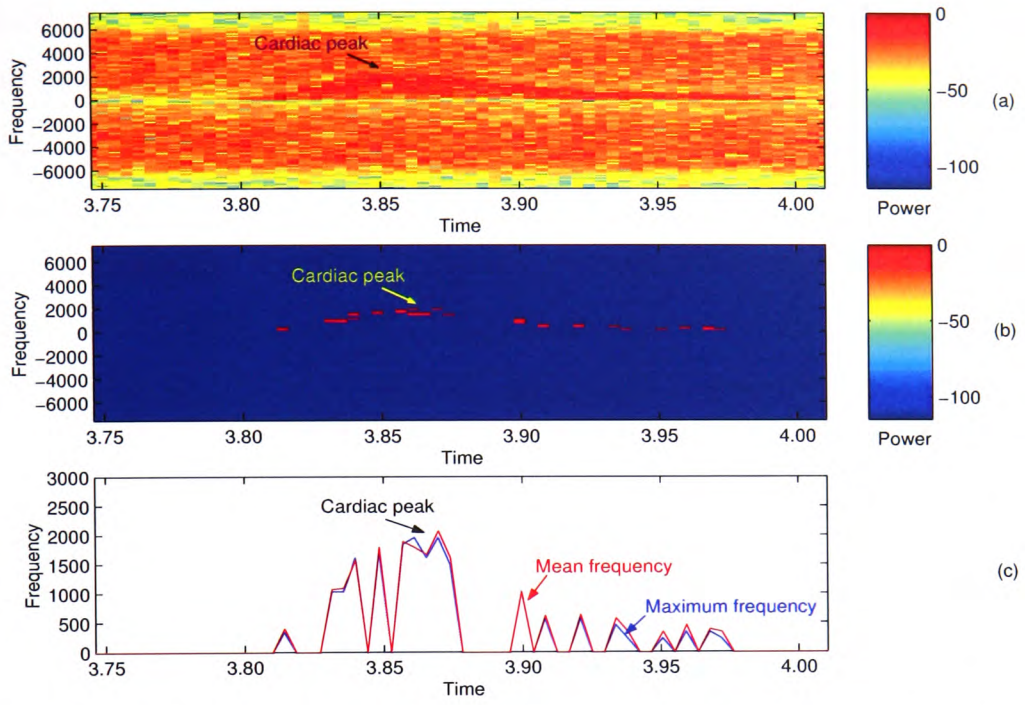

Figure 4.37: Original spectrogram (a), thresholded spectrogram (b) and MFE and mean frequency envelope (c).

exceeds the maximum frequency, giving a negative SBI value. Only 16 cardiac cycles out of approximately 1500 cardiac cycles used here gave a negative SBI value. All of these cardiac cycles came from signals that had a high noise floor.

It was reported in the literature that although there is a link between the SBI and the severity of the disease, the SBI is influenced by a number of other factors [69–71]. Chapter 5 evaluates the success rate of the classification and diagnosis stage with and without the SBI as a feature.

4.5 MFE Wavelet coefficients

In automated diagnosis approaches investigated in this study, the MFE was utilised as the feature vector, representing the profile of the velocity waveform over time.

Unfortunately, the required length of the MFE feature vector was rather long if it was to represent the velocity profile accurately. As an example, for a heart rate of 75 bpm, the cardiac cycle length was 0.8 s. Using a 15 kHz sampling frequency and an 128-point STFT with 50% overlap required a MFE with 187 points to cover the whole cardiac cycle.

Generally, it is advantageous to reduce the size of a feature vector to the fewest number of points. This reduces the computation complexity and increases the processing speed of the classification stage. It may even improve the performance. However, reducing the number of points of the MFE feature vector may reduce its information contents and compromise the performance of the diagnosis process.

Another issue of significant importance was the variability of the heart rates between different patients. This resulted in the need to use MFE vectors of different lengths to represent complete cardiac cycles for different heart rates. However, this was not a feasible option in automated classification as the length of the feature vectors have to be maintained at the same value for consistency.

Other researchers [18] who utilised ANNs in the classification of Doppler ultrasound blood flow signals, only used the first 100 points of the cardiac cycle. They argued that the area of interest within the cardiac cycle lied at the beginning of the cycle. This was further reduced to 50 points by simply removing every second sample.

This study investigated a different approach by keeping the entire cardiac cycle and maintaining a constant vector length. This was achieved by re-sampling the vector to a fixed length. The algorithm utilised here assumed that the length of the original cardiac cycle spanned one time unit. Based on this time unit the re-sampling algorithm changed the number of points in the vector to a constant number (Figure 4.38). The required filtering was implemented using zero-phase-shift FIR filters.

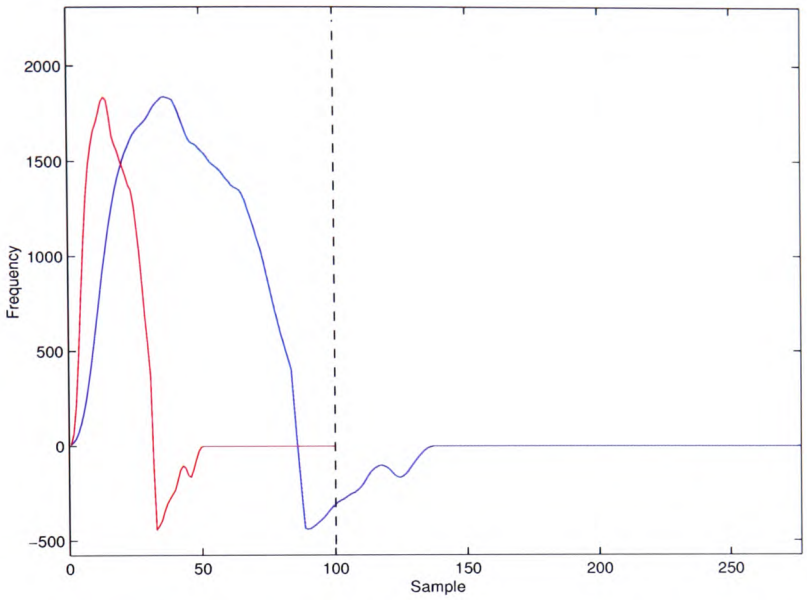

Figure 4.38: Original (blue) and re-sampled (red) MFE of a cardiac cycle from a healthy common femoral artery.

After the length of the feature vector was fixed to a constant length, this part of the study investigated an alternative approach to reduce the length of the feature vector whilst covering the entire cardiac cycle. Chapter 5 gives full details about all used feature vector length reduction methods.

One of the three main applications of the Wavelet Transform (WT) is compression (section 2.3). Although this is a lossy compression, the reconstructed signal matches the original signal quite closely even when only few coefficients were retained. The principle of WT based compression is the decomposition of the original signal into approximation and detail coefficients. Only the approximation wavelet coefficients and the most dominant detail coefficients are kept. The number of detail coefficients needed to achieve an acceptable reproduction of the original signal depends on the signal, the level of decomposition and the chosen wavelet base. The minimum number of coefficients is equal to the length of the approximation coefficients, which is a function of the chosen wavelet base, the level of decomposition

and the length of the input signal. Figure 4.39 shows the MFE of a cardiac cycle of a healthy CFA. The decomposition of the cardiac cycle is shown in figures 4.40 and 4.41, where two different wavelet bases were used.

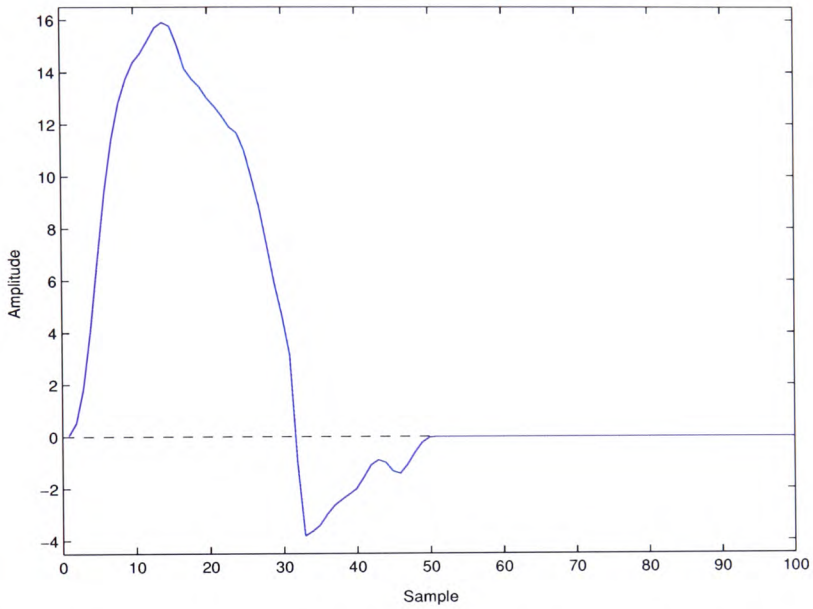

Figure 4.39: MFE of a cardiac cycle from a healthy common femoral artery.

Both figures highlight the fact that the choice of the wavelet base is very important for the efficiency of the wavelet compression. Although the approximation coefficients in figure 4.41(a) show a closer resemblance to the original vector than the one in figure 4.40(a), the reconstruction of the original vector is the same. The main difference in these two decompositions becomes clear when the length of the approximation coefficient vector is considered. The biorthogonal 3.1 wavelet has a much shorter vector and therefore, greater efficiency.

In addition to the decision on the optimum wavelet base, it is necessary to decide how many detail coefficients need to be retained and the depth of the decomposition. The selection of these parameters was made by calculating the root-mean-square error (RMSE) between the original and the reconstructed vectors. The following

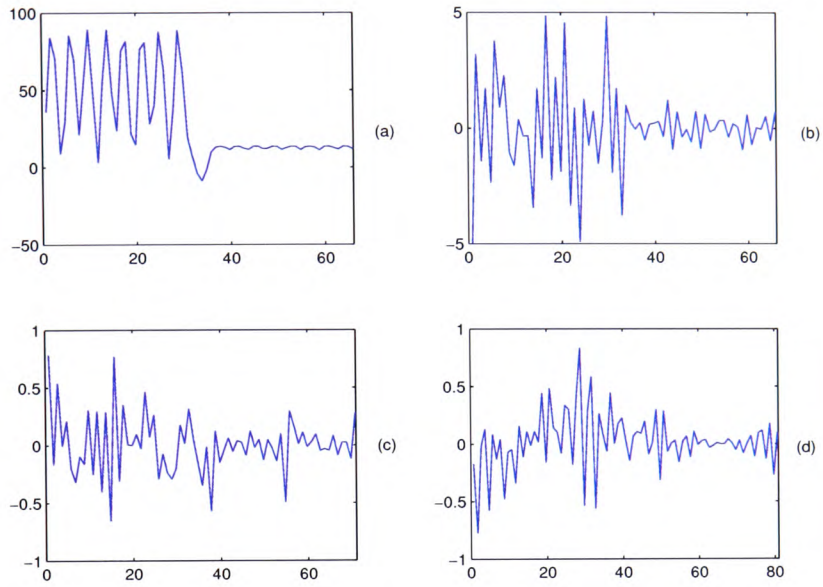

Figure 4.40: Wavelet Transform decomposition at level 3 of the MFE using the discrete Meyer wavelet. (a) Approximation, (b) detail level 3, (c) detail level 2, (d) detail level 1.

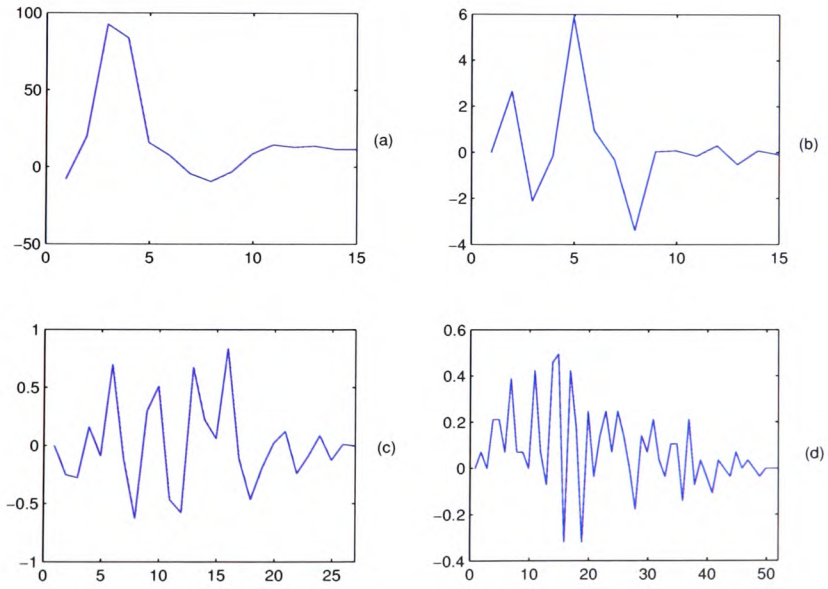

Figure 4.41: Wavelet Transform decomposition at level 3 of the MFE using the biorthogonal 3.1 wavelet. (a) Approximation, (b) detail level 3, (c) detail level 2, (d) detail level 1.

wavelet bases, which are widely used for signal processing applications, were used in this part of the study:

- Haar
- Daubechies 1 - 10
- Symlets 2 - 8
- Coiflets 1 - 5
- Biorthogonal
- Reverse Biorthogonal
- Discrete Meyer

Using a decomposition level of 1 will result in many approximation coefficients, reducing the efficiency of the compression. Although resulting in less approximation coefficients, higher decomposition levels need more detail coefficients to represent the signal. Decomposition levels 2 and 3 gave a good range of length of approximation coefficients. The number of retained detail coefficients was set to 0, 5, 10 and 15. Retaining too many detail coefficients again reduces the efficiency of the compression. Because each detail coefficient needed to be associated with a position, the efficiency is quickly reduced when including too many detail coefficients. An adaptive algorithm was developed in this study to select the threshold at which to remove the detail coefficients. The threshold was varied until only the required number of detail coefficients were left.

The wavelet compression was applied to all cardiac cycles and the mean and the standard deviation of the RMSE for all cardiac cycles of each wavelet base was calculated. Tables 4.1 and 4.2 show an extract of the error analysis results. The full results for the decomposition at levels 2 and 3 are shown in appendix A. The first column indicates the wavelet base and the length of the approximation coefficients in brackets.

From these results it can be seen that the biorthogonal wavelets, although they were not necessarily the best in terms of the RMSE, performed well. The biorthogonal 3.1 wavelet base, for example, yielded the best compression rate against

RMSE. The minimum length of the compressed vector was only 15 points for decomposition level 3.

Wavelet (length of a2)	Number of retained detail coefficients			
	0	5	10	15
db9 (37)	0.153 (0.144)	0.095 (0.062)	0.064 (0.041)	0.045 (0.028)
dmey (70)	0.156 (0.149)	0.104 (0.076)	0.084 (0.063)	0.071 (0.053)
bior3.1 (27)	0.165 (0.123)	0.08 (0.05)	0.048 (0.029)	0.031 (0.019)
bior3.5 (33)	0.153 (0.103)	0.085 (0.052)	0.055 (0.033)	0.039 (0.024)
rbio3.1 (27)	3.912 (2.334)	1.844 (1.095)	1.164 (0.682)	0.804 (0.469)

Table 4.1: Mean of the Root Mean Square Error (RMSE) for wavelet decomposition at level 2 over all Doppler signals with standard deviation given in brackets. All numbers are rounded to three digits after the decimal point. The length of the approximation coefficient vector a2 is given in brackets in the first column.

Wavelet (length of a3)	Number of retained detail coefficients			
	0	5	10	15
db9 (27)	0.541 (0.432)	0.349 (0.266)	0.215 (0.142)	0.142 (0.085)
dmey (65)	0.492 (0.364)	0.42 (0.329)	0.362 (0.271)	0.292 (0.22)
bior3.1 (15)	0.661 (0.513)	0.207 (0.126)	0.112 (0.068)	0.071 (0.045)
bior3.5 (22)	0.528 (0.394)	0.263 (0.161)	0.151 (0.089)	0.1 (0.063)
rbio3.1 (15)	9.98 (5.84)	3.876 (2.296)	2.318 (1.354)	1.552 (0.926)

Table 4.2: Mean of the Root Mean Square Error (RMSE) for wavelet decomposition at level 3 over all Doppler signals with standard deviation given in brackets. All numbers are rounded to three digits after the decimal point. The length of the approximation coefficient vector a3 is given in brackets in the first column.

Tables 4.1 and 4.2 also show the difference between compressions using a two and a three level decomposition. Decomposing the MFE to only two levels gave a much better reconstruction of the original MFE from the compressed MFE. This came with the cost of having a longer approximation coefficients vector. In the case of the biorthogonal 3.1 wavelet base, the approximation coefficients vector was almost twice as long using a level two rather than a level three decomposition.

Figure 4.42 shows the approximation and detail coefficients of a CFA decomposed with a discrete Meyer at level 3. The detail coefficients were thresholded and the number of retained detail coefficients was set to 5. The total number of coefficients was therefore 70, 65 for the approximation plus 5 for the detail coefficients. The original and the reconstructed MFE are shown in figure 4.43. Although the compressed signal contains 70 coefficients, the reconstructed MFE did not match the original MFE very well.

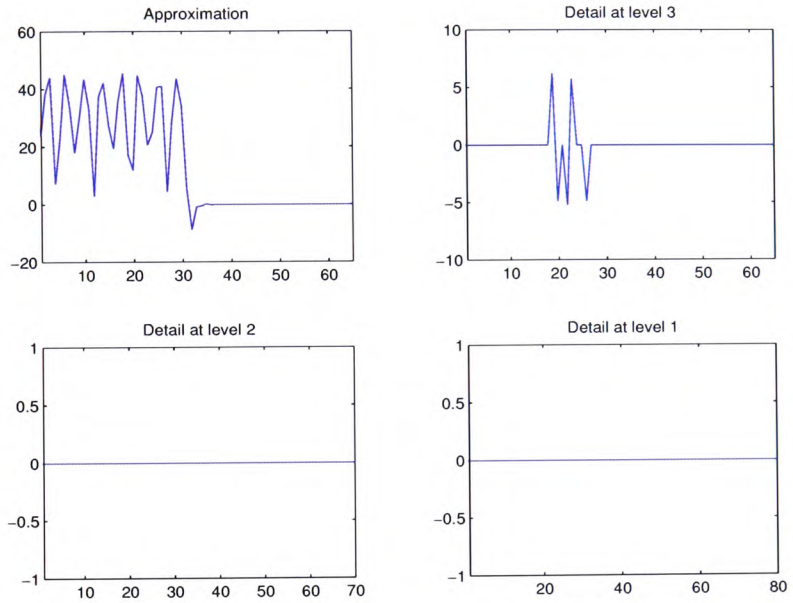

Figure 4.42: Wavelet coefficients of a common femoral MFE using the discrete Meyer wavelet. Coefficients thresholded to retain 5 detail coefficients. (a) Approximation, (b) detail level 3, (c) detail level 2, (d) detail level 1

Choosing the biorthogonal 3.1 wavelet as a base for the compression led to a much better result. Figure 4.44 shows the decomposition of the same waveform as in figure 4.42. Because the decomposition resulted in only 15 approximation coefficients the total number of coefficients for the compressed vector was only 20. Comparing the original and the reconstructed MFE in figure 4.45, it can be seen that the reconstructed MFE matched the original well.

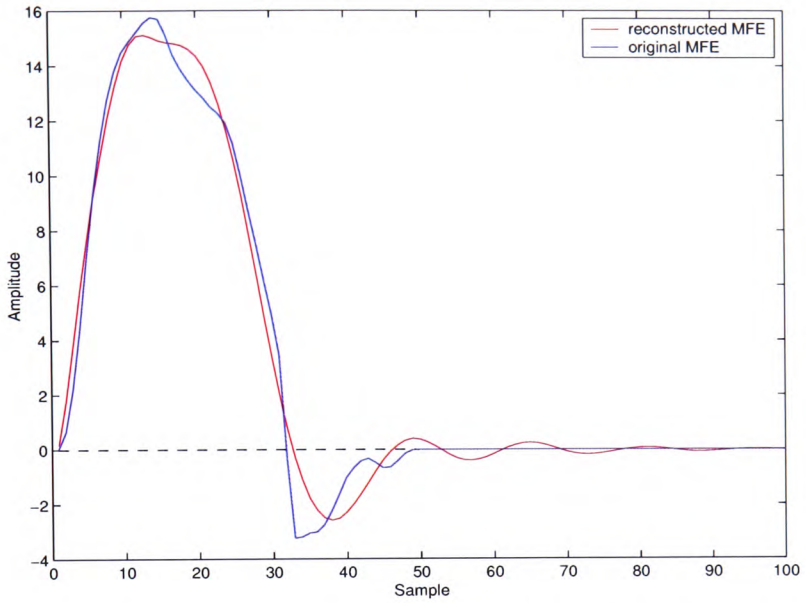

Figure 4.43: Reconstruction of the MFE from tresholded wavelet coefficients using 5 detail coefficients. Decomposition with the discrete Meyer wavelet at level 3.

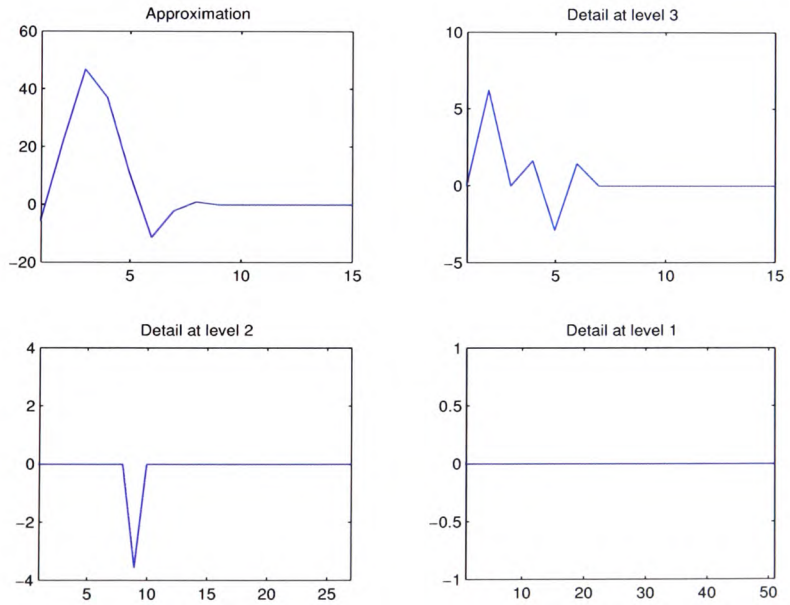

Figure 4.44: Wavelet coefficients of a common femoral MFE using the bi-orthogonal 3.1 wavelet. Coefficients thresholded to retain 5 detail coefficients. (a) Approximation, (b) detail level 3, (c) detail level 2, (d) detail level 1

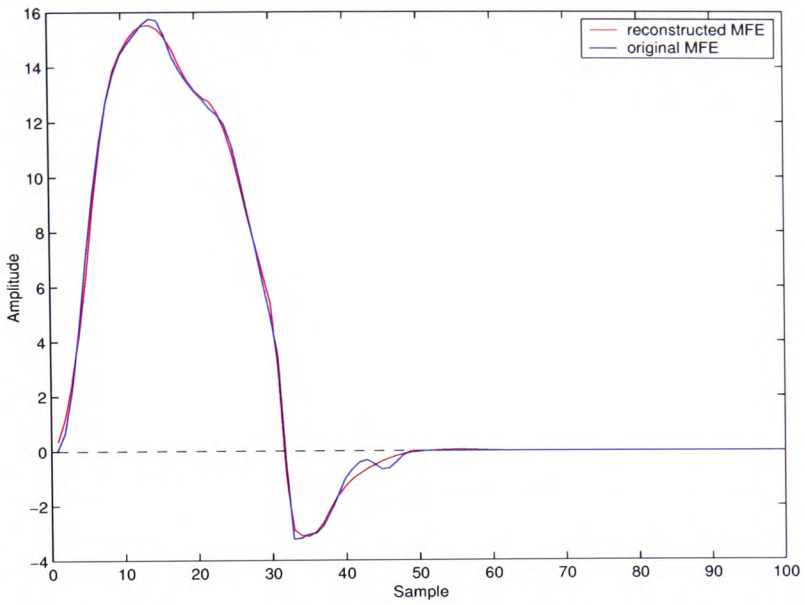

Figure 4.45: Reconstruction of the MFE from tresholded wavelet coefficients using 5 detail coefficients. Decomposition with the bi-orthogonal 3.1 wavelet at level 3.

After compressing the MFE by retaining only a limited number of detail coefficients, a new feature vector must be constructed. The new feature vector consisted of three sections: the approximation coefficients, the retained detail coefficients and the positions of the retained detail coefficients within the decomposition.

The wavelet decomposition vector was used to create the new feature vector. Figure 4.46 shows the decomposition vector of the MFE in figure 4.45 with all but the 5 most dominant detail coefficients set to zero. The beginning and end of each section is marked with a vertical dashed line. Section A3 consist of the approximation coefficients, while sections D3 to D1 hold the detail coefficients for levels 3 to 1, respectively.

Figure 4.47 shows an example of the composition of the new feature vector. Section (a) in the figure shows the approximation coefficients. In this example there are 15 approximation coefficients. The next section of the signal (b) holds the

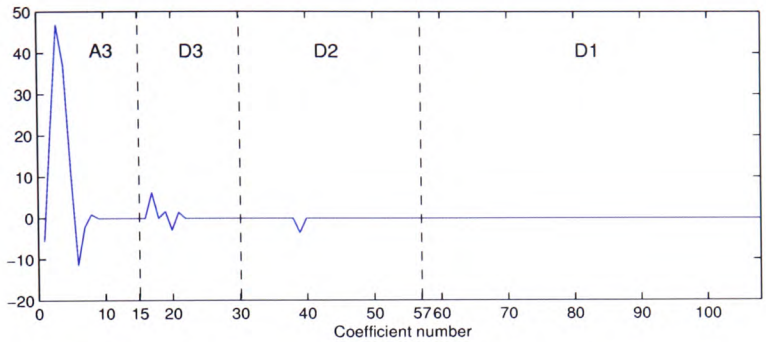

Figure 4.46: Wavelet decomposition vector. Approximation coefficients (A3), detail coefficients level 3 (D3), detail coefficients level 2 (D2) and detail coefficients level 1 (D1).

retained detail coefficients. The last section (c) is used to indicate the position of the retained detail coefficients within the decomposition. The length of section (c) is always the same as the length of section (b), as it is a direct map between value and position of the detail coefficient in the decomposition vector. The positions for the retained detail coefficients were counted from the beginning of the decomposition vector.

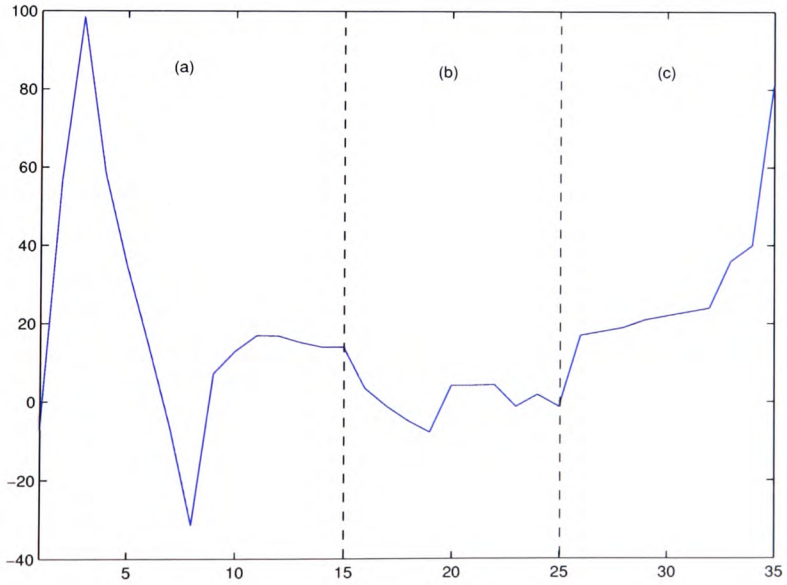

Figure 4.47: Wavelet coefficients classification input vector. (a) Approximation coefficients, (b) retained detail coefficients (c) position of the retained detail coefficients

4.6 Summary

This chapter has presented the feature extraction stage of the Doppler ultrasound blood flow analysis. It concentrated on three areas of feature extraction: the extraction of the MFE and the cardiac cycle, the calculation of the SBI and the reduction of the MFE length using wavelet-based compression.

All the processing stages for the extraction of the MFE were investigated. Existing methods were compared with new methods and the selection of the best performing methods were described.

The calculation of the SBI was presented and reasons were given for its selection. A new approach for the reduction of the MFE length was also presented and a selection of parameters for this method were given.

The key findings of this chapter can be summarised as follows:

1. The comparison of the MFE extraction algorithms showed that although the distance method was less susceptible to noise, the percentile method provided better results. Two reasons were attributed to the poorer performance of the distance method. An incorrect estimation of the maximum frequency occurred when a second knee was present in the spectrogram, and the distance method suffered from spikes when no signal was present.

2. The combination of the forward and reverse blood flow signal was improved by introducing a new algorithm that utilised a hysteresis parameter.

3. The extraction of the cardiac cycle was improved and automated by introducing a modified pulse-foot-seeking algorithm that included:

   (a) A new method of detecting the cardiac peak of the Doppler ultrasound blood flow signal.

(b) An improved detection of the gradient of the systolic upstroke, and therefore, the start of the cardiac cycle.

4. The SBI was extracted and was used as an additional feature in the decision making and diagnosis process described in chapter 5.

5. A lossy wavelet-based compression was able to reduce the length of the MFE considerably without losing significant details of the waveform shape. The best performing wavelets were the following,

   (a) Bi-orthogonal 3.1 at decomposition level 2.

   (b) Bi-orthogonal 3.1 at decomposition level 3.

   (c) Bi-orthogonal 2.2 at decomposition level 3.

Chapter 5

Decision Making and Diagnosis

The aim of this study is to investigate and develop methodologies for the automated diagnosis of vascular disease using Doppler ultrasound blood flow signals to support the clinical decision making process. This chapter presents the investigations conducted in this study in relation to the classification and decision making part of the process.

A number of classification techniques were previously applied to the common femoral artery (CFA) blood flow signal as stated in chapter 2. Artificial Neural Networks (ANNs) were used by several researchers to classify Doppler ultrasound blood flow signals [1,18–20,90,112]. These researchers used the maximum frequency envelope (MFE) as an input vector and presented it to a back-propagation ANN. Due to the nature of the problem and the characteristics of ANNs a similar approach was used in this study. A number of different data sets were used to investigate the influence of data set parameters on the classification performance.

The first section of this chapter (section 5.1) describes the reasons for the selection of the classifier. A review of statistical classifier and ANNs in Doppler ultrasound was already presented in section 2.5 of the literature review.

The structure and the size of each layer of the ANNs are presented in section 5.2. The ANN paradigm and training algorithm as well as the initial conditions are also described in this section.

Section 5.3 presents the performance metrics for the ANN. While a number of different performance metrics were considered in this study, only the percentage correct and the receiver operating characteristics were used.

The investigation into the influence of parameters, such as the feature vector length and automated pre-processing, required the generation of different data sets. Section 5.4 describes these data sets. It also includes a description of the clinical data used in this study.

The clinical CFA signals in this study were used in two investigations. The first investigation separated the signals into CFAs with no significant and significant proximal disease. This investigation was called the two-class problem. The results are presented in section 5.5 of this chapter. The second investigation partitioned the significant proximal disease into two classes: significant proximal disease and occlusion of the proximal segment. This investigation was called the three-class problem and the results are present in section 5.6.

5.1 The classification approach

ANNs model the human brain by using a set of interconnected artificial neurons thus forming a single or multi-layer network. A review of the benefits and disadvantages of ANNs was given in chapter 2.

The classification process of Doppler ultrasound blood flow signals is characterised by the following:

- Non-linear process.

- Unknown mathematical relationship between input and output.
- Long feature vector, when the MFE is used.
- Noisy and imperfect MFEs are possible.

Because ANNs are well suited to deal with such problems robustly, it was decided to use them as the classifier for the Doppler ultrasound signals in this study. Furthermore, studies carried out by other researchers showed that ANNs were successful in classifying Doppler ultrasound blood flow signals [1, 18–20, 90, 112].

5.2 Choice of ANN structure and parameters

The principle of ANNs was presented in chapter 2, but before an ANN can be constructed a number of issues need to be considered. These issues are covered in sections 5.2.1 to 5.2.6.

5.2.1 ANN paradigm and training algorithm

The choice for the ANN paradigm fell on the supervised network algorithm because the classification of the input signals is known. The network structure chosen for this study is the multi-layer perceptron as this has been used successfully in different signal classification problems, including Doppler ultrasound blood flow [1,18,19,112], EEG signal analysis [85, 113, 114] and speech recognition [88]. There are three distinctive characteristics that can be identified in a multi-layer perceptron:

- A smooth non-linear activation function at the output of each neuron.
- One or more hidden layers.
- A high degree of connectivity.

The most popular learning algorithm for these networks is the error back-propagation. It is also the most widely used algorithm for most successful applications of supervised learning algorithms [88]. Using the back-propagation learning algorithm a network is trained by forming an error signal from the comparison of the desired and actual network responses. The error is propagated backwards through the network. The free parameters of the network, usually the bias and the weights of the neurons, are adjusted to minimise the sum of squared errors.

A disadvantage of the back-propagation and other supervised learning algorithms is their poor scaling behaviour. Scaling, in this context, refers to the ability to train networks of large sizes. The time to train a network increases exponentially with the number of neurons and their interconnections. The learning process of large, and especially, heavily multi-layered networks may become unacceptably slow [88]. The networks in this study had a maximum of two hidden layers with a maximum of 40 neurons in each hidden layer. The number and size of the hidden layers is discussed in section 5.2.4.

5.2.1.1 Learning rate and momentum

One of the parameters of the back-propagation learning algorithms is the learning rate, which influences the speed of training. A small rate of learning will only generate small changes to the weights. This leads to longer learning periods but offers smoother adjustment of the weights and is less likely to find a local minimum [115]. On the other hand, if the rate of learning is set too high, training will be shortened but the network can become unstable. One method of avoiding the problem associated with the selection of the learning rate is to include a momentum term to the weight update [88]. The momentum acts like a low-pass filter and avoids radical changes to the weights. Without the momentum the network may incorrectly stop

at a local minimum [115, 116].

In this study a variable learning rate and a momentum term were used. The employed back-propagation learning algorithm adjusted the weight, w, and bias, b, variables according to the following rules [117]:

1. Should the squared error increase by more than a set percentage, ξ, after a weight update, then the weight update is discarded, the learning rate, lr, is multiplied by a factor, ρ ($0 < \rho < 1$), and the momentum, mc, is set to zero.

2. If the squared error decreases after a weight update, then the weight update is accepted, lr is multiplied by a factor, η ($\eta > 1$), and mc is restored to its original value if it had been set to zero previously.

3. If the squared error increases by less than ξ, then the weight update is accepted, lr and mc remain unchanged.

The following typical parameter values were chosen in this study [116, 117],

$$mc = 0.9, lr = 0.01, \eta = 1.05, \rho = 0.7, \text{ and } \xi = 4\% \tag{5.1}$$

5.2.1.2 Termination of training

Another important issue for a back-propagation ANN is when to stop the training period. In theory, the back-propagation algorithm cannot converge and no well-defined criteria for terminating the training are defined [88]. In practice, the termination criteria are chosen depending on the application. Common conditions are the error goal, the number of epochs and the error gradient.

The error goal is the accepted error for the ANN and is the difference between the target and the actual outputs. When the error goal is reached, the training algorithm stops.

The second method to stop the training process is to limit the number of epochs of the training stage. The number of epochs determines how often the full data set is presented to the ANN. A high number of epochs does not automatically equate to best performance. Trained for too long, an ANN can memorise the input data set and fails on the classification of previously unseen signal vectors. In other words, it may lose its ability to generalise.

A third criterion is used in some algorithms and terminates the learning process when the change of the error between one epoch and the next is below a minimum value.

All of the above three criteria were used to stop the training process in this study. The associated parameters were set to the following typical values,

- Error goal: 0.001.
- Maximum number of epochs: 5000.
- Error gradient: 10^{-10}.

The maximum number of epochs was chosen to be 5000 because it offered a time long enough to train the network without stopping the training prematurely. The number of epochs were varied between 500 and 10000 in order to study its effect. It was found that a limit of 500 epochs terminated the training prematurely, while 10000 epochs did not provide any improvement in performance.

The error goal is calculated as the mean square error between the target and actual output of the network [116],

$$mse = \frac{1}{N}\sum_{k=1}^{N} ek^2 = \frac{1}{N}\sum_{k=1}^{N}(t(k) - a(k))^2 \tag{5.2}$$

where N is the number of presented signal vectors, $e(k)$ the error of the k^{th} signal vector, $t(k)$ and $a(k)$ the target and actual output of the k^{th} signal vector, respectively.

5.2.2 Number of ANN inputs

The input layer of an ANN serves as a buffer to fan out the inputs to the next layer. There are two main issues that affect the input layer: its size and its range of the values for the input data.

The size of the input data is determined by the resolution and dimension of the input vector. The ANN becomes increasingly complex with longer input vectors. Each input is normally fully interconnect to the next layer and therefore, adding a multiplication and addition operations to the ANN. For fast processing, and small implementations, the ANN input layer should be as small as possible. The signal vectors in this study, which are presented in section 5.4, were all one dimensional with lengths between 16 and 121 points. In order to observe the effect of additional information on the classification process, each signal vector was presented to the ANN on its own and with the SBI as an appended additional input. The SBI is fully interconnected with the next layer. Figure 5.1 shows an example of the organisation of the input layer when the SBI was used.

The second issue concerning the input layer is the maximum and minimum value of the input data points. It was reported that the performance of an ANN might improve if the data points in the input vector are below 1 [115]. The values in the MFE vectors ranged between ± 65. Scaling was therefore used to reduce the range to ± 1 for the uncompressed MFE data. No scaling was applied to the compressed input vectors as part of the vector identified the position of the retained detail coefficient.

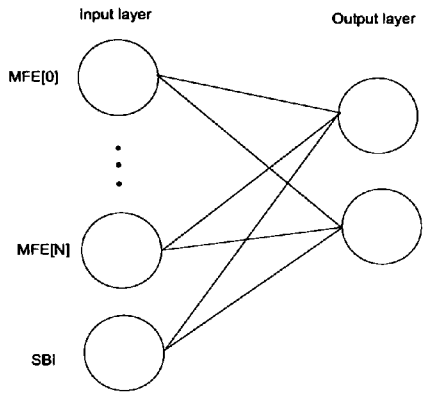

Figure 5.1: Example of the input data set using the MFE and the SBI.

5.2.3 Number of outputs

The number of outputs for the ANN is determined by the number of classes for input signal separation. Although it is possible to use only one output neuron for all classes by partitioning the range of output values. However, the decision making by the ANN is generally more robust when more than one output neuron is used [88].

This study looked at two cases of classification and diagnosis. The first case was to differentiate between signals from vessels with and without significant proximal disease. The second case went one step further and split the significant proximal disease class into two separate classes. These were significant proximal disease and proximal occlusion. The number of output neurons for the two-class problem was set to two, whilst the three-class problem networks had three output neurons, one for each class.

5.2.4 Number of hidden layers and number of neurons

No fixed rules exist to determine the optimal number of hidden layers and neurons in each hidden layer. The approach used to determine the most successful combination of hidden layers and neurons is usually trial and error. This approach was followed

here. A combination of one and two hidden layer ANNs were used to find the best performing network configuration. The number of neurons in each hidden layer were varied between 5 and 40 neurons. The following list shows the number of neurons in the hidden layers (1 or 2) of the ANNs used in this study:

• 5	• 10	• 20	• 30	• 40
• 5-5	• 5-10	• 5-20	• 5-30	• 5-40
• 10-5	• 10-10	• 10-20	• 10-30	• 10-40
• 20-5	• 20-10	• 20-20	• 20-30	• 20-40
• 30-5	• 30-10	• 30-20	• 30-30	• 30-40
• 40-5	• 40-10	• 40-20	• 40-30	• 40-40

A single number represents the number of neurons of the hidden layer in a single hidden layer ANN. Two numbers separated by a dash describe the numbers of neurons in the two hidden layer networks, with the first number representing the first hidden layer.

5.2.5 Transfer function of the neurons

One of the three characteristics of a multi-layer perceptron is the non-linearity at the outputs of its neurons. This non-linearity is usually called the transfer function as it transfers the sum of the weight-input product to the output of the neuron. Figure 5.2 shows a single neuron with the transfer function as a separate block.

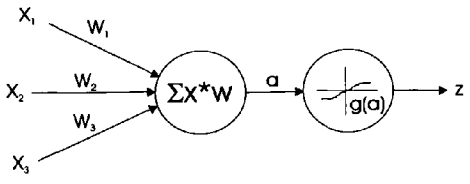

Figure 5.2: Single neuron with sum of input-weight product and transfer function.

A number of smooth non-linear neuron transfer functions exist, such as the hy-

perbolic tangent and sigmoid functions. The most commonly used transfer function is the sigmoid function and it was also used with all neurons in this study. This function is defined as [117],

$$z = g(a) = sig(a) = \frac{1}{1 + e^{-a}} \tag{5.3}$$

where z denotes the output and a denotes the input. Figure 5.3 shows the sigmoid function characteristics.

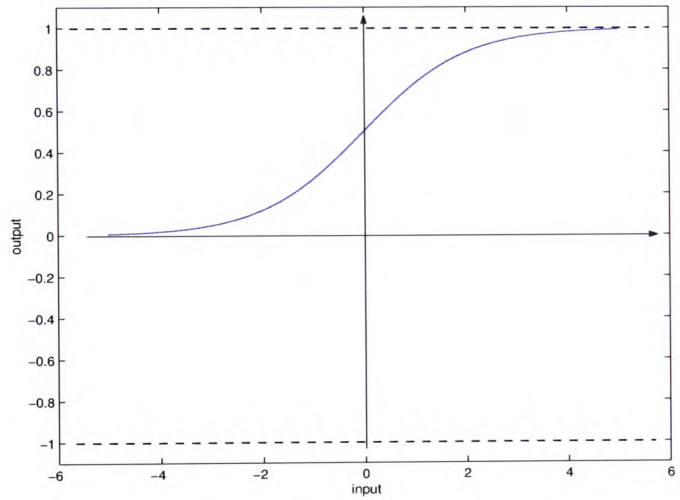

Figure 5.3: Sigmoid transfer function.

In the test, the output layer neurons only were subjected to an additional 'winner-takes-it-all' function. This function sets the output neuron with the largest value to one and the others to zero, giving a clear indication of the classification as the neuron outputs were mutually exclusive.

5.2.6 Initial conditions

Before the training of an ANN with a back-propagation learning algorithm can commence, the free parameters of the network must be initialised. If prior information

is available, the free parameters can be initialised using this information. No prior information was available in this study and all weights and biases were initialised to random values. Setting the initial weights to the wrong values can result in a situation known as premature saturation. This refers to a scenario where the error stays constant for some period of time and only starts to decrease afterwards. Early termination of the training stage due to a low error gradient may occur in this situation [88]. To avoid premature saturation, each network structure was trained with 10 runs. On each training run the free parameters were initialised to new random values. The best result was taken as the performance for the particular network structure.

5.3 ANN performance metrics

After extensive simulations of different ANN structures and different data sets the classification performance must be measured and compared. A number of different performance metrics were considered and are presented in the following sections.

5.3.1 Percentage correct

The simplest way to assess the performance of a classifier is to consider the number of correctly classified inputs. The signals in this study were judged against the classification obtained during the data collection, the 'gold standard'. The percentage correct was therefore, the ratio between the number of signals correctly identified by the ANN and the number of correct signals according to the 'gold standard'.

In this study, each data set used the same set of common femoral signals. The results for the percentage correct metric were therefore comparable between all ANNs. Furthermore, the percentage correct was only used as an initial indicator of per-

formance and additional performance metrics were used to identify the best ANN performance.

5.3.2 Average sum-squared error

The average sum-squared error is determined by calculating the difference between the actual output value and the target output value of the ANN. The error is compared with the error goal, which is one of the three training termination conditions used here. It was not used to evaluate the performance of the ANN.

5.3.3 Receiver operating characteristics

A useful tool to evaluate the performance of diagnostic systems are receiver operating characteristic curves, or ROC curves. The calculation of a ROC curve is used to evaluate the performance of the system for one given result, or a particular class [83]. The ROC curve is a plot of the true positive ratio over the false positive ratio, which is achieved by varying the decision threshold of the output. The larger the area underneath the ROC curve the better is the performance of the ANN. Because a 'winner-takes-it-all' strategy was implemented at the output stage of the ANN, the ROC curve was not used to compare the ANNs in this study.

Although ROC curve itself was not applied, the performance metrics used to calculate the ROC curve were used. Four possibilities exist with a single decision. The first is the true positive decision (TP), which gives the number of positive decisions of the ANN that coincide with the positive diagnosis of a 'gold standard'. The second possibility is the false positive decision (FP), in which the ANN made a positive decision that was not included in the 'gold standard'. The third is the false negative decision (FN), where a positive diagnosis of the 'gold standard' was not

made by the ANN. The last possibility is the true negative decision (TN), in which both the ANN and the 'gold standard' agree on the absence of a positive diagnosis. Table 5.1 shows these definitions [83], which can be absolute numbers or percentages of the total signal set.

A number of parameters can be derived from these definitions,

- The sensitivity gives the probability that an event is detected provided it is present.
- The specificity is the probability that the absence of an event is detected provided the event is absent.
- The false alarm rate is the probability that an event is falsely detected provided that the event did not occur.

The relationship between the ROC curve measures and these parameters is defined in equation 5.4 to 5.6 [83].

$$\text{Sensitivity} = \frac{TP}{TP + FN} \tag{5.4}$$

$$\text{Specificity} = \frac{TN}{TN + FP} \tag{5.5}$$

		ANN diagnosis	
		Positive	Negative
'Gold standard' diagnosis	Positive	TP (true positive)	FN (false negative)
	Negative	FP (false positive)	TN (true negative)

Table 5.1: ROC curve metrics definitions.

$$\text{False alarm rate} = \frac{FP}{FP + TN} = 1 - \text{specificity} \tag{5.6}$$

5.3.4 Recall and Precision

Recall and Precision are two performance metrics from the field of expert systems and databases [83]. They are defined as follows:

- Recall gives the ratio of the number of correct positive decisions made by the ANN and the total number of positive diagnoses made by the 'gold standard'.
- Precision is the ratio of the number of correct positive decisions made by the ANN and the total number of positive decisions made by the ANN.

Recall and precision can be linked to the ROC curve definitions using equations 5.7 and 5.8, respectively.

$$\text{Recall} = \frac{TP}{TP + FN} \tag{5.7}$$

$$\text{Precision} = \frac{TP}{TP + FP} \tag{5.8}$$

5.3.5 Chi-Square Test

The chi-square test examines the frequency distribution of all possible classes from an ANN. It measures how often a class has occurred compared to how often it should occur. Its main application is in situations where the correct answer is unknown. This may be the generation of music or the simulation of some process. In this study all answers were known and the chi-square test was not used as a performance metric.

5.4 Data selection and preparation

In order to train and validate an ANN, the appropriate training and test data sets must be selected. To avoid any bias for one class during training, the network was presented with an equal number of signals or input vectors per class. The maximum number of signals per class was therefore, determined by the size of the data set of the smallest class. Furthermore, to validate the performance of the network and its ability to generalise, a number of signals from each class were reserved for the test data set. To increase the number of signals in each class it is valid to use two cardiac cycles from each subject due to the known physiological differences from one cardiac cycle to the next [17].

Sections 5.4.1 and 5.4.2 describe the selection and preparation of the data sets which were presented to ANNs of this study.

5.4.1 Data selection

The signals used in this study were obtained from a database which was recorded, digitised and categorised by the University Hospital of Wales, Cardiff [1]. The signals were categorised into three classes:

- No significant aorto-iliac disease (less than 50% stenosis).
- Significant aorto-iliac disease (50% to 99% stenosis).
- Occlusion (over 99% stenosis) in the aorto-iliac segment.

The classification was made with reference to the proximal disease condition. The classes were chosen in accordance with general clinical management procedures of patients with peripheral vascular disease at the University Hospital of Wales [1]. All classes contained signals with and without multiple stenoses (proximal and distal)

in order to investigate the ability of the ANN to detect proximal disease even in the presence of distal disease.

Out of this database, 160 lower limb signals from 134 patients were used to develop the algorithms in chapters 3 and 4. For the investigation of the classification only 120 signals were used. The reason for this reduction is the requirement to provide equal number of signals of each class to the ANNs. The maximum number of signals in each class was therefore, determined by the smallest class.

The training set for the two-class problem comprised of 160 cardiac cycles with each signal contributing two cardiac cycles. The three-class problem used 120 cardiac cycles for the training data set, due to a smaller number of signals in the class of occlusive disease. The test sets for both problems were smaller and contained 80 cardiac cycles from 40 signals. There was no overlap between the training and test sets. This ensured that the performance of the ANN was based entirely on its ability to generalise.

All subjects underwent Doppler ankle-brachial systolic blood pressure (ABPI) measurements and those with a normal ABPI and normal-sounding (triphasic) ankle Doppler ultrasound waveforms were assumed to have no significant lower limb arterial disease. Those with a lower ABPI or an abnormal-sounding ankle waveform underwent Duplex scanning of the aorto-iliac and femoral-popliteal segments using a Toshiba SSA-270A Duplex ultrasound scanner incorporating a 5 MHz linear array probe with a Doppler reference frequency of 3.75 MHz. Furthermore, these subjects underwent arteriography and biplanar views were taken of the aorto-iliac segment. There was a mean interval of 7 days (0 - 90 days) between Duplex scanning and arteriography for those patients, with 92% of the entire cohort undergoing arteriography within 15 days of the Duplex scan. [1]

5.4.2 Data preparation

A number of algorithms were investigated in this study and presented in chapters 3 and 4 to convert the time domain signal into a MFE vector. Some of these algorithms improved on existing techniques, whilst others provided alternative approaches. In order to compare these algorithms different data sets were prepared. A data set was defined as a set of all signals prepared as ANN input vectors using a predefined algorithm. The data sets are labelled with a running number from A0 to A12.

The length of the ANN input vectors should be kept constant for all MFE vectors within a data set. However, the length of the cardiac cycle MFE varied depending on the heart rate of the patient. In order to eliminate this dependency, the input data should be either truncated or transformed to a constant length. Three methods were investigated in this study to maintain a constant length for the cardiac cycle. These methods were:

- Re-sampling the cardiac cycle MFE to a constant length (data sets A1 and A6).
- Truncating the cardiac cycle to different lengths and ignoring the remaining part of the cardiac cycle (data sets A0 and A2 to A5). This method was also used by Wright *et al* [1, 18].
- Compressing the cardiac cycle MFE using a wavelet compression algorithm.

Using these three methods the size of the input vector varied between 16 and 120 points.

All data sets were transformed using the STFT to calculate the spectrogram from the time domain signal. The STFT used an 128-point Hamming window with 50% overlap. Before further processing algorithms were applied to create the data

sets, the forward and reverse flow spectrogram sections were combined into a single time-frequency domain matrix.

A manually selected threshold was applied to remove the noise floor in two data sets (A0 and A1). This followed the approach used by previous researchers [1, 19] and was used here for comparison with the automated algorithms developed in this study. All other data sets (A2 - A12) used the new automated method proposed in this study, which reduced the noise floor using wavelet denoising. A Haar wavelet at decomposition level 9 provided sufficient noise reduction to extract the MFE without user intervention. Because the distance method did not provide the correct MFE when used without noise reduction algorithms, the percentile method (95%) was used to extract the MFE. The cardiac cycles were separated by applying the modified pulse-foot-seeking method.

Figure 5.4 gives a summary of the characteristics of the data sets. Each node on the right hand side (A0 - A12) represents one data set. The path from the original data set on the left to a data set on the right shows the pre-processing route. The pre-processing algorithms which were common to all data sets, such as the STFT, the MFE and the cardiac cycle extraction algorithms, are not shown in this figure.

To investigate possible performance improvements with additional features, the SBI was used together with the cardiac cycle MFE. All data sets were therefore, used twice in this study, with and without the SBI.

The data sets are grouped by investigation. The following sections describe the data sets and the associated investigations.

5.4.2.1 Investigation into the impact of noise reduction algorithms

A number of noise reduction or removal algorithms were investigated in this study and section 3.5 presented these algorithms in detail. Two methods were identified

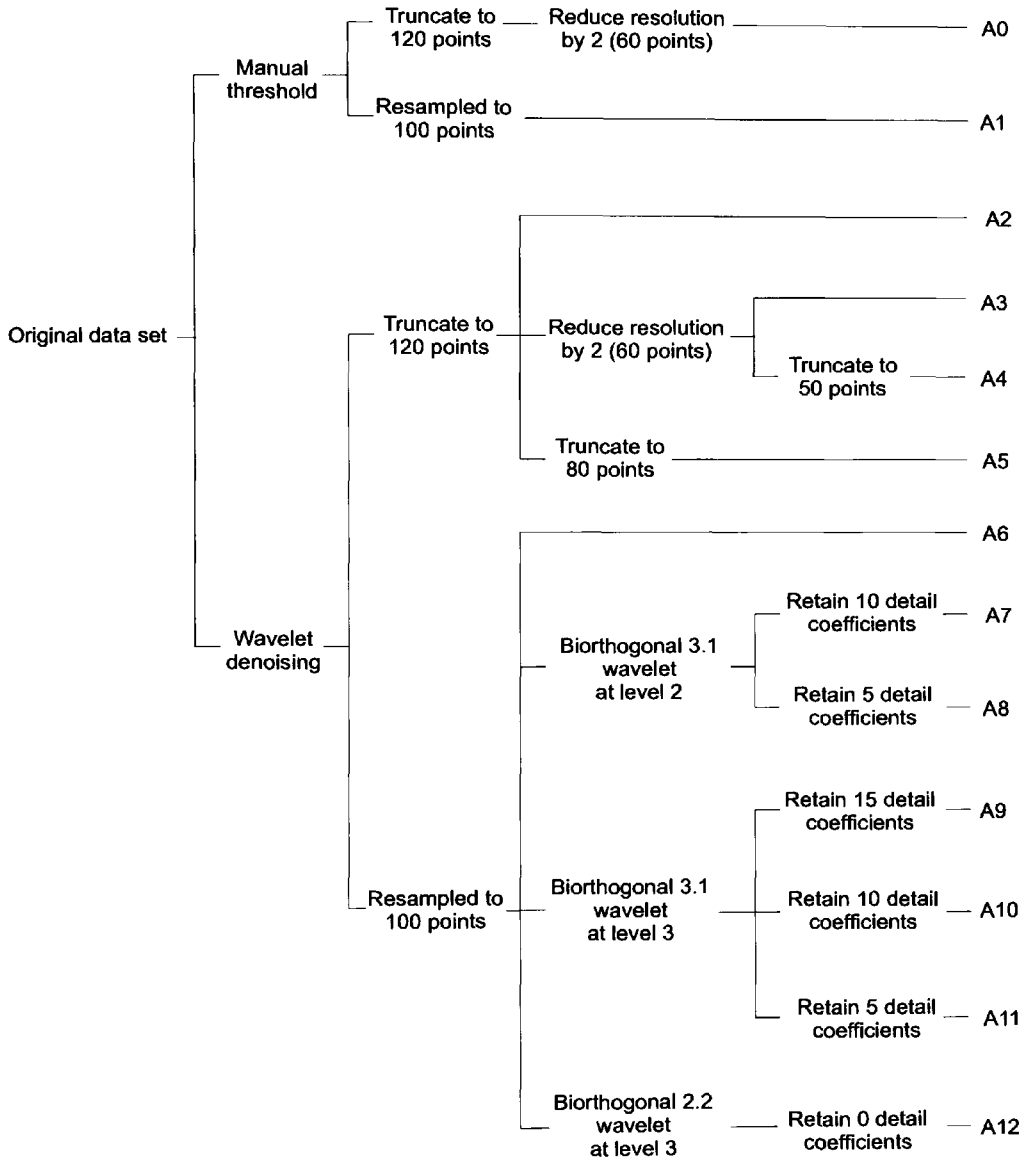

Figure 5.4: Tree for the generation of the data sets. Each node on the right hand side (A0 - A12) represents one data set.

to produce sufficient noise reduction for further processing. These were manual thresholding and two-dimensional wavelet denoising. The first method was not suitable for an automated processing of the Doppler ultrasound signals, but was included for comparison with the proposed wavelet denoising method and previous work.

This investigation was split into two parts. In each part two data sets were compared. The only difference between the data sets was the noise reduction method.

In the first part, the MFE was truncated to a constant length. The two data sets, A0 and A3, followed the same pre-processing route described above with the exception of the noise reduction. Data set A0 used a threshold that was manually selected for each signal to remove the noise components, while data set A3 used wavelet denoising. The MFE was first truncated to 120 points and then reduced to 60 points by taking every second point. This approach was also used by Wright *et.al.* [1, 19] and allowed comparison with these studies.

A similar investigation was performed in the second part. However, here the MFE was re-sampled to 100 points rather than truncated. This presented the entire MFE for one cardiac cycle to the ANN. It was felt necessary to investigate this case for both noise reduction methods in order to observe the effect of presenting the entire cardiac cycle MFE to the ANN. Data set A1 was created using the manual threshold approach, while data set A6 used the automated wavelet denoising algorithm. A sampling rate of 100 samples per cardiac cycle was chosen as it resulted in a sample period of 11.67 ms when based on an average heart rate of 70 bpm. Previous research suggested that the Doppler ultrasound blood flow signal can be assumed stationary for this period [43].

5.4.2.2 Investigation into the impact of MFE vector length reduction

This investigation was conducted to observe the impact of truncating the MFE of the cardiac cycle on the ANN results. All data sets used the same automated pre-processing route. Noise reduction was performed by applying wavelet denoising. A number of different methods were used to truncate the MFE, all of which were based on the work of Wright *et.al.* [1, 19]. Two main methods for the reduction of the MFE were followed. The first method was to truncate the MFE to a constant length. Data set A2 and A5 followed this approach. Data set A2 was truncated to 120 points, whilst data set A5 was truncated to 80 points. The second method was to reduce the resolution of the MFE by removing every second point from the vector. This was used in data set A3, which was based on a 120 point long truncated MFE and gave a 60 point MFE. Data set A4 combined these two methods again and truncated the data set A3 to only 50 points. For comparison, data set A6 was included in this investigation as it used the entire MFE, re-sampled to 100 points, as an ANN input vector.

Figure 5.5 shows the cardiac cycle MFE of one of the Doppler ultrasound blood flow signals used in this study. Part (a) of the figure displays the entire re-sampled MFE (data set A6). Figures 5.5(b) - (d) show data sets A2, A5, and A4, respectively. Data set A3 is not included in figure 5.5 as it is of almost identical shape to data set A2. From the figure it is apparent that the cardiac cycle is only fully represented in data set A6.

5.4.2.3 Investigation into the impact of MFE compression

A new approach of presenting the MFE to an ANN was proposed in this study. The previous data sets (A2 to A5) reduced the length of the MFE by truncating the signal vector. This method was not able to present the entire cardiac cycle to the

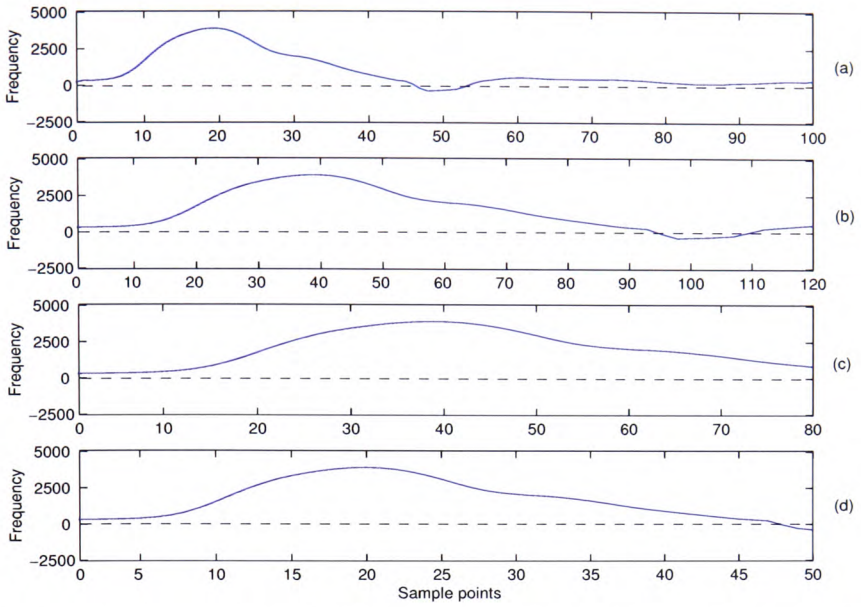

Figure 5.5: Example of MFEs: re-sampled to 100 points (data set A6) (a), truncated to 120 points (data set A2) (b), truncated to 80 points (data set A5) (c) and truncated to 50 points after reducing the resolution from 120 to 60 points (data set A4) (d).

ANN. The new approach, which was detailed in section 4.5, applied a wavelet-based compression algorithm to the MFE. This reduced the length of the MFE but retained the most dominant features of the entire cardiac cycle. To provide a consistent basis for the compression, the 100 sample point long cardiac cycle MFE from data set A6 formed the basis of this data set.

The data sets described in this section were used to investigate the effectiveness of the proposed approach on the classification results of the ANN. Six data sets (A7 to A12) were used for this investigation. The selection of these data sets was made from tables A.1 and A.2 in appendix A. These tables list the root mean square error (RMSE) between the reconstructed and the original MFE for different parameters. The parameters of the selected data sets were chosen to form an optimum compromise between low RMSE and a short vector length. The vector composition

was described in section 4.5. The data sets were,

- Data set A7; biorthogonal 3.1 wavelet at level 2 with 10 detail coefficients. (RMSE = 0.048, Length = 47 points)
- Data set A8; biorthogonal 3.1 wavelet at level 2 with 5 detail coefficients. (RMSE = 0.08, Length = 37 points)
- Data set A9; biorthogonal 3.1 wavelet at level 3 with 15 detail coefficients. (RMSE = 0.071, Length = 45 points)
- Data set A10; biorthogonal 3.1 wavelet at level 3 with 10 detail coefficients. (RMSE = 0.112, Length = 35 points)
- Data set A11; biorthogonal 3.1 wavelet at level 3 with 5 detail coefficients. (RMSE = 0.207, Length = 25 points)
- Data set A12; biorthogonal 2.2 wavelet at level 3 with 0 detail coefficients. (RMSE = 0.49, Length = 16 points)

5.5 Classification of proximal disease: The two-class problem

This section presents the results of the ANN performance on separating the input signals into two classes: no significant proximal disease (less than 50% stenosis) and significant proximal disease (over 50% stenosis). All the data sets previously introduced in section 5.4 were applied to all network structures presented in section 5.2.

The different network structures were identified by their number of hidden layers and the size of each hidden layer. A 10-20 layer network structure, therefore,

indicates a two hidden layer network with 10 neurons in the first and 20 neurons in the second hidden layer. The number of input neurons depended on the data set and ranged between 16 and 121, including the SBI. Two output neurons, one for each class, were used, and all ANNs were trained for 5000 epochs unless the error goal or the minimum error gradient was reached.

Each network structure was trained 10 times with each data set to avoid the influence of the initial values of the ANN, which were chosen randomly. The best performing ANN for each data set was initially selected by the percentage of correctly classified signals. Graphs that show the percentage correct for each network structure are included in appendix B.1. To further differentiate the performance of the ANNs with equal percentage correct, additional performance metrics were applied. These were sensitivity, specificity and false alarm rate. In cases where two or more ANNs achieved the same percentage correct performance, the ANN with the lowest false alarm rate in the no significant proximal disease class was selected. This criteria was chosen as it is important to have as few cases as possible where a significant proximal disease is falsely detected as no significant proximal disease. When ANNs had equal performance the one with the fewest number of neurons was selected. The following sections present the best ANN performance results for the smallest ANN structures only. The metrics for all the best performing ANNs are included in appendix B.2.

The results are split into the same groups as described in section 5.4. Each data set was used without and with the SBI. Both results are given here.

5.5.1 Investigation into the impact of the noise reduction algorithms

Four data sets were used to investigate the effect of the noise reduction algorithm, and therefore, the possibility of automating the diagnosis and decision making process. The first two data sets (A0 and A3) used a 60-point cardiac cycle MFE as an input vector for the ANN.

The best performing ANNs using data set A0, which utilised manual thresholding for noise reduction, had a classification rate of 92.5% without the SBI. That was reduced to 91.25% when the SBI was included. The smallest network that achieved this performance for data set A0 with and without SBI had one hidden layer with 20 neurons. Tables 5.2 and 5.3 show the result summary for data set A0 without and with the SBI, respectively.

	Classification (%)		*Performance measures*		
Disease condition	non-significant	significant	Sensitivity	Specificity	False alarm rate
no significant	**95**	5	0.950	0.900	0.100
significant	10	**90**	0.900	0.950	0.05
Average	92.5		n/a		

Table 5.2: Best achieved classification result for data set A0 without the SBI for the smallest ANN.

	Classification (%)		*Performance measures*		
Disease condition	non-significant	significant	Sensitivity	Specificity	False alarm rate
no significant	**92.5**	7.5	0.925	0.900	0.100
significant	10	**90**	0.900	0.925	0.075
Average	91.25		n/a		

Table 5.3: Best achieved classification result for data set A0 with the SBI for the smallest ANN.

ANNs using data set A3, which used the automated algorithm with the wavelet denoising, achieved slightly higher classification rates of 93.75% without and 95% with the SBI. The results are shown in tables 5.4 and 5.5. The smallest ANN achieving these classification rates had one hidden layer with 10 neurons. This was the same whether the SBI was used or not.

	Classification (%)		*Performance measures*		
Disease condition	non-significant	significant	Sensitivity	Specificity	False alarm rate
no significant	**97.5**	2.5	0.975	0.900	0.100
significant	10	**90**	0.900	0.975	0.025
Average	93.75		n/a		

Table 5.4: Best achieved classification result for data set A3 without the SBI for the smallest ANN.

	Classification (%)		*Performance measures*		
Disease condition	non-significant	significant	Sensitivity	Specificity	False alarm rate
no significant	**97.5**	2.5	0.975	0.925	0.075
significant	7.5	**92.5**	0.925	0.975	0.025
Average	95		n/a		

Table 5.5: Best achieved classification result for data set A3 with the SBI for the smallest ANN.

The use of the SBI as an additional feature resulted in a slightly decreased performance for data set A0, but an increased performance for data set A3. Also, the performance of the automated noise reduction algorithm produced better ANN perfomance results than those with manual thresholding.

The second pair of data sets (A1 and A6) used a 100-point re-sampled cardiac cycle MFE as an input vector for the ANN. Without the SBI as an additional feature the best performing network structures for data set A1, which employed manual thresholding, had a classification rate of 88.75%. The ANN had two hidden

layers with 10 neurons each. When the SBI was included in the input vector the network with 5 neurons in the first hidden layer and 20 neurons in the second hidden layer performed best. The classification rate was the same as for the input vector without the SBI. Tables 5.6 and 5.7 show the results for the smallest ANNs.

	Classification (%)		*Performance measures*		
Disease condition	non-significant	significant	Sensitivity	Specificity	False alarm rate
no significant	**92.5**	7.5	0.925	0.850	0.150
significant	15	**85**	0.850	0.925	0.075
Average	88.75		n/a		

Table 5.6: Best achieved classification result for data set A1 without the SBI for the smallest ANN.

	Classification (%)		*Performance measures*		
Disease condition	non-significant	significant	Sensitivity	Specificity	False alarm rate
no significant	**92.5**	7.5	0.925	0.850	0.150
significant	15	**85**	0.850	0.925	0.075
Average	88.75		n/a		

Table 5.7: Best achieved classification result for data set A1 with the SBI for the smallest ANN.

Data set A6, which used the automated noise reduction algorithm, achieved a classification rate of 92.5% in both cases, without and with SBI. The best performing network structure without the SBI used one hidden layer with 10 neurons. When the SBI was included in the input vector the network with 5 neurons in the first and 5 neurons in the second hidden layer performed best. The classification matrices are shown in tables 5.8 and 5.9.

These results show that the data sets with the automated algorithm, A3 and A6, yielded improved performance results over data sets A0 and A1, which used manual thresholding. Furthermore, the introduction of the SBI into the ANN input vector

	Classification (%)		*Performance measures*		
Disease condition	non-significant	significant	Sensitivity	Specificity	False alarm rate
no significant	**95**	5	0.950	0.900	0.100
significant	10	**90**	0.900	0.950	0.050
Average	92.5		n/a		

Table 5.8: Best achieved classification result for data set A6 without the SBI for the smallest ANN.

	Classification (%)		*Performance measures*		
Disease condition	non-significant	significant	Sensitivity	Specificity	False alarm rate
no significant	**95**	5	0.950	0.900	0.100
significant	10	**90**	0.900	0.950	0.050
Average	92.5		n/a		

Table 5.9: Best achieved classification result for data set A6 with the SBI for the smallest ANN.

only improve the classification in data set A3 by 2.5%. It can also be observed that the truncated ANN input vectors performed better than the entire cardiac cycle MFE, which was re-sampled to 100 points.

5.5.2 Investigation into the impact of MFE vector length reduction

Truncating the cardiac cycle MFE to obtain a constant length ANN input vector was a technique previously used by other researchers [1, 19, 112]. The previous section has already shown that the truncated ANN input vector performed better than the ANN input vector with the entire cardiac cycle MFE.

This investigation used four different data sets, all of which used truncated cardiac cycle MFEs. For comparison data set A6, which used the entire cardiac cycle MFE, was included. All data sets used algorithms that automated pre-processing,

including the automated wavelet denoising algorithm.

Data set A2 presented the first 120 points of the cardiac cycle MFE to the ANN. When used without the SBI the best performing ANN had 5 neurons in the first hidden layer and 10 neurons in the second hidden layer. The classification rate for this ANN was 95%. This decreased to 92.5% when the SBI was used with an ANN that had 5 neurons in its hidden layer. The results are shown in tables 5.10 and 5.11.

	Classification (%)		*Performance measures*		
Disease condition	non-significant	significant	Sensitivity	Specificity	False alarm rate
no significant	**97.5**	2.5	0.975	0.925	0.075
significant	7.5	**92.5**	0.925	0.975	0.025
Average	95		n/a		

Table 5.10: Best achieved classification result for data set A2 without the SBI for the smallest ANN.

	Classification (%)		*Performance measures*		
Disease condition	non-significant	significant	Sensitivity	Specificity	False alarm rate
no significant	**92.5**	7.5	0.925	0.925	0.075
significant	7.5	**92.5**	0.925	0.925	0.075
Average	92.5		n/a		

Table 5.11: Best achieved classification result for data set A2 with the SBI for the smallest ANN.

The next data set, A3, reduced the input vector to 60 points by taking every second sample. The performance decreased to 93.75% when no SBI was used, but increased to 95% when the SBI was included in the input vector. The ANN had in both cases 10 neurons in the hidden layer. Tables 5.12 and 5.13 show the performance for this data set. The tables are repeated here for convenience.

	Classification (%)		*Performance measures*		
Disease condition	non-significant	significant	Sensitivity	Specificity	False alarm rate
no significant	**97.5**	2.5	0.975	0.900	0.100
significant	10	**90**	0.900	0.975	0.025
Average	93.75		n/a		

Table 5.12: Best achieved classification result for data set A3 without the SBI for the smallest ANN.

	Classification (%)		*Performance measures*		
Disease condition	non-significant	significant	Sensitivity	Specificity	False alarm rate
no significant	**97.5**	2.5	0.975	0.925	0.075
significant	7.5	**92.5**	0.925	0.975	0.025
Average	95		n/a		

Table 5.13: Best achieved classification result for data set A3 with the SBI for the smallest ANN.

The third data set, A4, truncated the input vector from data set A3 further to include only 50 points. Without the SBI an ANN with 10 neurons in the hidden layer achieved a classification rate of 93.75%. Including the SBI increased the classification rate to 96.25% using an ANN with 10 neurons in its hidden layer. The results are shown in tables 5.14 and 5.15.

	Classification (%)		*Performance measures*		
Disease condition	non-significant	significant	Sensitivity	Specificity	False alarm rate
no significant	**95**	5	0.950	0.925	0.075
significant	7.5	**92.5**	0.925	0.950	0.005
Average	93.75		n/a		

Table 5.14: Best achieved classification result for data set A4 without the SBI for the smallest ANN.

Data set A5 is similar to data set A2 in the way that it simply truncated the cardiac cycle MFE. The difference with data set A2 was that data set A5 only used

	Classification (%)		*Performance measures*		
Disease condition	non-significant	significant	Sensitivity	Specificity	False alarm rate
no significant	**97.5**	2.5	0.975	0.950	0.050
significant	5	**95**	0.950	0.975	0.025
Average	96.25		n/a		

Table 5.15: Best achieved classification result for data set A4 with the SBI for the smallest ANN.

the first 80 points of the cardiac cycle MFE as an input vector. The classification rate for this data set without the SBI decreased further to 92.5%, which was the lowest rate of all four data sets. This performance was achieved with an ANN that had 10 neurons in its hidden layer. Including the SBI increased the classification rate to 95% with an ANN that had 5 neurons in the first and 30 neurons in the second hidden layer. Tables 5.16 and 5.17 show the performance for data set A5.

	Classification (%)		*Performance measures*		
Disease condition	non-significant	significant	Sensitivity	Specificity	False alarm rate
no significant	**92.5**	7.5	0.925	0.925	0.075
significant	7.5	**92.5**	0.925	0.925	0.075
Average	92.5		n/a		

Table 5.16: Best achieved classification result for data set A5 without the SBI for the smallest ANN.

	Classification (%)		*Performance measures*		
Disease condition	non-significant	significant	Sensitivity	Specificity	False alarm rate
no significant	**95**	5	0.950	0.950	0.050
significant	5	**95**	0.950	0.950	0.050
Average	95		n/a		

Table 5.17: Best achieved classification result for data set A5 with the SBI for the smallest ANN.

Data set A6 was included in this investigation for comparison reasons and the tables are repeated here for convenience (tables 5.18 and 5.19). The classification rate without and with the SBI was 92.5%, which was equal to or worse than the classification of the truncated cardiac cycle MFEs.

	Classification (%)		*Performance measures*		
Disease condition	non-significant	significant	Sensitivity	Specificity	False alarm rate
no significant	**95**	5	0.950	0.900	0.100
significant	10	**90**	0.900	0.950	0.050
Average	92.5		n/a		

Table 5.18: Best achieved classification result for data set A6 without the SBI for the smallest ANN.

	Classification (%)		*Performance measures*		
Disease condition	non-significant	significant	Sensitivity	Specificity	False alarm rate
no significant	**95**	5	0.950	0.900	0.100
significant	10	**90**	0.900	0.950	0.050
Average	92.5		n/a		

Table 5.19: Best achieved classification result for data set A6 with the SBI for the smallest ANN.

The investigation showed that the use of the entire cardiac cycle MFE did not give the best performance. In fact, the best classification rate was achieved with the shortest input vector (50 points) when used with the SBI (96.25%). The use of the SBI improved the classification rate of most data sets.

5.5.3 Investigation into the impact of wavelet compression

This investigation examined the performance of the newly proposed method of reducing the feature vector length of the cardiac cycle MFE. Six data sets were used in this investigation.

The first data set, A7, compressed the cardiac cycle MFE to 47 points using a bi-orthogonal 3.1 wavelet at level 2 with 10 retained detail coefficients. The classification rate without the use of the SBI was 91.25% and increased to 92.5% when the SBI was included. Without the SBI an ANN with 10 neurons in the first and 5 neurons in the second hidden layer performed best. When the SBI was included the best performing ANN had a first hidden layer with 10 neurons and a second hidden layer with 20 neurons. Tables 5.20 and 5.21 show the performance for data set A7.

	Classification (%)		*Performance measures*		
Disease condition	non-significant	significant	Sensitivity	Specificity	False alarm rate
no significant	**92.5**	7.5	0.925	0.900	0.100
significant	10	**90**	0.900	0.925	0.075
Average	91.25		n/a		

Table 5.20: Best achieved classification result for data set A7 without the SBI for the smallest ANN.

	Classification (%)		*Performance measures*		
Disease condition	non-significant	significant	Sensitivity	Specificity	False alarm rate
no significant	**95**	5	0.950	0.900	0.100
significant	10	**90**	0.900	0.950	0.050
Average	92.5		n/a		

Table 5.21: Best achieved classification result for data set A7 with the SBI for the smallest ANN.

The next data set, A8, reduced the length of the input vector to 37 points by retaining only 5 detail coefficients. The performance improved slightly and the classification rate was 92.5% without and 93.75% with the SBI. The first ANN had 10 neurons in the hidden layer, whilst the second ANN had 30 neurons in the first and 20 in the second hidden layer. The results are shown in tables 5.22 and 5.23.

	Classification (%)		*Performance measures*		
Disease condition	non-significant	significant	Sensitivity	Specificity	False alarm rate
no significant	**95**	5	0.950	0.900	0.100
significant	10	**90**	0.900	0.950	0.050
Average	92.5		n/a		

Table 5.22: Best achieved classification result for data set A8 without the SBI for the smallest ANN.

	Classification (%)		*Performance measures*		
Disease condition	non-significant	significant	Sensitivity	Specificity	False alarm rate
no significant	**97.5**	2.5	0.975	0.900	0.100
significant	10	**90**	0.900	0.975	0.025
Average	93.75		n/a		

Table 5.23: Best achieved classification result for data set A8 with the SBI for the smallest ANN.

The wavelet decomposition of data set A9 was increased to level 3, giving a shorter approximation coefficient length. After retaining 15 detail coefficients the ANN input vector had a total length of 45 points. The classification rate decreased when compared with data sets A7 and A8. Without the SBI the ANN achieved 90% and with the SBI 91.75% classification. The first ANN had only 5 neurons in its hidden layer, whilst the second ANN used 40 neurons in the first and second hidden layer. The performance results are shown in tables 5.24 and 5.25.

	Classification (%)		*Performance measures*		
Disease condition	non-significant	significant	Sensitivity	Specificity	False alarm rate
no significant	**90**	10	0.900	0.900	0.100
significant	10	**90**	0.900	0.900	0.100
Average	90		n/a		

Table 5.24: Best achieved classification result for data set A9 without the SBI for the smallest ANN.

	Classification (%)		*Performance measures*		
Disease condition	non-significant	significant	Sensitivity	Specificity	False alarm rate
no significant	**92.5**	7.5	0.925	0.900	0.100
significant	10	**90**	0.900	0.925	0.075
Average	91.75		n/a		

Table 5.25: Best achieved classification result for data set A9 with the SBI for the smallest ANN.

Reducing the number of retained detail coefficients to 10, data set A10, improved the classification rate for the ANN when the SBI was included. The performance was 90% without and 92.5% with the SBI. The network structure for the ANN was a single hidden layer with 5 neurons and a two hidden layer structure with 20 neurons in the first and 30 neurons in the second hidden layer, respectively. Tables 5.26 and 5.27 show the result.

	Classification (%)		*Performance measures*		
Disease condition	non-significant	significant	Sensitivity	Specificity	False alarm rate
no significant	**90**	10	0.900	0.900	0.100
significant	10	**90**	0.900	0.900	0.100
Average	90		n/a		

Table 5.26: Best achieved classification result for data set A10 without the SBI for the smallest ANN.

	Classification (%)		*Performance measures*		
Disease condition	non-significant	significant	Sensitivity	Specificity	False alarm rate
no significant	**95**	5	0.950	0.900	0.100
significant	10	**90**	0.900	0.950	0.050
Average	92.5		n/a		

Table 5.27: Best achieved classification result for data set A10 with the SBI for the smallest ANN.

Data set A11 reduced the input vector length further by only retaining 5 detail coefficients, therefore, creating a 25 point input vector. The classification rate without and with the SBI was 92.5%. The ANN had 10 neurons in the first and 5 neurons in the second hidden layer to achieve this performance without the use of the SBI. When the SBI was included the ANN structure had 10 neurons in the single hidden layer. The result of data set A11 is shown in tables 5.28 and 5.29.

	Classification (%)		*Performance measures*		
Disease condition	non-significant	significant	Sensitivity	Specificity	False alarm rate
no significant	**95**	5	0.950	0.900	0.100
significant	10	**90**	0.900	0.950	0.050
Average	92.5		n/a		

Table 5.28: Best achieved classification result for data set A11 without the SBI for the smallest ANN.

	Classification (%)		*Performance measures*		
Disease condition	non-significant	significant	Sensitivity	Specificity	False alarm rate
no significant	**95**	5	0.950	0.900	0.100
significant	10	**90**	0.900	0.950	0.050
Average	92.5		n/a		

Table 5.29: Best achieved classification result for data set A11 with the SBI for the smallest ANN.

The last data set in this investigtion used a bi-orthogonal 2.2 wavelet at level 3 without any detail coefficients. The ANN input vector had a length of 16 points only. The classification rate improved to 96.25% without the SBI and 95% with the SBI. The ANN for the data set without the SBI had 20 neurons in the first and 5 neurons in the second hidden layer. This changed to 20 neurons in the first and 30 neurons in the second hidden layer when the SBI was included. Tables 5.30 and 5.31 show the result.

	Classification (%)		*Performance measures*		
Disease condition	non-significant	significant	Sensitivity	Specificity	False alarm rate
no significant	**100**	7.5	1.0	0.925	0.075
significant	0	**92.5**	0.925	1.0	0
Average	96.25		n/a		

Table 5.30: Best achieved classification result for data set A12 without the SBI for the smallest ANN.

	Classification (%)		*Performance measures*		
Disease condition	non-significant	significant	Sensitivity	Specificity	False alarm rate
no significant	**100**	10	1.0	0.900	0.100
significant	0	**90**	0.900	1.0	0
Average	95		n/a		

Table 5.31: Best achieved classification result for data set A12 with the SBI for the smallest ANN.

The investigation showed that the ANN that used data set A12 performed the best amongst all six data sets. It is also the data set with the shortest ANN input vector.

5.6 Classification of proximal disease: The three-class problem

This section presents the results of the ANN performance in solving the three-class problem. The three-class problem involved the separation of the input signals into three classes. These were, no significant proximal disease, significant proximal disease and proximal occlusion. All of the data sets described in section 5.4 were applied to the network structures presented in section 5.2. Three output neurons, one for each class, were used for all ANNs. All ANNs were trained as described in

section 5.5.

The same procedure as in section 5.5 was used to select the best performing ANN. Graphs that show the percentage correct for each network structure are included in appendix C.1 and tables with detailed information of the best performing ANN are included in appendix C.2. The results were split into the same groups as introduced in section 5.4.

5.6.1 Investigation into the impact of noise reduction algorithms

The investigation into noise reduction algorithms for the two-class problem showed improvements in the classification rate when the wavelet denoising algorithm was applied. In this investigation the same four data sets were used to investigate the effect on the three-class problem.

First, data sets A0 and A3 were compared. Both data sets used a 60-point cardiac cycle MFE as the ANN input vector. The best performance for data set A0, which used a manually selected threshold for noise reduction, without the SBI was achieved by an ANN with 10 neurons in the first and 5 neurons in the second hidden layer. This ANN classified 72.5% of all signals correctly. Including the SBI into the input vector improved the classification rate to 77.5% using an ANN with 20 neurons in the first and 5 neurons in the second hidden layer. Both results are detailed in tables 5.32 and 5.33.

Exchanging the method of manually selecting the threshold for the automated wavelet denoising algorithm, data set A3, improved the classification result without and with the SBI by 10% and 3.75%, respectively. The classification rate was therefore, 82.5% and 81.25%, respectively. The structure of the ANN changed to 5 neur-

	Classification (%)			*Performance measures*		
Disease condition	non-significant	sig-nificant	occ-lusion	Sen-sitivity	Spe-cificity	False alarm rate
no significant	**92.5**	5	2.5	0.925	0.900	0.100
significant	20	**35**	45	0.350	0.867	0.133
occlusion	0	30	**70**	0.700	0.833	0.167
Average	72.5			n/a		

Table 5.32: Best achieved classification result for data set A0 without the SBI for the smallest ANN.

ons in the first and 30 neurons in the second hidden layer for the case without the SBI. When the SBI was included, the ANN had one hidden layer with 20 neurons. Tables 5.34 and 5.35 present these results.

	Classification (%)			*Performance measures*		
Disease condition	non-significant	sig-nificant	occ-lusion	Sen-sitivity	Spe-cificity	False alarm rate
no significant	**90**	5	15	0.900	0.850	0.150
significant	25	**45**	30	0.450	0.950	0.05
occlusion	5	10	**85**	0.850	0.850	0.150
Average	77.5			n/a		

Table 5.33: Best achieved classification result for data set A0 with the SBI for the smallest ANN.

Using the SBI as an additional feature had a positive effect only with data set A0. Data set A3, which showed a considerable improvement over data set A0, did not indicate an improvement in classification rate when the SBI was included.

The second pair of data sets that were used to investigate the effect of the noise reduction algorithms on the classification rate of the ANN were A1 and A6. Both data sets used the entire cardic cycle MFE, which was re-sampled to 100 points. Data set A1, which used the manually selected threshold, achieved a classification rate of 76.25% using an ANN with 20 neurons in the first and 30 neurons in the second hidden layer. This classification rate improved to 81.25% when the SBI was

	Classification (%)			*Performance measures*		
Disease condition	non-significant	sig-nificant	occ-lusion	Sen-sitivity	Spe-cificity	False alarm rate
no significant	**97.5**	2.5	0	0.975	0.900	0.100
significant	15	**60**	25	0.600	0.917	0.083
occlusion	5	20	**75**	0.750	0.917	0.083
Average	82.5			n/a		

Table 5.34: Best achieved classification result for data set A3 without the SBI for the smallest ANN.

included in the input vector of the ANN. The ANN that achieved this performance had two hidden layers with 40 neurons each. The classification matrices are shown in tables 5.36 and 5.37.

	Classification (%)			*Performance measures*		
Disease condition	non-significant	sig-nificant	occ-lusion	Sen-sitivity	Spe-cificity	False alarm rate
no significant	**95**	5	0	0.950	0.950	0.050
significant	10	**60**	30	0.600	0.883	0.117
occlusion	0	25	**75**	0.750	0.900	0.100
Average	81.25			n/a		

Table 5.35: Best achieved classification result for data set A3 with the SBI for the smallest ANN.

The performance of the ANN improved by 1.25% when the manual selection of the threshold was replaced by the automated wavelet denoising algorithm. Data set A6 achieved a classification rate of 77.5% using a two hidden layer ANN with 10 neurons in the first and 40 neurons in the second hidden layer when the SBI was not used. The two hidden layer ANN with 5 neurons in each hidden layer achieved the best classification rate of 82.5% with the use of the SBI. Results are shown in tables 5.38 and 5.39.

The investigation showed that using the wavelet denoising algorithm as a replacement of the manual thresholding for noise reduction did not only allow automation

	Classification (%)			*Performance measures*		
Disease condition	non-significant	sig-nificant	occ-lusion	Sen-sitivity	Spe-cificity	False alarm rate
no significant	**87.5**	7.5	5	0.875	0.875	0.125
significant	25	**60**	15	0.6050	0.850	0.150
occlusion	0	30	**70**	0.700	0.917	0.083
Average	76.25			n/a		

Table 5.36: Best achieved classification result for data set A1 without the SBI for the smallest ANN.

	Classification (%)			*Performance measures*		
Disease condition	non-significant	sig-nificant	occ-lusion	Sen-sitivity	Spe-cificity	False alarm rate
no significant	**87.5**	7.5	5	0.875	0.850	0.150
significant	30	**50**	20	0.500	0.950	0.050
occlusion	0	0	**100**	1	0.900	0.100
Average	81.25			n/a		

Table 5.37: Best achieved classification result for data set A1 with the SBI for the smallest ANN.

	Classification (%)			*Performance measures*		
Disease condition	non-significant	sig-nificant	occ-lusion	Sen-sitivity	Spe-cificity	False alarm rate
no significant	**90**	7.5	2.5	0.900	0.900	0.100
significant	20	**55**	25	0.550	0.867	0.133
occlusion	0	25	**75**	0.750	0.900	0.100
Average	77.5			n/a		

Table 5.38: Best achieved classification result for data set A6 without the SBI for the smallest ANN.

	Classification (%)			*Performance measures*		
Disease condition	non-significant	sig-nificant	occ-lusion	Sen-sitivity	Spe-cificity	False alarm rate
no significant	**87.5**	10	2.5	0.875	0.900	0.100
significant	20	**60**	20	0.600	0.917	0.083
occlusion	0	5	**95**	0.950	0.917	0.083
Average	82.5			n/a		

Table 5.39: Best achieved classification result for data set A6 with the SBI for the smallest ANN.

of the process but also improved performance.

5.6.2 Investigation into the impact of MFE vector length reduction

The same investigation as described in section 5.5 was conducted here to compare the performance of ANNs with feature vectors of different lengths for the three-class problem.

The performance of the ANNs using the input vector of data set A2 without and with the SBI was 83.75%. This was achieved by an ANN with 5 hidden neurons when the SBI was not used and by an ANN with 5 neurons in the first and 30 neurons in the second hidden layer when the SBI was used. Tables 5.40 and 5.41 show the results in detail.

The second data set, A3, reduced the input vector to 60 points by taking every second sample from data set A2. Tables 5.42 and 5.43 show that the classification rate decreased in both cases. Without the use of the SBI an ANN with 5 neurons in the first and 30 neurons in the second hidden layer achieved a classification rate of 82.5%. By including the SBI into the input vector an ANN with 20 neurons in its hidden layer achieved a classification rate of 81.25%.

	Classification (%)			*Performance measures*		
Disease condition	non-significant	sig-nificant	occ-lusion	Sen-sitivity	Spe-cificity	False alarm rate
no significant	**90**	7.5	2.5	0.900	0.925	0.075
significant	15	**60**	25	0.600	0.933	0.067
occlusion	0	5	**95**	0.950	0.900	0.100
Average	83.75			n/a		

Table 5.40: Best achieved classification result for data set A2 without the SBI for the smallest ANN.

	Classification (%)			*Performance measures*		
Disease condition	non-significant	sig-nificant	occ-lusion	Sen-sitivity	Spe-cificity	False alarm rate
no significant	**95**	5	0	0.975	0.900	0.100
significant	10	**70**	20	0.700	0.917	0.083
occlusion	10	20	**70**	0.700	0.933	0.067
Average	83.75			n/a		

Table 5.41: Best achieved classification result for data set A2 with the SBI for the smallest ANN.

	Classification (%)			*Performance measures*		
Disease condition	non-significant	sig-nificant	occ-lusion	Sen-sitivity	Spe-cificity	False alarm rate
no significant	**97.5**	2.5	0	0.975	0.900	0.100
significant	15	**60**	25	0.600	0.917	0.083
occlusion	5	20	**75**	0.750	0.917	0.083
Average	82.5			n/a		

Table 5.42: Best achieved classification result for data set A3 without the SBI for the smallest ANN.

	Classification (%)			*Performance measures*		
Disease condition	non-significant	sig-nificant	occ-lusion	Sen-sitivity	Spe-cificity	False alarm rate
no significant	**95**	5	0	0.950	0.950	0.050
significant	10	**60**	30	0.600	0.883	0.117
occlusion	0	25	**75**	0.750	0.900	0.100
Average	81.25			n/a		

Table 5.43: Best achieved classification result for data set A3 with the SBI for the smallest ANN.

The third data set, A4, in this investigation was created by reducing the length of data set A3 further by truncating it to 50 points only. An ANN with 40 neurons in the hidden layer and without the use of the SBI achieved a classification rate of 82.5%. This performance increased by 1.25% to 83.75% when the SBI was included. The ANN achieving this performance had 5 neurons in the first and 10 neurons in the second hidden layer. Overall the performance decreased when compared to data set A3. The results are shown in tables 5.44 and 5.45.

	Classification (%)			*Performance measures*		
Disease condition	non-significant	sig-nificant	occ-lusion	Sen-sitivity	Spe-cificity	False alarm rate
no significant	**95**	2.5	2.5	0.950	0.925	0.075
significant	15	**55**	30	0.550	0.933	0.067
occlusion	0	15	**85**	0.850	0.883	0.117
Average	82.5			n/a		

Table 5.44: Best achieved classification result for data set A4 without the SBI for the smallest ANN.

Data set A5 truncated the cardiac cycle MFE to 80 points. The classification rate for this data set improved by 1.25% to 83.75% without the SBI when compared to data set A4. This was achieved with an ANN that had a single 5 neuron hidden layer. The performance improved by 2.5% to 86.25% when the SBI was included. The ANN achieving this had 30 neurons in the first and 5 neurons in the second

	Classification (%)			*Performance measures*		
Disease condition	non-significant	sig-nificant	occ-lusion	Sen-sitivity	Spe-cificity	False alarm rate
no significant	**95**	5	0	0.950	1.0	0.0
significant	0	**75**	25	0.750	0.867	0.133
occlusion	0	30	**70**	0.700	0.917	0.083
Average	83.75			n/a		

Table 5.45: Best achieved classification result for data set A4 with the SBI for the smallest ANN.

layer. The classification matrices are shown in tables 5.46 and 5.47.

	Classification (%)			*Performance measures*		
Disease condition	non-significant	sig-nificant	occ-lusion	Sen-sitivity	Spe-cificity	False alarm rate
no significant	**92.5**	5	2.5	0.925	0.925	0.075
significant	15	**60**	25	0.600	0.933	0.067
occlusion	0	10	**90**	0.900	0.900	0.100
Average	83.75			n/a		

Table 5.46: Best achieved classification result for data set A5 without the SBI for the smallest ANN.

The results from data set A6, which used the entire cardiac cycle MFE, is repeated here for comparison. Tables 5.48 and 5.49 show that this data set had the lowest classification rate (77.5%) of this investigation when used without the SBI. This only improved marginally when the SBI was included. The data set achieved 82.5% classification, which ranked amongst the lower classification rates in this investigation.

The results of this investigation reaffirmed those from the investigation conducted with the two-class problem. It showed that the best performance is not achieved with the entire cardiac cycle MFE, but with data set A5 when used with the SBI. Data set A5 used an 80-point long input vector by truncating the cardiac cycle MFE to that length. The use of the SBI improved the performance of the ANN in all

	Classification (%)			*Performance measures*		
Disease condition	non-significant	sig-nificant	occ-lusion	Sen-sitivity	Spe-cificity	False alarm rate
no significant	**92.5**	7.5	0	0.975	0.950	0.050
significant	10	**70**	20	0.700	0.883	0.117
occlusion	10	0	**90**	0.700	0.933	0.067
Average	86.25			n/a		

Table 5.47: Best achieved classification result for data set A5 with the SBI for the smallest ANN.

	Classification (%)			*Performance measures*		
Disease condition	non-significant	sig-nificant	occ-lusion	Sen-sitivity	Spe-cificity	False alarm rate
no significant	**90**	7.5	2.5	0.900	0.900	0.100
significant	20	**55**	25	0.550	0.867	0.133
occlusion	0	25	**75**	0.750	0.900	0.100
Average	77.5			n/a		

Table 5.48: Best achieved classification result for data set A6 without the SBI for the smallest ANN.

	Classification (%)			*Performance measures*		
Disease condition	non-significant	sig-nificant	occ-lusion	Sen-sitivity	Spe-cificity	False alarm rate
no significant	**87.5**	10	2.5	0.875	0.900	0.100
significant	20	**60**	20	0.600	0.917	0.083
occlusion	0	5	**95**	0.950	0.917	0.083
Average	82.5			n/a		

Table 5.49: Best achieved classification result for data set A6 with the SBI for the smallest ANN.

but two cases. In one case it did not show any change and in the other case the performance decreased marginally.

5.6.3 Investigation into the impact of wavelet compression

The investigation into ANNs using wavelet compressed feature vectors conducted for the two-class problem in section 5.5 was repeated here for the three-class problem.

The classification rate of data set A7 without the SBI was 77.5%. The ANN had two hidden layers with 30 neurons in the first and 20 neurons in the second hidden layer. Including the SBI into the input vector improved the classification rate to 81.25% using an ANN with 10 neurons in its hidden layer. The classification matrices are shown in tables 5.50 and 5.51.

	Classification (%)			*Performance measures*		
Disease condition	non-significant	sig-nificant	occ-lusion	Sen-sitivity	Spe-cificity	False alarm rate
no significant	**90**	5	5	0.900	0.825	0.175
significant	30	**35**	35	0.350	0.967	0.033
occlusion	5	0	**95**	0.950	0.850	0.150
Average	77.5			n/a		

Table 5.50: Best achieved classification result for data set A7 without the SBI for the smallest ANN.

	Classification (%)			*Performance measures*		
Disease condition	non-significant	sig-nificant	occ-lusion	Sen-sitivity	Spe-cificity	False alarm rate
no significant	**82.5**	12.5	5	0.825	0.925	0.075
significant	15	**65**	20	0.650	0.900	0.100
occlusion	0	5	**95**	0.950	0.900	0.100
Average	81.25			n/a		

Table 5.51: Best achieved classification result for data set A7 with the SBI for the smallest ANN.

The performance for both cases improved with data set A8. Without the SBI 80% of the signals were correctly classified. This increased to 82.5% when the SBI was included. The ANNs used to achieve these performances had 10 neurons in its hidden layer when used without the SBI and 20 neurons in its hidden layer when used with SBI. Tables 5.52 and 5.53 shows the results.

	Classification (%)			*Performance measures*		
Disease condition	non-significant	sig-nificant	occ-lusion	Sen-sitivity	Spe-cificity	False alarm rate
no significant	**92.5**	15	0	0.925	0.875	0.125
significant	20	**65**	15	0.650	0.867	0.133
occlusion	5	25	**70**	0.700	0.950	0.050
Average	80			n/a		

Table 5.52: Best achieved classification result for data set A8 without the SBI for the smallest ANN.

	Classification (%)			*Performance measures*		
Disease condition	non-significant	sig-nificant	occ-lusion	Sen-sitivity	Spe-cificity	False alarm rate
no significant	**87.5**	7.5	5	0.850	0.900	0.100
significant	20	**60**	20	0.600	0.917	0.083
occlusion	0	5	**95**	0.950	0.900	0.100
Average	82.5			n/a		

Table 5.53: Best achieved classification result for data set A8 with the SBI for the smallest ANN.

The classification rate for data set A9 increased in both cases by 2.5%. Without the SBI an ANN with 30 neurons in the first and 5 neurons in the second layer achieved a classification rate of 82.5%. Including the SBI improved the classification rate to 85% using a two hidden layer ANN with 20 neurons in the first and 10 neurons in the second hidden layer. Details are shown in tables 5.54 and 5.55.

Reducing the number of retained detail coefficients to 10, data set A10, decreased the classification rate by 7.5% and 5% compared with data set A9. The classification

rate without the use of the SBI was 75% using an ANN with 20 neurons in the first and 30 neurons in the second hidden layer. The classification rate improved to 80% when the SBI was included. This was achieved with an ANN that had 10 neurons in the first and 40 neurons in the second hidden layer. Tables 5.56 and 5.57 show the result of this data set.

	Classification (%)			*Performance measures*		
Disease condition	non-significant	sig-nificant	occ-lusion	Sen-sitivity	Spe-cificity	False alarm rate
no significant	**87.5**	7.5	5	0.875	0.925	0.075
significant	15	**75**	10	0.750	0.883	0.117
occlusion	0	20	**80**	0.800	0.933	0.067
Average	82.5			n/a		

Table 5.54: Best achieved classification result for data set A9 without the SBI for the smallest ANN.

	Classification (%)			*Performance measures*		
Disease condition	non-significant	sig-nificant	occ-lusion	Sen-sitivity	Spe-cificity	False alarm rate
no significant	**92.5**	5	2.5	0.925	0.900	0.100
significant	20	**65**	15	0.650	0.933	0.067
occlusion	0	10	**90**	0.900	0.933	0.067
Average	85			n/a		

Table 5.55: Best achieved classification result for data set A9 with the SBI for the smallest ANN.

Without the SBI, data set A11 achieved a better classification rate than data set A10. The classification rate of 78.75% was achieved using an ANN with 5 neurons in its hidden layer. This improved to 80% when the SBI was used. The ANN achieving this performance had 10 neurons in the first and 20 neurons in the second layer. The classification matrices are shown in tables 5.58 and 5.59.

The performance of the ANN using data set A12 without the SBI was the second lowest in this investigation. The ANN had 10 neurons in the first and 30 neurons in

	Classification (%)			*Performance measures*		
Disease condition	non-significant	sig-nificant	occ-lusion	Sen-sitivity	Spe-cificity	False alarm rate
no significant	**87.5**	10	2.5	0.875	0.900	0.100
significant	20	**55**	25	0.550	0.833	0.167
occlusion	0	30	**70**	0.700	0.900	0.100
Average	75			n/a		

Table 5.56: Best achieved classification result for data set A10 without the SBI for the smallest ANN.

	Classification (%)			*Performance measures*		
Disease condition	non-significant	sig-nificant	occ-lusion	Sen-sitivity	Spe-cificity	False alarm rate
no significant	**82.5**	12.5	5	0.825	0.875	0.125
significant	20	**60**	20	0.600	0.917	0.083
occlusion	5	0	**95**	0.950	0.900	0.100
Average	80			n/a		

Table 5.57: Best achieved classification result for data set A10 with the SBI for the smallest ANN.

	Classification (%)			*Performance measures*		
Disease condition	non-significant	sig-nificant	occ-lusion	Sen-sitivity	Spe-cificity	False alarm rate
no significant	**80**	12.5	7.5	0.800	0.925	0.075
significant	15	**60**	15	0.700	0.867	0.133
occlusion	0	15	**85**	0.850	0.900	0.100
Average	78.75			n/a		

Table 5.58: Best achieved classification result for data set A11 without the SBI for the smallest ANN.

	Classification (%)			*Performance measures*		
Disease condition	non-significant	sig-nificant	occ-lusion	Sen-sitivity	Spe-cificity	False alarm rate
no significant	**82.5**	10	7.5	0.825	0.900	0.100
significant	15	**65**	20	0.650	0.917	0.083
occlusion	5	5	**90**	0.900	0.883	0.117
Average	80			n/a		

Table 5.59: Best achieved classification result for data set A11 with the SBI for the smallest ANN.

the second hidden layer and achieved a classification rate of 76.25%. This improved by 7.5% to 83.75% when the SBI was included in the input vector. The ANN had two hidden layers with 5 neurons in each hidden layer. The results are shown in tables 5.60 and 5.61.

	Classification (%)			*Performance measures*		
Disease condition	non-significant	sig-nificant	occ-lusion	Sen-sitivity	Spe-cificity	False alarm rate
no significant	**82.5**	10	7.5	0.825	0.900	0.100
significant	15	**60**	25	0.600	0.883	0.117
occlusion	5	15	**80**	0.800	0.867	0.133
Average	76.25			n/a		

Table 5.60: Best achieved classification result for data set A12 without the SBI for the smallest ANN.

This investigation showed that the proposed method of compressing the feature vector using the Wavelet Transform (WT) delivered a good performance. The best performing data set used a bi-orthogonal 3.1 wavelet at level 3 with 15 detail coefficients retained (data set A9).

	Classification (%)			*Performance measures*		
Disease condition	non-significant	sig-nificant	occ-lusion	Sen-sitivity	Spe-cificity	False alarm rate
no significant	**92.5**	5	2.5	0.925	0.900	0.100
significant	15	**55**	30	0.550	0.967	0.033
occlusion	5	0	**95**	0.950	0.883	0.117
Average	83.75			n/a		

Table 5.61: Best achieved classification result for data set A12 with the SBI for the smallest ANN.

5.7 Summary

This chapter has presented the classification approach that was used to identify the severity of the vascular disease from the Doppler ultrasound blood flow signals. It focused on both the classification approach itself and the data sets used for classification.

Different classification methods were presented and the reasons for selecting the ANN approach were described. Furthermore, this chapter presented the key issues associated with the design of ANNs. Performance metrics were introduced to measure the success of each ANN in classifying the Doppler ultrasound blood flow signals correctly.

The pre-processing methods, which were proposed and investigated in chapters 3 and 4, were combined with different approaches. Each of these approaches led to a data set that was used as a collection of input vectors for the ANNs. All data sets were detailed in this chapter. A number of different ANNs were used to determine the optimal structure for a particular data set.

The ability to classify the Doppler ultrasound blood flow signals was investigated using two problems: the two-class and the three-class problems. The key findings of this chapter can be summarised as follows:

1. The introduction of the wavelet denoising algorithm in the noise reduction stage did not only automate this stage but also improved the classification performance.

2. In general, data sets with truncated cardiac cycle MFE performed better than data sets with the entire cardiac cycle MFE. Only when data set A3, which used a truncated cardiac cycle MFE, was combined with the SBI in the three-class problem the performance worsened relative to the entire cardiac cycle MFE (data set A6) with the SBI.

3. Compressing the ANN input vector using the WT gave good results. In the two-class problem these data sets delivered the best performing ANN, together with a data set that used truncation. For the three-class problem the wavelet compressed data sets delivered the third best result.

4. The introduction of the SBI into the ANN input vector did improve the performance in a majority of the cases. In the two-class problem only three out of 13 data sets decreased their performance when the SBI was introduced. The three-class problem performance was generally better with the SBI than without. Only one data set performed worse when the SBI was included.

5. The size and structure of the best performing ANNs was independent from the length of the ANN input vector. The introduction of the SBI seemed to have resulted into more complex ANN structures in general. The best performing ANNs in the two-class problem without the SBI had a low number of hidden layer neurons. The ANNs for the three-class problem generally required larger hidden layers.

Table 5.62 shows a summary of the results for all data sets in both problems

with and without the SBI. The classification rate of the best performing ANN is shown in the table for each data set, with the best results for each data set shown in bold. The size and the structure of the best performing ANNs for each data set is given in table 5.63.

Data set	Vector length	*Classification (%)*			
		Two-class problem		Three-class problem	
		no SBI	SBI	no SBI	SBI
A0	60	**92.5**	91.25	72.5	**77.5**
A1	100	**88.75**	**88.75**	76.25	**81.25**
A2	120	**95**	92.5	**83.75**	**83.75**
A3	60	93.75	**95**	**82.5**	81.25
A4	50	93.75	**96.25**	82.5	**83.75**
A5	80	92.5	**95**	83.75	**86.25**
A6	100	**92.5**	**92.5**	77.5	**82.5**
A7	47	91.25	**92.5**	77.5	**81.25**
A8	37	92.5	**93.75**	80	**82.5**
A9	45	90	**91.75**	82.5	**85**
A10	35	90	**92.5**	75	**80**
A11	25	**92.5**	**92.5**	78.75	**80**
A12	16	**96.25**	95	76.25	**83.75**

Table 5.62: Best classification result for data sets A0 to A12. The value in bold face shows the best value for the data set. The length of the data set is given without the SBI appended.

Data set	Vector length	*ANN size and structure*			
		Two-class problem		Three-class problem	
		no SBI	SBI	no SBI	SBI
A0	60	20	20	10-5	20-5
A1	100	10-10	5-20	20-30	40-40
A2	120	5-10	5	5	5-30
A3	60	10	10	5-30	20
A4	50	10	10	40	5-10
A5	80	10	5-30	5	30-5
A6	100	10	5-5	10-40	5-5
A7	47	10-5	10-20	30-20	10
A8	37	10	30-20	10	10-20
A9	45	5	40-40	30-5	20-10
A10	35	5	20-30	20-30	10-40
A11	25	10-5	10	5	10-20
A12	16	20-5	20-30	10-30	5-5

Table 5.63: Size and structure of the best performing ANNs for data sets A0 to A12. The length of the data set is given without the SBI appended.

Chapter 6

Discussion

The aim of this study was to investigate techniques for the automated classification and diagnosis of Doppler ultrasound blood flow signals. To achieve this aim, previous research work was reviewed and a signal processing and analysis strategy was proposed. Doppler ultrasound blood flow signals recorded from the common femoral artery (CFA) were selected to provide the data sets for this investigation. Algorithms at each stage of the proposed strategy were identified and investigated. New approaches to improve and automate the Doppler ultrasound blood flow classification and diagnosis were developed and compared with existing methods. The processing and analysis methods used in this study provided improved results in the classification and diagnosis of Doppler ultrasound blood flow signals when compared with previous work.

This chapter discusses the results of the investigations conducted during this study. Section 6.1 discusses the importance of signal pre-processing and the results of the investigations into signal transformation and noise reduction algorithms. Feature extraction and data reduction are discussed in section 6.2. This includes the results of the comparative investigation into existing and newly developed algorithms. The

classification and decision making stage is covered in section 6.3 together with the results of the overall investigation.

6.1 Signal transformation and noise reduction

This section presents the discussion of the investigations into signal transformation and noise reduction, which were described in chapter 3.

6.1.1 Signal transformation

The transformation of the Doppler ultrasound blood flow signal into the time-frequency domain is a very important step in the analysis of these signals. It forms the basis for further processing and therefore, influences the classification results and clinical diagnoses. In order to achieve a good classification result, the signal transformation algorithm should represent the Doppler signal as accurately as possible in the time-frequency domain. But not only the accuracy of the signal representation is important. Other factors to consider are the signal-to-noise ratio (SNR) in the time-frequency domain and computational complexity. A high SNR will improve the performance of the following processing stages, whilst a low computational complexity allows the implementation of the algorithm into lower cost equipment, therefore enabling their acceptance in the primary healthcare market.

An investigation into available signal transformation algorithms, which are suitable for Doppler ultrasound blood flow signals, was conducted in chapter 3. The investigation was performed with respect to the three points identified above and focused on new techniques compared to traditional approaches.

One of the signal transformation algorithms that has received significant attention in the past decade is the Wavelet Transform (WT). Chapters 2 and 3 reviewed

the WT and its suitability for the transformation of Doppler ultrasound blood flow signals. It was concluded that the WT was incompatible to the requirements of Doppler ultrasound blood flow signal analysis. This was mainly due to the poor frequency resolution at high frequencies and the poor time resolution at low frequencies. Due to this disadvantages, the WT was not investigated further in this study.

Recently, researchers have studied the application of the WT to Doppler ultrasound signals [48–50]. Matani *et al* [48] avoided the problem of low frequency resolution at high frequencies by introducing wavelet voices between the integer wavelet scales. Although this approach yielded good results, it is not economically viable as it required the use of a parallel computer with 36 CPUs.

The continuous WT was also applied successfully to Doppler ultrasound quadrature signals [49]. Güler *et al* [50] compared the STFT, autoregressive modelling (AR) modelling and the WT with Doppler ultrasound signals to detect aorta failure. Although their investigation showed that the WT performed best, it is important to note that the window used for the STFT was chosen to be 25.6ms. This was too long to assume stationarity and therefore, might have invalidated the results. Mo *et al* [43] stated that the Doppler signal can be assumed stationary for a period of approximately 10 ms.

A solution to the time and frequency resolution problem of the WT that was considered was its generalisation, the Wavelet Packet Transform (WPT) described in chapters 2 and 3. The WPT has a uniform time and frequency resolution based on wavelet packet bases. Furthermore, the WPT was not applied to Doppler ultrasound blood flow signals previously. The WPT and the STFT were therefore, investigated in this study (chapter 3).

As with the STFT the time and frequency resolution of the WPT depended

largely on the selected parameters. The WPT showed its best result on the Doppler signal when a discrete Meyer wavelet packet base was used. It was further shown that the STFT with an 128-point window yielded a time resolution of 8.53 ms and a frequency resolution of 117.19 Hz. Whilst the frequency resolution for the WPT was identical, the time resolution was improved to 4.27 ms, when using a decomposition level of 6. The introduction of a 50% overlap improved the apparent time resolution of the STFT to 4.27 ms, matching the WPT's time resolution. Although the underlying signal was only analysed on a basis of a window length of 8.53 ms (128-points at 15 kHz sampling frequency), a spectral point was generated for every 4.27 ms. The comparison of the maximum frequency envelope (MFE) extracted from the STFT and WPT showed that both MFEs had almost the same timing (figure 3.13).

Further comparisons between the STFT and the WPT in this study showed that the time-frequency distribution (TFD) of the WPT gave a higher noise floor than the STFT. Using a noise free signal the noise floor of the STFT was -65.7 dB, whilst the noise floor of the WPT was only -42 dB. By adding a -10 dB noise component to an artificially created time domain signal both TFDs had higher noise floors. For the STFT it increased to -40 dB and for the WPT to -37.7 dB. This is interesting as the noise floor of the WPT only increased by a small amount compared to that of the STFT. Further investigations in section 3.4.3 showed that the difference between the noise floors of the STFT and the WPT became smaller with increased levels of noise. Overall the STFT offered a better signal-to-noise ratio (SNR), especially at lower levels of noise in the time domain signal, where the difference is significant.

The overall result from the comparison between the STFT and the WPT was unexpected. It was assumed that the WPT would yield a noticeably better time-frequency resolution in the extracted MFE, which was not the case when the overlap

for the STFT window was introduced. Although this did not mean that the STFT had the same time-frequency resolution as the WPT, it showed that the resolution provided by the STFT is sufficient for Doppler ultrasound signal analysis. The reason for this may be that the Doppler ultrasound blood flow signal can be assumed to be stationary for 8.53 ms, and that the improved time resolution of the WPT is not required.

The WPT also showed more spectral broadening in some signal parts and an overall higher noise floor than the STFT. This may be explained by the fact that both algorithms use different principal components to analyse the time domain signal. While the STFT uses infinitely long sinusoidal waves, the WPT uses a finite length wavelet similar to a sinusoid (discrete Meyer wavelet packet base). The finite length, and the fact that the wavelet contracts and dilates during the analysis, may cause the higher noise floor and broader spectrum in some parts.

Overall the STFT was preferred because of its simplicity and higher SNR. Furthermore, the processing time of the STFT was significantly shorter than of the WPT. The investigations in section 3.4.3 showed a ratio of 36.2 between the STFT and the WPT in favour of the STFT with the same computer running Matlab 6.1. Equations 3.6 and 3.8 in the same section showed a similar relationship between the numbers of multiplications and additions for the STFT and the WPT.

Studies by other researchers concluded similarly in favour for the STFT [8,25,50, 61,62,64]. Problems found with alternative algorithms included increased computational complexity, high dependency on correctly estimated parameters and inconclusive results with *in-vivo* data. Overall, all studies agreed with this investigation that the STFT was the best compromise due to its simplicity and processing speed. More details about these studies were given in chapter 2.

6.1.2 Noise reduction

The spectrogram that was generated from the Doppler ultrasound blood flow signals by the STFT is normally noisy. Frequency components generated by wall and probe movement, reflection from tissue boundaries and electronic noise are part of a noise floor of the Doppler signal spectrum. This noise floor should be lowered or removed before extracting the features from the spectrum of the Doppler ultrasound blood flow signal. The noise reduction process is normally performed by an operator, who selects a threshold that sets all elements of the spectrogram below it to zero. The threshold is usually varied until the operator is satisfied with the visual appearance of the spectrogram. This iterative method is very subjective, and very difficult to repeat. To achieve consistent classification results the selection of the threshold should be removed from the operator's control. Furthermore, the removal of the operator from this stage would allow the automation of this stage.

Because the thresholding method normally used is not suitable for automated processing, wavelet denoising was investigated in this study. It was shown in chapter 3 that the use of the soft-thresholding wavelet denoising algorithm gave very good results when applied to the spectrogram rather than to the time domain signal. The two-dimensional algorithm achieved an almost complete removal of the background noise and improved the spectrogram significantly when compared to results reported in the literature [118, 119]. A sliding neighbourhood window was used to remove the occasional remaining spikes in the spectrogram. Although this method did not remove or reduce the background noise before the signal was transformed into the time-frequency domain, it removed the background noise before the feature extraction stage. Furthermore, this method can be used without the interaction of an operator, unlike the manual thresholding method reported by Wright *et al* [1] and used in commercial Doppler ultrasound scanners.

Recently, researchers investigated the wavelet denoising approach in Doppler ultrasound. Liu *et al* [118] investigated wavelet denoising using the soft-thresholding approach proposed by Donoho [104]. The algorithm was applied to the time domain signal of unidirectional Doppler ultrasound signal and enhanced the spectrogram. The approach was further studied by Zhang *et al* [119], who used Wavelet Frames. The study showed an improvement on the work of Liu *et al* and was also applied to unidirectional signals.

Wright *et al* [1, 18, 19] used a simple thresholding method to remove the background noise in the spectrogram. Although this method was very effective in the removal of the unwanted components, it needed manual intervention of an operator. Hoskins *et al* [120] compared two noise reduction algorithms: the double window modified trimmed mean (DWMTM) filter and a method using a two-dimensional filter. The DWMTM was applied to the MFE after its extraction from the spectrogram. It therefore, did not reduce the background noise from the spectrogram itself but reduced the effect of noise after it had already propagated into the feature extraction stage. The second method was more successful in smoothing the spikes in the spectrogram, but it did not remove the background noise.

The effect of the thresholding method used by Wright *et al* [1, 18, 19] and the wavelet denosing algorithm on the classification of clinical signals was investigated in this study. The results were given in chapter 5 and are discussed in section 6.3 of this chapter.

6.2 Feature extraction

This section presents the discussion of the work reported in chapter 4. It is divided into five parts, each discussing a section of the chapter.

6.2.1 Extraction of the MFE

Although the MFE ignored information present in the spectrogram of the Doppler ultrasound blood flow signal, it is the most common feature extracted from the spectrogram. It is a simple representation of the maximum blood flow velocity over time and the basis for a number of indices.

Four MFE extraction methods were previously investigated in a study by Mo *et al* [43]. The study compared the percentile method with the D'Alessio's threshold crossing method, the modified threshold crossing method and the hybrid method. The study used simulated continuous wave Doppler signals of the carotid arteries with SNR between 9 dB and 17 dB, which were used without prior noise reduction of the spectrogram. Although the alternative methods showed improvements over the percentile method, the study found that none of the methods exhibited marked superiority over all performed tests.

In this study, the percentile method was used because of its simplicity and compared with a new algorithm, the distance method. The distance method was proposed with the aim of reducing, or avoiding, the need of a background noise reduction or noise removal algorithm for the spectrogram. Although the distance method showed an improved ability to deal with background noise in the spectrogram, it suffered from spikes in the extracted MFE. These spikes occurred in time intervals where no signal was present. Spikes could also occur when the spectrogram of the signal had a reduced amplitude in the higher frequency band. This amplitude drop in the spectrogram presented a second knee in the cumulative power vector which caused the wrong estimation of the maximum frequency. The integration of the signal collection and digitising stages would reduce or avoid this effect.

Although the distance method showed a number of problems, the performance improved when used on a spectrogram where noise reduction had been applied. On

the other hand, when the noise floor was lowered, the percentile method delivered a more reliable MFE with less spikes.

6.2.2 Combination of the MFE

The blood flow of the CFA is normally triphasic. It has a forward flow, followed by a reverse flow and another forward flow component. The MFEs for both, forward and reverse flows, were extracted separately and therefore, needed to be combined. The combination of the two flows also halved the overall length of the feature vector. This is a non-trivial process, as the forward and reverse flow components overlapped in parts.

Wright *et al* [18] described the comparison method for the combination of the forward and reverse flow envelopes. This method was compared with the subtraction method and a modified comparison method proposed in this study. The MFE created by the subtraction method suffered from reduced absolute values due to reverse flow during the systolic peak. Although this was avoided by the comparison method, the transitions between forward and reverse flow showed oscillations when the forward and reverse flow components subsided gradually. The method proposed in this study, the modified comparison method, reduced the frequency with which the oscillations occurred and showed the best result of the three combination algorithms. The success of the modified comparison method can be attributed to the hysteresis parameter. It forms a tolerance band around the combined MFE, therefore allowing only definite changes in direction to affect the combined MFE.

The combination of the forward and reverse blood flow of the CFA using the R-wave was described by Gibbons *et al* [105]. Their study investigated the use of a microcomputer to calculate the Pulsatility Index (PI), for which the combination of the forward and reverse flow was necessary. The R-wave was used to remove the

whole reverse flow component between the R-wave peak and the forward flow peak. Furthermore, the reverse flow was removed when a significant forward flow existed. This method required the acquisition of the ECG in order to detect the R-wave. This is impractical, as it increases the demand on the operator and increases the complexity of the measurement.

6.2.3 Extraction of the cardiac cycle

The information provided by the MFE is repetitive and based on the cardiac cycle. It is therefore, only necessary to use one cardiac cycle of the MFE for the classification of Doppler ultrasound blood flow signals. This provides the feature vector for further processing stages. The automated extraction of the cardiac cycle MFE is difficult due to the possible range of different MFEs. Figure 4.21 in section 4.3.1 showed three examples of possible MFE waveform shape.

A semi-automatic algorithm was proposed by Evans [92]. His study described a pulse-foot-seeking algorithm that was used successfully on a large number of Doppler ultrasound blood flow signals. The algorithm was not completely automated, as it relied on the manual selection of the heart rate range by an operator. Because this algorithm gave good results, it was included in this study and compared to the first derivative algorithm described by Wright *et al* [18] and to a modified pulse-foot-seeking algorithm, which was proposed in this study. The first derivative algorithm did not perform well and missed some cardiac cycles completely due to the variability in the amplitude of the cardiac cycle peaks. The pulse-foot-seeking algorithm by Evans performed well, but was restricted to a limited heart rate range. One reason for this was the requirement of setting the length of windows, in which the start of the cardiac cycle was to be found. This limited the suitability of the algorithm, as the required window length varied with the heart rate. The proposed modified

algorithm avoided this dependency by automatically detecting the heart rate from the MFE. A second modification eased the constrains on the maximum length of the processing windows. This algorithm showed improved results and worked with a larger range of heart rates (50 bpm to 150 bpm).

Two main reasons for the success of the modified pulse-foot-seeking method can be found. Firstly, the proposed algorithm for the detection of the cardiac cycle peaks allowed the modified pulse-foot-seeking method to extend the range of heart rates it can operate with. Secondly, the modification in the determination of the beginning of the systolic upstroke enabled the new method to extend the search window for this point. This was the major contributor to the improved detection performance.

Another approach to find the start of the cardiac cycle, which is necessary for the extraction of the cardiac cycle, was reported by Hoskins *et al* [121] and Wright *et al* [18]. Both described a matched filter approach, where the start of the cardiac cycle was detected by correlating the MFE with a selected transfer function. This approach was not suitable for this study as it required the manual selection of the transfer function.

Johnston *et al* [93] described a microcomputer-based system with a waveform identification process to extract a cardiac cycle for the calculation of the PI. The system was able to identify and extract 96% of the waveforms, using visual feedback as guidance. This algorithm was based on identifying the maximum values and averaging five cardiac cycles with less than 20% beat-to-beat rate variance. This approach was not suitable for this study, as the averaging of the cardiac cycles of different lengths distorted the waveform shape, which carries the required classification features.

6.2.4 Spectral broadening

The MFE is the most commonly extracted feature of the spectrogram of the Doppler ultrasound blood flow signal. However, it is believed that the blood flow signal and its time-frequency representation include additional information of value in the clinical diagnosis of vascular disease and the assessment of its severity. This view has been confirmed by the human observers who classified the signals used in this study. Their classification results are discussed in section 6.3.

An important item of information in the spectrogram that is not represented by the MFE is the spectral broadening, which is believed to provide an indication of the severity of the disease condition in the blood vessel. Kassam *et al* [69] stated that there are at least two features in the carotid spectral waveform that can be used for classification, the peak frequency of the cardiac cycle and spectral broadening. As a result it was decided in this study to utilise the Spectral Broadening Index (SBI) as an additional parameter alongside the MFE and to investigate its impact on the classification of the clinical blood flow signals. The results of using the SBI were presented in sections 5.5 and 5.6 and are discussed in section 6.3.

This study used the definition given by Johnston *et al* [71] to calculate the SBI. With the exception of three cardiac cycles, the calculation of the SBI gave good results. Three cardiac cycles caused problems as their signal bandwidth during the cardiac peak was very small. Due to the different algorithms used to calculate the maximum frequency (95% percentile) and the mean frequency, the mean frequency was calculated to be larger than the maximum frequency in these cases. This resulted in a negative value for the SBI as described in section 4.4. The cardiac cycles, however, were still used in the classification process.

6.2.5 MFE Wavelet coefficients

The possibility of reducing the length of the feature vector was also investigated. Pittner *et al* [122] reported an algorithm for reducing the number of features for classification problems that was based on clustering wavelet coefficients. In this study a different approach was followed. The feature vector, MFE, was lossy compressed using a method called wavelet compression. It was shown that the compressed feature vector maintained the dominant features of the original vector by measuring the root-mean-square-error (RMSE) of the reconstructed feature vector against the original one. This method was also used to select the wavelet compression parameters. The good reconstruction results of the lossy wavelet compression can be attributed to the selection of the wavelet base. As the investigation showed in figures 4.40 and 4.41, an optimally selected wavelet base is able to present the signal with the minimum of wavelet coefficients.

The effect of the compression on the classification and diagnosis was presented in sections 5.5 and 5.6 and is discussed in section 6.3.

Overall the investigations in chapter 4 showed that it is possible to fully automate the feature extraction stage of the Doppler ultrasound blood flow classification and diagnosis process. Although the individual automation of some of existing algorithms were previously reported [92], the combination and automation of all algorithms necessary to extract one cardiac cycle MFE from the spectrogram were not reported by other researchers.

6.3 Classification and decision making

Chapter 5 has presented the reasons for selecting Artificial Neural Networks (ANNs) as the classification algorithm in this study. In principle, ANNs are suited for applications where there are no established mathematical relationships between the input feature vectors and the classification results, which is the case for Doppler ultrasound blood flow signals and the vascular disease condition. Although the shape of the MFE provides an indication of the severity of vascular disease, the exact relationship between the two is not fully understood.

In addition, ANNs have been previously used in signal recognition tasks and lend themselves to automation, which is one of the main objectives of this study. Their suitability for use in Doppler ultrasound blood flow applications was confirmed by previous researchers [1, 18–20, 112].

The Doppler ultrasound blood flow signals used in this study came from the CFA in the lower limb. The aim of the classification of these signals was to detect the presents of proximal disease regardless of presence of distal disease. The problem with the detection of proximal disease using Duplex scanners is related to the location of the aorto-iliac segment. Bowel gas and obesity in patients make an image scan less reliable. Furthermore, the classification of proximal disease using indices derived from the MFE is reduced in the presence of distal disease.

The signals for this study were collected over a period of one year from different patients and changes in the day to day performance of the operator provided a wide range of signals. This approach ensured that the recorded Doppler ultrasound blood flow signals were comparable to signals used normally in clinical investigations. The availability of signals with a wide quality range has enabled this study to be very realistic. Software simulation and data collection from controlled environments, such

as flow model and animals, have the advantage of giving well defined signals, but lack the variety of quality that are exhibited by real signals. Furthermore, controlled signals do not show the impact of real clinical conditions such as distal or multiple stenoses unlike the signals used in this study. These clinical conditions were reported to reduce the classification abilities of different indices significantly [7, 15].

The following sections discuss the classification results together with the effect of noise reduction, feature vector length, SBI and overall automation of the clinical decision making process.

6.3.1 Classification results

The results of the investigations presented in chapter 5 showed good classification rates for both, the two-class and the three-class problem. The two-class problem achieved a maximum classification rate of 96.25%, whilst the highest rate for the three-class problem was 86.25%. The lower result for the three-class problem was expected, as it is generally more difficult to separate three classes than two. Furthermore, the third class was very narrow and only covered arteries with 99 to 100% occlusion. This was likely to be a factor contributing to the lower classification result in the three-class problem.

The best result for the two-class problem was achieved by two ANNs. The first used a 50-point feature vector that was truncated, decimated and truncated again (data set A4). The second ANN used the 16-point wavelet compressed feature vector, which was the shortest feature vector available (data set A12). The SBI was utilised in the first ANN but not in the second. The ANN achieving the best result in the three-class problem utilised a feature vector truncated to 80 points and used the SBI (data set A5). The third best performance was achieved by the shortest feature vector, the 16-point wavelet compressed MFE, plus the SBI (data set A12).

As the two highest performances were achieved by ANNs using short feature vectors, it might be possible that there was a trend. It was reported that a high ratio between the numbers of training vectors and the number of ANN inputs normally delivers a better trained ANN [123]. As the number of training vectors stayed constant, this would be the case for the shorter feature vectors of this study. Figures 6.1 and 6.2 show the classification results, ordered by increasing feature vector length, for the two-class and three-class problem, respectively. It can be seen that there is no trend linking the ANN performance with the length of the feature vector.

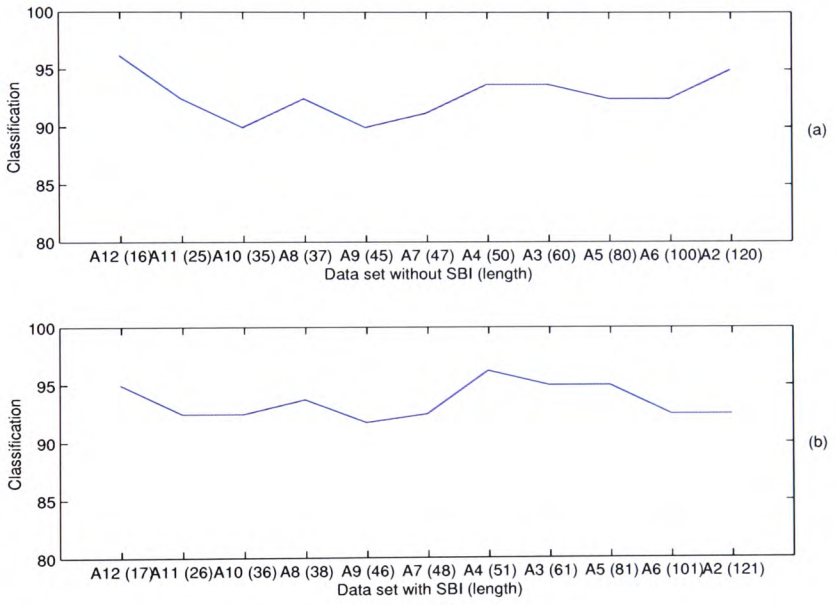

Figure 6.1: Classification result from the two-class problem, re-ordered by length of the feature vector. Only the results from the automated approaches are displayed. (a) results without SBI, (b) results with SBI.

A study conducted by Wright [1] used Doppler ultrasound blood flow signals from the same database as this study. Wright used manual thresholding for noise reduction and an ANN for classification. The best performing ANN was presented with truncated and decimated 20-point feature vectors and achieved a classification rate of 82.5% for the two-class problem and 71% for the three-class problem.

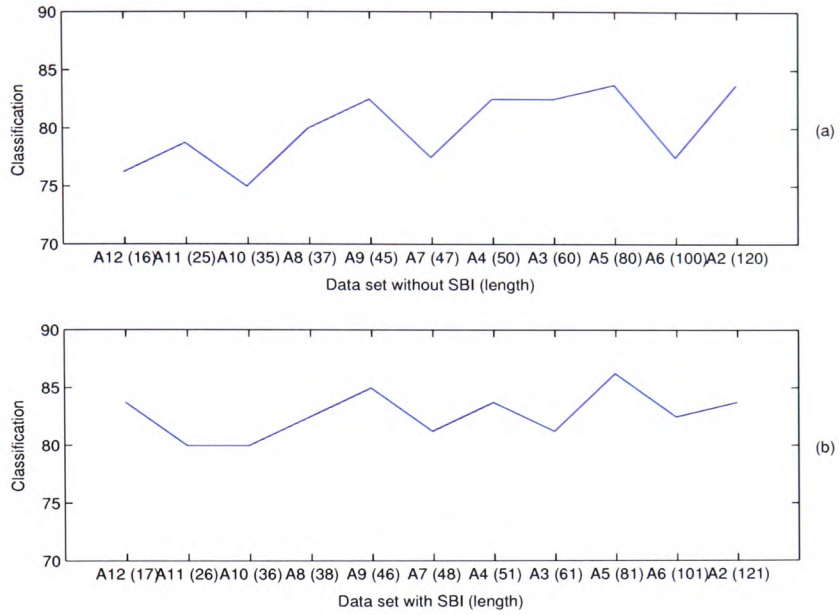

Figure 6.2: Classification result from the three-class problem, re-ordered by length of the feature vector. Only the results from the automated approaches are displayed. (a) results without SBI, (b) results with SBI.

The classification rates of this study were significantly better than those reported by Wright for both, the two- and three-class problems. A comparison of Wright's results and the results of this study can be seen in table 6.1 for the two-class problem and in table 6.2 for the three-class problem. The classification results used for the comparison were the best performing ANNs from this study. The 16-point long wavelet compressed feature vector without the SBI was used for the two-class problem as it was the smaller of the two best performing ANNs. The ANN for the three-class problem used an 80-point truncated feature vector with the SBI (81 points in total).

Both studies showed a similar pattern, where signals with significant disease performed worst than the other classes in both problems. Also interesting to note is that the third class, occlusion, in the three-class problem showed only a small improvement, whilst the other two classes resulted in a significant increase in performance.

	Classification (%)	
	this study	Wright's study
no significant disease	100	90
significant disease	92.5	75
overall	96.25	82.5

Table 6.1: Best classification result of the two-class problem for this and Wright's study [1].

	Classification (%)	
	this study	Wright's study
no significant disease	92.5	75
significant disease	70	50
occlusion	90	88
overall	86.25	71

Table 6.2: Best classification result of the three-class problem for this and Wright's study [1].

This suggests that the initial reason given earlier for the poorer performance of the three-class problem might be correct, and that the class is too narrow. The difference in performance cannot be explained directly with these results, as a number of parameters differed between the two studies. Wright's study used manual thresholding and the first derivative method for the cardiac cycle extraction, whilst this study used an automated process for both. The influence of the different parameters were investigated in this study and are discussed later in this section.

The Pulsatility Index (PI) was calculated for all signals used in the test set of this study because of the reported high classification rate associated with its use [6]. Figure 6.3 shows the distribution of the PI for each class of the Doppler ultrasound signals. The figure shows that a separation of the signals using the PI into two classes would achieve a classification rate of approximately 85 to 90%. Separating the signals into the three classes using the PI is clearly impossible.

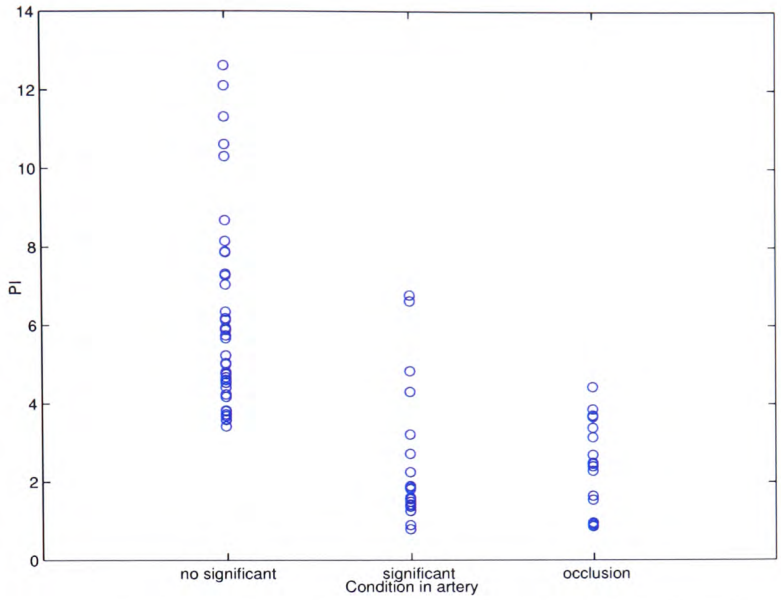

Figure 6.3: PI of the Doppler ultrasound signals used in this study.

In an earlier study Johnston *et al* [124] found that the PI had values between 3 and 17 for the no significant disease class, 1 and 7 for the significant disease class, and 0.5 and 4 for the occlusion class. Similarly, Demorais *et al* [37] reported that no significant stenosis was present when the PI was greater than 6, whilst a significant disease was found when the PI was less than 5. This not only confirmed the results of the calculations of the PI in this study, but also that there is a significant overlap between all three classes.

A number of studies were conducted to investigate the classification of Doppler ultrasound blood flow signals using the MFE [1, 6, 11, 12, 18–20, 39, 112]. These studies used a number of different approaches and signal features. A summary of these studies and the reported best classification figures are shown in table 6.3.

Although the classification figures listed in table 6.3 are high, it was reported that the classification rate is reduced for Doppler ultrasound blood flow signals with distal or multiple stenoses [2, 6]. Furthermore, processing in all studies listed in

Approach/Parameter	Best reported classification performance	Reference
Pulsatility Index (PI)	96%	Johnston *et al* [6]
Principal Components Analysis (PCA)	86.2%	Macpherson *et al* [12]
Laplace Transform (LTA)	92%	Johnston *et al* [6]
Transfer Function Analysis (TFA)	53.8%	Evans *et al* [11]
Height Width Index (HWI)	95.6%	Johnston *et al* [6]
Path Length Index (PLI)	91.6%	Johnston *et al* [6]
Artificial Neural Networks (ANN)	82.5%	Wright [1]

Table 6.3: Best reported classification result of studies using the MFE for classification of Doppler ultrasound blood flow signals.

table 6.3 used manual intervention by an operator at different levels and were not automated. This clearly demonstrates the approaches proposed in this study and their objectivity due to the elimination of the need for human intervention.

6.3.2 Misclassification

Analysing the results of the best performing ANNs for each data set showed that a small number of signals were misclassified across the data sets in more than 50% of the cases. For the two-class problem the result for the 106 best performing ANNs [1] can be summarised as follows:

- 21 out of 80 cardiac cycles were at least misclassified once.
- 6 out of these 21 cardiac cycles were misclassified in at least 50% of the ANNs.
- The 6 misclassified cardiac cycles came from 4 different Doppler ultrasound signals.

[1] In most data sets more than one ANN network structure achieved the best classification result.

Two of the four most misclassified Doppler ultrasound signals were from the significant disease class, whilst the other two were from the no significant disease class. Figure 6.4 shows the MFE of these six cardiac cycles.

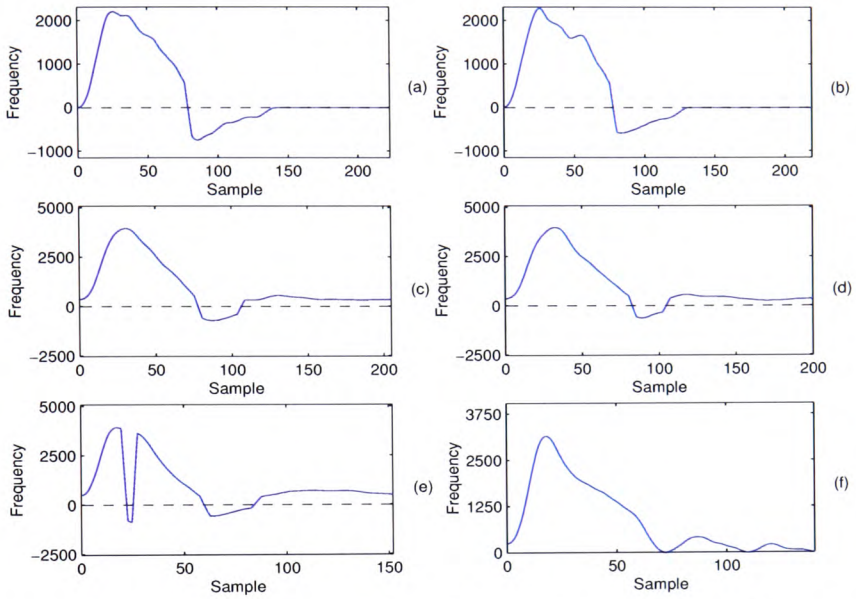

Figure 6.4: Cardiac cycle MFE of the most often misclassified signals in the two-class problem. (a) - (d): significant diseased signals, (e) - (f): no significant diseased signals.

Figures 6.4(a) to (d) show the four cardiac cycles of the significant diseased signals, all of which exhibit reverse flow components. The loss of the reverse flow, with the dampening of the amplitude and spectral broadening, are some of the features of a stenosed common femoral Doppler ultrasound blood flow signal as described in chapter 2. The fact that these signals were still showing reverse flow may be because their stenosis is close to 50%, which was the degree of stenosis separating the two classes. In fact, the cardiac cycles in figure 6.4(c) and 6.4(d) are from a CFA that was labelled during the initial classification by the operator as showing a stenosis of around 50%. These two cardiac cycles were misclassified in 72.6% (figure 6.4(c)) and 98.1% (figure 6.4(d)) of all cases.

Figure 6.4(f) shows the reverse behaviour, where the reverse flow vanished although the signal did not represent significant disease. It is very likely that this signal also represented a degree of stenosis close to 50%, and as such it was misclassified as representing significant disease. Comments in the signals database by the operator showed that this signal represented distal occlusion, a situation that can also be found in other signals. Figure 6.4(e) on the other hand shows a considerable spike into the reverse flow region at the cardiac peak. The reason for this can be seen in its spectrogram (figure 6.5). The spectrogram indicates that the quality of the recording was poor and that part of the forward flow is mirrored into reverse flow, showing in some areas the same power amplitude as the forward flow. The pre-processing and feature extraction algorithms were not able to cope with such a signal, as the mirrored forward flow was recognised as a genuine reverse flow component. This type of misclassification, which can affect any classification approach, can be avoided in a system by only recording signals of reasonable quality level. These cardiac cycles showed misclassification rates of 99% (figure 6.4(a)), 98.1% (figure 6.4(b)), 79.2% (figure 6.4(e)) and 64.2% (figure 6.4(f)).

For the three-class problem the misclassification by the 38 best performing ANNs can be summarised as follows[2]:

- 52 out of 80 cardiac cycles were at least misclassified once.
- 10 out of these 52 cardiac cycles were misclassified in at least 50% of the ANNs.
- The 10 misclassified cardiac cycles came from 7 different Doppler ultrasound signals.
- All cardiac cycles misclassified in the two class problem were also misclassified in the three-class problem.

[2]In most data sets more than one ANN network structure achieved the best classification result.

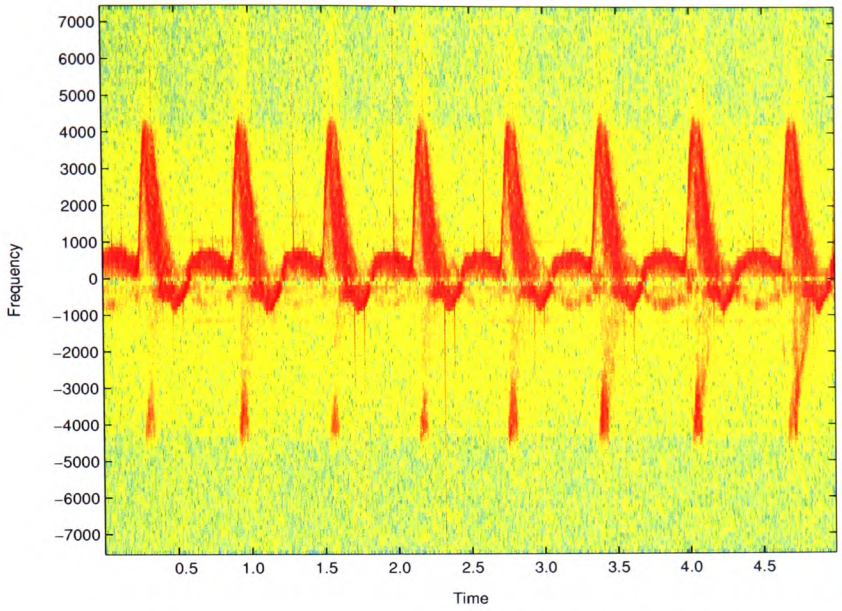

Figure 6.5: Spectrogram of the misclassified cardiac cycle MFE in figure 6.4 (e).

Four of the most misclassified signals belonged to the significant disease class and three belonged to the no significant disease class. The six most misclassified cardiac cycles in the two-class problem formed a subset of the misclassified cardiac cycles in the three-class problem and their discussion is not repeated here. The remaining four cardiac cycles are presented in figure 6.6.

All four cardiac cycles were classified as occlusions. Three of the cardiac cycles belonged to the significant disease class, whilst one belonged to the no significant disease class (figure 6.6(d)). The cardiac cycles in figure 6.6(a) and 6.6(b) are very damped, which is normally the case for MFEs from occluded arteries. It is therefore, very likely that the source of the two cardiac cycles is highly stenosed, causing the misclassification. The cardiac cycle in figure 6.6(c) resembled the one in figure 6.6(a), although the amplitude was higher. The similarities between these two waveforms and between the waveform in figure 6.6(a) and an occluded waveform, is likely to be the reason for this misclassification. The last cardiac cycle (figure 6.6(d)) had

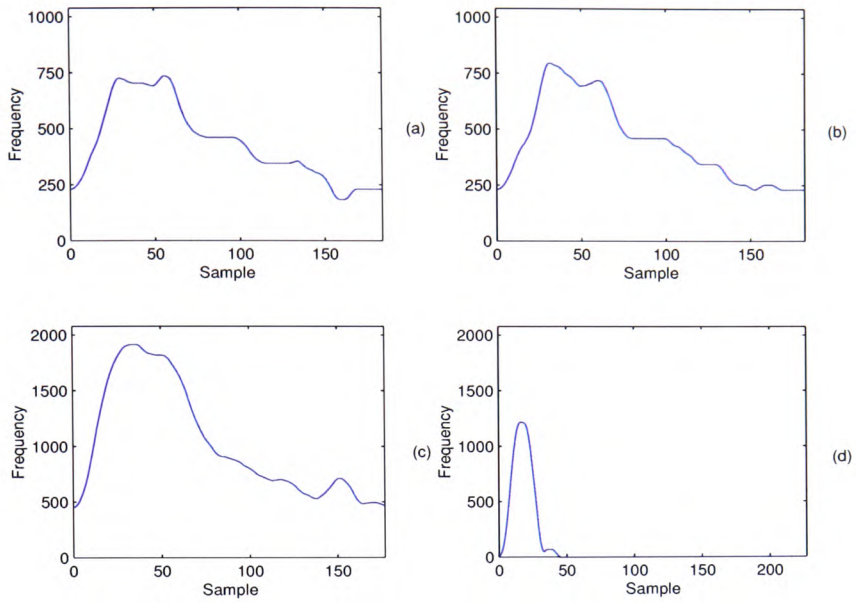

Figure 6.6: Cardiac cycle MFE of the most often misclassified signals in the three-class problem. (a) - (c): significant diseased signals, (d): no significant disease.

an unusual shape, which was likely to be the cause of the misclassification. The spectrogram of this signals (figure 6.7) was of very poor quality. The background noise was very high and had almost the same level as the signal. The cardiac cycles showed misclassification rates of 52.6% (figure 6.4(a)), 81.6% (figure 6.4(b)), 89.5% (figure 6.4(c)), 86.8% (figure 6.4(d)), 73.7% (figure 6.4(e)), 55.3% (figure 6.4(f)), 94.7% (figure 6.6(a) and (figure 6.6(b))), 71.1% (figure 6.6(c)) and 57.9% (figure 6.6(d)). The signals that provided the cardiac cycles shown in figure 6.4(e) and figure 6.6(d) should not have been included in the classification because of their poor quality.

From the above analysis of the misclassified signals the reasons for misclassification can be attributed to the following two reasons

- Signals with a degree of stenosis close to the border between two classes.
- Poor quality Doppler ultrasound signals.

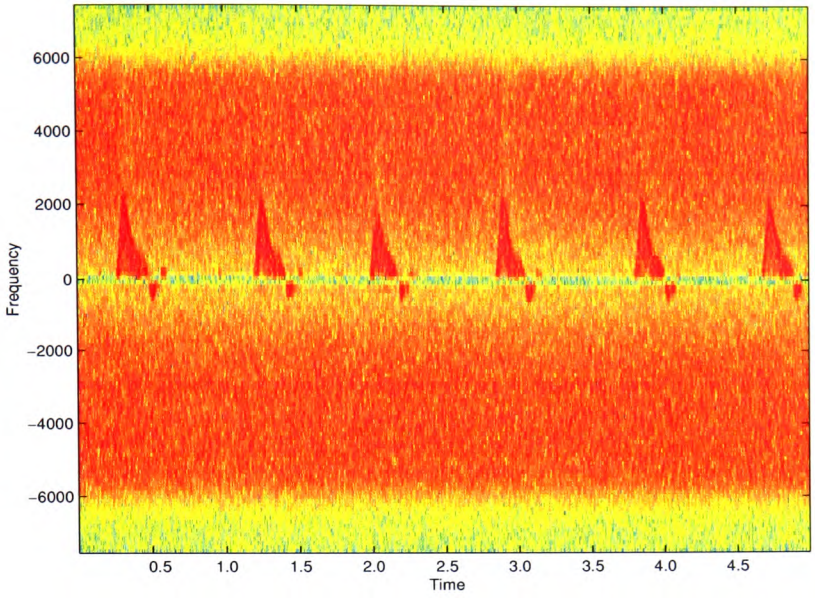

Figure 6.7: Spectrogram of the misclassified cardiac cycle MFE in figure 6.6(d).

6.3.3 Comparison with human observers

The study conducted by Wright [1] compared the classification results with those achieved by two human observers using the same Doppler ultrasound signals. The human observers were experienced personnel from the University of Wales College of Medicine and used the MFE and the sonogram (tables 6.4 and 6.5) for their classification. The results for the two-class problem showed classification rates of 79.5% for observer 1 and 82.5% for observer 2 using the MFE, and 87.5% for observer 1 and 85.5% for observer 2 using the sonogram. The three-class problem produced classification rates of 66.7% by observer 1 and 64.7% by observer 2 using the MFE, and 72% by observer 1 and 72.3% by observer 2 for the sonogram.

A comparison of Wright's results, the best human observer and the results of this study can be seen in table 6.6 and 6.7. The classification results used for the two-class problem in this study were from an ANN with 16-point long wavelet compressed feature vector without the SBI. The ANN for the three-class problem

	Classification (%)			
	human observer 1		human observer 2	
	MFE	sonogram	MFE	sonogram
no significant disease	80	89	94	85
significant disease	79	86	71	86
overall	79.5	87.5	82.5	85.5

Table 6.4: Classification results produced by human observers [1] for the two-class problem.

	Classification (%)			
	human observer 1		human observer 2	
	MFE	sonogram	MFE	sonogram
no significant disease	72	78	87	73
significant disease	38	53	32	48
occlusion	90	85	75	96
overall	66.7	72	64.7	72.3

Table 6.5: Classification results produced by human observers [1] for the three-class problem.

used an 80-point truncated feature vector with the SBI (81 points in total). The classification rate of this study outperformed the other two results. This is a clear indication that the algorithms and methodology proposed in this study did not only provide an automated approach to assist in clinical decision making, but can improve on the performance of experienced operators.

Interestingly, the tables show that the human observer classification using the sonogram was better than using the MFE. This supports the suggestion that the MFE does not include all the disease related features of the spectrogram.

6.3.4 Noise reduction

The automation of the noise reduction algorithm was one of the main aims of this study. Eliminating the need for the intervention by an operator removes the sub-

	Classification (%)			
	This study	Wright's study	best human observer MFE	best human observer sonogram
no significant disease	100	90	94	89
significant disease	92.5	75	71	86
overall	96.25	82.5	82.5	87.5

Table 6.6: Comparison of the best classification rates achieved in this study, Wright's study and the human observers for the two-class problem.

	Classification (%)			
	this study	Wright's study	best human observer MFE	best human observer sonogram
no significant disease	92.5	75	72	73
significant disease	70	50	38	48
occlusion	90	88	90	96
overall	86.25	71	66.7	72.3

Table 6.7: Comparison of the best classification rates achieved in this study, Wright's study and the human observers for the three-class problem.

jectivity and variability from the extracted features. The use of an algorithm that allows the automation of the noise reduction stage is only valid if the classification rate does not suffer. This study has investigated the wavelet denoising algorithm and compared it to the manual thresholding method. Four different feature vectors were prepared to investigate the effect of the noise reduction on the overall classification result. Two feature vectors were used for each noise reduction method as described in section 5.4.2.

The results of the investigation showed clearly that the automated noise reduction approach delivered a superior performance over the manual grass-cutting method. For the two-class problem the performance improved by 2.5% and 3.75% for the two feature vectors, whilst an increase of 5% was achieved for both feature vectors in the three-class problem. The results were reproduced in table 6.8.

		Classification (%)			
		Two-class problem		Three-class problem	
		no SBI	SBI	no SBI	SBI
feature vector A	manual	**92.5**	91.25	72.5	**77.5**
	automatic	93.75	**95**	**82.5**	81.25
feature vector B	manual	**88.75**	**88.75**	76.25	**81.25**
	automatic	**92.5**	**92.5**	77.5	**82.5**

Table 6.8: Comparison between automated (wavelet denoising) and manual (grass-cutting threshold) noise reduction. Feature vector A: MFE truncated to 120 points and decimated to 60 points (data set A0 & A3). Feature vector B: MFE re-sampled to 100 points (data set A1 & A6).

This study has shown that the automation of the noise reduction stage using the wavelet denoising algorithm was not detrimental to the performance, but actually improved the classification. This indicates that the manual selection of the grass-cutting threshold introduced a variability that decreased the classification rate.

6.3.5 Feature vector length

In order to optimise the complexity and performance of the ANN the impact of the feature vector length was investigated. Two different methods were used. The first method was used by Wright *et al* [1, 18, 19] and simply truncated and decimated the feature vector. The second method used a different approach of selecting and retaining the most dominant features of the vector by utilising wavelet compression. Both methods were compared with each other and with a feature vector containing the entire cardiac cycle as described in section 5.4.2.

Table 6.9 shows the ANN classification results for different levels of cardiac cycle truncation. Interestingly, the performance of the ANN using the entire cardiac cycle as a feature vector was not as good as the one using truncated cardiac cycles. The difference in performance was up to 3.75%. The best performing ANN in the two-

class problem achieved 96.25% using a 50-point feature vector. In the three-class problem an 80-point feature vector achieved 86.25%. Both results were the highest within the study.

Feature vector length (Data set)	*Classification (%)*			
	Two-class problem		Three-class problem	
	no SBI	SBI	no SBI	SBI
120 points (A2)	**95**	92.5	**83.75**	**83.75**
80 points (A5)	92.5	**95**	83.75	**86.25**
60 points (A3)	93.75	**95**	**82.5**	81.25
50 points (A4)	93.75	**96.25**	82.5	**83.75**
100 points/full cardiac cycle (A6)	**92.5**	**92.5**	77.5	**82.5**

Table 6.9: Comparison between truncated and entire cardiac cycles.

The second method of reducing the feature vector length was the reduction of the feature vector length using the wavelet compression algorithm. Table 6.10 shows the results. The shortest feature vector achieved the highest classification rate (96.25%) in the investigation of the two-class problem. This was the same rate as the one from the 50-point truncated feature vector. The result is interesting as no detail coefficients were retained and only the approximation coefficients were used. It suggests that the basic shape of the MFE, after being transformed by the WT, is enough to detect the state of the artery. In the three-class problem the shortest feature vector only achieved the second highest classification rate of this group and the third highest of the study. The 45-point feature vector, which was compressed at level 3 with a bi-orthogonal 3.1 wavelet, performed best in this group when the SBI was used (46 points in total).

Comparing the results of the two methods, it is evident that the wavelet compression method delivered classification results which were similar to the ones from the truncation method. The advantage of the wavelet compression method, however,

Feature vector length (Data set)	*Classification (%)*			
	Two-class problem		Three-class problem	
	no SBI	SBI	no SBI	SBI
47 points (A7)	91.25	**92.5**	77.5	**81.25**
45 points (A9)	90	**91.75**	82.5	**85**
37 points (A8)	92.5	**93.75**	80	**82.5**
35 points (A10)	90	**92.5**	75	**80**
25 points (A11)	**92.5**	**92.5**	78.75	**80**
16 points (A12)	**96.25**	95	76.25	**83.75**
100 points/full cardiac cycle (A6)	**92.5**	**92.5**	77.5	**82.5**

Table 6.10: Comparison between the wavelet compressed and the entire cardiac cycle feature vectors.

was the shorter feature vector, which was 16 versus 51 points for the two-class problem and 46 versus 81 points for the three-class problem[3]. The performance of the wavelet compressed feature vector was 1.25% lower than with the truncated feature vector in the three-class problem.

The good result of the truncated feature vectors indicates that the most important information is located within the first part of the cardiac cycle. This means that only the first two phases of the common femoral MFE are required. Wright [1] reported a similar conclusion, but did not compare the results of the truncated MFE with a MFE containing the entire cycle.

Wavelet compression of the MFE performed equally well as the truncated MFE. The advantage of wavelet compression was that it allowed fine details to be separated from larger trends. This enabled the compression of both the fine details and the larger trends with suitable quantisation. The favourable results of using the compressed feature vector as an input to the ANN suggested that the ANN performed some kind of decompression internally. It is also interesting to note that

[3]An additional point for the feature vector was necessary to accommodate the SBI

the maximum and minimum performances of the wavelet compressed feature vectors within one data set were generally closer together in ANN networks with 30 or 40 neurons in the first hidden layer than in ANNs with smaller first hidden layer. The exception of this general trend iwas the smallest feature vector (data set A12). This data set retained only the approximation coefficients. This trend can be observed in figures B.8 to B.13 in appendix B.1 for the two-class problem and figures C.8 to C.13 in appendix C.1 for the three-class problem. The reason may be that the ANN required a sufficient number of neurons to perform the operation consistently with less dependency on the initial weights and biases of the ANN.

Furthermore, it is also interesting that the wavelet compressed feature vector, which was based on the entire MFE cardiac cycle, performed better than the feature vector that contained the entire cardiac cycle. This may indicate that wavelet compression performs a form of additional feature extraction.

6.3.6 Spectral Broadening Index

The SBI was introduced as an additional feature to the MFE in this study. Whilst the MFE offers only information about the maximum blood flow velocity, the SBI adds information about the range of the blood flow velocities at the cardiac cycle peak. Spectral broadening normally increases due to turbulence in diseased arteries. Sheldon *et al* [74] and Johnston *et al* [71] suggested that the SBI is of diagnostic value.

All 13 data sets in this study were investigated with and without the SBI as an additional feature. In the two-class problem, from the best performing ANN of each data set, 7 showed an improvement, 3 did not show a change and 3 showed a decrease in performance. The best performance of all ANNs was shared between a truncated feature vector that included the SBI and a compressed feature vector that

did not include the SBI. Both achieved a classification rate of 96.25%. The effect of the SBI on classification increased further in the three-class problem, where 11 feature vectors showed an improvement, one did not show any change and only one showed a decrease in performance. The results are summarised in table 6.11.

	Performance		
	decrease	no change	increase
Two-class problem	3	3	7
Three-class problem	1	1	11

Table 6.11: Effect of the SBI on the ANN classification performance.

The results clearly show that the SBI improved the ANN classification performance. In both problems the best performing ANN and data set used the SBI as an additional parameter. This supports the initial reasoning for the introduction of the SBI in this study. It was argued that the SBI would provide useful information because an increase of spectral broadening at the cardiac peak indicates an increased number of blood flow velocities as found in diseased arteries. Severe cases of vascular disease can cause turbulence, which increases the spectral broadening even further. The window underneath the cardiac peak, which is reduced by spectral broadening, is normally one indicator used by clinicians to detect vascular disease. Most often, the SBI is used in carotid arteries, but this study showed that it also improved the classification performance in the diagnosis of vascular disease in lower limb arteries.

6.3.7 Automation of the classification and diagnosis process

The automation of the Doppler ultrasound blood flow classification and diagnosis process was a fundamental aim of this study. The entire classification and diagnosis process of Doppler ultrasound blood flow signals starting from the digitised signal was investigated in this study. To achieve the automation of this process two areas

were targeted specifically. These were noise reduction and the extraction of the cardiac cycle.

The reduction, or removal, of background noise was successfully shown using a two-dimensional wavelet denoising process. This eliminated the interaction of an operator and therefore, removed the variability and subjectivity introduced by manual selection of the grass-cutting threshold. Furthermore, it allowed automation of this stage of the process. A similarly successful method has not yet been reported in literature.

The automated extraction of the cardiac cycle over a wide range of heart rates was successfully achieved in this study. The proposed algorithms performed well on very damped MFEs, MFEs with different offsets and MFE waveforms with a variability in the amplitude of the cardiac cycle peak over a number of cycles. A semi-automated cardiac cycle extraction method was reported previously, but relied on the setting of some parameters by an operator [92, 105].

The ANN was chosen as the classifier for this study, as it lends itself well for automation. Once trained, no interaction with an operator is needed to perform classification. The automated calculation of the SBI and the wavelet compression complemented the overall process and allowed a fully automated classification and diagnosis of the Doppler ultrasound blood flow signals.

Automated systems were reported by Başaran *et al* [94] and Das *et al* [95]. Başaran *et al* described an automated system based on the PI, Pourcelot's Resistance Index (RI) and A/B ratio, but no results were given. A knowledge-based system, which used the autoregressive moving average (ARMA) model and an ANN for the determination of the parameters for the ARMA model was described by Das *et al*. The results for this system were not reported in the literature.

Overall this study was able to demonstrate that by combining the investigated

and proposed algorithms and presenting them to an ANN, it is possible to automate the classification of Doppler ultrasound blood flow signals for the purpose of disease assessment. An integration of these algorithms with the Doppler ultrasound signal collection system would improve the classification process further. For this study the Doppler ultrasound signals were collected using commercial Doppler ultrasound scanner. Digitisation was performed off-line after the analogue Doppler ultrasound signals were recorded from the Doppler scanner onto an audio tape. It is very likely that the SNR of the Doppler ultrasound signal was reduced through this process. An integration of the signal collection and digitising stages would improve the classification process, by enhancing the SNR and linking the different filter stages together.

It was noticed in this study that some Doppler signals showed a reduced amplitude at higher frequencies in the spectrogram. Figure 4.8, which is repeated here for convenience (figure 6.8), shows a spectrogram that has such a frequency band with reduced amplitude.

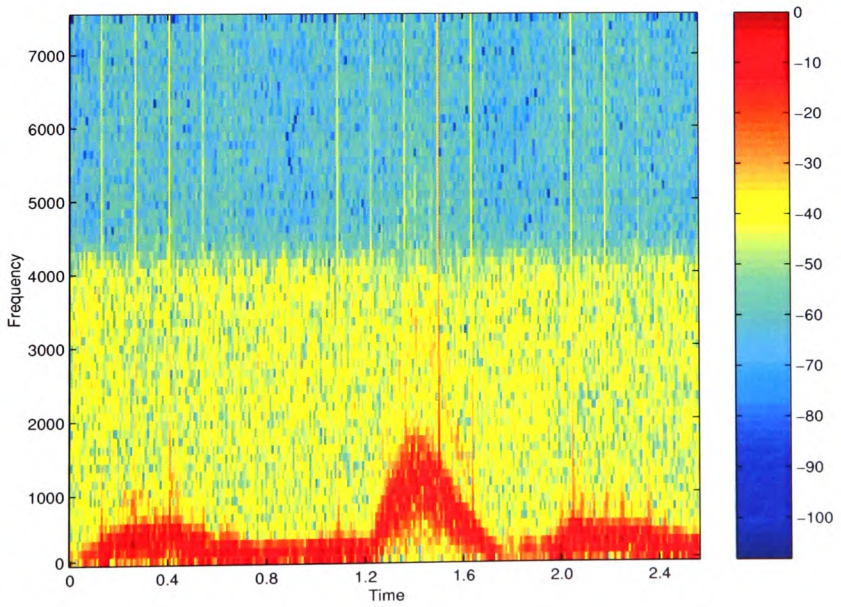

Figure 6.8: STFT spectrum of a real common femoral artery

It is believed that this amplitude reduction is caused by a low-pass filter within the Doppler scanner. The integration of the collection and digitisation stage could allow to match the parameters of the low-pass filter to the parameters of the digitising process, and vice versa. The low-pass filter could be set to have a cut-off frequency equal to the required anti-aliasing filter frequency. Alternatively, the low-pass filter cut-off frequency could be held constant for all signal acquisitions, which would allow the simple removal of this frequency band in the spectrogram. Both approaches would optimise the overall performance.

The low amplitude in these signals caused problems in the noise reduction and the MFE extraction stages. The algorithms used for the two stages were robust enough to cope with this problem, but the removal of this amplitude reduction could improve the classification process. Furthermore, it could simplify the noise reduction stage, which would only have to deal with a uniform noise floor.

The study showed successfully the full automation of the classification of the Doppler ultrasound blood flow signals. The two major problems which had to be overcome were the elimination of the operator from the noise removal and the cardiac cycle extraction processes. Both problems have not been solved previously to a level that would allow the complete automation of the classification process. The complete automation of the process achieved in this study and the moderate complexity of its stages make it suitable for implementation in a low cost commercial instrument. Such an instrument can deliver objective and more reliable diagnoses, which will be reproducible at different health centres. Offering objective diagnosis, such an instrument can also be used very effectively for training purposes. Primary healthcare is another major application area where an objective and more reliable first line of diagnosis is very useful prior to making decisions about patient referrals to specialists.

Furthermore, looking at the signals used in this study, the developed methodology was able detect disease in the aorto-iliac segment regardless of the state of the femoral-popliteal segment to a high degree of accuracy. This is an important result, as the accuracy of traditional methods were reduced when the femoral-popliteal segment was diseased. The results from this study therefore, did not only offer an automated process for the classification of Doppler ultrasound blood flow signals, but also a more reliable detection of proximal disease in the presence of distal disease.

Chapter 7

Conclusion and further work

This chapter presents the conclusion of the study (section 7.1) and provides recommendations for further work (section 7.2).

7.1 Conclusion

The primary aim of this study was to investigate the signal processing algorithms and decision making methodologies for the purpose of automating the process of assessment of lower limb vascular disease from Doppler ultrasound blood flow signals. Real clinical signals from the common femoral artery were used in the various investigations of this study to enable a valid analysis of the investigated processing algorithms and classification methods.

All aspects of the problem definition in section 1.1 were covered in this study and the objectives of this research project outlined in section 1.2 were achieved. The literature survey has shown that the classification and diagnosis of Doppler ultrasound blood flow signals has not been investigated as an integrated process and that no results were reported for a fully automated process. The work presented in

this thesis and the associated signal processing, analysis and classification results have demonstrated a fully integrated and automated diagnosis system for the assessment of vascular disease in the lower limb that removes the need for any human intervention. This clearly shows that the study has achieved its main objective and that the original work described in this thesis represents a significant contribution to knowledge in the field of Doppler ultrasound blood flow analysis.

The investigations in this study led to the following conclusions:

1. An experienced clinician can achieve a good result in classifying the Doppler ultrasound blood flow signals by visual inspection of their spectrograms only [34]. Unfortunately, this method relies on years of experience and is subject to the bias of the clinician, and the results are generally not reproducible. This study has shown that objective methods based on robust classifiers, such as Artificial Neural Networks (ANN), can produce better results than human observers.

2. The pre-processing stages of Doppler ultrasound blood flow analysis traditionally requires a number of manual interventions by an operator in order to produce a feature vector for a classifier stage. One stage is the noise reduction from the spectrogram, where the operator traditionally selects a manual threshold. The results of this study have proven that it is possible to remove the operator from this stage by introducing a two-dimensional wavelet denoising process. This novel approach did not only automated this pre-processing stage, but also improved the classification result over the traditional thresholding approach.

3. The cardiac cycle is normally used as a feature vector for the classifier in Doppler ultrasound blood flow analysis. The extraction of the cardiac cycle is

difficult and usually performed by an operator. Only a few approaches were made to extract the cardiac cycle from the MFE automatically. This study has shown that it is possible to extract the cardiac cycle accurately from the MFE over a wide range of heart rates. This was achieved by introducing new methods for the detection of the cardiac cycle peak and the gradient of the systolic upstroke in to this stage.

4. The MFE is the most important, and most commonly used, feature in the classification of Doppler ultrasound blood flow signals for the assessment of vascular disease. However, using only the MFE discards other information available in the sonogram. The results of this study showed that the Spectral Broadening Index (SBI) yields valuable information when used as an additional feature in the classification phase. The SBI improved the performance of the classification process in the majority of cases (greater than 69%). Only 15% of the cases showed a reduced classification rate, while the remaining ANNs showed no change.

5. The length of the cardiac cycle MFE is not constant and varies with the heart rate. Truncation of the MFE is the usual method of obtaining a constant length vector. Although re-sampling the cardiac cycle MFE to a constant length should provide more information, it was shown in this study that truncation of the cardiac cycle MFE yielded better results. This has confirmed that the important information is located in the first section of the MFE.

6. Wavelet compression has been applied to one- and two-dimensional data for the reduction of storage or transmission bandwidth requirement. The application of wavelet compression, to reduce the length of the feature vector, is a novel approach to Doppler ultrasound blood flow analysis. The results of

this investigation showed that an optimally selected wavelet base was able to reduce the length of the feature vector dramatically, while retaining the prominent features. In fact, in the two-class problem, the best performance was achieved by a compressed feature vector. In this case, the feature vector was compressed to 16% of its original length, and 32% of the length of a truncated feature vector with equal performance. Wavelet compression is therefore, a valid alternative to truncation, yielding shorter feature vectors with similar classification performance.

7. The detection of disease in the aorto-iliac segment from Doppler ultrasound blood flow signals is difficult in the presence of disease in the femoral-popliteal segment using standard methods. The investigations in this study showed that it is possible to detect proximal disease in the presence of distal disease to a high degree of accuracy. The results showed a classification rate of up to 96.25% for the two-class and 86.25% for the three-class problem. This was a significant improvement over previously reported results in the literature.

7.2 Further work

This study has shown that the classification and diagnosis of Doppler ultrasound blood flow signals can be automated and that the classification can be improved over the performance of human observers. During the investigations existing algorithms were modified and new algorithms were proposed to achieve this aim. From the literature review and the investigations in this study, the following recommendations are given for future research work in this field:

1. Investigation into the possible integration of the Doppler ultrasound flowmeter and scanner circuitry and the digitising stage of the Doppler ultrasound sig-

nals. This would lead to improvements of the system hardware and link the pre-processing and the data collection stage, avoiding filter cut-off frequency mismatch and intermediate signal storage on tapes. This will potentially improve the classification performance.

2. Verification of the classification approach proposed in this study using more clinical data. This may include the collection of data for a larger group of patients and the classification of theses signals into alternative bands of disease severity. As an example these bands may be 0–30%, 30%–70%, and 70%–100% stenosis.

3. Investigation into more advanced use of the spectral broadening information in the classification process. Spectral broadening can be calculated at a number of key points in the cardiac cycle and presented to the ANN as a separate feature vector.

4. Investigation of the use of additional feature vectors for presentation to the ANN in order to enhance the disease assessment. Instead of using only the MFE, the mean frequency envelope may be used together with the MFE to supply information about the spectral width of the Doppler signal.

5. Investigation into the detection of proximal and distal disease as individual cases and a combination.

References

[1] Isabel A. Wright, *Artificial Neural Network Analysis of Doppler Shift Signals*, PhD thesis, University of Wales College of Medicine, 1998.

[2] Abigail Thrush and Tim Hartshorne, *Peripheral Vascular Ultrasound: How, Why and When*, Churchill Livingstone, 1999, ISBN 0-443-06049-5.

[3] P. Atkinson and J.P. Woodcock, *Doppler Ultrasound and its Use in Clinical Measurements*, Academic Press, 1982.

[4] J.P. Woodcock, "Special ultrasonic methods for the assessment and imaging of systemic arterial disease", *British Journal of Anaesthesia*, vol. 53, pp. 719–730, 1981.

[5] Louis Allard, Guy Cloutier, Louis-Gilles Durand, Ghislaine O Roederer, and Yves E Langlois, "Limitations of ultrasonic duplex scanning for diagnosing lower limb arterial stenoses in the presence of adjacent segment disease", *Journal of Vascular Surgery*, vol. 19, no. 4, pp. 650–657, 1994.

[6] K.W. Johnston, M. Kassam, J. Koers, R.S.C. Cobbold, and D. MacHattie, "Comparative study of four methods for quantifying Doppler ultrasound waveforms from the femoral artery", *Ultrasound in Medicine & Biology*, vol. 10, no. 1, pp. 1–12, 1984.

[7] J. Dennis Baker, Herbert I. Machleder, and Robert Skidmore, "Analysis of femoral artery Doppler signals by Laplace transform damping method", *Journal of Vascular Surgery*, vol. 1, no. 4, pp. 520–524, July 1984.

[8] Z. Guo, L.-G. Durand, and H.C. Lee, "Comparison of time-frequency distribution techniques for analysis of simulated Doppler ultrasound signals of the femoral artery", *IEEE Transaction on Biomedical Engineering*, vol. 41, no. 4, pp. 332–342, April 1994.

[9] P.G. Kalman, K.W. Johnston, P. Zuech, M. Kassam, and K. Poots, "In-vitro comparison of alternative methods for quantifying the severity of Doppler spectral broadening for the diagnosis of carotid arterial occlusive disease", *Ultrasound in Medicine & Biology*, vol. 11, no. 3, pp. 435–440, 1985.

[10] D.H. Evans, W.W. Barrie, M.J. Asher, S. Bentley, and P.R.F. Bell, "The relationship between ultrasonic pulsatility index and proximal arterial stenosis in a canine model", *Circulation Research*, vol. 46, no. 4, pp. 470–475, April 1980.

[11] D.H. Evans, D.S. MacPherson, S. Bentley, M.J. Asher, and P.R.F. Bell, "The effect of proximal stenosis on Doppler waveforms: A comparison of three methods of waveform analysis in an animal model", *Clin. Phys. Physiol. Meas.*, vol. 2, no. 1, pp. 17–25, 1981.

[12] D.S. Macpherson, D.H. Evans, and P.R.F. Bell, "Common femoral artery Doppler waveforms: A comparison of three methods of objective analysis with direct pressure measurements", *British Journal of Surgery*, vol. 71, pp. 46–49, January 1984.

[13] R. Skidmore and J.P. Woodcock, "Physiological interpretation of Doppler-shift waveforms – I: Theoretical considerations", *Ultrasound in Medicine & Biology*, vol. 6, pp. 7–10, 1980.

[14] D.A. Legemate, C. Teeuwen, H. Hoeneveld, R.G.A. Ackerstaff, and B.C. Eikelboom, "Spectral analysis criteria in Duplex scanning of aortoilliac and femoropopliteal arterial disease", *Ultrasound in Biology & Medicine*, vol. 17, no. 8, pp. 769–776, 1991.

[15] R.N. Baird, D.R. Baird, P.C. Clifford, R.J. Lusby, R. Skidmoore, and J.P. Woodcock, "Upstream stenosis", *Arch. Surg.*, vol. 115, pp. 1316–1322, November 1980.

[16] A. Auckland and R. A. Hurlow, "Spectral analysis of Doppler ultrasound: Its clinical application in lower limb ischaemia", *British Journal of Surgery*, vol. 69, pp. 539–542, 1982.

[17] D.H. Evans, W.N. McDicken, R. Skidmore, and J.P. Woodcock, *Doppler Ultrasound: Physics, Instrumentation and Clinical Applications*, John Wiley, 1989, ISBN 0 471 91489 4.

[18] Isabel A. Wright, Nigel A.J. Gough, Frank Rakebrandt, Mohamed Wahab, and John P. Woodcock, "Neural network analysis of Doppler ultrasound blood flow signals: A pilot study", *Ultrasound in Medicine and Biology*, vol. 23, no. 5, pp. 683–690, 1997.

[19] Isabel A. Wright and Nigel A.J. Gough, "Artificial neural network analysis of common femoral artery Doppler shift signals: Classification of proximal disease", *Ultrasound in Medicine & Biology*, vol. 24, no. 5, pp. 735–743, 1999.

[20] J.H. Smith, J. Graham, and R.J. Taylor, "The application of an artificial neural network to Doppler ultrasound waveforms for the classification of arterial disease", *International Journal of Clinical Monitoring and Computing*, vol. 13, pp. 85–91, 1996.

[21] O. Meste, H. Rix, P. Caminal, and N.V. Thakor, "Ventricular late potentials characterization in time-frequency domain by means of a Wavelet Transform", *IEEE Transactions on Biomedical Engineering*, vol. 41, no. 7, pp. 625–634, July 1994.

[22] O. Bertrand, J. Bohorquez, and J. Pernier, "Time-frequency digital filtering based on an invertible Wavelet Transform: An application to evoked potentials", *IEEE Transaction on Biomedical Engineering*, vol. 41, no. 1, pp. 77–88, January 1994.

[23] C. Li, Ch. Zheng, and CH. Tai, "Detection of ECG characteristic points using Wavelet Transforms", *IEEE Transactions on Biomedical Engineering*, vol. 42, no. 1, pp. 21–28, 1995.

[24] M. Akay, Y. Akay, P. Cheng, and H.H. Szeto, "Time-frequency analysis of the electrocortical activity during maturation using Wavelet Transform", *Biological Cybernetics*, vol. 71, pp. 169–176, 1994.

[25] S. Pola, A. Macerata, M. Emdin, and C. Marchesi, "Estimation of the power spectral density in nonstationary cardiovascular time series: Assessing the role of the time-frequency representations (TFR)", *IEEE Transaction on Biomedical Engineering*, vol. 43, no. 1, pp. 46–59, January 1996.

[26] P.J. Fish, "Ultrasonic investigation of blood flow", *Journal of Engineering in Medicine*, vol. 213, no. 3, pp. 169–180, May 1999.

[27] J.P. Woodcock, "Developments in the clinical application of Doppler ultrasound", in *EEC - CRM/CREST Committee on Medical and Public Health Research, Proceedings of Workshop on the Clinical and Analytical Evaluation of Doppler Ultrasound Blood Flow Measurement*, M.M. Black and R. Van Noort, Eds., 1982, pp. 28–46.

[28] Keith A. Fujioka, "Effects of carotid artery obstructions", in *7th Int Symposium and Tutorials on Cerebral Hemodynamics: Basic Tutorial - Transcranial Doppler.* Institute of Applied Physiology & Medicine and The International Cerebral Hemodynamics Society, February 1993, pp. 25–46, SciMed, Unit 5, Avon Business Park, Lodge Causeway, Fishponds, Bristol BS16 3JP, UK.

[29] P.R. Hoskins, "Measurement of arterial blood flow by Doppler ultrasound", *Clinical Physics and Physiological Measurement*, vol. 11, no. 1, pp. 1–26, 1990.

[30] T.R. Kohler, D.R. Nance, M.M. Cramer, N. Vandenburghe, and D.E. Strandness Jr, "Duplex scanning for diagnosis of aortoiliac and femoropopliteal disease: A prospective study", *Circulation*, vol. 76, no. 5, pp. 1074–1080, November 1987.

[31] K.W. Johnston, B.C. Maruzzo, M. Kassam, and R.S.C. Cobbold, "Methods for obtaining, processing and quantifying Doppler blood velocity waveforms", in *Investigation of Vascular Disorders*, J S T Yao and A N Nicolaides, Eds. 1981, pp. 532 – 558, Churchill Livingstone.

[32] A.R. Baker, D.R. Prytherch, D.H. Evans, and P.R.F. Bell, "Doppler ultrasound assessment of the femoro-popliteal segment: Comparison of different

methods using ROC curve analysis", *Ultrasound in Medicine & Biology*, vol. 12, no. 6, pp. 473–482, 1986.

[33] S. Rosfors, M. Eriksson, N. Höglund, and G. Johansson, "Duplex ultrasound in patients with suspected aorto-iliac occlusive disease", *European Journal of Vascular Surgery*, vol. 7, pp. 513–517, September 1993.

[34] L. Walton and T.R.P. Martin, "Prospective assessment of the aorto-iliac segment by visual interpretation of frequency analysed Doppler waveforms — A comparison with arteriography", *Ultrasound in Medicine & Biology*, vol. 10, no. 1, pp. 27–32, 1984.

[35] K.W. Johnston and I. Taraschuk, "Validation of the role of pulsatility index in quantitation of the severity of peripheral arterial occlusive disease", *The American Journal of Surgery*, vol. 131, pp. 295–297, March 1976.

[36] K.N. Humphries, T.K. Hames, S.W.J. Smith, V.A. Cannon, and A.D.B. Chant, "Quantitative assessment of the common femoral to popliteal arterial segment using continuous wave Doppler ultrasound", *Ultrasound in Medicine & Biology*, vol. 6, pp. 99–105, 1980.

[37] D. Demorais and K.W. Johnston, "Assessment of aorto-iliac disease by non-invasive quantitative Doppler waveform analysis", *British Journal of Surgery*, vol. 68, pp. 789–792, November 1981.

[38] A.N. Nicolaides, I.C. Gordon-Smith, J. Dayandas, and H.H.G. Eastcott, "The value of Doppler blood velocity tracings in the detection of aortoiliac disease in patients with intermittent claudication", *Surgery*, vol. 80, no. 6, pp. 774–778, December 1976.

[39] J. Dennis Baker, Robert Skidmore, and Susan E. A. Cole, "Laplace transform analysis of femoral artery Doppler signals: The state of the art", *Ultrasound in Medicine & Biology*, vol. 15, no. 1, pp. 13–20, 1989.

[40] D.B. Keenan, F.J. Owens, M.S. Murphy, and D. Need, "Removal of wall-motion artefacts in Doppler ultrasound signals using linear prediction filtering", *Electronics Letters*, vol. 35, no. 4, Feburary 1999.

[41] Stéphane Mallat, *A Wavelet Tour of Signal Processing*, Academic Press, 525 B Street, Suite 1900, San Diego, CA 92101-4495, USA, 2nd edition, 1998.

[42] A.V. Oppenheim and R.W. Schafer, *Discrete-Time Signal Processing*, Prentice Hall, 2nd edition, 1989.

[43] L.Y.L. Mo, L.C.M. Yun, and R.S.C. Cobbold, "Comparison of four digital maximum frequency estimators for Doppler ultrasound", *Ultrasound in Medicine & Biology*, vol. 14, no. 5, pp. 355–363, 1988.

[44] Olivier Rioul and Martin Vetterli, "Wavelets and signal processing", *IEEE SP Magazine*, pp. 14–38, October 1991.

[45] C. Francalancia, V. Di Virgilio, E. Conti, M.L. Finocchiaro, A. Lupi, and S. Cerutti, "Parameter measurement of coronary blood flow velocity using a fast Wavelet Transform based algorithm", *18th Annual Intl. Conf. of the IEEE Engineering in Medicine and Biology Society*, pp. 875–876, 1996.

[46] B. Günther, R.F. Jimenez, and C. Picarte, "Wavelet analysis of arterial pressure and blood velocity pulsations in the aorta of anesthetized dogs", *Biology Research*, vol. 26, no. 3, pp. 391–396, 1993.

[47] F.S. Schlindwein, F. Bereksi Reguig, and P.I.J. Keeton, "Noise removal from Doppler ultrasound blood velocity signals using Wavelets", *IEE Colloquium on Medical Applications of Signal Processing*, pp. 5/1–5/6, October 1999, Ref. No. (1999/107).

[48] Ayumu Matani, Osamu Oshiro, and Kunihiro Chihara, "Doppler signal processing of blood flow using a Wavelet Transform", *Japanese Journal of Applied Physics*, vol. 35, no. 5B, pp. 3131–3134, May 1996.

[49] N. Aydin and H.S. Markus, "Wavelet analysis of quadrature Doppler ultrasound signals", in *Advances in Medical Signal and Information Processing, IEE Conference Publication No. 476*, 2000, pp. 251–256.

[50] İnan Güler, Firat Hardalaç, and Serdar Müldür, "Determination of aorta failure with the application of FFT, AR and Wavelet methods to Doppler technique", *Computers in Biology and Medicine*, vol. 31, pp. 229–238, 2001.

[51] R. Yu, A. R. Allen, and J. Watson, "An optimal Wavelet thresholding method for speckle noise reduction", *Summer School on Wavelets: Papers*, pp. 77–81, 1996, ISBN: 83-904743-3-6.

[52] Mike Sablatash and Todor Cooklev, "Compression of high-quality audio signals, including recent methods using Wavelet Packets", *Digital Signal Processing*, vol. 6, pp. 96–107, 1996.

[53] L. Pesu, E. Ademovic, J.-C. Pesquet, and P. Helistö, "Wavelet Packet based respiratory sound classification", in *Proceedings of the IEEE-SP International Symposium on Time-Frequency and Time-Scale Analysis.* The IEEE Signal Processing Society and Le Centre National de la Rechere Scientifique, June 1996, pp. 377–380.

[54] A. Quinquis, "A few practical applications of Wavelet Packets", *Digital Signal Processing*, vol. 8, pp. 49–60, 1998.

[55] Ronald R. Coifman and Mladen Victor Wickerhauser, *Experiments with Adapted Wavelet De-Noising for Medical Signals and Images*, IEEE Press, May 1995.

[56] Ronald R. Coifman and Mladen Victor Wickerhauser, "Adapted waveform de-noising for medical signals and images", *IEEE Engineering in Medicine and Biology*, vol. 14, no. 5, pp. 578–586, Sep - Oct 1995.

[57] R. R. Coifman and M. V. Wickerhauser, "Wavelets, adapted waveforms, and de-noising", *Electroencephalography & Clinical Neurophysiology - Supplement*, , no. 45, pp. 57–78, 1996.

[58] Jean-Yves David, Steven A. Jones, and Don P. Giddens, "Modern spectral analysis techniques for blood flow velocity and spectral measurements with pulsed Doppler ultrasound", *IEEE Transaction on Biomedical Engineering*, vol. 38, no. 6, pp. 589–596, June 1991.

[59] P.J. Vaitkus and R.S.C. Cobbold, "A comparative study and assessment of Doppler ultrasound spectral estimation techniques part 1: Estimation methods", *Ultrasound in Med. & Biol.*, vol. 14, no. 8, pp. 661–672, 1988.

[60] P.J. Vaitkus, R.S.C. Cobbold, and K.W. Johnston, "A comparative study and assessment of Doppler ultrasound spectral estimation techniques part II: Methods and results", *Ultrasound in Medicine & Biology*, vol. 14, no. 8, pp. 673–688, 1988.

[61] T. Kadado, D. Maulik, and S. Chakrabarti, "Comparison of parametric and

nonparametric spectral estimation of continuous ultrasound shift waveforms", *IEEE*, pp. 145–148, 1994.

[62] J.A. Jensen, C. Buelund, A. Jørgensen, and P. Munk, "Estimation of the blood velocity spectrum using a recursive lattice filter", in *Proceedings of IEEE International Ultrasonics Symposium.* 1996, IEEE.

[63] Flemming Forsberg and Harry Oung, "Comparison of time-frequency distributions for Doppler spectral estimation", *1995 IEEE Ultrasonic Symposium*, pp. 1519–1522, 1995.

[64] Flemming Forsberg, Harry Oung, and Laurence Needleman, "Doppler spectral estimation using time-frequency distributions", *IEEE Transactions on Ultrasonics, Ferroelectrics, and Frequency Control*, vol. 46, no. 3, pp. 595–608, May 1999.

[65] R.G. Gosling, D.H. King, D.L. Newman, and J.P. Woodcock, "Transcutaneous measurement of arterial blood-velocity by ultrasound", in *Ultrasonics for Industry Conference Papers.* 1969, pp. 16–23, Guildfort: IPC.

[66] R.G. Gosling et al., "The quantitative analysis of occlusive peripheral arterial disease by a non-intrusive ultrasonic technique", *Angiology*, vol. 22, pp. 52–55, 1971.

[67] K.W. Johnston, B.C. Maruzzo, and R.S.C. Cobbold, "Doppler methods for quantitative measurement and localization of peripheral arterial occlusive disease by analysis of the blood flow velocity waveform", *Untrasoun in Medicine & Biology*, vol. 4, pp. 209–223, 1978.

[68] K.C. Bodily, R.E. Zierler, M.R. Marinelli, B.L. Thiele, F.M. Greene Jr, and

D.E. Strandness Jr, "Flow disturbances following carotid endarterectomy", *Surgery, Gynecology & Obstetrics*, vol. 151, pp. 77–80, July 1980.

[69] M. Kassam, R.S.C. Cobbold, P. Zuech, and K.W. Johnston, "Quantification of carotid arterial disease by Doppler ultrasound", *IEEE Ultrasonics Symposium*, pp. 675–680, 1982.

[70] M. Kassam, K.W. Johnstone, and R.S.C. Cobbold, "Quantitative estimation of spectral broadening for the diagnosis of carotid arterial disease: Method and in vitro results", *Ultrasound in Medicine & Biology*, vol. 11, no. 3, pp. 425–433, 1985.

[71] K.W. Johnston et al., "Quantitative analysis of continuous-wave Doppler spectral broadening for the diagnosis of carotid disease: Results of a multicenter study", *Journal of Vascular Surgery*, vol. 4, pp. 493–504, 1986.

[72] S.E. Rittgers, B.M. Thornhill, and R.W. Barnes, "Quantitative analysis of carotid artery Doppler spectral waveforms: Diagnostic value of parameters", *Ultrasound in Medicine & Biology*, vol. 9, no. 3, pp. 255–264, 1983.

[73] P.M. Brown et al., "A critical study of ultrasound Doppler spectral analysis for detecting carotid disease", *Ultrasound in Medicine & Biology*, vol. 8, no. 5, pp. 515–523, 1982.

[74] C.D. Sheldon, J.A. Murie, and R.O. Quin, "Ultrasonic Doppler spectral broadening in the diagnosis of internal carotid artery stenosis", *Ultrasound in Medicine & Biology*, vol. 9, no. 6, pp. 575–580, 1983.

[75] R. Skidmore and J.P. Woodcock, "Physiological interpretation of Doppler-shift waveforms — II", *Ultrasound in Medicine &Biology*, vol. 6, pp. 219–225, 1980.

[76] R. Skidmore, J.P. Woodcock, and P.N.T. Wells, "Physiological interpretation of Doppler-shift waveforms — III: Clinical results", *Ultrasound in Medicine &Biology*, vol. 6, pp. 227–231, 1980.

[77] Y.F. Law, J.C. Graham, L.T. Cotton, and V.C. Roberts, "Validity of the transfer function model of the human arterial system of the lower limb in man", *Med. & Biol. Eng. & Comput.*, vol. 22, pp. 537–542, 1984.

[78] T.R.P. Martin et al., "Objective feature extraction applied to the diagnosis of carotid artery disease using a doppler ultrasound technique", *Clin. Phys. Physiol. Meas.*, vol. 1, no. 1, pp. 71–81, 1980.

[79] S.B. Sherriff, D.C. Barber, and T.R.P. Martin, "Use of principal component factor analysis in the detection of carotid artery disease from Doppler ultrasound", *Medical & Biological Engineering & Computing*, vol. 20, pp. 351–356, 1982.

[80] A. Cohen, *Biomedical Signal Processing: Volume II - Compression and Automatic Recognition*, CRC Press, Inc., 2000 Corporate Blvd., N.W., Boca Raton, Florida, 33431, 1986.

[81] D.H. Evans and A. Caprihan, "The application of classification techniques to biomedical data, with particular reference to ultrasonic doppler blood velocity waveforms", *IEEE Transactions on Biomedical Engineering*, vol. BME-32, no. 5, pp. 301–311, May 1985.

[82] F.M. Greene, Jr., K. Beach, D.E. Strandness, Jr., G. Fell, and D.J. Phillips, "Computer based pattern recognition of carotid arterial disease using pulsed Doppler ultrasound", *Ultrasound in Medicine & Biology*, vol. 8, no. 2, pp. 161–176, 1982.

[83] Russell C. Eberhart and Roy W. Dobbins, Eds., *Neural Network PC Tools: A Practical Guide*, Academic Press, Inc., San Diego, California CA92101, USA, 1990.

[84] B.W. Jervis et al., "Artificial neural network and spectrum analysis methods for detecting brain diseases from the CNV response in the electroencephalogram", *IEE Proc.-Sci. Meas. Technol.*, vol. 141, no. 6, pp. 432–440, November 1994.

[85] Andrew J. Gabor and Masud Seyal, "Automated interictal EEG spike detection using artificial neural networks", *Electroencephalography and clinical Neurophysiology*, vol. 83, pp. 271–280, 1992.

[86] U. Wienrich, *Wear Characterisation and Usage Level Estimation of Small DC Motors*, PhD thesis, School of Electronics, University of Glamorgan, 1999.

[87] A. Zell, *Simulation Neuronaler Netze*, Addison-Wesley, Bonn, 1994, ISBN 3-89319-554-8.

[88] Simon Haykin, *Neural Networks - A Comprehensive Foundation*, Macmillan College Publishing Company, Inc, 866 Third Avenue, New York, New York 10022, USA, 1994.

[89] Jari J. Forsström and Kevin J. Dalton, "Artificial neural networks for decision support in clinical medicine", *Annals of Medicine*, vol. 27, pp. 509–517, 1995.

[90] N. Baykal, J.A. Reggia, N. Yalabik, A. Erkmen, and M.S. Beksac, "Feature discovery and classification of Doppler ultrasound umbilical artery blood flow velocity waveforms", *Computers in Medicine and Biology*, vol. 26, no. 6, pp. 451–462, 1996.

[91] Marilyn McCord Nelson and W.T. Illingworth, *A Practical Guide to Neural Nets*, Addison-Wesley, 1992.

[92] D.H. Evans, "A pulse-foot-seeking algorithm for Doppler ultrasound waveforms", *Clin. Phys. Physiol. Meas.*, vol. 9, no. 3, pp. 267–271, 1988.

[93] K.W. Johnston, M. Kassam, and R.S.C. Cobbold, "Online identifying and quantifying Doppler ultrasound waveforms", *Medicine & Biology in Engineering & Computing*, vol. 20, pp. 336–342, May 1982.

[94] Funda Başaran, M. Sinan Beksaç, and Aydan M. Erkmen, "An automated system for the evaluation of antepartum blood flow velocity waveforms: Feature extraction", *Turkish Journal of Medical Sciences*, vol. 18, pp. 227–232, 1993.

[95] B. Das and Swapna Banerjee, "Knowledge-based Doppler blood-velocimeter system", *1998 Second Int. Conf. on Knowledge-Based Intelligent Electronic Systems*, pp. 334–339, April 1998.

[96] Juerg Tschirren, Ronald M. Lauer, and Milan Sonka, "Determination of the envelope function (maximum velocity curve) in Doppler ultrasound flow velocity diagrams", in *Medical Imaging 2000: Image Processing*, K.M. Hanson, Ed., Bellingham WA, 2000, vol. 3979, pp. 1516–1527, SPIE Proceedings.

[97] Juerg Tschirren, Ronald M. Lauer, and Milan Sonka, "Automated analysis of Doppler ultrasound velocity flow diagrams", *IEEE Transaction on Medical Imaging*, vol. 20, no. 12, pp. 1422–1425, December 2001.

[98] Juerg Tschirren, Ronald M. Lauer, and Milan Sonka, "Doppler blood velocity assessment based on image analysis of video tape recorded image data", in

Medical Imaging 2001: Image Processing, Chin-Tu Chen and Anne V. Clough, Eds., Bellingham WA, 2001, vol. 4321, pp. 305–311, SPIE Proceedings.

[99] T. Van Merode, Paul Hick, Arnold P.G. Hoeks, and Robert S. Reneman, "Limitations of Doppler spectral broadening in the early detection of carotid artery disease due to the size of the sample volume", *Ultrasound in Medicine & Biology*, vol. 9, no. 6, pp. 581–586, 1983.

[100] E. C. Ifeachor and B. W. Jervis, *Digital Signal Processing: A Practical Approach*, Addison Wesley Longman Limited, Edinburgh Gate, Harlow, Essex CM20 2JE, England, 1993.

[101] Paul I.J. Keeton, *Modern Digital Signal Processing Techniques Applied to Doppler Ultrasound*, PhD thesis, BTSP Research Group, Department of Engineering, University of Leicester, April 1997.

[102] Hong Lui and Hanoch Lev-Ari, "Optimized filter banks for efficient subband-domain estimation", Tech. Rep. TR-CDSP-96-40, Center for Communications and Digital Signal Processing, Department of Electrical and Computer Engineering, Northeastern University, Boston, MA 02115, September 1996.

[103] M. Lang, H. Guo, J. E. Odegard, and C. S. Burrus, "Nonlinear processing of a shift invariant DWT for noise reduction", in *Proceedings of SPIE Mathematical Imaging: Wavelet Applications for Dual Use.* SPIE, April 1995.

[104] David L. Donoho, "De-noising by soft-thresholding", *IEEE Transaction on Imformation Theory*, vol. 41, no. 3, pp. 613–627, May 1995.

[105] D.T. Gibbons, D.H. Evans, W.W. Barrie, and P.S. Cosgriff, "Real-time calculation of ultrasonic pulsatility index", *Medicine & Biology in Engineering & Computing*, vol. 19, pp. 28–34, January 1981.

[106] D.A. McDonald, *Blood Flow in Arteries*, London: Edward Arnold, 2nd edition, 1974.

[107] D.H. Evans, L.N.J. Archer, and M.I. Levene, "The detection of abnormal neonatal cerebral haemodynamics using principal component analysis of the doppler ultrasound waveform", *Ultarsound in Medicine & Biology*, vol. 11, no. 3, pp. 441–449, 1985.

[108] Tae Hong Park, "Salient feature extraction of musical instrument signals", Master of arts, Dartmouth College, Hanover, New Hampshire, June 2000.

[109] J.D. Touch, "A statistical method for detecting peaks in electrocardiogram signals", Tech. Rep., December 1986, Basis of: "An Exprimental ECG Scanning System, K.P. Birman and J.D. Touch, Proc. of the Ninth Annual Conf. of the IEEE Engineering in Medicine and Biology, Boston, Nov. 1987".

[110] Mateo Aboy, James McNames, and Brahm Goldstein, "Automatic detection algorithm of intracranial pressure waveform components", *Proceedings of the 23rd Annual Intl. Conf. of the IEEE Engineering in Medicine and Biology Society*, 2001.

[111] M. Aboy, C. Crespo, J. McNames, and B. Goldstein, "Automatic detection algorithm for physiologic pressure signal components", *accepted to "The Second Joint Meeting of the IEEE Engineering in Medicine and Biology Society and Biomedical Engineering Society"*, 2002.

[112] F. Rakebrandt, "Recognition and classification of Doppler ultrasound medical signals", Master's thesis, University of Glamorgan, Dept. of Electronics & IT, 1995.

[113] Ping Wu, Emmanuel C. Ifeachor, Elaine M. Allen, and Nigel R. Hudson, "An EEG feature extraction system using neural networks and statistical analysis", in *Proc. Of the Int. Conf. On Neural Networks and Expert Systems in Medicine and Healthcare*, Emmanuel C. Ifeachor and Karl G. Rosén, Eds. August 1994, pp. 542–549, Intelligent Medical Systems Series.

[114] Ji Wu, Emmanuel C. Ifeachor, Elaine M. Allen, and Nigel R. Hudson, "A neural network based artefact detection system for EEG signal processing", in *Proc. Of the Int. Conf. On Neural Networks and Expert Systems in Medicine and Healthcare*, Emmanuel C. Ifeachor and Karl G. Rosén, Eds. University of Plymouth, August 1994, pp. 257–266, Intelligent Medical Systems Series.

[115] Sholom M. Weiss and Casimir A. Kulikowski, *Computer Systems That Learn*, Morgan Kaufmann Publishers, Inc, 2929 Campus Drive, Suite 260, San Mateo, California 94403, 1991.

[116] Howard Demuth and Mark Beale, *Neural Network Toolbox for Use with Matlab, Version*, Mathworks, Inc, 24 Prime Park Way, Natick, MA 01760-1500, USA, 1998.

[117] M.T. Hagan, H.B. Demuth, and M. Beale, *Neural Network Design*, PWS Publishing Company, 20 Park Plaza, Boston, MA 02116, 1995, ISBN 0-534-94332-2 (hardcover).

[118] Bin Liu, Yuanyuan Wang, and Weiqi Wang, "Spectrogram enhancement algorithm: A soft thresholding-based approach", *Ultrasound in Medicine & Biology*, vol. 25, no. 5, pp. 839–846, 1999.

[119] Yu Zhang, Yuanyuan Wang, Weiqi Wang, and Bin Liu, "Doppler ultrasound signal denoising based on Wavelet Frames", *IEEE Transactions on Ultrason-*

ics, Ferroelectrics, and Frequency Control, vol. 48, no. 3, pp. 709–716, May 2001.

[120] P.R. Hoskins, "An investigation of simulated umbilical artery Doppler waveforms. III the effect of noise reduction algorithms on the maximum frequency envelope and on the pulsatility index", *Ultrasound in Medicine & Biology*, vol. 17, no. 7, pp. 703–708, 1991.

[121] P.R. Hoskins, T. Loupas, and W.N. McDicken, "An investigation of simulated umbilical artery doppler waveforms. i. the effect of three physical parameters on the maximum frequency envelope and on pulsatility index", *Ultrasound in Medicine & Biology*, vol. 17, no. 1, pp. 7–21, 1991.

[122] S. Pittner and S.V. Kamarthi, "Feature extraction from wavelet coefficients for pattern recognition tasks", *IEEE Transactions on Pattern Analysis and Machine Intelligence*, vol. 21, no. 1, pp. 83–88, January 1999.

[123] H.M. Kayaleh and D.A. Landgrebe, "Predicting the required number of training samples", *IEEE Transaction on Pattern Analysis and Machine Intelligence*, vol. 6, no. PAMI-5, pp. 664–667, 1983.

[124] K.W. Johnston, B.C. Maruzzo, M. Kassam, and R.S.C. Cobbold, "Quantitative analysis of Doppler blood flow velocity recordings using pulsatility index", in *Investigation of Vascular Disorders*, A N Nicolaides and J S T Yao, Eds. 1981, pp. 274 – 290, Churchill Livingstone.

Appendix A

Wavelet compression

The reduction of the feature vector using wavelet-based compression was investigated in section 4.5 of this study. The root mean square error (RMSE) between the original and the reconstructed feature vector was used to determine the best wavelet bases for the compression. The bases were chosen to offered the best comprise between the length of the compressed feature vector and the RMSE. The tables 4.1 and 4.2 in section 4.5 gave only an extract of the results of the investigation. This appendix presents the full results of the work conducted. Tables A.1 and A.2 show the results for the wavelet compression at decomposition level 2 and 3, respectively. The RMSE and the standard deviation are listed for each of the used signals.

Table A.1: Root Mean Square Error (RMSE) for wavelet decomposition at level 2 over all Doppler signals with standard deviation given in brackets. (Both rounded to three digits after the decimal point)

Wavelet	Number of retained coefficients			
(length of a2)	0	5	10	15
haar (25)	0.678 (0.442)	0.477 (0.27)	0.331 (0.186)	0.239 (0.132)

Table A.1: (continued)

Wavelet (length of a2)	Number of retained coefficients 0	5	10	15
db1 (25)	0.678 (0.442)	0.477 (0.27)	0.331 (0.186)	0.239 (0.132)
db2 (27)	0.3 (0.215)	0.158 (0.092)	0.102 (0.055)	0.072 (0.039)
db3 (28)	0.23 (0.162)	0.122 (0.073)	0.074 (0.042)	0.049 (0.028)
db4 (30)	0.186 (0.133)	0.098 (0.059)	0.061 (0.036)	0.042 (0.025)
db5 (31)	0.191 (0.179)	0.106 (0.068)	0.063 (0.038)	0.041 (0.025)
db6 (33)	0.174 (0.133)	0.106 (0.068)	0.064 (0.038)	0.043 (0.027)
db7 (34)	0.173 (0.149)	0.108 (0.07)	0.067 (0.041)	0.045 (0.027)
db8 (36)	0.159 (0.149)	0.106 (0.074)	0.069 (0.043)	0.046 (0.028)
db9 (37)	0.153 (0.144)	0.095 (0.062)	0.064 (0.041)	0.045 (0.028)
db10 (39)	0.163 (0.137)	0.096 (0.061)	0.066 (0.042)	0.046 (0.029)
sym2 (27)	0.3 (0.215)	0.158 (0.092)	0.102 (0.055)	0.072 (0.039)
sym3 (28)	0.23 (0.162)	0.122 (0.073)	0.074 (0.042)	0.049 (0.028)
sym4 (30)	0.211 (0.145)	0.113 (0.069)	0.067 (0.039)	0.045 (0.026)
sym5 (31)	0.194 (0.169)	0.109 (0.065)	0.065 (0.039)	0.043 (0.026)
sym6 (33)	0.186 (0.15)	0.104 (0.065)	0.065 (0.039)	0.044 (0.026)
sym7 (34)	0.169 (0.135)	0.106 (0.063)	0.067 (0.04)	0.044 (0.027)
sym8 (36)	0.178 (0.135)	0.112 (0.072)	0.069 (0.043)	0.046 (0.028)
coif1 (28)	0.322 (0.219)	0.16 (0.089)	0.102 (0.052)	0.073 (0.038)
coif2 (33)	0.198 (0.163)	0.118 (0.072)	0.071 (0.041)	0.047 (0.028)
coif3 (37)	0.169 (0.135)	0.102 (0.064)	0.068 (0.04)	0.047 (0.028)
coif4 (42)	0.161 (0.13)	0.097 (0.063)	0.067 (0.04)	0.048 (0.029)

Table A.1: (continued)

Wavelet (length of a2)	Number of retained coefficients			
	0	5	10	15
coif5 (46)	0.158 (0.149)	0.095 (0.068)	0.069 (0.047)	0.051 (0.033)
dmey (70)	0.156 (0.149)	0.104 (0.076)	0.084 (0.063)	0.071 (0.053)
bior1.1 (25)	0.678 (0.442)	0.477 (0.27)	0.331 (0.186)	0.239 (0.132)
bior1.3 (28)	0.693 (0.427)	0.473 (0.268)	0.327 (0.183)	0.236 (0.13)
bior1.5 (31)	0.724 (0.453)	0.537 (0.298)	0.397 (0.213)	0.297 (0.156)
bior2.2 (28)	0.232 (0.178)	0.116 (0.064)	0.075 (0.039)	0.054 (0.028)
bior2.4 (31)	0.229 (0.162)	0.135 (0.078)	0.087 (0.046)	0.062 (0.033)
bior2.6 (34)	0.227 (0.175)	0.151 (0.091)	0.098 (0.054)	0.069 (0.036)
bior2.8 (37)	0.23 (0.163)	0.148 (0.086)	0.105 (0.057)	0.074 (0.038)
bior3.1 (27)	0.165 (0.123)	0.08 (0.05)	0.048 (0.029)	0.031 (0.019)
bior3.3 (30)	0.172 (0.172)	0.083 (0.051)	0.052 (0.031)	0.035 (0.021)
bior3.5 (33)	0.153 (0.103)	0.085 (0.052)	0.055 (0.033)	0.039 (0.024)
bior3.7 (36)	0.16 (0.162)	0.091 (0.055)	0.06 (0.036)	0.042 (0.026)
bior3.9 (39)	0.153 (0.104)	0.096 (0.06)	0.065 (0.039)	0.046 (0.028)
bior4.4 (31)	0.181 (0.134)	0.1 (0.062)	0.061 (0.036)	0.041 (0.024)
bior5.5 (33)	0.169 (0.131)	0.102 (0.064)	0.063 (0.039)	0.042 (0.027)
bior6.8 (37)	0.163 (0.125)	0.099 (0.062)	0.067 (0.04)	0.046 (0.027)
rbio1.1 (25)	0.678 (0.442)	0.477 (0.27)	0.331 (0.186)	0.239 (0.132)
rbio1.3 (28)	0.223 (0.152)	0.123 (0.071)	0.073 (0.041)	0.049 (0.028)
rbio1.5 (31)	0.192 (0.183)	0.108 (0.067)	0.064 (0.038)	0.043 (0.026)
rbio2.2 (28)	0.553 (0.357)	0.274 (0.157)	0.168 (0.089)	0.117 (0.061)

Table A.1: (continued)

Wavelet (length of a2)	Number of retained coefficients 0	5	10	15
rbio2.4 (31)	0.27 (0.201)	0.166 (0.103)	0.096 (0.056)	0.062 (0.037)
rbio2.6 (34)	0.196 (0.169)	0.135 (0.087)	0.084 (0.05)	0.056 (0.033)
rbio2.8 (37)	0.175 (0.146)	0.126 (0.079)	0.085 (0.052)	0.058 (0.035)
rbio3.1 (27)	3.912 (2.334)	1.844 (1.095)	1.164 (0.682)	0.804 (0.469)
rbio3.3 (30)	0.599 (0.427)	0.295 (0.181)	0.179 (0.102)	0.118 (0.068)
rbio3.5 (33)	0.316 (0.214)	0.2 (0.129)	0.126 (0.078)	0.081 (0.05)
rbio3.7 (36)	0.238 (0.209)	0.148 (0.097)	0.099 (0.062)	0.069 (0.047)
rbio3.9 (39)	0.204 (0.152)	0.139 (0.092)	0.101 (0.064)	0.072 (0.046)
rbio4.4 (31)	0.252 (0.188)	0.15 (0.092)	0.088 (0.052)	0.058 (0.034)
rbio5.5 (33)	0.238 (0.177)	0.142 (0.091)	0.087 (0.049)	0.058 (0.033)
rbio6.8 (37)	0.173 (0.138)	0.116 (0.073)	0.079 (0.047)	0.053 (0.032)

Table A.2: Root Mean Square Error (RMSE) for wavelet decomposition at level 3 over all Doppler signals with standard deviation given in brackets. (Both rounded to three digits after the decimal point)

Wavelet (length of a3)	Number of retained coefficients 0	5	10	15
haar (13)	1.282 (0.826)	0.767 (0.446)	0.515 (0.29)	0.376 (0.213)
db1 (13)	1.282 (0.826)	0.767 (0.446)	0.515 (0.29)	0.376 (0.213)
db2 (15)	0.816 (0.575)	0.336 (0.2)	0.195 (0.109)	0.132 (0.071)
db3 (16)	0.7 (0.509)	0.283 (0.167)	0.175 (0.098)	0.116 (0.066)

Table A.2: (continued)

Wavelet (length of a3)	Number of retained coefficients 0	5	10	15
db4 (18)	0.747 (0.523)	0.338 (0.211)	0.176 (0.102)	0.11 (0.065)
db5 (20)	0.835 (0.637)	0.33 (0.211)	0.197 (0.119)	0.126 (0.075)
db6 (22)	0.662 (0.46)	0.39 (0.253)	0.215 (0.129)	0.136 (0.08)
db7 (23)	0.639 (0.47)	0.412 (0.267)	0.23 (0.144)	0.147 (0.087)
db8 (25)	0.595 (0.442)	0.365 (0.239)	0.203 (0.12)	0.141 (0.083)
db9 (27)	0.541 (0.432)	0.349 (0.266)	0.215 (0.142)	0.142 (0.085)
db10 (29)	0.62 (0.484)	0.455 (0.357)	0.286 (0.22)	0.168 (0.105)
sym2 (15)	0.816 (0.575)	0.336 (0.2)	0.195 (0.109)	0.132 (0.071)
sym3 (16)	0.7 (0.509)	0.283 (0.167)	0.175 (0.098)	0.116 (0.066)
sym4 (18)	0.58 (0.438)	0.291 (0.18)	0.178 (0.104)	0.115 (0.067)
sym5 (20)	0.49 (0.342)	0.274 (0.158)	0.163 (0.09)	0.109 (0.06)
sym6 (22)	0.731 (0.555)	0.318 (0.195)	0.186 (0.106)	0.122 (0.071)
sym7 (23)	0.531 (0.405)	0.374 (0.237)	0.212 (0.123)	0.139 (0.079)
sym8 (25)	0.756 (0.516)	0.427 (0.285)	0.249 (0.153)	0.161 (0.095)
coif1 (16)	0.652 (0.468)	0.335 (0.193)	0.203 (0.11)	0.136 (0.071)
coif2 (22)	0.793 (0.55)	0.407 (0.267)	0.213 (0.125)	0.131 (0.074)
coif3 (27)	0.602 (0.458)	0.419 (0.267)	0.249 (0.146)	0.155 (0.092)
coif4 (32)	0.543 (0.386)	0.41 (0.309)	0.242 (0.158)	0.16 (0.099)
coif5 (37)	0.569 (0.483)	0.418 (0.318)	0.279 (0.19)	0.194 (0.128)
dmey (65)	0.492 (0.364)	0.42 (0.329)	0.362 (0.271)	0.292 (0.22)
bior1.1 (13)	1.282 (0.826)	0.767 (0.446)	0.515 (0.29)	0.376 (0.213)

Table A.2: (continued)

Wavelet (length of a3)	Number of retained coefficients			
	0	5	10	15
bior1.3 (16)	1.29 (0.806)	0.762 (0.443)	0.506 (0.286)	0.368 (0.207)
bior1.5 (20)	1.298 (0.806)	0.768 (0.43)	0.558 (0.3)	0.432 (0.228)
bior2.2 (16)	0.49 (0.393)	0.225 (0.123)	0.142 (0.074)	0.099 (0.05)
bior2.4 (20)	0.739 (0.564)	0.301 (0.174)	0.19 (0.104)	0.132 (0.072)
bior2.6 (23)	0.72 (0.484)	0.425 (0.265)	0.243 (0.139)	0.171 (0.095)
bior2.8 (27)	0.633 (0.422)	0.533 (0.353)	0.305 (0.182)	0.199 (0.111)
bior3.1 (15)	0.661 (0.513)	0.207 (0.126)	0.112 (0.068)	0.071 (0.045)
bior3.3 (18)	0.698 (0.498)	0.253 (0.148)	0.127 (0.074)	0.083 (0.052)
bior3.5 (22)	0.528 (0.394)	0.263 (0.161)	0.151 (0.089)	0.1 (0.063)
bior3.7 (25)	0.639 (0.533)	0.285 (0.189)	0.163 (0.096)	0.113 (0.066)
bior3.9 (29)	0.682 (0.5)	0.326 (0.205)	0.188 (0.107)	0.133 (0.082)
bior4.4 (20)	0.686 (0.545)	0.271 (0.157)	0.164 (0.094)	0.109 (0.062)
bior5.5 (22)	0.811 (0.6)	0.368 (0.231)	0.217 (0.125)	0.13 (0.075)
bior6.8 (27)	0.527 (0.346)	0.468 (0.313)	0.247 (0.149)	0.157 (0.09)
rbio1.1 (13)	1.282 (0.826)	0.767 (0.446)	0.515 (0.29)	0.376 (0.213)
rbio1.3 (16)	0.599 (0.438)	0.319 (0.195)	0.181 (0.102)	0.115 (0.064)
rbio1.5 (20)	0.591 (0.411)	0.297 (0.175)	0.173 (0.096)	0.117 (0.065)
rbio2.2 (16)	1.195 (0.778)	0.621 (0.368)	0.358 (0.201)	0.233 (0.125)
rbio2.4 (20)	0.876 (0.631)	0.407 (0.255)	0.25 (0.15)	0.167 (0.094)
rbio2.6 (23)	0.927 (0.654)	0.546 (0.368)	0.286 (0.173)	0.174 (0.101)
rbio2.8 (27)	0.57 (0.387)	0.55 (0.375)	0.338 (0.209)	0.211 (0.125)

Table A.2: (continued)

Wavelet (length of a3)	Number of retained coefficients 0	5	10	15
rbio3.1 (15)	9.98 (5.84)	3.876 (2.296)	2.318 (1.354)	1.552 (0.926)
rbio3.3 (18)	1.894 (1.251)	0.918 (0.611)	0.461 (0.273)	0.298 (0.176)
rbio3.5 (22)	0.867 (0.603)	0.65 (0.425)	0.374 (0.218)	0.246 (0.146)
rbio3.7 (25)	0.854 (0.653)	0.728 (0.517)	0.346 (0.223)	0.208 (0.126)
rbio3.9 (29)	0.921 (0.702)	0.942 (0.688)	0.451 (0.317)	0.232 (0.138)
rbio4.4 (20)	0.807 (0.595)	0.357 (0.222)	0.215 (0.126)	0.14 (0.08)
rbio5.5 (22)	0.728 (0.507)	0.369 (0.229)	0.226 (0.133)	0.155 (0.086)
rbio6.8 (27)	0.568 (0.38)	0.528 (0.356)	0.291 (0.179)	0.185 (0.109)

Appendix B

Two-class problem

The results of the classification for the two-class problem were presented in chapter 5. The results given showed only the best classification for each data set. This appendix presents the full results.

B.1 Percentage correct

Each data set was classified by a number of ANNs with different network structures. Details about the ANN network structures used can be found in chapter 5. In addition, each data set was used 10 times with every network structure. The following figures (B.1 - B.13) show the best, the worst and the median classification result in percentage correct for each data set and network structure. The data sets that did not use the Spectral Broadening Index (SBI) as an additional feature are shown in blue, while the ones that used the SBI are shown in red. Figure B.14 shows a summary of the best classification results over all data set.

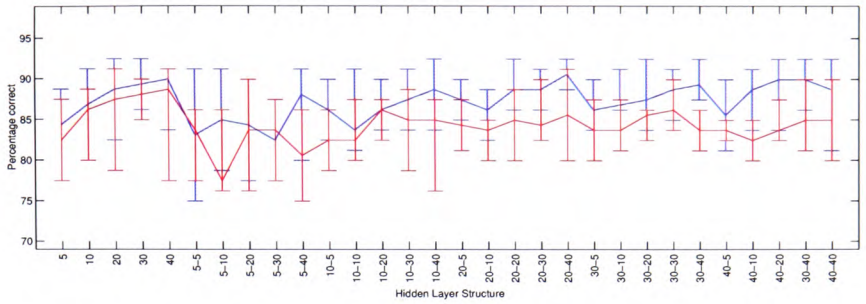

Figure B.1: Best, worst and median performance, measured as percentage correct, of ANNs using the A0 data set over the network structure (5000 epochs). Performance with (red) and without SBI (blue).

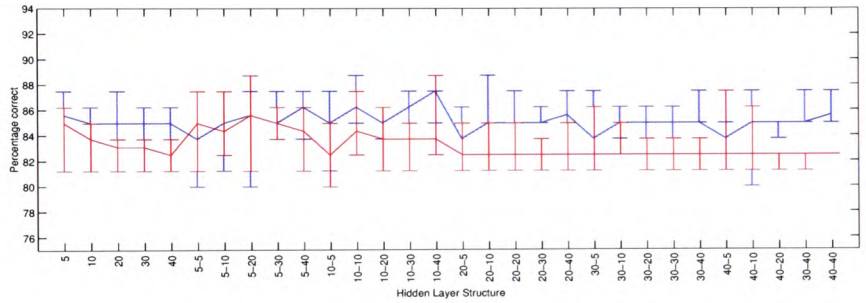

Figure B.2: Best, worst and median performance, measured as percentage correct, of ANNs using the A1 data set over the network structure (5000 epochs). Performance with (red) and without SBI (blue).

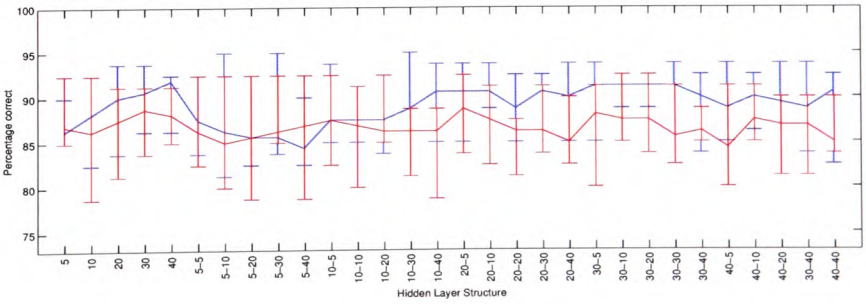

Figure B.3: Best, worst and median performance, measured as percentage correct, of ANNs using the A2 data set over the network structure (5000 epochs). Performance with (red) and without SBI (blue).

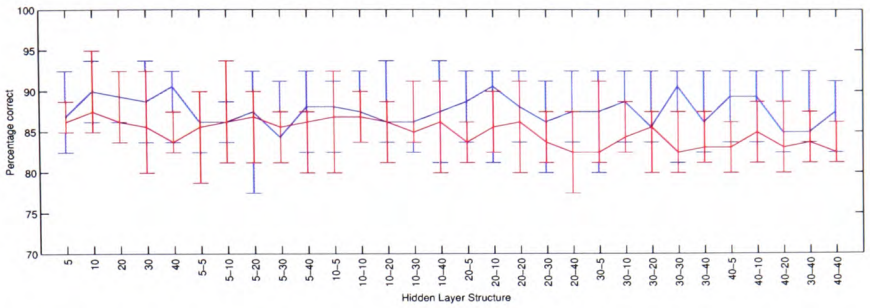

Figure B.4: Best, worst and median performance, measured as percentage correct, of ANNs using the A3 data set over the network structure (5000 epochs). Performance with (red) and without SBI (blue).

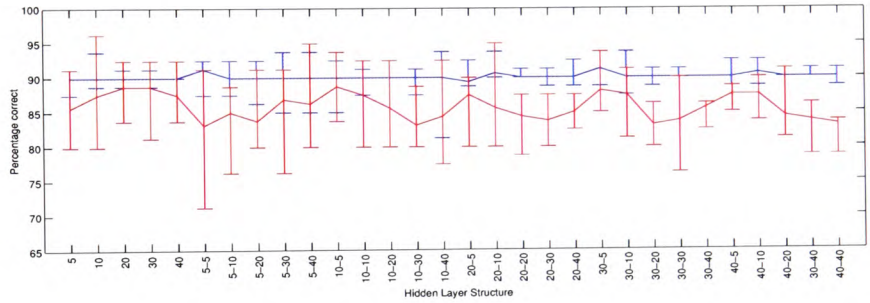

Figure B.5: Best, worst and median performance, measured as percentage correct, of ANNs using the A4 data set over the network structure (5000 epochs). Performance with (red) and without SBI (blue).

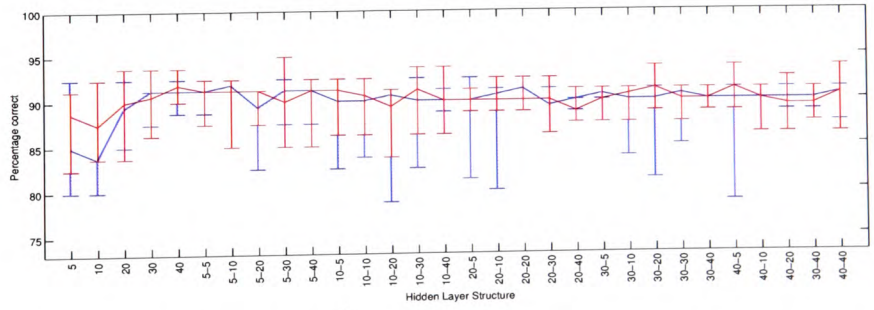

Figure B.6: Best, worst and median performance, measured as percentage correct, of ANNs using the A5 data set over the network structure (5000 epochs). Performance with (red) and without SBI (blue).

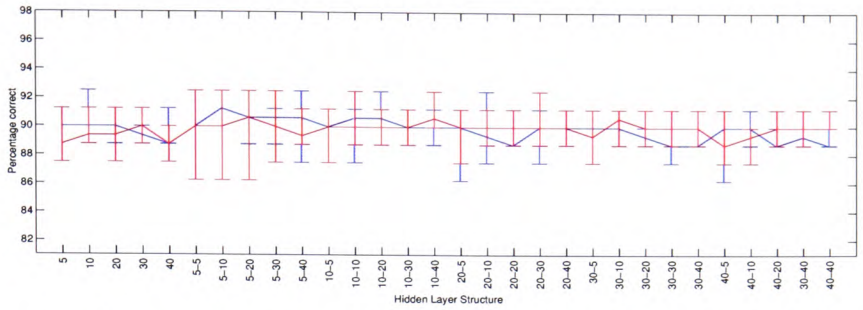

Figure B.7: Best, worst and median performance, measured as percentage correct, of ANNs using the A6 data set over the network structure (5000 epochs). Performance with (red) and without SBI (blue).

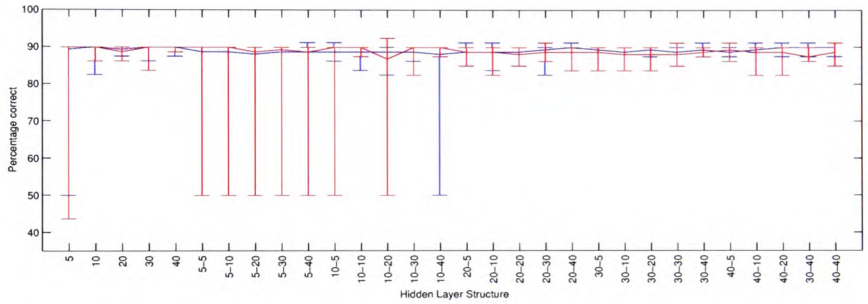

Figure B.8: Best, worst and median performance, measured as percentage correct, of ANNs using the A7 data set over the network structure (5000 epochs). Performance with (red) and without SBI (blue).

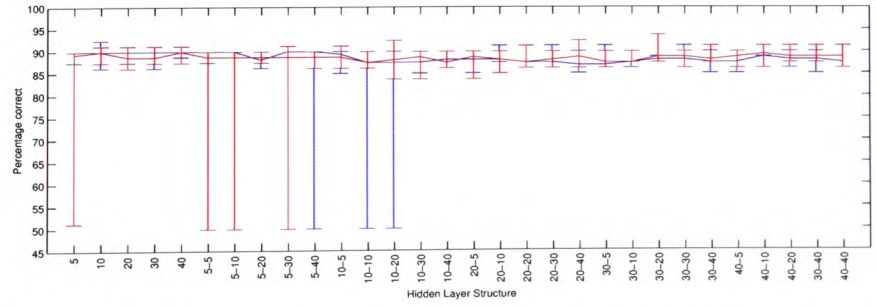

Figure B.9: Best, worst and median performance, measured as percentage correct, of ANNs using the A8 data set over the network structure (5000 epochs). Performance with (red) and without SBI (blue).

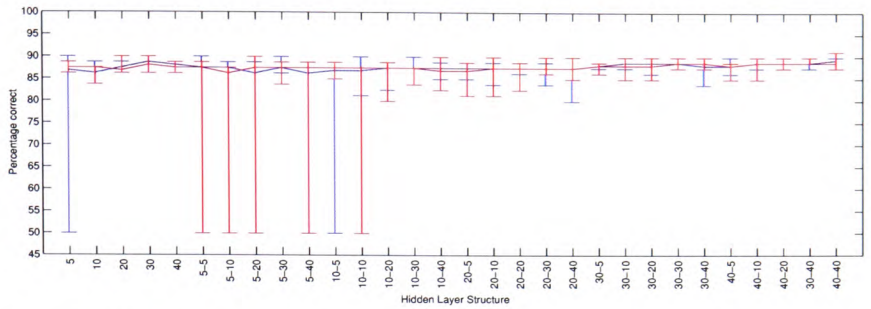

Figure B.10: Best, worst and median performance, measured as percentage correct, of ANNs using the A9 data set over the network structure (5000 epochs). Performance with (red) and without SBI (blue).

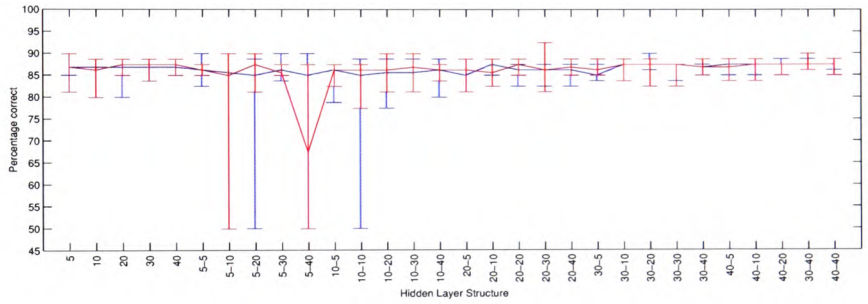

Figure B.11: Best, worst and median performance, measured as percentage correct, of ANNs using the A10 data set over the network structure (5000 epochs). Performance with (red) and without SBI (blue).

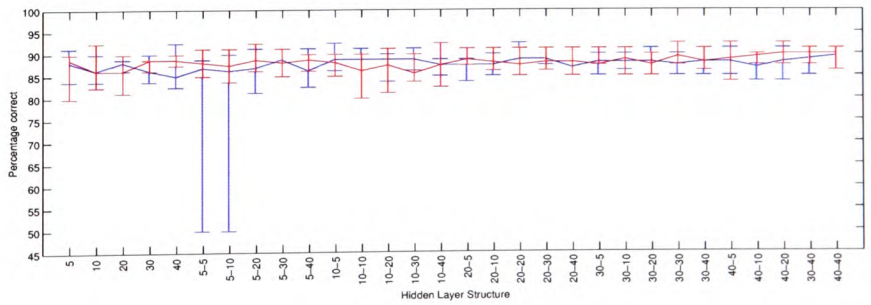

Figure B.12: Best, worst and median performance, measured as percentage correct, of ANNs using the A11 data set over the network structure (5000 epochs). Performance with (red) and without SBI (blue).

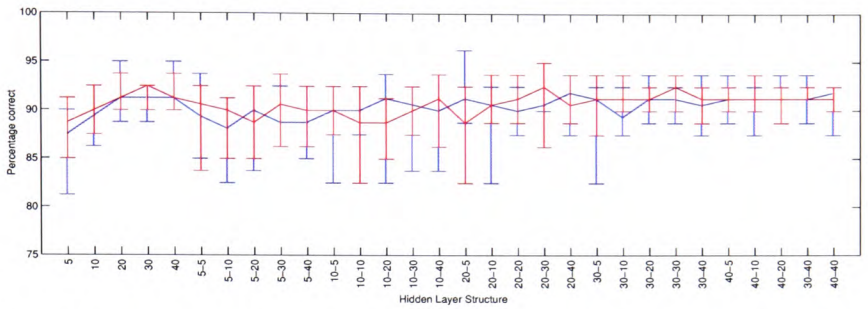

Figure B.13: Best, worst and median performance, measured as percentage correct, of ANNs using the A12 data set over the network structure (5000 epochs). Performance with (red) and without SBI (blue).

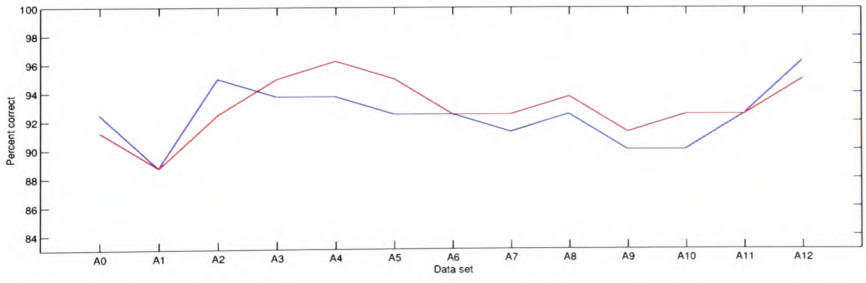

Figure B.14: Best performance, measured as percentage correct, of ANNs across data sets(5000 epochs). Performance with (red) and without SBI (blue).

B.2 Performance metrics

Chapter 5 presented a summary of the performance metrics for the best ANN network structure for each data set. Only the smallest ANN was presented earlier when more than one ANN network structure achieved the best classification result. This section presents the performance metrics for all best performing ANNs.

Table B.1: Performance metrics of the best performing ANN structures presented with data set A0. Best performing network structures without SBI: 20, 30, 10-40, 20-20, 20-40, 30-20, 30-40, 40-20, 40-30 and 40-40. Best performing network structures with SBI: 20, 40 and 20-40.

Performance metric		Performance without SBI	Performance with SBI
Percentage correct		92.5%	91.25%
No significant disease	Recall	0.950	0.925
	Precision	0.905	0.902
	Sensitivity	0.95	0.925
	Specificity	0.90	0.900
	False Alarm Rate	0.100	0.100
Significant disease	Recall	0.900	0.900
	Precision	0.947	0.923
	Sensitivity	0.900	0.900
	Specificity	0.950	0.925
	False Alarm Rate	0.05	0.075

Table B.2: Performance metrics of the best performing ANN structures presented with data set A1. Best performing network structures without SBI: 10-10 and 20-10. Best performing network structures with SBI: 5-20 and 10-40.

Performance metric		Performance without SBI	Performance with SBI
Percentage correct		88.75%	88.75%
No significant disease	Recall	0.925	0.925
	Precision	0.860	0.860
	Sensitivity	0.925	0.925
	Specificity	0.850	0.850
	False Alarm Rate	0.150	0.150
Significant disease	Recall	0.850	0.850
	Precision	0.919	0.919
	Sensitivity	0.850	0.850
	Specificity	0.925	0.925
	False Alarm Rate	0.075	0.075

Table B.3: Performance metrics of the best performing ANN structures presented with data set A2. Best performing network structures without SBI: 5-10, 5-30 and 10-30. Best performing network structures with SBI: 5, 5-5 and 5-20 (all group A); 10 (group B); 5-10, 5-30, 5-40, 10-5, 10-20, 20-5, 30-10 and 30-20 (all group C).

Performance metric		Performance without SBI	Performance with SBI		
			A	B	C
Percentage correct		95%	92.5%		
No significant disease	Recall	0.975	0.925	0.975	0.95
	Precision	0.923	0.925	0.886	0.905
	Sensitivity	0.975	0.925	0.975	0.95
	Specificity	0.925	0.925	0.875	0.9
	False Alarm Rate	0.075	0.075	0.125	0.1
Significant disease	Recall	0.925	0.925	0.875	0.9
	Precision	0.974	0.925	0.972	0.947
	Sensitivity	0.925	0.925	0.875	0.9
	Specificity	0.975	0.925	0.975	0.95
	False Alarm Rate	0.025	0.075	0.025	0.05

Table B.4: Performance metrics of the best performing ANN structures presented with data set A3. Best performing network structures without SBI: 10, 30, 10-20 and 10-40. Best performing network structures with SBI: 10.

Performance metric		Performance without SBI	Performance with SBI
Percentage correct		93.75%	95%
No significant disease	Recall	0.975	0.975
	Precision	0.907	0.929
	Sensitivity	0.975	0.975
	Specificity	0.9	0.925
	False Alarm Rate	0.1	0.075
Significant disease	Recall	0.9	0.925
	Precision	0.973	0.974
	Sensitivity	0.9	0.925
	Specificity	0.975	0.975
	False Alarm Rate	0.025	0.025

Table B.5: Performance metrics of the best performing ANN structures presented with data set A4. Best performing network structures without SBI: 10, 5-30 and 5-40 (all group A); 10-40, 20-10, 30-5 and 30-10 (all group B). Best performing network structures with SBI: 10.

Performance metric		Performance without SBI		Performance with SBI
		A	B	
Percentage correct		93.75%		96.25%
No significant disease	Recall	0.95	0.975	0.975
	Precision	0.927	0.907	0.951
	Sensitivity	0.95	0.975	0.975
	Specificity	0.925	0.9	0.95
	False Alarm Rate	0.075	0.1	0.05
Significant disease	Recall	0.925	0.9	0.95
	Precision	0.949	0.973	0.974
	Sensitivity	0.925	0.9	0.95
	Specificity	0.95	0.975	0.975
	False Alarm Rate	0.05	0.025	0.025

Table B.6: Performance metrics of the best performing ANN structures presented with data set A5. Best performing network structures without SBI: 5 (group A); 10, 20, 40, 5-5, 5-10, 5-30, 5-40, 10-5, 10-10, 10-30, 20-5 and 20-20 (all group B). Best performing network structures with SBI: 5-30.

Performance metric		Performance without SBI A	Performance without SBI B	Performance with SBI
Percentage correct		92.5%		95%
No significant disease	Recall	0.95	0.925	0.95
	Precision	0.905	0.925	0.95
	Sensitivity	0.95	0.925	0.95
	Specificity	0.9	0.925	0.95
	False Alarm Rate	0.1	0.075	0.05
Significant disease	Recall	0.9	0.925	0.95
	Precision	0.947	0.925	0.95
	Sensitivity	0.9	0.925	0.95
	Specificity	0.95	0.925	0.95
	False Alarm Rate	0.05	0.075	0.05

Table B.7: Performance metrics of the best performing ANN structures presented with data set A6. Best performing network structures without SBI: 10, 5-10, 5-40, 10-20 and 20-10 (all group A); 5-5 and 5-20 (both group B). Best performing network structures with SBI: 5-5, 10-10, 10-40 and 20-30 (all group A); 5-20 and 5-30 (both group B).

Performance metric		Performance without SBI A	Performance without SBI B	Performance with SBI A	Performance with SBI B
Percentage correct		92.5%		92.5%	
No significant disease	Recall	0.95	0.975	0.95	0.975
	Precision	0.905	0.886	0.909	0.886
	Sensitivity	0.95	0.975	0.95	0.975
	Specificity	0.9	0.875	0.9	0.875
	False Alarm Rate	0.1	0.125	0.1	0.125
Significant disease	Recall	0.9	0.875	0.9	0.875
	Precision	0.947	0.972	0.947	0.972
	Sensitivity	0.9	0.875	0.9	0.875
	Specificity	0.95	0.975	0.95	0.975
	False Alarm Rate	0.05	0.025	0.05	0.025

Table B.8: Performance metrics of the best performing ANN structures presented with data set A7. Best performing network structures without SBI: 10-5, 20-5, 20-40, 40-10, 40-20, 40-30 and 40-40 (all group A); 5-40 and 30-40 (both group B). Best performing network structures with SBI: 10-20.

Performance metric		Performance without SBI A	Performance without SBI B	Performance with SBI
Percentage correct		91.25%		92.5%
No significant disease	Recall	0.925	0.95	0.95
	Precision	0.903	0.884	0.905
	Sensitivity	0.925	0.95	0.95
	Specificity	0.9	0.875	0.9
	False Alarm Rate	0.1	0.125	0.1
Significant disease	Recall	0.9	0.875	0.9
	Precision	0.923	0.946	0.947
	Sensitivity	0.9	0.875	0.9
	Specificity	0.925	0.95	0.95
	False Alarm Rate	0.075	0.05	0.05

Table B.9: Performance metrics of the best performing ANN structures presented with data set A8. Best performing network structures without SBI: 10. Best performing network structures with SBI: 30-20.

Performance metric		Performance without SBI	Performance with SBI
Percentage correct		92.5%	93.75%
No significant disease	Recall	0.95	0.975
	Precision	0.905	0.907
	Sensitivity	0.95	0.975
	Specificity	0.9	0.9
	False Alarm Rate	0.1	0.1
Significant disease	Recall	0.9	0.9
	Precision	0.947	0.973
	Sensitivity	0.9	0.9
	Specificity	0.95	0.975
	False Alarm Rate	0.05	0.025

Table B.10: Performance metrics of the best performing ANN structures presented with data set A9. Best performing network structures without SBI: 5, 30, 5-5, 5-30, 10-10, 10-30, 20-40, 30-10, 30-20, 30-30, 30-40, 40-5, 40-10, 40-20, 40-30 and 40-40. Best performing network structures with SBI: 40-40.

Performance metric		Performance without SBI	Performance with SBI
Percentage correct		90%	91.25%
No significant disease	Recall	0.9	0.925
	Precision	0.9	0.902
	Sensitivity	0.9	0.925
	Specificity	0.9	0.9
	False Alarm Rate	0.1	0.1
Significant disease	Recall	0.9	0.9
	Precision	0.9	0.923
	Sensitivity	0.9	0.9
	Specificity	0.9	0.925
	False Alarm Rate	0.1	0.075

Table B.11: Performance metrics of the best performing ANN structures presented with data set A10. Best performing network structures without SBI: 5, 5-5, 5-10, 5-30, 5-40 and 30-20. Best performing network structures with SBI: 20-30.

Performance metric		Performance without SBI	Performance with SBI
Percentage correct		90%	92.5%
No significant disease	Recall	0.9	0.95
	Precision	0.9	0.905
	Sensitivity	0.9	0.95
	Specificity	0.9	0.9
	False Alarm Rate	0.1	0.1
Significant disease	Recall	0.9	0.9
	Precision	0.9	0.947
	Sensitivity	0.9	0.9
	Specificity	0.9	0.95
	False Alarm Rate	0.1	0.05

Table B.12: Performance metrics of the best performing ANN structures presented with data set A11. Best performing network structures without SBI: 40, 10-5 and 20-20. Best performing network structures with SBI:10, 10-40, 30-30, 40-5 and 40-20 (all group A); 5-20 (group B).

Performance metric		Performance without SBI	with SBI A	with SBI B
Percentage correct		92.5%	92.5%	
No significant disease	Recall	0.95	0.95	0.975
	Precision	0.905	0.905	0.882
	Sensitivity	0.95	0.95	0.975
	Specificity	0.9	0.9	0.875
	False Alarm Rate	0.1	0.1	0.125
Significant disease	Recall	0.9	0.9	0.875
	Precision	0.947	0.947	0.972
	Sensitivity	0.9	0.9	0.875
	Specificity	0.95	0.95	0.975
	False Alarm Rate	0.05	0.05	0.025

Table B.13: Performance metrics of the best performing ANN structures presented with data set A12. Best performing network structures without SBI: 20-5. Best performing network structures with SBI: 20-30.

Performance metric		Performance without SBI	with SBI
Percentage correct		96.25%	95%
No significant disease	Recall	1.0	1.0
	Precision	0.93	0.909
	Sensitivity	1.0	1.0
	Specificity	0.925	0.9
	False Alarm Rate	0.075	0.1
Significant disease	Recall	0.925	0.9
	Precision	1.0	1.0
	Sensitivity	0.925	0.9
	Specificity	1.0	1.0
	False Alarm Rate	0	0

Appendix C

Three-class problem

The results of the classification for the two-class problem were presented in chapter 5. The results given showed only the best classification for each data set. This appendix presents the full results.

C.1 Percentage correct

Each data set was classified by a number of ANNs with different network structures. Details about the ANN network structures used can be found in chapter 5. In addition, each data set was used 10 times with every network structure. The following figures (C.1 - C.13) show the best, the worst and the median classification result in percentage correct for each data set and network structure. The data sets that did not use the Spectral Broadening Index (SBI) as an additional feature are shown in blue, while the ones that used the SBI are shown in red. Figure C.14 shows a summary of the best classification results over all data set.

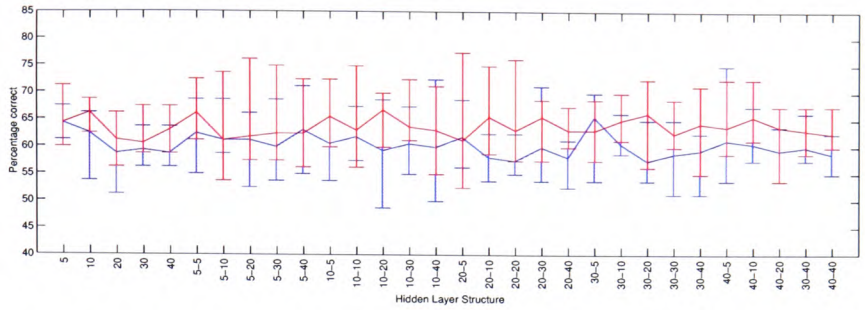

Figure C.1: Best, worst and median performance, measured as percentage correct, of ANNs using the A0 data set over the network structure (5000 epochs). Performance with (red) and without SBI (blue).

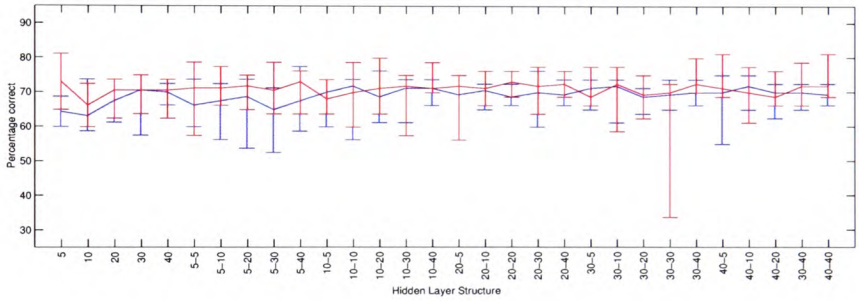

Figure C.2: Best, worst and median performance, measured as percentage correct, of ANNs using the A1 data set over the network structure (5000 epochs). Performance with (red) and without SBI (blue).

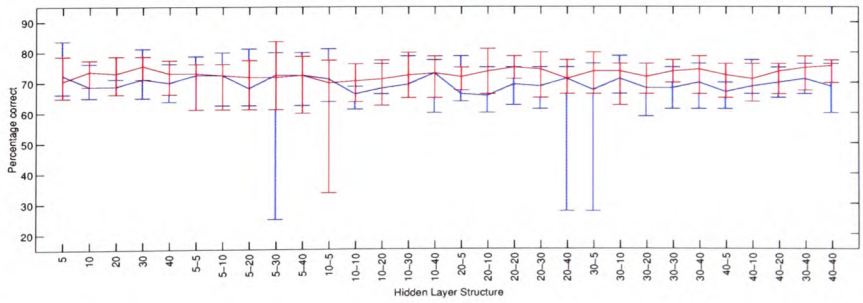

Figure C.3: Best, worst and median performance, measured as percentage correct, of ANNs using the A2 data set over the network structure (5000 epochs). Performance with (red) and without SBI (blue).

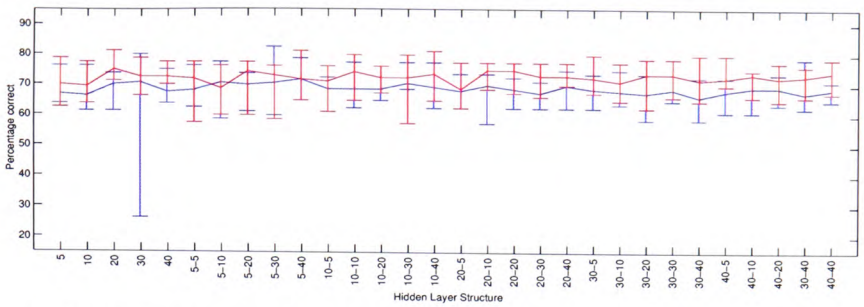

Figure C.4: Best, worst and median performance, measured as percentage correct, of ANNs using the A3 data set over the network structure (5000 epochs). Performance with (red) and without SBI (blue).

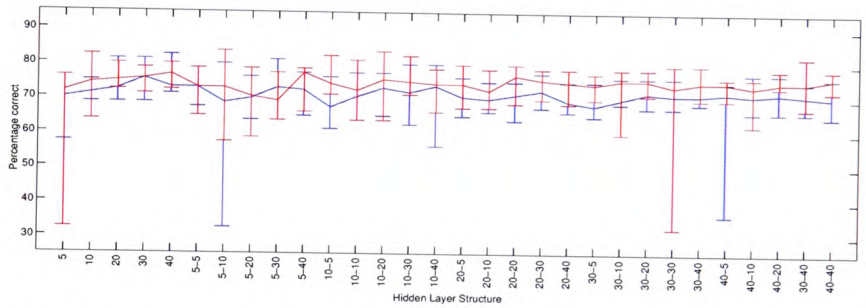

Figure C.5: Best, worst and median performance, measured as percentage correct, of ANNs using the A4 data set over the network structure (5000 epochs). Performance with (red) and without SBI (blue).

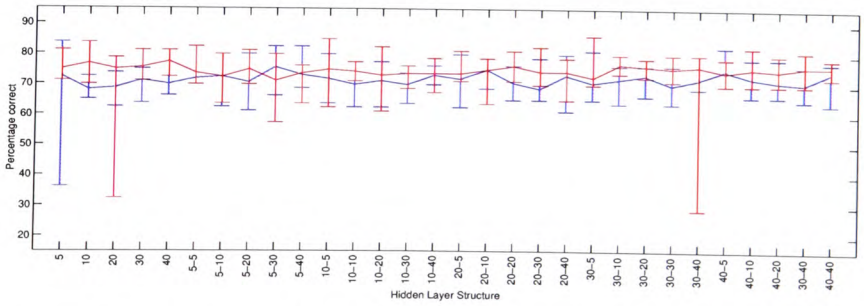

Figure C.6: Best, worst and median performance, measured as percentage correct, of ANNs using the A5 data set over the network structure (5000 epochs). Performance with (red) and without SBI (blue).

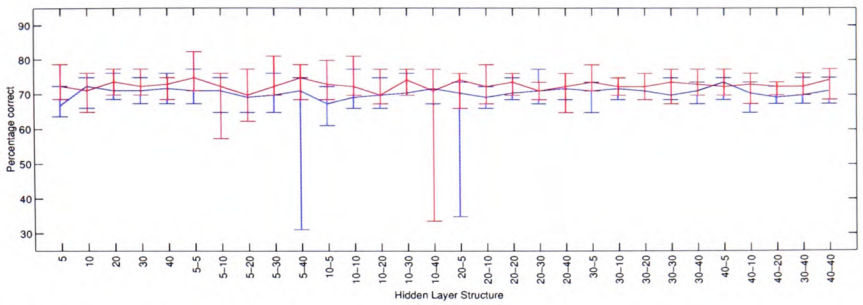

Figure C.7: Best, worst and median performance, measured as percentage correct, of ANNs using the A6 data set over the network structure (5000 epochs). Performance with (red) and without SBI (blue).

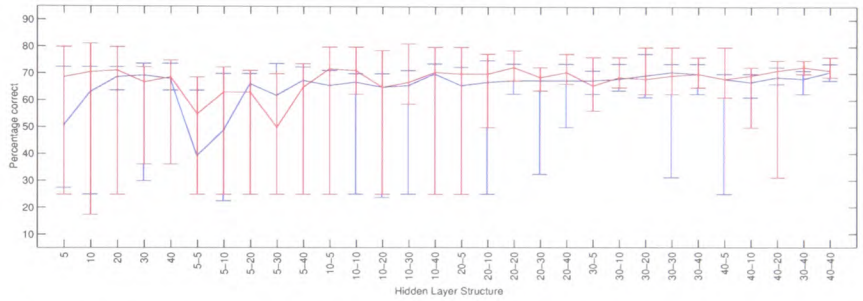

Figure C.8: Best, worst and median performance, measured as percentage correct, of ANNs using the A7 data set over the network structure (5000 epochs). Performance with (red) and without SBI (blue).

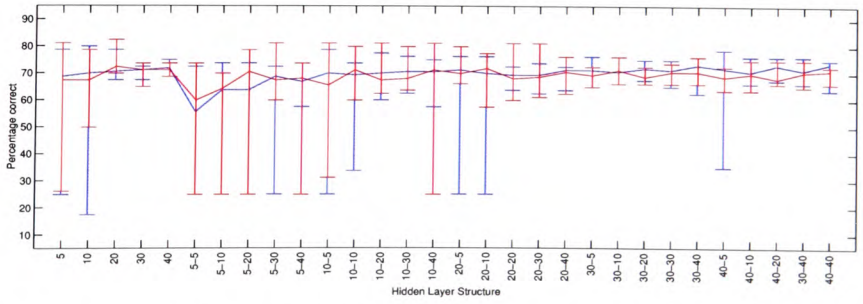

Figure C.9: Best, worst and median performance, measured as percentage correct, of ANNs using the A8 data set over the network structure (5000 epochs). Performance with (red) and without SBI (blue).

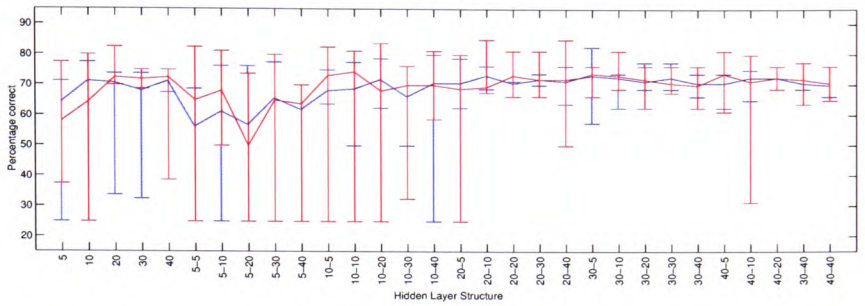

Figure C.10: Best, worst and median performance, measured as percentage correct, of ANNs using the A9 data set over the network structure (5000 epochs). Performance with (red) and without SBI (blue).

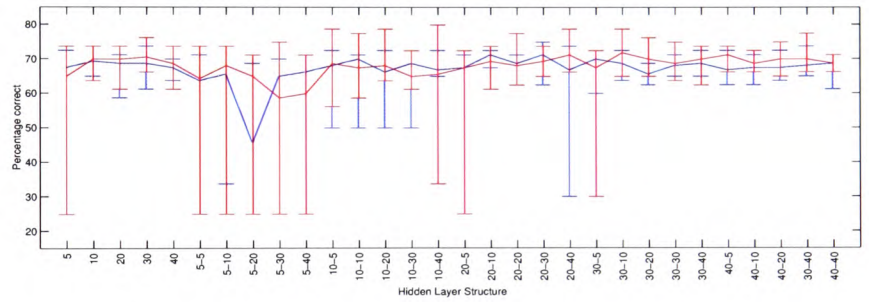

Figure C.11: Best, worst and median performance, measured as percentage correct, of ANNs using the A10 data set over the network structure (5000 epochs). Performance with (red) and without SBI (blue).

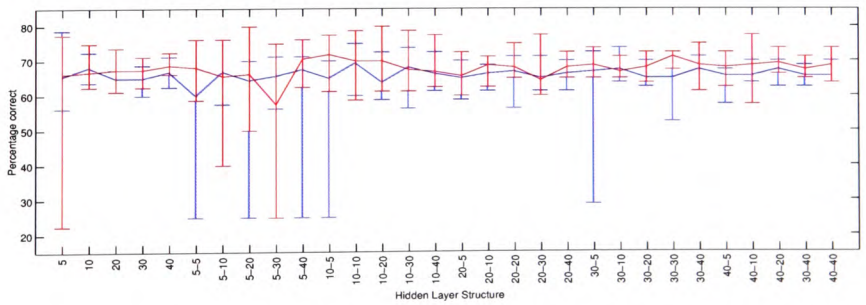

Figure C.12: Best, worst and median performance, measured as percentage correct, of ANNs using the A11 data set over the network structure (5000 epochs). Performance with (red) and without SBI (blue).

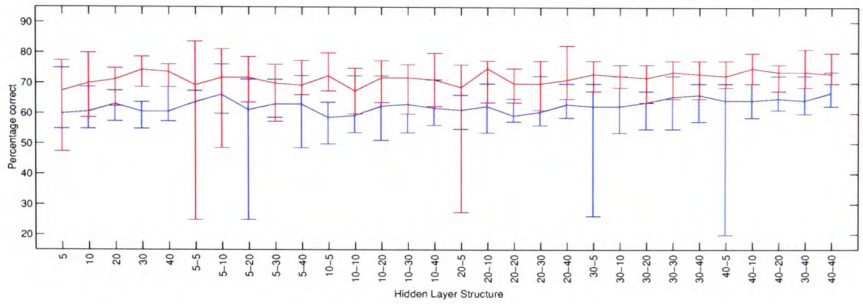

Figure C.13: Best, worst and median performance, measured as percentage correct, of ANNs using the A12 data set over the network structure (5000 epochs). Performance with (red) and without SBI (blue).

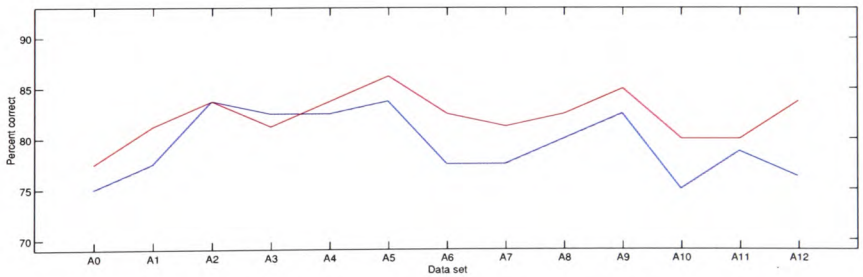

Figure C.14: Best performance, measured as percentage correct, of ANNs across data sets(5000 epochs). Performance with (red) and without SBI (blue).

C.2 Performance metrics

Chapter 5 presented a summary of the performance metrics for the best ANN network structure for each data set. Only the smallest ANN was presented earlier when more than one ANN network structure achieved the best classification result. This section presents the performance metrics for all best performing ANNs.

Table C.1: Performance metrics of the best performing ANN structures presented with data set A0. Best performing network structures without SBI: 10-5. Best performing network structures with SBI: 20-5.

Performance metric		Performance without SBI 10-5	Performance with SBI 20-5
Percentage correct		72.5%	77.5%
No significant disease	Recall	0.925	0.9
	Precision	0.902	0.857
	Sensitivity	0.925	0.900
	Specificity	0.900	0.850
	False Alarm Rate	0.100	0.150
Significant disease	Recall	0.35	0.45
	Precision	0.467	0.75
	Sensitivity	0.35	0.45
	Specificity	0.867	0.95
	False Alarm Rate	0.133	0.05
Occlusive disease	Recall	0.7	0.85
	Precision	0.583	0.654
	Sensitivity	0.7	0.85
	Specificity	0.833	0.85
	False Alarm Rate	0.167	0.15

Table C.2: Performance metrics of the best performing ANN structures presented with data set A1. Best performing network structures without SBI: 20-5. Best performing network structures with SBI: 20-30.

Performance metric		Performance				
		without SBI		with SBI		
		10-20	20-30	5	40-5	40-40
Percentage correct		76.25%		81.25%		
No significant disease	Recall	0.875	0.875	0.9	0.85	0.875
	Precision	0.534	0.875	0.837	0.85	0.854
	Sensitivity	0.875	0.875	0.9	0.85	0.875
	Specificity	0.85	0.875	0.825	0.85	0.85
	False Alarm Rate	0.150	0.125	0.175	0.15	0.15
Significant disease	Recall	0.55	0.6	0.55	0.55	0.5
	Precision	0.579	0.571	0.688	0.733	0.769
	Sensitivity	0.55	0.6	0.55	0.55	0.5
	Specificity	0.867	0.85	0.917	0.933	0.95
	False Alarm Rate	0.133	0.15	0.083	0.067	0.05
Occlusive disease	Recall	0.75	0.7	0.9	1.0	1.0
	Precision	0.75	0.737	0.857	0.8	0.769
	Sensitivity	0.75	0.7	0.9	1.0	1.0
	Specificity	0.917	0.917	0.95	0.917	0.9
	False Alarm Rate	0.083	0.083	0.05	0.083	0.1

Table C.3: Performance metrics of the best performing ANN structures presented with data set A2.

Performance metric		Performance without SBI 5	Performance with SBI 5-30
Percentage correct		83.75%	83.75%
No significant disease	Recall	0.9	0.975
	Precision	0.923	0.907
	Sensitivity	0.9	0.975
	Specificity	0.925	0.9
	False Alarm Rate	0.075	0.1
Significant disease	Recall	0.6	0.7
	Precision	0.75	0.737
	Sensitivity	0.6	0.7
	Specificity	0.933	0.917
	False Alarm Rate	0.067	0.083
Occlusive disease	Recall	0.95	0.7
	Precision	0.76	0.778
	Sensitivity	0.95	0.7
	Specificity	0.9	0.933
	False Alarm Rate	0.1	0.067

Table C.4: Performance metrics of the best performing ANN structures presented with data set A3.

Performance metric		Performance without SBI 5-30	Performance with SBI 20	5-40	10-40
Percentage correct		82.5%	81.25%		
No significant disease	Recall	0.975	0.95	0.925	0.95
	Precision	0.907	0.95	0.902	0.927
	Sensitivity	0.975	0.95	0.925	0.95
	Specificity	0.9	0.95	0.9	0.925
	False Alarm Rate	0.1	0.05	0.1	0.075
Significant disease	Recall	0.6	0.6	0.7	0.65
	Precision	0.706	0.632	0.609	0.65
	Sensitivity	0.6	0.6	0.7	0.65
	Specificity	0.917	0.883	0.85	0.883
	False Alarm Rate	0.083	0.117	0.15	0.117
Occlusive disease	Recall	0.75	0.75	0.7	0.7
	Precision	0.75	0.714	0.875	0.737
	Sensitivity	0.75	0.75	0.7	0.7
	Specificity	0.917	0.9	0.967	0.917
	False Alarm Rate	0.083	0.1	0.033	0.083

Table C.5: Performance metrics of the best performing ANN structures presented with data set A4.

Performance metric		Performance without SBI 40	Performance with SBI 5-10	Performance with SBI 10-20
Percentage correct		82.5%	83.75%	
No significant disease	Recall	0.95	0.95	0.975
	Precision	0.927	1.0	0.951
	Sensitivity	0.95	0.95	0.975
	Specificity	0.925	1.0	0.95
	False Alarm Rate	0.075	0.0	0.05
Significant disease	Recall	0.55	0.75	0.7
	Precision	0.733	0.652	0.667
	Sensitivity	0.55	0.75	0.7
	Specificity	0.933	0.867	0.883
	False Alarm Rate	0.067	0.133	0.117
Occlusive disease	Recall	0.85	0.7	0.7
	Precision	0.708	0.737	0.778
	Sensitivity	0.85	0.7	0.7
	Specificity	0.883	0.917	0.933
	False Alarm Rate	0.117	0.083	0.067

Table C.6: Performance metrics of the best performing ANN structures presented with data set A5.

Performance metric		Performance without SBI 5	Performance with SBI 30-5
Percentage correct		83.75%	86.25%
No significant disease	Recall	0.925	0.925
	Precision	0.925	0.902
	Sensitivity	0.925	0.925
	Specificity	0.925	0.9
	False Alarm Rate	0.075	0.1
Significant disease	Recall	0.6	0.7
	Precision	0.75	0.824
	Sensitivity	0.6	0.7
	Specificity	0.933	0.95
	False Alarm Rate	0.067	0.05
Occlusive disease	Recall	0.9	0.9
	Precision	0.75	0.818
	Sensitivity	0.9	0.9
	Specificity	0.9	0.933
	False Alarm Rate	0.1	0.067

Table C.7: Performance metrics of the best performing ANN structures presented with data set A6.

Performance metric		Performance without SBI					with SBI
		5-5	5-20	10-10	10-40	20-30	5-5
Percentage correct		77.5%					82.5%
No significant disease	Recall	0.9	0.9	0.925	0.9	0.9	0.875
	Precision	0.878	0.878	0.902	0.9	0.878	0.897
	Sensitivity	0.9	0.9	0.925	0.9	0.9	0.875
	Specificity	0.875	0.875	0.9	0.9	0.875	0.9
	False Alarm Rate	0.125	0.125	0.1	0.1	0.125	0.1
Significant disease	Recall	0.55	0.55	0.5	0.55	0.6	0.6
	Precision	0.611	0.579	0.556	0.579	0.6	0.706
	Sensitivity	0.55	0.55	0.5	0.55	0.6	0.6
	Specificity	0.883	0.867	0.867	0.867	0.867	0.917
	False Alarm Rate	0.117	0.133	0.133	0.133	0.133	0.083
Occlusive disease	Recall	0.75	0.75	0.75	0.75	0.7	0.95
	Precision	0.714	0.75	0.714	0.714	0.737	0.792
	Sensitivity	0.75	0.75	0.75	0.75	0.7	0.95
	Specificity	0.9	0.917	0.9	0.9	0.917	0.917
	False Alarm Rate	0.1	0.083	0.1	0.1	0.083	0.083

Table C.8: Performance metrics of the best performing ANN structures presented with data set A7.

Performance metric		Performance without SBI	with SBI	
		30-20	10	10-30
Percentage correct		77.5%	81.25%	
No significant disease	Recall	0.9	0.825	0.85
	Precision	0.837	0.917	0.895
	Sensitivity	0.9	0.825	0.85
	Specificity	0.825	0.925	0.9
	False Alarm Rate	0.175	0.075	0.1
Significant disease	Recall	0.35	0.65	0.6
	Precision	0.778	0.684	0.706
	Sensitivity	0.35	0.65	0.6
	Specificity	0.967	0.9	0.917
	False Alarm Rate	0.033	0.1	0.083
Occlusive disease	Recall	0.95	0.95	0.95
	Precision	0.679	0.76	0.76
	Sensitivity	0.95	0.95	0.95
	Specificity	0.85	0.9	0.9
	False Alarm Rate	0.15	0.1	0.1

Table C.9: Performance metrics of the best performing ANN structures presented with data set A8.

Performance metric		Performance without SBI 10	Performance with SBI 20
Percentage correct		80%	82.5%
No significant disease	Recall	0.925	0.875
	Precision	0.881	0.897
	Sensitivity	0.925	0.875
	Specificity	0.875	0.9
	False Alarm Rate	0.125	0.1
Significant disease	Recall	0.65	0.6
	Precision	0.619	0.75
	Sensitivity	0.65	0.6
	Specificity	0.867	0.933
	False Alarm Rate	0.133	0.067
Occlusive disease	Recall	0.7	0.95
	Precision	0.824	0.76
	Sensitivity	0.7	0.95
	Specificity	0.95	0.9
	False Alarm Rate	0.05	0.1

Table C.10: Performance metrics of the best performing ANN structures presented with data set A9.

Performance metric		Performance without SBI 30-5	Performance with SBI 20-10
Percentage correct		82.5%	85%
No significant disease	Recall	0.875	0.925
	Precision	0.921	0.902
	Sensitivity	0.875	0.925
	Specificity	0.925	0.9
	False Alarm Rate	0.075	0.1
Significant disease	Recall	0.75	0.65
	Precision	0.682	0.765
	Sensitivity	0.75	0.65
	Specificity	0.883	0.933
	False Alarm Rate	0.117	0.067
Occlusive disease	Recall	0.8	0.9
	Precision	0.8	0.818
	Sensitivity	0.8	0.9
	Specificity	0.933	0.933
	False Alarm Rate	0.067	0.067

Table C.11: Performance metrics of the best performing ANN structures presented with data set A10.

Performance metric		Performance without SBI 20-30	Performance with SBI 10-40
Percentage correct		75%	80%
No significant disease	Recall	0.875	0.825
	Precision	0.897	0.868
	Sensitivity	0.875	0.825
	Specificity	0.9	0.875
	False Alarm Rate	0.1	0.125
Significant disease	Recall	0.55	0.6
	Precision	0.524	0.706
	Sensitivity	0.55	0.6
	Specificity	0.833	0.917
	False Alarm Rate	0.167	0.083
Occlusive disease	Recall	0.7	0.95
	Precision	0.7	0.76
	Sensitivity	0.7	0.95
	Specificity	0.9	0.9
	False Alarm Rate	0.1	0.1

Table C.12: Performance metrics of the best performing ANN structures presented with data set A11.

Performance metric		Performance without SBI	Performance with SBI	
		5	5-20	10-20
Percentage correct		78.75%	80%	
No significant disease	Recall	0.8	0.8	0.825
	Precision	0.914	0.889	0.892
	Sensitivity	0.8	0.8	0.825
	Specificity	0.925	0.9	0.9
	False Alarm Rate	0.075	0.1	0.1
Significant disease	Recall	0.7	0.7	0.65
	Precision	0.636	0.667	0.722
	Sensitivity	0.7	0.7	0.65
	Specificity	0.867	0.883	0.917
	False Alarm Rate	0.133	0.117	0.083
Occlusive disease	Recall	0.85	0.9	0.9
	Precision	0.739	0.783	0.72
	Sensitivity	0.85	0.9	0.9
	Specificity	0.9	0.917	0.883
	False Alarm Rate	0.1	0.083	0.117

Table C.13: Performance metrics of the best performing ANN structures presented with data set A12.

Performance metric		Performance without SBI 10-30	Performance with SBI 5-5
Percentage correct		76.25%	83.75%
No significant disease	Recall	0.825	0.925
	Precision	0.892	0.902
	Sensitivity	0.825	0.925
	Specificity	0.9	0.9
	False Alarm Rate	0.1	0.1
Significant disease	Recall	0.6	0.55
	Precision	0.632	0.846
	Sensitivity	0.6	0.55
	Specificity	0.883	0.967
	False Alarm Rate	0.117	0.033
Occlusive disease	Recall	0.8	0.95
	Precision	0.667	0.731
	Sensitivity	0.8	0.95
	Specificity	0.867	0.883
	False Alarm Rate	0.133	0.117